Title
Robust Control of the Sit-To-Stand Movement for Powered Lower Limb Orthoses

Author
Narvaez Aroche, Octavio

Publication Date
2019

Peer reviewed|Thesis/dissertation

Robust Control of the Sit-To-Stand Movement for Powered Lower Limb Orthoses

by

Octavio Narvaez Aroche

A dissertation submitted in partial satisfaction of the

requirements for the degree of

Doctor of Philosophy

in

Engineering - Mechanical Engineering

in the

Graduate Division

of the

University of California, Berkeley

Committee in charge:

Professor Andrew Packard, Chair
Professor Murat Arcak
Professor Francesco Borrelli

Spring 2019

Robust Control of the Sit-To-Stand Movement for Powered Lower Limb Orthoses

Abstract

Robust Control of the Sit-To-Stand Movement for Powered Lower Limb Orthoses

by

Octavio Narvaez Aroche

Doctor of Philosophy in Engineering - Mechanical Engineering

University of California, Berkeley

Professor Andrew Packard, Chair

Safety in the execution of the sit-to-stand movement is a key feature for wide adoption of powered lower limb orthoses that assist the mobility of patients with complete paraplegia. This work provides techniques for planning the motion of these medical devices to yield biomechanically sound configurations, designing tracking controllers for the reference trajectories of the movements, evaluating the robustness of the controllers against parameter uncertainty, and assessing the ability of a proxy for the user to coordinate with the control input during rehabilitation and physical therapy sessions. Although our ideas can be applied to analyze any powered orthosis in the market, the featured numerical simulations consider a minimally actuated orthosis at the hips.

The orthosis and its user are modeled as a three-link planar robot. The reference trajectories for the angular position of the links are defined from the desired behavior for the Center of Mass of the system, and the corresponding input trajectory is obtained using a computed torque method with control allocation. With the Jacobian linearization of the dynamics about the reference trajectories, a pool of finite time horizon LQR gains are designed assuming that there is control authority over the actuators of the orthosis, and the torque and forces that are applied by the user. Conducting reachability analysis, we define a performance metric for the robustness of the closed-loop system against parameter uncertainty, and choose the gain from the pool that optimizes it. Replacing the presumed controlled actions of the user with an Iterative Learning Control algorithm as a substitute for human experiments, we find that the algorithm obtains torque and forces that result in successful sit-to-stand movement, regardless of parameter uncertainty, and factors deliberately introduced to hinder learning. Thus we conclude that it is reasonable to expect that the superior cognitive skills of real users will enable them to synchronize with the controller of the hips through training. Further tests are performed to verify the robustness of the system in feedback with the LQR gain in the presence of measurement noise, and model uncertainty.

We believe that our tests can set a good benchmark to systematically choose actuators for fitting a large variety of users, and develop a protocol for assessing the robustness of the sit-to-stand movement in clinical trials. This would then help to close the gap between these medical devices and standing wheelchairs, which still remain the most reliable mobility solution for patients with complete paraplegia.

¿Qué es la vida? Un frenesí.
¿Qué es la vida? Una ilusión,
una sombra, una ficción;
y el mayor bien es pequeño;
que toda la vida es sueño,
y los sueños, sueños son.

Fragmento del monólogo de Segismundo en
"La Vida es Sueño" por Calderón de la Barca.

Para los soñadores... No hay muros que nos detengan.

What is life? A frenzy.
What is life? An illusion,
a shadow, a fiction;
and the greatest good is but small;
that all life is a dream,
and dreams themselves, are dreams.

Excerpt from the reflections of Segismundo in
"Life is a Dream" by Calderón de la Barca.

For the dreamers... No walls can stop us.

Contents

List of Figures

List of Tables

Acknowledgments

The contents of this book encompass six years of intensive learning at U.C. Berkeley, and while that might sound overwhelming on itself, the reality is that those six years are part of a much longer and complex story arch. Some might say that it dates back to the first half of the 20th century, when my grandparents left their small villages in Oaxaca behind, and headed to Mexico City in search of better horizons. While I inherited their courage and hard work, and I hope that they would be proud of my accomplishments, I know for sure that the idea of pursuing a Ph.D. was a self-inception, spurred by my dreams about unveiling the secrets for creating new technologies. The road was longer and more winding than what I could had possibly imagined, and I can only be grateful that in the midst of the chaos driving our lives, mine converged here. There are truly no words to describe my sense of self-fulfillment.

This quantum leap would had been impossible without the most important supporters in my life: my parents María Luisa and Octavio, and sisters Marilú and Mili. Figure A.3f is a reflection of my unconditional love for you. Mom, you are the light that guides me and you gave me all the affection I needed. I try to carry myself with the highest example of grace and righteousness that you have set for us. Dad, there are still plenty of tricks to be learned - your patience and perseverance have inspired me to never give up, and there is nothing like your words of wisdom whenever I feel lost. Marilú and Mili, you have endured my absence the most, and yet you have always been there for me. That speaks louder than words about your love. Marilú, I admire your ability to look at the bright side of life, and enjoy it to the fullest. Mili, your sensitivity has no match and it means a lot that you still consider me as your rock. I sincerely hope I will not let you down.

Aunt Tatá, your beautiful letters and persistent devotion kept me motivated in the face of adversity. Uncle David, you never stop rooting for me. Uncle Carlos, you have shown me the importance of being true to oneself, and to never look back. Uncle Luis, you set the foundation of my career by patiently teaching me how to use the IBM PS/2 and opened the gates to the fascinating world of engineering. I could not be more thankful to you.

Ema, you are an amazing godmother, always watching my path with love and encouragement.

The best years of my youth will always belong to the Colegio Madrid, not only for providing the great times and teachers that shaped my character, but also for being the stage where I built my everlasting relationship with Adrián, Pollo, David C., Teo, Arturo, Moy, Ulises, David P., and Manolo. Our paths might have diverged over time, but the brotherhood remains.

I am grateful to my gymnastics instructors Abraham, Chispa, and Chucho, who taught me that only practice makes perfect. As well to my guitar instructor, counselor, and friend Hugo, who in addition contributed on putting together Known Return. Sharon, Max, and Poncho, the music we created resonates forever in my heart.

The intellectual growth at my alma mater, the School of Engineering of the Universidad Nacional Autónoma de México (UNAM), was the cornerstone for succeeding at U.C. Berkeley. I am glad that I had the full support from Professors Alejandro Ramírez-Reivich, Marcelo López-Parra, Vicente Borja-Ramírez, and Francisco Cuenca-Jiménez. Thank you Edmundo Rocha-Cózatl for giving me the Controls bug. UNAM also gave me the opportunity of making great friends in Nayeli, Alejandra, Ezequiel, Everardo, Rafa, and Mike. Mike, I have yet to meet someone in Mechatronics

that surpasses your talent or passion. It saddens me that you left us too soon, you would had certainly changed the world.

Gaby, I treasure the great adventures that we had together, you made me very happy over the time we shared together, and helped me grow in ways that I had never imagined, I am full of gratitude towards you.

Juan Pablo, no one has believed more in my engineering skills than you. Developing the delta robots at Automatische Technik was a dream come true and the best part of it is that we have remained as close as brothers ever since.

Thank you to the families Narváez-Manzo, Ruiz-Gutiérrez, Furlong Rodríguez, Agulleiro-Tostado, Martínez-Ruiz, Navarro-Bribiesca, and Tostado-Rodríguez, for sharing wonderful moments with us, and supporting the endeavors of the Narváez-Aroche family through the years. I owe a special thanks to Mario, for helping me relocate to California and having look over my well being ever since.

Patricia, you were my closest companion during the Ph.D. program and I am forever in debt for your lovely help and support. I will hold you, Katrina, Skye, Ciela, and Todd very close to my heart.

Antoine you were not a good housemate, but a terrific one. Melissa, you could not had arrived to La Loma at a better time - the bike rides, sunsets, puzzles, moon sights, and music we shared were crucial for getting me over the toughest months of my life at Berkeley. I really value your friendship and I look forward to crossing paths again with you.

Thank you to Manuel, Esteban, Cecilia, Helke, César, Dany, Diego, Gerardo, Jaya, Julio, Nicolás, and Alfonso for including me as a founding member of the Mexican Association of Students at Berkeley (MEXASB). It was an honor to be elected President of the Association, and a real pleasure to work together with Ana Sofía, Daniela, Paloma, Carla, Cindy, Sofía, Nain, Jorge, Marcos, Luis, Augusto, and Héctor for organizing all the activities.

I am grateful with my friends from the Human Engineering and Robotics Laboratory (HEL) Lily, Minerva, Yoon, Lydia, Hayley, Mimi, Stephen, Michael, Wayne, Jason, Brad, Nick, Logan, Nate, Nathan, José, and Lee for making the transition from industry to UC Berkeley as smooth as it was. A special shout-out to Homayoon Kazerooni for granting me admission to HEL. I feel flattered that you decided to use the name of Phoenix for the medical exoskeleton built by SuitX after my recommendation.

My dear friend Grace, I am proud that we had a shared vision of the purpose and importance of graduate school, and managed to complete the program despite all the obstacles.

The Green Yogi was a true haven during my time in Berkeley, and I deeply appreciate the teachings of Kari, Maria-Christina, Reba, and Alyssa. Namaste.

Thank you Capitán Hector, Eric, and Yujia for your guidance during the job hunting season.

Maria and Karla, thanks for your artistic contributions in Figures 1.1 and 2.1.

It was a privilege to work with Pierre-Jean and Stephen for the contents of Chapters 4 and 5. The knowledge that I got from our conversations is invaluable.

I would like to extend my gratitude to my dissertation and qualifying exam committees. The inspiring classes by Professors Alice Agogino, Francesco Borrelli, Karl Hedrick, Pieter Abbeel, and Roberto Horowitz made me feel that I was truly surrounded by the best. Prof. Murat Arcak, I

appreciate your careful review of this document, your insightful comments regarding our research, and really going beyond to provide me support. Thanks to Prof. Kameshwar Poolla for bringing his unique sense of humor, Aeron chairs, and Glassboards into the Berkeley Center for Control and Identification (BCCI).

I cannot think of better colleagues than the remarkable people I met at BCCI. Chris, Jared, Jon, Deepan, Arun, Jim, Max, Maria, Wei, Momo, Sam, Kia, Pratyush, Donya, Henning, Junjie, Kate, Hamid, Sen, Akhil, Emmanuel, and Galaxy. We were together in sickness, and health, through graveyard shifts, and karaoke nights. You embraced my simple jokes, and randomness, but most importantly, you gave me a meaningful role in your lives that made me feel that I really belonged here. I was very fortunate to have shared this dream with you. Otherwise, I would not had made it through the end. Saying that I will miss you is an understatement. You've Got A Friend In Me.

Andy, no one knows me from the intellectual standpoint better than you, and there is no one else I would rather have as a mentor. I could not ask for a better example of resiliency in the face of adversity, and devotion to excellence. Even when you were the toughest, I knew that you were committed to my growth, and you were trying to push me forward. When I first moved into our lab you told me that someday I was going to regret it... I do not think I will ever do that. If anything, I only wish I had arrived earlier in my career, and in better shape to do research with you. I will always thank you from the bottom of my heart for giving me the extraordinary opportunity of being your student. Learning from you was, by far, the best part of the Ph.D. program.

Finally, I would like to gratefully acknowledge the Consejo Nacional de Ciencia y Tecnología (CONACYT), the Fulbright-García Robles program, the University of California Institute for Mexico and the United States (UC MEXUS), and the FANUC Corporation through the FANUC Chair in Mechanical Engineering at UC Berkeley for the fellowships that made possible my Ph.D.

This research used the Savio computational cluster resource provided by the Berkeley Research Computing program at the University of California, Berkeley (supported by the UC Berkeley Chancellor, Vice Chancellor for Research, and Chief Information Officer).

Chapter 1

Introduction

Wearable robots are complex biomechatronics systems that must work in synchrony with the body of its user in order to perform a mechanical task. They can be worn in series to replace missing extremities (powered prostheses), or in parallel to provide power augmentation or rehabilitation (powered orthoses) [1]. Powered lower limb orthoses (PLLOs) are wearable robots designed as medical devices that aid the mobility and enhance the strength of the legs or their individual joints to assist standing and/or walking. We study a class of these orthoses (also referred to as medical exoskeletons) whose purpose is to restore the gait of people with complete paralysis of the lower part of the body ($\approx 114,000$ individuals in the USA [2]), by providing physical support and load transfer to the ground with externally coupled rigid links. Their users must have good mobility in hands, arms, and shoulders; as well as healthy enough skeletal, cardiovascular, vestibular, and visual systems to tolerate standing.

The majority of state of the art PLLOs such as EksoGT [3], HAL [4], Indego [5], ReWalk [6], and Roki [7] provide actuation at the hips and knees, and rely on the interaction of their users with the ground by means of crutches. Inspired by the gait of bilateral transfemoral amputees with passive knee prostheses [8], PhoeniX [9] uses a minimally actuated architecture where torque is exclusively applied at the hips as a key feature to reduce mass, design complexity, and ultimately cost [10]. Resembling fully actuated bipedal robots, ATALANTE [11], and REX [12] are equipped with actuators at the hips, knees, and ankles to allow hands-free walking.

By enabling people with paraplegia to perform ambulatory functions, PLLOs target to prevent conditions that arise from prolonged sitting, e.g., osteoporosis, muscular atrophy, pressure ulcers, decreased blood flow to the legs, renal and urinary tract calculi, and decreased gastrointestinal activity. Nevertheless, in order to be able to walk, users need to safely perform the sit-to-stand movement first.

The sit-to-stand (STS) movement is the sequence of actions that are executed for rising from a chair, in order to stabilize the center of mass (CoM) of the human body directly above the support polygon created by the contact of the feet with the ground. Biomechanically, it is considered a complex daily living activity because it requires adequate position and torque control at each joint of the legs, precise spatial and temporal coordination of all body segments with feedback from the equilibrium sense [13], and demands more strength and greater ranges of motion than walking or

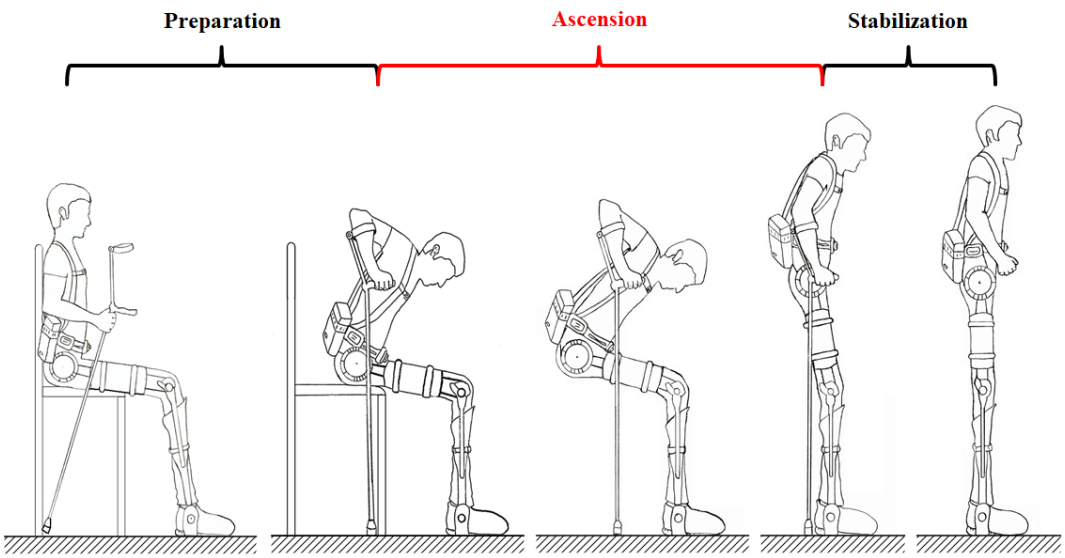

Figure 1.1: Phases of a sit-to-stand movement for a powered lower limb orthosis.

stair climbing [14].

The STS movement is studied in three distinctive phases: preparation, ascension, and stabilization, as illustrated in Figure 1.1. In the preparation phase the user donning the PLLO reaches for crutches with the intention to rise, moves to the edge of the chair, leans the torso forward, and puts the crutches in a comfortable position for propelling upwards. Ascension starts at seat-off and ends when the links of the shanks and thighs segments almost align with the vertical, and the torso has a slight forward tilt, with all angular velocities close to zero in order to facilitate stabilization about the standing position. Once equilibrium is reached, the crutches are no longer required for support. Ascension is the most challenging phase because it requires precise coordination between the actuators of the PLLO and the loads applied by the upper limbs of the user to avoid sit-back or step failures [15].

Most of the publications on the control of assistive devices focus almost entirely on their walking strategies and scarcely mention the STS movement (e.g., [16–19]). Therefore, this dissertation aims to provide analysis tools for the ascension phase of PLLOs that can be used to determine the reference trajectories that better balance the input applied by the actuators available in the device, and the loads required from the user; predict if a controller could overcome the daily changes in the weight of a user without dangerous degradation of its performance; and evaluate if a user would be able to learn how to coordinate with the input commanded by a controller. These have all been previously identified as key technical challenges to yield the desired rehabilitation of the users of assistive devices [20]. The content and contributions of each chapter are briefly described below.

Chapter 2 presents a strategy for planning the ascension phase of the sit-to-stand movement of powered lower limb orthoses (PLLOs). Modeling the system as a three rigid link planar robot, we rely on its kinematic equations to obtain a transformation that allows us to compute reference trajectories for the angular positions, velocities, and accelerations of the links, starting from a

desired kinematic behavior for the center of mass of the robot and the link representing the thighs segment. Our STS motion planning strategy reduces the task to only choosing initial and final points with zero slope boundary conditions that result in simulations of biomechanically sound movements. The material in this chapter is reported in [21].

Chapter 3 derives feedback linearization and finite time horizon LQR controllers to track the reference trajectories of STS movements under the provisional assumption that the controllers have authority not only over the torque of the actuators of the PLLO, but also over the torque and forces at the shoulders of the user. The material in this chapter is reported in [21, 22].

Chapter 4 provides a performance metric to quantify the robustness against parameter uncertainty of a controller for the ascension phase of a PLLO using a sensitivity-based reachability analysis for computing over-approximations of reachable sets. We select from a pool of finite horizon LQR controllers the one that optimizes the robust performance metric. The material in this chapter is reported in [23].

Chapter 5 proposes an ILC algorithm to simulate the loads at the shoulders that would be applied by a user, when being trained to perform the ascending phase of the STS movement in closed-loop with an optimal controller driving the actuators of the PLLO. To avoid identification experiments that would expose the user to non validated controllers, we tune the internal gains of the ILC with a reinforcement learning approach. We confirm through simulations that the simple proxy for the user achieves successful STS movements after a reasonable number of iterations despite considerable weight fluctuations and factors hindering learning. The material in this chapter is expanded on from [24].

Chapter 6 derives finite time horizon LQG controllers to track the reference trajectories of STS movements in the presence of measurement noise, considering different configurations of rotary encoders at the joints of the PLLO to identify the output that in feedback with the controller gives the best robustness against parameter uncertainty.

Chapter 7 tests the robustness in the presence of model uncertainty of the finite time horizon LQR controller chosen with the proposed performance metric, by modeling the system with a four-link planar robot that allows the movement of the neck, and head of the user with respect to the torso.

Note that the contents of Chapters 5 and 7 provide analysis tools to assess the performance of the controller that is to be implemented in the PLLO with the results in Chapters 2, 3, 4, and 6. This is discussed in detail as part of the conclusions in **Chapter 8**.

Companies producing PLLOs for people with complete paraplegia are moving towards stand-alone mobility solutions that can be operated outside of rehabilitation centres, and without the supervision of a specially trained physical therapist. This calls for extensive clinical trials for certifying the safety and feasibility of their designs to stand up and walk under a wide variety of conditions, as was done in [25, 26] to certify the potential benefits on gait function and balance. Even though our simulations cannot replace such tests, they can be valuable tools for improving both the mechanical design and control strategies of the devices prior to a comprehensive training protocol for the STS movement.

1.1 Notation

Denote $c_i := \cos\theta_i$, $c_{ij} := \cos\left(\theta_i + \theta_j\right)$, $c_{ijk} := \cos\left(\theta_i + \theta_j + \theta_k\right)$, $c_{ijkl} := \cos\left(\theta_i + \theta_j + \theta_k + \theta_l\right)$, and similarly for $\sin(\cdot)$.

For $a, b \in \mathbb{R}^n$ we use the notation $a \leq b$ to mean $a_i \leq b_i \; \forall i$, with similar element-wise definitions for $\leq$, $\geq$, and $>$.

Define an interval of $\mathbb{R}^n$ as $[a,b] := \{\xi \in \mathbb{R}^n | a \leq \xi \leq b\} \subseteq \mathbb{R}^n$, and compute its volume $\text{vol}([a,b]) \in \mathbb{R}$ as:

$$\text{vol}([a,b]) = \prod_{i \in \{1,\ldots,n\}} (b_i - a_i).$$

Define the saturation of $c \in \mathbb{R}^n$ over the interval $[a, b] \subseteq \mathbb{R}^n$ as the element-wise min/max operation:

$$\text{sat}(c, [a, b]) := \min(b, \max(a, c)).$$

For matrices $\Lambda, \underline{\Lambda}, \overline{\Lambda} \in \mathbb{R}^{n \times m}$ we write $\Lambda \in \left[\underline{\Lambda}, \overline{\Lambda}\right]$ if $\Lambda_{ij} \in \left[\underline{\Lambda}_{ij}, \overline{\Lambda}_{ij}\right] \; \forall (i, j) \in \{1, \ldots, n\} \times \{1, \ldots, m\}$.

The center of the interval matrix $\left[\underline{\Lambda}, \overline{\Lambda}\right]$ is represented by $\hat{\Lambda}$.

The finite time horizon 2-norm of a signal $v : [0,T] \to \mathbb{R}^n$ is defined as

$$\|v\|_{2,[0,T]} := \left(\int_0^T v(t)^\top v(t)\, dt\right)^{1/2}.$$

If $\|v\|_{2,[0,T]}$ is finite then $v \in \mathcal{L}_2[0,T]$.

1.2 Acronyms

STS sit-to-stand.

STS 1 ascending phase of a sit-to-stand movement starting with the shanks and torso segments parallel to the vertical, and the thighs segment parallel to the horizontal, by using the initial condition $\hat{\theta}(t_0) = [90[^\circ]; -90[^\circ]; 90[^\circ]]$.

STS 2 ascending phase of a sit-to-stand movement starting with the thighs segment parallel to the horizontal, and the center of mass vertically aligned with the ankle joints, by using the initial condition $\hat{\theta}(t_0) = [120[^\circ]; -120[^\circ]; 111[^\circ]]$.

PLLO powered lower limb orthosis.

PLLOs powered lower limb orthoses.

CoM center of mass.

CoMs centers of mass.

LQR linear-quadratic regulator.

LTV linear time-varying.

ILC Iterative Learning Control.

LQG linear-quadratic Gaussian.

Chapter 2

Sit-To-Stand Motion Planning

Based on the evidence that three rigid link dynamic models have been used to accurately describe the STS movement of different subjects [15], we model the system comprised of a PLLO and its user as a three-link planar robot, where the interaction of the subject with the ground through crutches is represented by reactive loads acting on the location of the shoulder joints. Since biomechanical studies measure the kinematics of the CoM of the human body to classify and assess the dynamic balance of the STS movement [27] rather than joint angles, we propose to plan the ascension phase of the STS movement in terms of the desired trajectory for the position of the CoM of the three-link robot, and the angular position of the link representing the segment of the thighs. In order to determine the angular configurations of the remaining links (representing the segments of the shanks, and the torso) required for the desired motion, we use the kinematic equations of the three-link robot to derive a nonlinear mapping that is valid for all feasible and realistic ascension maneuvers. With reference trajectories for the angular positions, velocities, and accelerations of the links at hand, we use a computed torque approach for obtaining reference trajectories for the input. To illustrate our motion planning method, we compute reference trajectories for two relevant STS movements, considering the three main architectures of commercially available PLLOs.

2.1 Model for Powered Lower Limb Orthoses and their Users

Assuming sagittal symmetry, no movement of the neck, and head relative to the torso, and that the feet are fixed to the ground, we model the user, crutches and PLLO as a three-link planar robot with revolute joints coaxial to the ankles, knees and hips, as shown in Figure 2.1. θ_1 is the angular position of link 1 (shanks) measured from the horizontal, θ_2 is the angular position of link 2 (thighs) relative to link 1, and θ_3 is the angular position of link 3 (torso, neck, and head) relative to link 2. The system parameters are the masses of the links m_1, m_2, and m_3; the moments of inertia about their respective CoMs I_1, I_2, and I_3; their lengths l_1, l_2, and l_3; and the distances of their CoMs from the joints l_{c_1}, l_{c_2}, and l_{c_3}. Depending on its architecture, the actuators of an orthosis might exert torque about the ankles τ_a, knees τ_k, and hips τ_h. The torque τ_s, horizontal force F_x, and vertical force F_y aim to capture the inertial and gravitational forces of the arms, as well as the loads

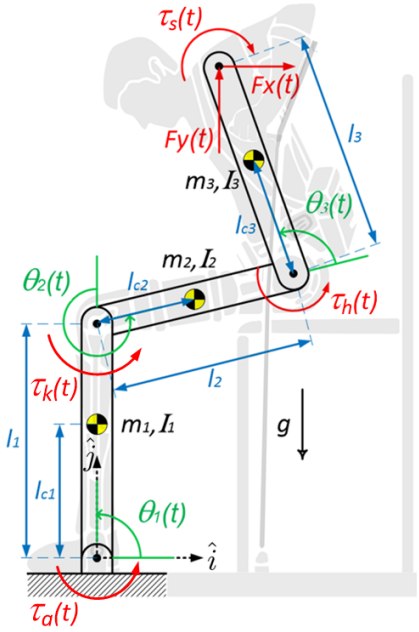

Figure 2.1: Three-link planar robot for modeling PLLOs during a STS movement.

applied on the shoulders by the user.

The Euler-Lagrange equations of the three-link planar robot in Figure 2.1 were obtained by using the symbolic multibody dynamics package PyDy (short for Python Dynamics) [28]. In terms of the joint angles $\theta := [\theta_1;\ \theta_2;\ \theta_3] \in \mathbb{R}^3$, the m external torques and forces of the PLLO lumped in the input of the system $u \in \mathbb{R}^m$, and parameter

$$p := \left[m_1;\ m_2;\ m_3;\ I_1;\ I_2;\ I_3;\ l_1;\ l_2;\ l_3;\ l_{c_1};\ l_{c_2};\ l_{c_3}\right] \in \mathbb{R}^{12}, \tag{2.1}$$

the Euler-Lagrange equations can be written as

$$M(\theta, p)\ddot{\theta} + F\left(\theta, \dot{\theta}, p\right) = A_\tau(\theta, p)u, \tag{2.2}$$

where $M(\theta, p) \in \mathbb{R}^{3\times3}$, $M(\theta, p) \succ 0$ is the symmetric mass matrix of the system, $F\left(\theta, \dot{\theta}, p\right) \in \mathbb{R}^3$ is the vector of energy contributions due to the acceleration of gravity and Coriolis forces, and $A_\tau(\theta, p) \in \mathbb{R}^{3\times m}$ is the generalized force matrix, whose entries relative to the loads contained in u are described below.

For notational convenience define the coefficients

$$\begin{aligned} k_0(p) &:= (m_1 + m_2 + m_3)^{-1}, & k_1(p) &:= l_{c_1}m_1 + l_1(m_2 + m_3), \\ k_2(p) &:= l_{c_2}m_2 + l_2m_3, & k_3(p) &:= l_{c_3}m_3, \end{aligned}$$

their explicit dependence with respect to the parameter p is omitted onwards for compactness.

The entries of the symmetric mass matrix $M(\theta, p) \in \mathbb{R}^{3\times3}$ in (2.2) are

$$
\begin{aligned}
M_{11} =& I_1 + I_2 + I_3 + l_{c_1}^2 m_1 + m_2\left(l_1^2 + 2l_1 l_{c_2} c_2 + l_{c_2}^2\right) + m_3\left(l_1^2 + 2l_1 l_2 c_2 + 2l_1 l_{c_3} c_{23} + l_2^2 + 2l_2 l_{c_3} c_3 + l_{c_3}^2\right)\\
M_{12} =& I_2 + I_3 + l_{c_2} m_2\left(l_1 c_2 + l_{c_2}\right) + m_3\left(l_1 l_2 c_2 + l_1 l_{c_3} c_{23} + l_2^2 + 2l_2 l_{c_3} c_3 + l_{c_3}^2\right)\\
M_{13} =& I_3 + l_{c_3} m_3\left(l_1 c_{23} + l_2 c_3 + l_{c_3}\right)\\
M_{22} =& I_2 + I_3 + l_{c_2}^2 m_2 + m_3\left(l_2^2 + 2l_2 l_{c_3} c_3 + l_{c_3}^2\right)\\
M_{23} =& I_3 + l_{c_3} m_3\left(l_2 c_3 + l_{c_3}\right)\\
M_{33} =& I_3 + l_{c_3}^2 m_3.
\end{aligned}
$$

The vector of energy contributions due to the acceleration of gravity $\mathrm{g} := 9.81\,[m/s^2]$ and Coriolis forces $F\left(\theta, \dot{\theta}, p\right) \in \mathbb{R}^3$ is

$$
F\left(\theta, \dot{\theta}, p\right) = \Omega(\theta, p)\begin{bmatrix} \dot{\theta}_1^2 \\ \left(\dot{\theta}_1 + \dot{\theta}_2\right)^2 \\ \left(\dot{\theta}_1 + \dot{\theta}_2 + \dot{\theta}_3\right)^2 \end{bmatrix} + \mathrm{g}\begin{bmatrix} k_1 c_1 + k_2 c_{12} + k_3 c_{123} \\ k_2 c_{12} + k_3 c_{123} \\ k_3 c_{123} \end{bmatrix},
$$

with $\Omega(\theta, p) \in \mathbb{R}^{3\times3}$ defined as

$$
\Omega(\theta, p) := \begin{bmatrix} l_1\left(k_2 s_2 + k_3 s_{23}\right) & -k_2 l_1 s_2 + k_3 l_2 s_3 & -k_3\left(l_1 s_{23} + l_2 s_3\right) \\ l_1\left(k_2 s_2 + k_3 s_{23}\right) & k_3 l_2 s_3 & -k_3 l_2 s_3 \\ l_1 k_3 s_{23} & k_3 l_2 s_3 & 0 \end{bmatrix}.
$$

For minimally actuated PLLOs at the hips [9], where $u = \left[\tau_h;\ \tau_s;\ F_x;\ F_y\right]$, the generalized force matrix $A_\tau(\theta, p) \in \mathbb{R}^{3\times4}$ is

$$
A_\tau(\theta, p) = \begin{bmatrix} 0 & -1 & -l_1 s_1 - l_2 s_{12} - l_3 s_{123} & l_1 c_1 + l_2 c_{12} + l_3 c_{123} \\ 0 & -1 & -l_2 s_{12} - l_3 s_{123} & l_2 c_{12} + l_3 c_{123} \\ 1 & -1 & -l_3 s_{123} & l_3 c_{123} \end{bmatrix}. \tag{2.3}
$$

For PLLOs with actuators at the knees and hips [3–7], where $u = \left[\tau_k;\ \tau_h;\ \tau_s;\ F_x;\ F_y\right]$, the generalized force matrix $A_\tau(\theta, p) \in \mathbb{R}^{3\times5}$ is

$$
A_\tau(\theta, p) = \begin{bmatrix} 0 & 0 & -1 & -l_1 s_1 - l_2 s_{12} - l_3 s_{123} & l_1 c_1 + l_2 c_{12} + l_3 c_{123} \\ 1 & 0 & -1 & -l_2 s_{12} - l_3 s_{123} & l_2 c_{12} + l_3 c_{123} \\ 0 & 1 & -1 & -l_3 s_{123} & l_3 c_{123} \end{bmatrix}. \tag{2.4}
$$

For hands-free, fully actuated PLLOs [11, 12], where $u := [\tau_a;\ \tau_k;\ \tau_h]$, the generalized force matrix is the identity $A_\tau(\theta, p) = I_3$.

Three rigid link dynamic models of this form have been used to accurately describe the STS movement of human subjects [15].

2.2 Kinematics of the Center of Mass of the Three-Link Robot

The position $[x_{\text{CoM}}; y_{\text{CoM}}] \in \mathbb{R}^2$, velocity $[\dot{x}_{\text{CoM}}; \dot{y}_{\text{CoM}}] \in \mathbb{R}^2$, and acceleration $[\ddot{x}_{\text{CoM}}; \ddot{y}_{\text{CoM}}] \in \mathbb{R}^2$ coordinates of the CoM of the three-link robot, relative to the inertial frame $\hat{i}\hat{j}$ in Figure 2.1, are

$$x_{\text{CoM}} = k_0 (k_1 c_1 + k_2 c_{12} + k_3 c_{123}), \tag{2.5}$$
$$y_{\text{CoM}} = k_0 (k_1 s_1 + k_2 s_{12} + k_3 s_{123}), \tag{2.6}$$

$$\dot{x}_{\text{CoM}} = -\dot{\theta}_1 y_{\text{CoM}} - \dot{\theta}_2 k_0 (k_2 s_{12} + k_3 s_{123}) - \dot{\theta}_3 k_0 k_3 s_{123}, \tag{2.7}$$
$$\dot{y}_{\text{CoM}} = \dot{\theta}_1 x_{\text{CoM}} + \dot{\theta}_2 k_0 (k_2 c_{12} + k_3 c_{123}) + \dot{\theta}_3 k_0 k_3 c_{123}, \tag{2.8}$$

$$\begin{aligned}\ddot{x}_{\text{CoM}} = &-\dot{\theta}_1^2 x_{\text{CoM}} - \dot{\theta}_2^2 k_0 (k_2 c_{12} + k_3 c_{123}) - \dot{\theta}_3^2 k_0 k_3 c_{123} - 2\dot{\theta}_1 \dot{\theta}_2 k_0 (k_2 c_{12} + k_3 c_{123}) \\ &- 2 (\dot{\theta}_1 + \dot{\theta}_2) \dot{\theta}_3 k_0 k_3 c_{123} - \ddot{\theta}_1 y_{\text{CoM}} - \ddot{\theta}_2 k_0 (k_2 s_{12} + k_3 s_{123}) - \ddot{\theta}_3 k_0 k_3 s_{123},\end{aligned} \tag{2.9}$$

$$\begin{aligned}\ddot{y}_{\text{CoM}} = &-\dot{\theta}_1^2 y_{\text{CoM}} - \dot{\theta}_2^2 k_0 (k_2 s_{12} + k_3 s_{123}) - \dot{\theta}_3^2 k_0 k_3 s_{123} - 2\dot{\theta}_1 \dot{\theta}_2 k_0 (k_2 s_{12} + k_3 s_{123}) \\ &- 2 (\dot{\theta}_1 + \dot{\theta}_2) \dot{\theta}_3 k_0 k_3 s_{123} + \ddot{\theta}_1 x_{\text{CoM}} + \ddot{\theta}_2 k_0 (k_2 c_{12} + k_3 c_{123}) + \ddot{\theta}_3 k_0 k_3 c_{123}.\end{aligned} \tag{2.10}$$

If the position of the CoM is given for specific values of the parameters in p, (2.5) and (2.6) constitute a system of 2 equations in 3 unknowns. In order to have the same number of equations and unknowns, we could choose to give the angular position of any link. STS movements of healthy individuals exhibit continuous extension of the knee joints that can be approximated using simple monotonically increasing functions to describe the angular position of link 2 in Figure 2.1, whereas the joints at the ankles and hips have a more complex behavior. Therefore, defining $z := [\theta_2; x_{\text{CoM}}; y_{\text{CoM}}]$, we derive a transformation $h_1 : \mathbb{R}^3 \times \mathbb{R}^{12} \to \mathbb{R}^3$ of the form

$$\theta = h_1 (z, p),$$

that we can use to compute reference trajectories in the space of θ from natural looking STS movements planned in the space of z.

2.3 Transformation from the Space of z to the Space of θ

From equations (2.5) and (2.6), the position of the CoM of the three-link robot can be expressed as a sum of three vectors whose geometric representation is shown in Figure 2.2:

$$\begin{aligned}\begin{bmatrix} x_{\text{CoM}} \\ y_{\text{CoM}} \end{bmatrix} &= k_0 k_1 \begin{bmatrix} c_1 \\ s_1 \end{bmatrix} + k_0 k_2 \begin{bmatrix} c_{12} \\ s_{12} \end{bmatrix} + k_0 k_3 \begin{bmatrix} c_{123} \\ s_{123} \end{bmatrix} \\ &=: r_1 + r_2 + r_3.\end{aligned} \tag{2.11}$$

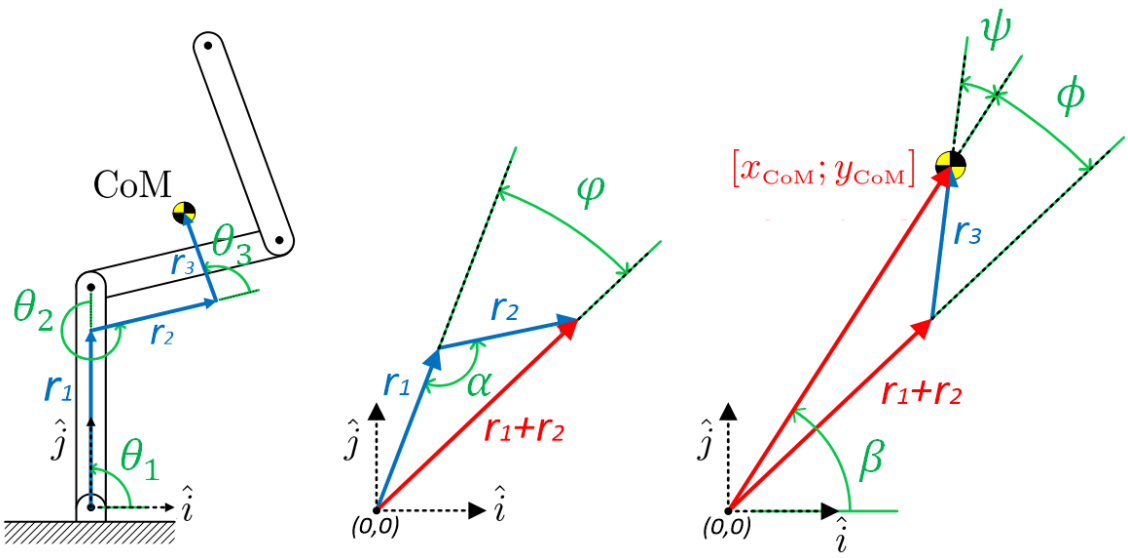

Figure 2.2: Geometric representation of vectors and angles used for expressing θ_1 and θ_3 as a function of $[x_{\mathrm{CoM}}; y_{\mathrm{CoM}}]$ and θ_2.

According to the angles drawn in Figure 2.2, we can establish the following relationships:

$$\alpha = \theta_2 - \pi,$$

$$\beta = \arctan\left(\frac{y_{\mathrm{CoM}}}{x_{\mathrm{CoM}}}\right), \tag{2.12}$$

$$\theta_1 = \beta - \phi + \varphi, \tag{2.13}$$

$$\theta_3 = \beta + \psi - (\theta_1 + \theta_2), \tag{2.14}$$

where for feasible and realistic STS movements $\phi \geq 0$, and $\varphi, \psi \in \left[-\frac{\pi}{2}, \frac{\pi}{2}\right]$.

Applying the law of cosines to the triangle formed by vectors $r_1 + r_2$, r_3, and $[x_{\mathrm{CoM}}; y_{\mathrm{CoM}}]$, as well as using the trigonometric identity $c_2 = c_{12}c_1 + s_{12}s_1$, we have

$$\begin{aligned}\phi(z) &= \arccos\left(\frac{\|r_3\|^2 - \|r_1 + r_2\|^2 - \left(x_{\mathrm{CoM}}^2 + y_{\mathrm{CoM}}^2\right)}{-2\,\|r_1 + r_2\|\sqrt{x_{\mathrm{CoM}}^2 + y_{\mathrm{CoM}}^2}}\right) \\ &= \arccos\left(\frac{(k_0k_3)^2 - k_0^2\left(k_1^2 + k_2^2 + 2k_1k_2c_2\right) - \left(x_{\mathrm{CoM}}^2 + y_{\mathrm{CoM}}^2\right)}{-2k_0\sqrt{k_1^2 + k_2^2 + 2k_1k_2c_2}\sqrt{x_{\mathrm{CoM}}^2 + y_{\mathrm{CoM}}^2}}\right).\end{aligned} \tag{2.15}$$

From the law of sines, for the triangle of vectors r_1, r_2, and $r_1 + r_2$, we know

$$\varphi(z) = \arcsin\left(\frac{\|r_2\|\sin\alpha}{\|r_1+r_2\|}\right) = \arcsin\left(\frac{k_2\sin(\theta_2-\pi)}{\sqrt{k_1^2+k_2^2+2k_1k_2c_2}}\right), \tag{2.16}$$

$$\psi(z) = \arcsin\left(\frac{\|r_1+r_2\|\sin\phi(z)}{\|r_3\|}\right) = \arcsin\left(\frac{\sqrt{k_1^2+k_2^2+2k_1k_2c_2}\sin\phi(z)}{k_3}\right). \tag{2.17}$$

Plugging (2.12), (2.15), and (2.16) into (2.13), as well as (2.12), and (2.17) into (2.14), we define the transformation $h_1 : z, p \to \theta$ as

$$\theta = \begin{bmatrix} \arctan\left(\frac{y_{\text{CoM}}}{x_{\text{CoM}}}\right) - \phi(z) + \varphi(z) \\ \theta_2 \\ \arctan\left(\frac{y_{\text{CoM}}}{x_{\text{CoM}}}\right) + \psi(z) - (\theta_1(z) + \theta_2) \end{bmatrix} =: h_1(z,p). \tag{2.18}$$

Because this transformation relies on the triangulation of the vectors in equation (2.11), it does not hold in the vertical position, where $\theta_1 = \frac{\pi}{2}$ and $\theta_2 = \theta_3 = 0$.

From equations (2.7) and (2.8), the velocity of the CoM of the three-link robot is

$$\begin{bmatrix} \dot{x}_{\text{CoM}} \\ \dot{y}_{\text{CoM}} \end{bmatrix} = k_0\dot{\theta}_2 \begin{bmatrix} -k_2s_{12} - k_3s_{123} \\ k_2c_{12} + k_3c_{123} \end{bmatrix} + \begin{bmatrix} -y_{\text{CoM}} & -k_0k_3s_{123} \\ x_{\text{CoM}} & k_0k_3c_{123} \end{bmatrix} \begin{bmatrix} \dot{\theta}_1 \\ \dot{\theta}_3 \end{bmatrix}.$$

The determinant $k_0k_3s_{123}x_{\text{CoM}} - k_0k_3c_{123}y_{\text{CoM}} = 0$ if $\theta_1 + \theta_2 + \theta_3 = \arctan\left(\frac{y_{\text{CoM}}}{x_{\text{CoM}}}\right)$, and according to expressions (2.12) and (2.14) this condition will hold if and only if $\psi = 0$; which requires vectors $r_1 + r_2$ and r_3 to be aligned. In the case of feasible and realistic STS movements, this will only occur in the vertical position. For all other configurations, we calculate the angular velocities of links 1 and 3 as

$$\begin{aligned} \begin{bmatrix} \dot{\theta}_1 \\ \dot{\theta}_3 \end{bmatrix} &= \begin{bmatrix} -y_{\text{CoM}} & -k_0k_3s_{123} \\ x_{\text{CoM}} & k_0k_3c_{123} \end{bmatrix}^{-1} \left(\begin{bmatrix} \dot{x}_{\text{CoM}} \\ \dot{y}_{\text{CoM}} \end{bmatrix} - k_0\dot{\theta}_2 \begin{bmatrix} -k_2s_{12} - k_3s_{123} \\ k_2c_{12} + k_3c_{123} \end{bmatrix} \right) \\ &=: V(z, \dot{z}, p), \end{aligned}$$

so that the transformation $h_2 : z, \dot{z}, p \to \dot{\theta}$ is defined

$$\dot{\theta} = \begin{bmatrix} 1 & 0 \\ 0 & 0 \\ 0 & 1 \end{bmatrix} V(z, \dot{z}, p) + \begin{bmatrix} 0 \\ \dot{\theta}_2 \\ 0 \end{bmatrix} =: h_2(z, \dot{z}, p).$$

From equations (2.9) and (2.10), the acceleration of the CoM is

$$\begin{bmatrix} \ddot{x}_{\text{CoM}} \\ \ddot{y}_{\text{CoM}} \end{bmatrix} = a(h_1(z,p), h_2(z,\dot{z},p), \ddot{z}, p) + \begin{bmatrix} -y_{\text{CoM}} & -k_0k_3s_{123} \\ x_{\text{CoM}} & k_0k_3c_{123} \end{bmatrix} \begin{bmatrix} \ddot{\theta}_1 \\ \ddot{\theta}_3 \end{bmatrix},$$

where

$$a\left(\theta,\dot{\theta},\ddot{z},p\right) := -\begin{bmatrix} x_{\text{CoM}} & k_0\left(k_2c_{12}+k_3c_{123}\right) & k_0k_3c_{123} \\ y_{\text{CoM}} & k_0\left(k_2s_{12}+k_3s_{123}\right) & k_0k_3s_{123} \end{bmatrix}\begin{bmatrix} \dot{\theta}_1^2 \\ \dot{\theta}_2^2 \\ \dot{\theta}_3^2 \end{bmatrix} - 2k_0\dot{\theta}_1\dot{\theta}_2\begin{bmatrix} k_2c_{12}+k_3c_{123} \\ k_2s_{12}+k_3s_{123} \end{bmatrix}$$
$$- 2k_0k_3\left(\dot{\theta}_1+\dot{\theta}_2\right)\dot{\theta}_3\begin{bmatrix} c_{123} \\ s_{123} \end{bmatrix} + k_0\ddot{\theta}_2\begin{bmatrix} -k_2s_{12}-k_3s_{123} \\ k_2c_{12}+k_3c_{123} \end{bmatrix}.$$

Thus

$$\begin{bmatrix} \ddot{\theta}_1 \\ \ddot{\theta}_3 \end{bmatrix} = \begin{bmatrix} -y_{\text{CoM}} & -k_0k_3s_{123} \\ x_{\text{CoM}} & k_0k_3c_{123} \end{bmatrix}^{-1}\left(\begin{bmatrix} \ddot{x}_{\text{CoM}} \\ \ddot{y}_{\text{CoM}} \end{bmatrix} - a\left(h_1(z,p),h_2(z,\dot{z},p),\ddot{z},p\right)\right)$$

and we can define the transformation $h_3 : z,\dot{z},\ddot{z},p \to \ddot{\theta}$ as

$$\begin{aligned}\ddot{\theta} &= \begin{bmatrix} 1 & 0 \\ 0 & 0 \\ 0 & 1 \end{bmatrix}\begin{bmatrix} -y_{\text{CoM}} & -k_0k_3s_{123} \\ x_{\text{CoM}} & k_0k_3c_{123} \end{bmatrix}^{-1}\left(\begin{bmatrix} \ddot{x}_{\text{CoM}} \\ \ddot{y}_{\text{CoM}} \end{bmatrix} - a\left(h_1(z,p),h_2(z,\dot{z},p),\ddot{z},p\right)\right) + \begin{bmatrix} 0 \\ \ddot{\theta}_2 \\ 0 \end{bmatrix} \\ &=: h_3\left(z,\dot{z},\ddot{z},p\right).\end{aligned}$$

For compactness, we use

$$h\left(z,\dot{z},\ddot{z},p\right) := \left[h_1(z,p);\ h_2(z,\dot{z},p);\ h_3(z,\dot{z},\ddot{z},p)\right] \tag{2.19}$$

to denote the transformation from the space of z to the space of θ.

2.4 Reference Trajectories for the Sit-To-Stand Movement

To plan the ascension phase of the STS movement for PLLOs according to the desired angular position of the second link, and the position coordinates of the CoM of the three-link robot in Figure 2.1, we compute the reference trajectory $\hat{z}(t) := \left[\hat{\theta}_2(t);\hat{x}_{\text{CoM}}(t);\hat{y}_{\text{CoM}}(t)\right]$ over the time horizon $t \in \left[t_0,t_f\right]$ as

$$\begin{aligned}\hat{\theta}_2(t) &= \hat{\theta}_2(t_0) + \left(\hat{\theta}_2\left(t_f\right) - \hat{\theta}_2(t_0)\right)\Theta\left(t,t_f\right), \\ \hat{x}_{\text{CoM}}(t) &= \hat{x}_{\text{CoM}}(t_0) + \left(\hat{x}_{\text{CoM}}\left(t_f\right) - \hat{x}_{\text{CoM}}(t_0)\right)\Theta\left(t,t_f\right), \\ \hat{y}_{\text{CoM}}(t) &= \hat{y}_{\text{CoM}}(t_0) + \left(\hat{y}_{\text{CoM}}\left(t_f\right) - \hat{y}_{\text{CoM}}(t_0)\right)\Theta\left(t,t_f\right).\end{aligned} \tag{2.20}$$

For a rest-to-rest maneuver from $\hat{z}(t_0)$ to $\hat{z}\left(t_f\right)$, define $\Theta\left(t,t_f\right) := -2\frac{t^3}{t_f^3} + 3\frac{t^2}{t_f^2}$; which is the only cubic polynomial satisfying $\dot{\Theta}\left(t_0,t_f\right) = \dot{\Theta}\left(t_f,t_f\right) = 0$, $\Theta\left(t_0,t_f\right) = 0$, and $\Theta\left(t_f,t_f\right) = 1$.

STS movements planned in the space of z are mapped into reference trajectories in the space of θ by plugging the nominal value of the parameter $\hat{p}$, together with the evaluation of (2.20), and its first and second time derivatives for all $t \in \left[t_0,t_f\right]$ into transformation (2.19). So that

$$\left[\hat{\theta}(t);\ \dot{\hat{\theta}}(t);\ \ddot{\hat{\theta}}(t)\right] = h\left(\hat{z}(t),\dot{\hat{z}}(t),\ddot{\hat{z}}(t),\hat{p}\right). \tag{2.21}$$

We apply the computed torque method [29] to get reference trajectories for the input $\hat{u}(t) \in \mathbb{R}^m$. However, as the system of equations in (2.2) is underdetermined when $m > 3$, a control allocation problem [30] is solved at every $t \in \left[t_0, t_f\right]$ to minimize the 2-norm of the input weighted by $W_u \in \mathbb{R}^{m \times m}$ in the presence of box constraints $\underline{u}, \overline{u} \in \mathbb{R}^m$:

$$\begin{aligned} \hat{u}(t) = \underset{\xi \in \mathbb{R}^m}{\arg\min} \quad & \frac{1}{2} \left\| W_u \, \xi \right\|_2^2 \\ \text{subject to} \quad & \\ & A_\tau \left(\hat{\theta}(t), \hat{p} \right) \xi = M \left(\hat{\theta}(t), \hat{p} \right) \ddot{\hat{\theta}}(t) + F \left(\hat{\theta}(t), \dot{\hat{\theta}}(t), \hat{p} \right) \\ & \underline{u} \leq \xi \leq \overline{u}. \end{aligned} \tag{2.22}$$

This formulation allows to find reference trajectories for the inputs of every possible architecture of PLLO.

Different values for W_u, $\underline{u}$, and $\overline{u}$ might lead to different $\hat{u}(t)$ for the same $\hat{\theta}(t)$, $\dot{\hat{\theta}}(t)$, $\ddot{\hat{\theta}}(t)$, and $\hat{p}$. Since a subject pushes the crutches down to propel upwards during a STS movement, the constraint $F_y(t) \geq 0$ must always be imposed.

2.5 Reference Trajectories of Two Relevant Sit-To-Stand Movements for Different Architectures of PLLOs

There are two main strategies to execute STS movements, they are referred in the biomechanical literature as dynamic and quasi-static [13]. In a dynamic STS movement the torso generates forward momentum and transfers it into vertical momentum while ascending. In a quasi-static STS movement the CoM is vertically aligned with the feet prior to seat-off, and then the leg joints are slowly extended. Most healthy people use the quasi-static strategy because it is safer and reduces the overall work; however, people with reduced knee strength tend to use a dynamic strategy. We illustrate the motion planning method detailed in this chapter by obtaining reference trajectories of two ascension movements that mimic these strategies for three architectures of commercially available PLLOs.

The ascension phase of the dynamic STS movement (STS 1) starts with the shanks and torso segments parallel to the vertical, and the thighs segment parallel to the horizontal, as depicted in Figure 2.3a. Setting $\hat{\theta}(t_0) = [90[^\circ];\ -90[^\circ];\ 90[^\circ]]$ and considering the nominal parameter values

$$\begin{aligned} \hat{p} = [&9.68\,[\mathrm{kg}];\ 12.59\,[\mathrm{kg}];\ 44.57\,[\mathrm{kg}];1.16\left[\mathrm{kg}\cdot\mathrm{m}^2\right];\ 0.52\left[\mathrm{kg}\cdot\mathrm{m}^2\right];\ 2.56\left[\mathrm{kg}\cdot\mathrm{m}^2\right];\ldots \\ &0.53\,[\mathrm{m}];\ 0.41\,[\mathrm{m}];\ 0.52\,[\mathrm{m}];0.27\,[\mathrm{m}];\ 0.21\,[\mathrm{m}];\ 0.26\,[\mathrm{m}]], \end{aligned} \tag{2.23}$$

the corresponding initial position of the CoM of the three-link robot from (2.5) and (2.6) is $[\hat{x}_{\mathrm{CoM}}(t_0);\ \hat{y}_{\mathrm{CoM}}(t_0)] = [0.31;\ 0.67][\mathrm{m}]$. The quasi-static STS movement (STS 2) starts as shown in Figure 2.3b with the CoM of the robot and ankle joints vertically aligned by choosing the initial condition $\hat{\theta}(t_0) = [120[^\circ];\ -120[^\circ];\ 111[^\circ]]$, which gives $[\hat{x}_{\mathrm{CoM}}(t_0);\ \hat{y}_{\mathrm{CoM}}(t_0)] = [0.31;\ 0.67][\mathrm{m}]$ using $p = \hat{p}$ in (2.5) and (2.6).

For both movements $\hat{z}\left(t_f\right) = [-5[^\circ]; 0[\text{m}]; 0.97[\text{m}]]$, so that the final positions of the three links place the CoM of the robot directly above the ankle joints (Figure 2.3c). Due to the lack of data on comfortable STS duration for subjects with complete spinal cord injuries, we pick one reported in [31] for stroke patients; leading to a finite time horizon between $t_0 := 0[\text{s}]$ and $t_f := 3.5[\text{s}]$.

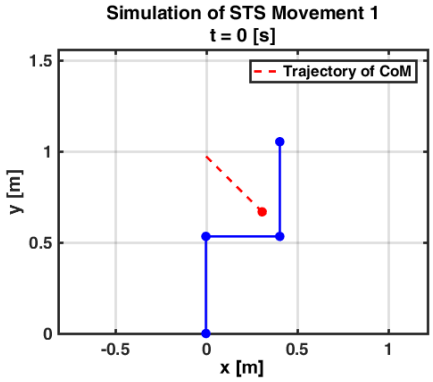

(a) Initial position for STS 1.

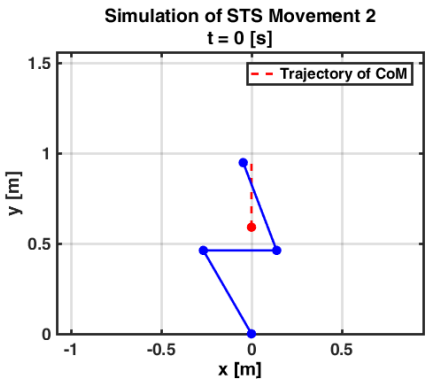

(b) Initial position for STS 2.

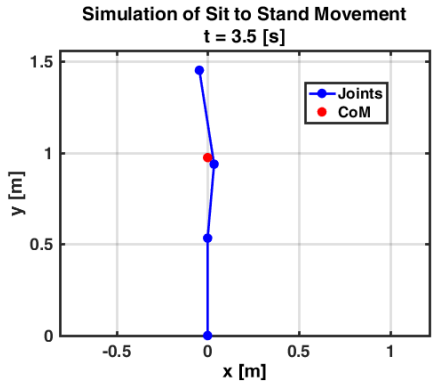

(c) Final position for STS 1 & 2.

Figure 2.3: Rest-to-rest positions for planning two relevant STS movements for PLLOs. The red dashed lines represent the reference trajectories of the CoM of the three-link robot in blue.

Plugging $\hat{z}(t_0)$ and $\hat{z}\left(t_f\right)$ for STS 1 & 2 into (2.20), and calculating the first and second time derivatives of the resulting cubic polynomials, we obtain $\hat{z}(t)$, $\dot{\hat{z}}(t)$, and $\ddot{\hat{z}}(t)$, which are shown in Figure 2.4. The corresponding reference trajectories in the space of θ are computed from (2.21) for $t \in \left[t_0, t_f\right]$ and shown in Figure 2.5, where $\hat{\theta}_2(t)$, $\dot{\hat{\theta}}_2(t)$, and $\ddot{\hat{\theta}}_2(t)$ are omitted to avoid redundancy.

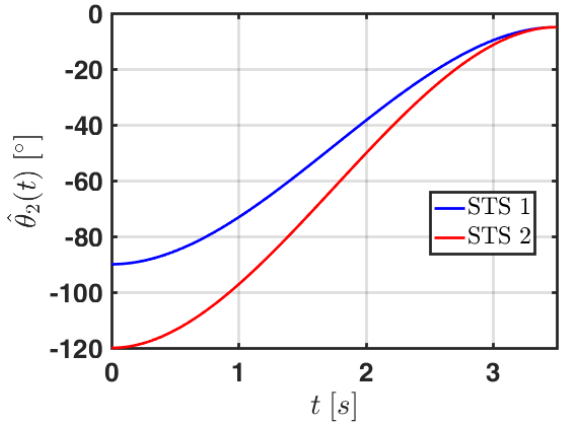

(a) Reference for angular position of link 2.

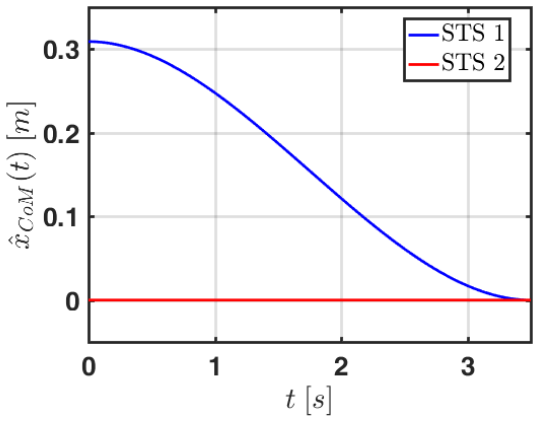

(b) Reference for horizontal position of the CoM.

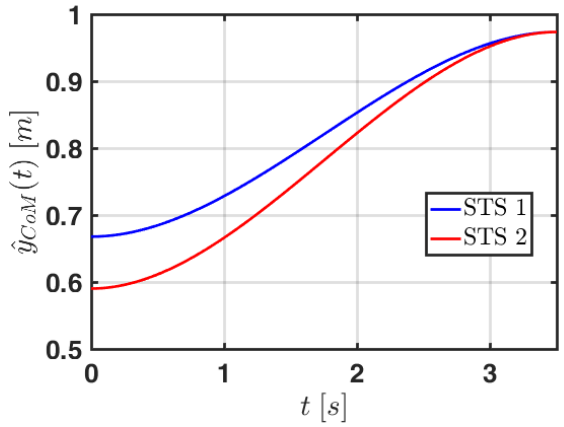

(c) Reference for vertical position of the CoM.

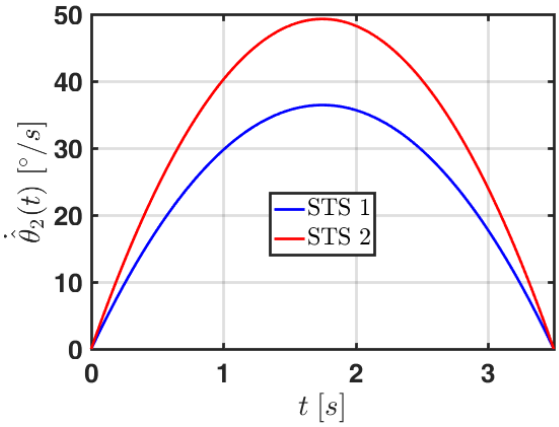

(d) Reference for angular velocity of link 2.

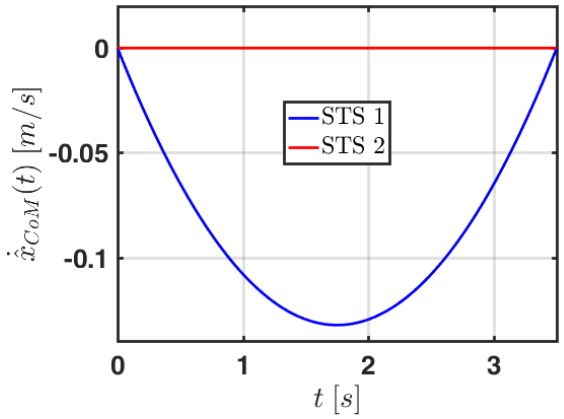

(e) Reference for horizontal velocity of the CoM.

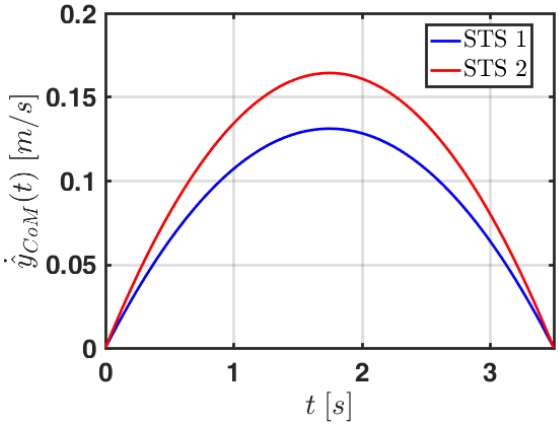

(f) Reference for vertical velocity of the CoM.

Figure 2.4: Reference trajectories in the space of z.

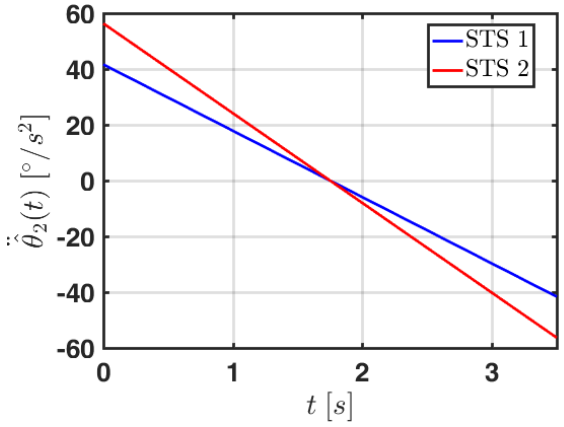

(g) Reference for angular acceleration of link 2.

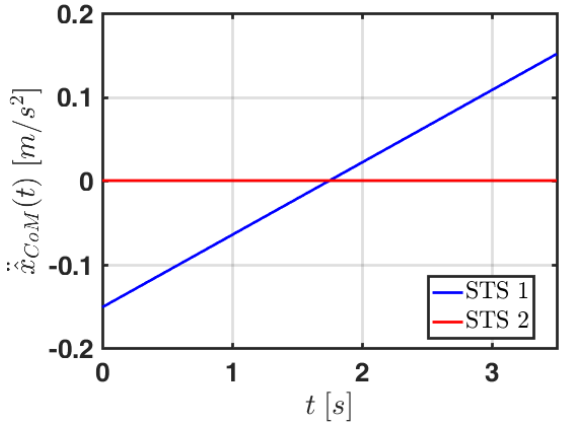

(h) Reference for horizontal acceleration of the CoM.

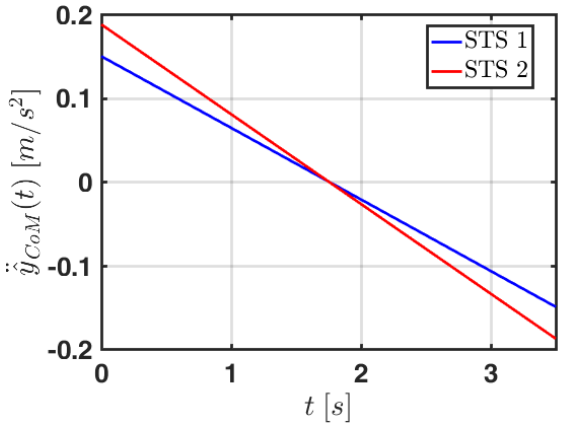

(i) Reference for vertical acceleration of the CoM.

Figure 2.4: Reference trajectories in the space of z (continued).

While the cubic expressions used to determine $\hat{z}(t)$ in Figures 2.4a to 2.4c are simple, merely connecting starting and final points with zero slope boundary conditions, $\hat{\theta}_1(t)$ and $\hat{\theta}_3(t)$ in Figures 2.5a and 2.5b are complex in shape, and it is not apparent how one would intuitively choose them as references. Moreover, stick figure animations of STS 1 & 2 following the angular trajectories in Figures 2.4 and 2.5 display flexion and extension of the ankles and hips that provide a natural look. By contrast, using cubic expressions to directly define $\hat{\theta}(t)$ leads to unrealistic STS movements as shown in Appendix A. This is the prime motivation for having derived the transformation (2.19), we plan the STS motion in the space of z instead of θ to obtain biomechanically sound trajectories.

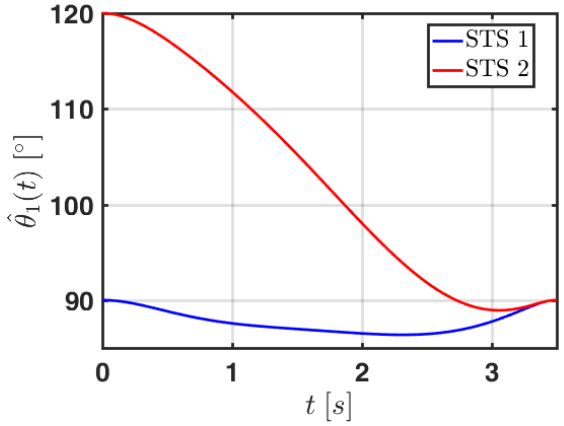

(a) Reference for angular position of link 1.

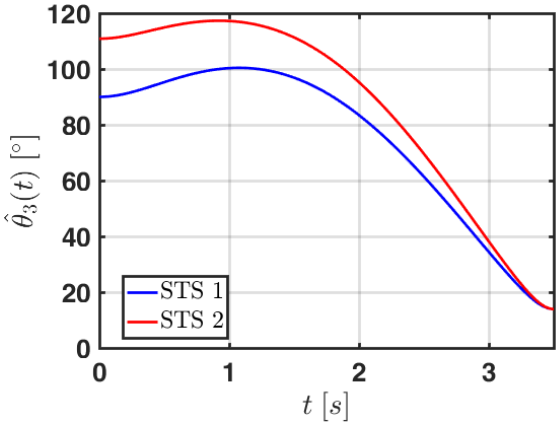

(b) Reference for angular position of link 3.

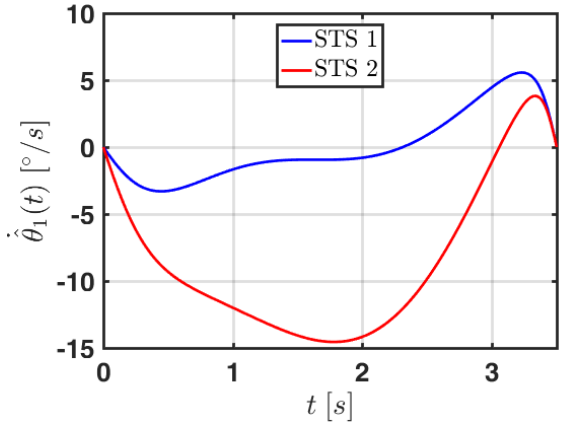

(c) Reference for angular velocity of link 1.

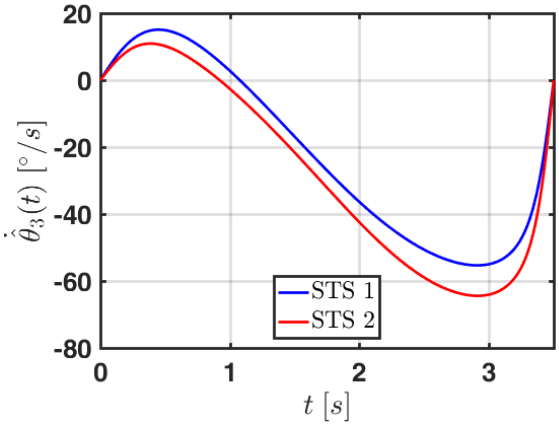

(d) Reference for angular velocity of link 3.

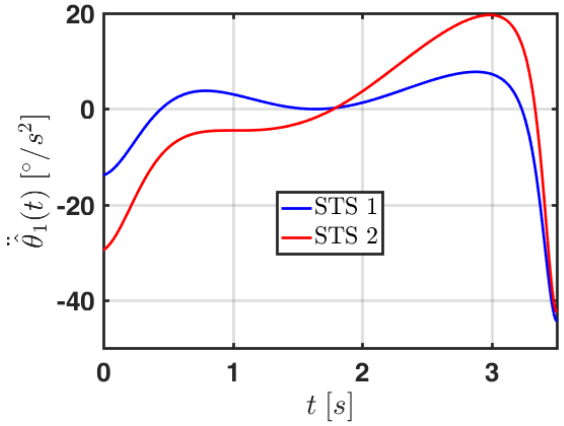

(e) Reference for angular acceleration of link 1.

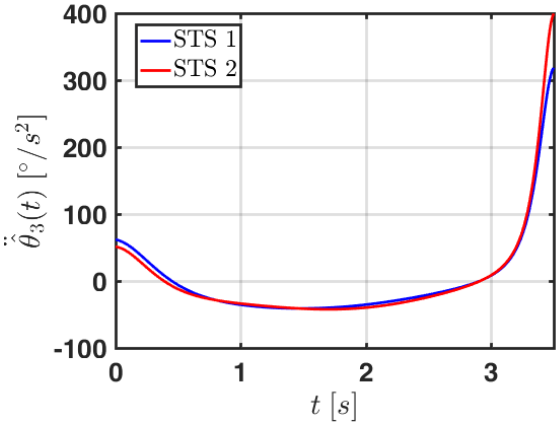

(f) Reference for angular acceleration of link 3.

Figure 2.5: Reference trajectories in the space of θ.

In order to solve for $\hat{u}(t) \in \mathbb{R}^m$, we must take into account specific architectures of PLLOs to pick proper $A_\tau(\theta, p)$, W_u, $\underline{u}$, and $\overline{u}$ in (2.22). The choices for the entries of W_u enforce that the contributions from $\tau_a(t)$, $\tau_k(t)$, $\tau_h(t)$, $\tau_s(t)$, and $F_y(t)$ outweigh $F_x(t)$. For minimally actuated PLLOs at the hips [9] we use the generalized force matrix in (2.3), and $W_u = \text{diag}([1, 1, 10, 1])$. For PLLOs with actuators at the knees and hips [3–7] we use the generalized force matrix in (2.4), and $W_u = \text{diag}([1, 1, 1, 10, 1])$. For hands-free, fully actuated PLLOs [11, 12] we have $A_\tau(\theta, p) = W_u = I_3$. Because the user of the PLLO always pushes the crutches down to propel upwards, we only impose the constraint $F_y(t) \geq 0$ and leave all other inputs unconstrained.

Solving (2.22) over $t \in [t_0, t_f]$ for the reference trajectories of STS 1 & 2 in the space of θ, we obtain the reference trajectories for the inputs of the different PLLOs. From the plots in Figure 2.6, we can tell that executing STS 2 with a minimally actuated PLLO would require applying a vertical force greater than the weight of the user, while executing STS 1 would keep it within a comfortable level.

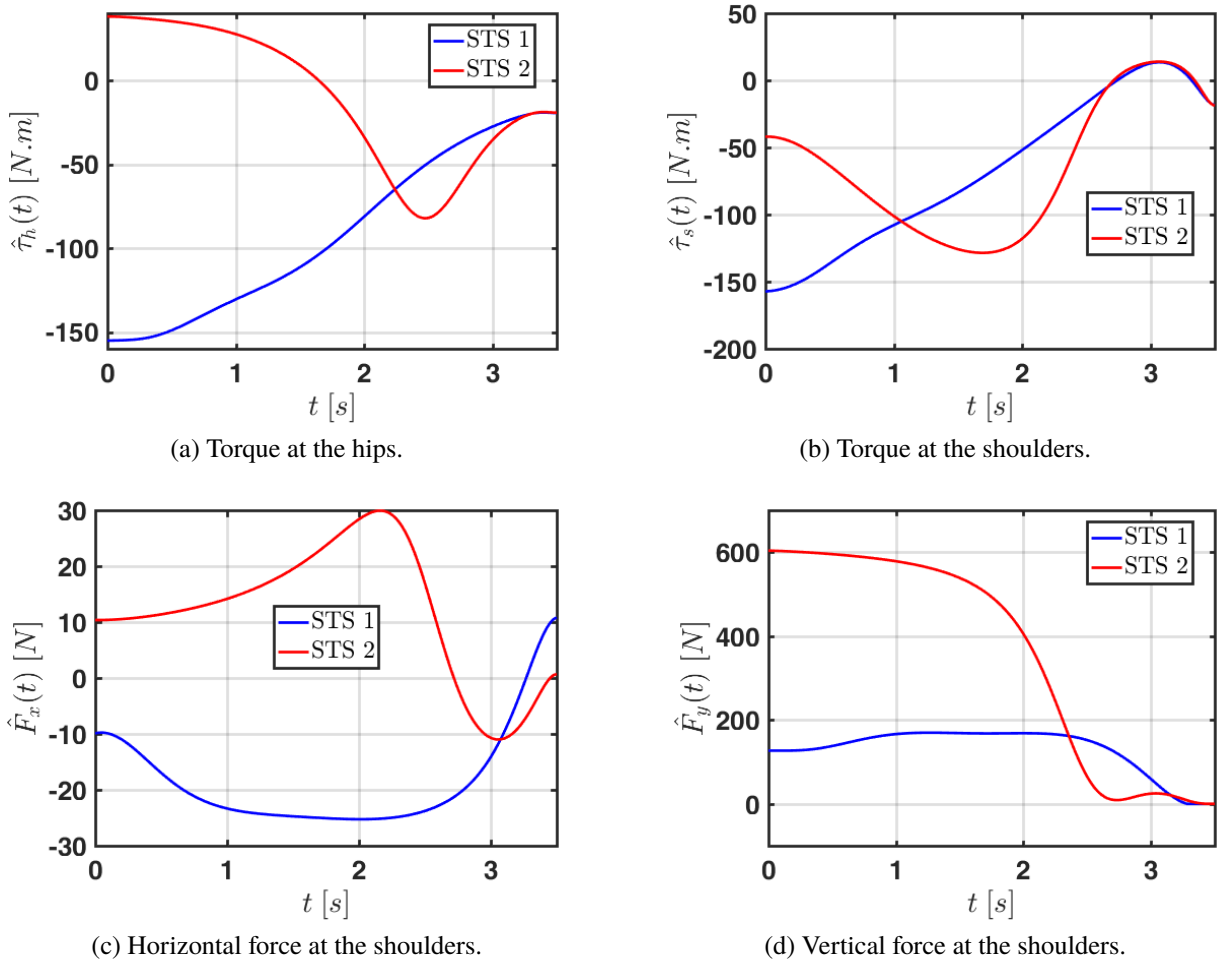

(a) Torque at the hips.

(b) Torque at the shoulders.

(c) Horizontal force at the shoulders.

(d) Vertical force at the shoulders.

Figure 2.6: Reference input for a minimally actuated PLLO at the hips.

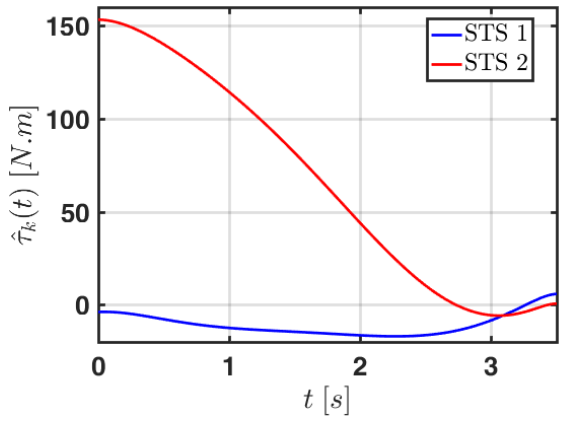

(a) Torque at the knees.

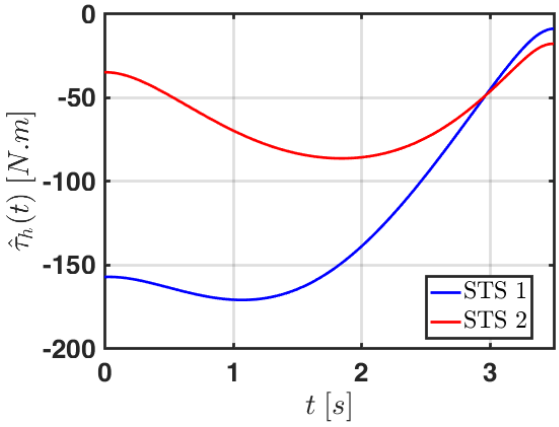

(b) Torque at the hips.

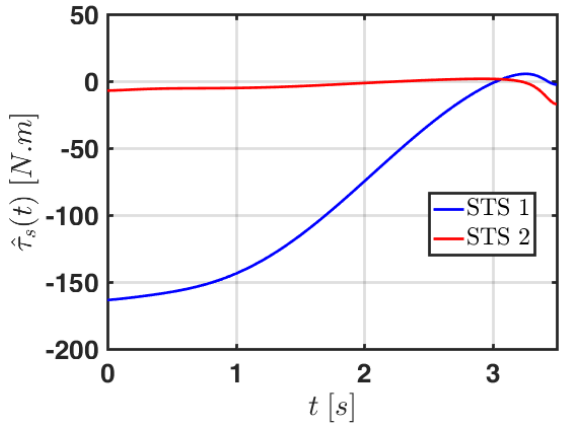

(c) Torque at the shoulders.

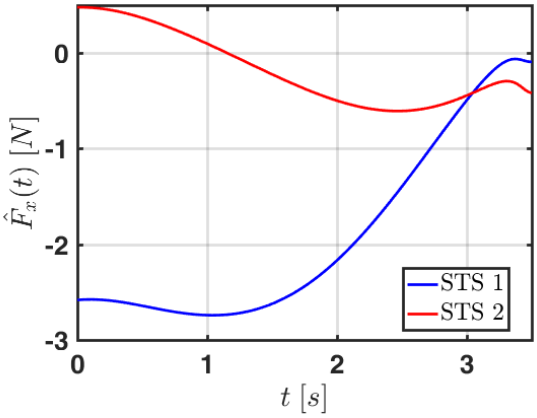

(d) Horizontal force at the shoulders.

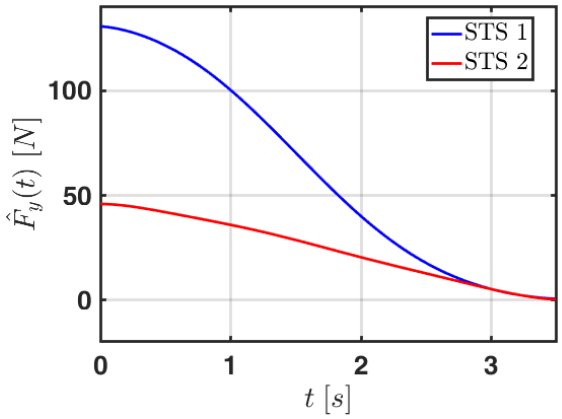

(e) Vertical force at the shoulders.

Figure 2.7: Reference input for a PLLO actuated at the knees and hips.

Figure 2.7 shows that performing STS 1 with a PLLO actuated at the knees and hips drastically reduces the torque at the knees, with increased loads at the shoulders and torque at the hips; in contrast, STS 2 leans heavily on the torque at the knees to reduce the participation of all other inputs.

Figure 2.8 highlights that a fully actuated PLLO relies mostly on the torque at the knees to accomplish both STS movements, with STS 1 involving a large torque at the ankles.

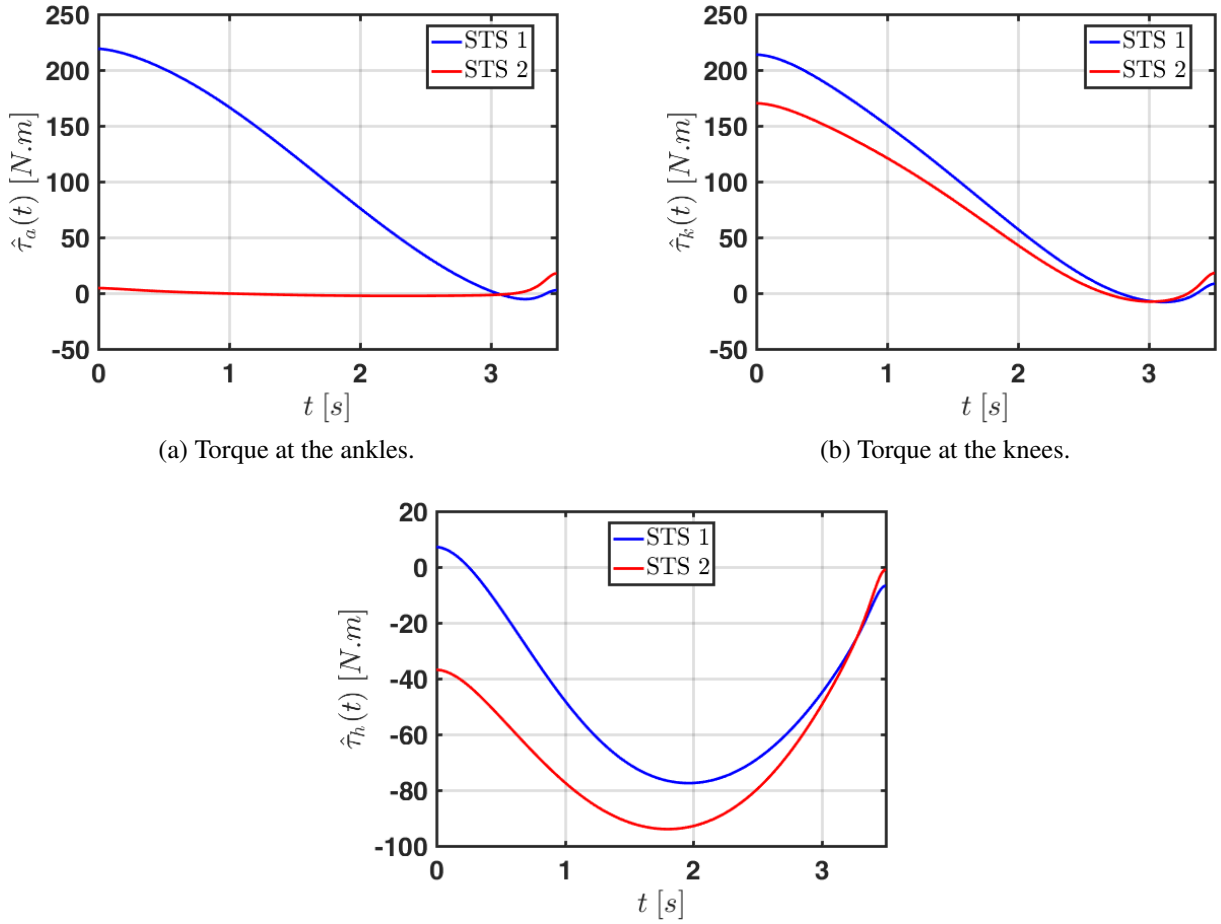

(a) Torque at the ankles.

(b) Torque at the knees.

(c) Torque at the hips.

Figure 2.8: Reference input for a hands-free fully actuated PLLO.

The comparison of the reference trajectories of the inputs for different PLLOs illustrates that our motion planning algorithm can also be a great analysis tool to provide valuable insight during the design stage of the devices, especially assisting to set the specifications of the actuators.

Other strategies for planning the STS movement of PLLOs are available in the literature. For example, the STS movement of the Robot Suit HAL [4] is planned in terms of the center of pressure, and the angles of hips and knees, without assuming sagittal symmetry. The desired center of pressure is fixed in front of the ankles, the reference trajectories for the knees are tuned from motion capture of a healthy person, and the trajectories for the hips are updated online, with measurements of the angles of the knees and ankles. The torque applied at the joints is then governed by a PD controller with feedback of the error with respect to the reference trajectories [32].

Our motion planning strategy does not rely on data collected from healthy subjects. The reference trajectories for the PLLOs are specifically adapted to the physical characteristics of the user by the definition of the parameter values in $\hat{p}$, and the time horizon for the ascension phase of the STS movement can be changed to offer a comfortable feeling.

In the next chapter we design feedback controllers for tracking the reference trajectories obtained in this section for a minimally actuated PLLO at the hips.

Chapter 3

Tracking Controllers

This chapter presents the design of feedback controllers for the ascension phase of STS movements for PLLOs under the provisional assumption that the controller has authority not only over the torque of the actuators available in the PLLO, but also over the torque and forces at the shoulders of the user. This assumption will be removed in Chapter 5.

The first controller uses feedback linearization of the Euler-Lagrange equations of the three-link robot, which due to our choice of input, also requires solving a control allocation program. The second controller is a finite time horizon LQR.

As an initial assessment of the robustness of the controllers, we simulate a minimally actuated PLLO at the hips tracking the reference trajectories of the two relevant STS movements of Section 2.5 in the presence of parameter uncertainty, i.e., when p in (2.2) is an unknown constant lying within an interval $p \in \left[\underline{p}, \overline{p}\right] \subseteq \mathbb{R}^{12}$.

There is no guarantee that a particular choice of weight matrices in the design of the finite time horizon LQR controller achieves a safe STS movement in the presence of parameter uncertainty, i.e., when p is an unknown constant lying within an interval, due to manufacturing variability of the links of the PLLO and weight fluctuations of its user. Therefore, the weight matrices of the LQR controller are chosen from a pool of candidates as to optimize a performance metric involving induced gains that measure the deviation of variables of interest in LTV systems, at specific times, caused by perturbation signals modeling the variation of the parameters. The deduction of such LTV systems follows from the nonlinear dynamics model, the reference trajectories obtained from our motion planning strategy, and the kinematic equations of the CoM of the three-link robot.

3.1 Feedback Linearization with Control Allocation

If the input $u \in \mathbb{R}^m$ satisfies

$$A_\tau(\theta,p)u = M(\theta,p)\left(-K_p\left(\theta-\hat{\theta}(t)\right)-K_d\left(\dot{\theta}-\dot{\hat{\theta}}(t)\right)+\ddot{\hat{\theta}}(t)\right)+F\left(\theta,\dot{\theta},p\right), \tag{3.1}$$

then the dynamics of the three-link robot described by $M(\theta,p)\ddot{\theta}+F\left(\theta,\dot{\theta},p\right)=A_\tau(\theta,p)u$, result in a linear differential equation governing the tracking error of the form

$$\ddot{\theta}-\ddot{\hat{\theta}}(t)+K_d\left(\dot{\theta}-\dot{\hat{\theta}}(t)\right)+K_p\left(\theta-\hat{\theta}(t)\right)=0.$$

With the synthetic input $v(t)\in\mathbb{R}^3$, defined as

$$v(t) := -K_p\left(\theta-\hat{\theta}(t)\right)-K_d\left(\dot{\theta}-\dot{\hat{\theta}}(t)\right), \tag{3.2}$$

the feedback linearized [33] equations are $\ddot{\theta}-\ddot{\hat{\theta}}(t)=v(t)$. The gain matrices $K_p, K_d \in \mathbb{R}^{3\times3}$ can be chosen from a LQR optimal gain for the system

$$\begin{bmatrix} \dot{\theta}-\dot{\hat{\theta}}(t) \\ \ddot{\theta}-\ddot{\hat{\theta}}(t) \end{bmatrix} = \begin{bmatrix} 0 & I_3 \\ 0 & 0 \end{bmatrix}\begin{bmatrix} \theta-\hat{\theta}(t) \\ \dot{\theta}-\dot{\hat{\theta}}(t) \end{bmatrix}+\begin{bmatrix} 0 \\ I_3 \end{bmatrix}v(t), \tag{3.3}$$

which achieves asymptotically zero tracking error of the reference trajectories. For notational purposes define

$$b\left(t,\theta,\dot{\theta},p\right) := M(\theta,p)\left(-K_p\left(\theta-\hat{\theta}(t)\right)-K_d\left(\dot{\theta}-\dot{\hat{\theta}}(t)\right)+\ddot{\hat{\theta}}(t)\right)+F\left(\theta,\dot{\theta},p\right).$$

Since (3.1) is underdetermined for $m > 3$, to compute the feedback linearizing input we solve the control allocation [30] at every time $t \in \left[t_0, t_f\right]$ with the constrained least-squares program

$$\begin{aligned} u(t) = \underset{\xi\in\mathbb{R}^m}{\arg\min} \quad & \frac{1}{2}\left\|W_u\,\xi\right\|_2^2. \\ \text{subject to} \quad & \\ & A_\tau\left(\hat{\theta}(t),\hat{p}\right)\xi = b\left(t,\theta,\dot{\theta},\hat{p}\right) \\ & \underline{u} \le \xi \le \overline{u} \end{aligned} \tag{3.4}$$

The nominal parameter $\hat{p}$, user specified weights $W_u \in \mathbb{R}^{m\times m}$, and box constraints $\underline{u}, \overline{u} \in \mathbb{R}^m$ were described in Section 2.4.

3.2 Finite Time Horizon LQR

Defining the state $x \in \mathbb{R}^6$ as $x := \left[\theta; \dot{\theta}\right]$, we first note from (2.2) that the first order dynamics of the three-link planar robot are

$$\begin{aligned} \dot{x}(t) &= \begin{bmatrix} \dot{\theta}(t) \\ M^{-1}(\theta(t), p)\left(A_\tau(\theta(t), p)u(t) - F\left(\theta(t), \dot{\theta}(t), p\right)\right) \end{bmatrix} \\ &=: f(x(t), p, u(t)). \end{aligned} \tag{3.5}$$

Next we linearize (3.5) to design a finite time horizon LQR controller for tracking the reference state trajectory $\hat{x}(t) := \left[\hat{\theta}(t), \dot{\hat{\theta}}(t)\right]$ obtained from (2.20) and (2.21). The state deviation variable $\delta_x(t) := x(t) - \hat{x}(t)$ satisfies

$$\dot{\delta}_x(t) = f(x(t), p, u(t)) - f(\hat{x}(t), \hat{p}, \hat{u}(t)),$$

which can be approximated with a first order Taylor series expansion of $f(x(t), p, u(t))$ about $\hat{x}(t)$, nominal parameter $\hat{p}$, and reference input trajectory $\hat{u}(t)$:

$$\begin{aligned} \dot{\delta}_x(t) \approx{}& \left.\frac{\partial f(x,p,u)}{\partial x}\right|_{\substack{x=\hat{x}(t)\\ p=\hat{p}\\ u=\hat{u}(t)}} (x(t) - \hat{x}(t)) + \left.\frac{\partial f(x,p,u)}{\partial p}\right|_{\substack{x=\hat{x}(t)\\ p=\hat{p}\\ u=\hat{u}(t)}} (p - \hat{p}) \\ &+ \left.\frac{\partial f(x,p,u)}{\partial u}\right|_{\substack{x=\hat{x}(t)\\ p=\hat{p}\\ u=\hat{u}(t)}} (u(t) - \hat{u}(t)) \\ =:{}& A(t)\delta_x(t) + B_1(t)\delta_p + B_2(t)\delta_u(t). \end{aligned} \tag{3.6}$$

From [34], for unconstrained $\delta_u(t)$, symmetric matrices $Q, S \succeq 0$, and $R \succ 0$, the optimal control of the stabilizable linear time-varying system in (3.6) with quadratic cost

$$J_{\text{LQR}} = \frac{1}{2}\delta_x^\top\left(t_f\right) S \delta_x\left(t_f\right) + \frac{1}{2}\int_{t_0}^{t_f} \left(\delta_x^\top(t) Q \delta_x(t) + \delta_u^\top(t) R \delta_u(t)\right) dt \tag{3.7}$$

exists, and is unique, given by the time-varying formula

$$\begin{aligned} \delta_u(t) &= -R^{-1} B_2^\top(t) P(t) \delta_x(t) \\ &=: -K_{\text{LQR}}(t)\delta_x(t), \end{aligned} \tag{3.8}$$

where $P(t) \in \mathbb{R}^{6\times 6}$ is the solution of the Riccati matrix differential equation

$$\dot{P}(t) = -P(t)A(t) - A^\top(t)P(t) + P(t)B_2(t)R^{-1}B_2^\top(t)P(t) - Q, \tag{3.9}$$

with the boundary condition $P\left(t_f\right) = S$.

The nonlinear dynamics of the three-link robot under state feedback control with the time-varying matrix gain $K_{\text{LQR}}(t) \in \mathbb{R}^{m\times 6}$, become

$$\begin{aligned} \dot{x}(t) &= f\left(x(t), p, \hat{u}(t) - K_{\text{LQR}}(t)(x(t) - \hat{x}(t))\right) \\ &=: \varphi(t, x, p). \end{aligned} \tag{3.10}$$

3.3 Simulation of Two Relevant Sit-To-Stand Movements Under Parameter Uncertainty

We illustrate the behavior of the three-link robot model in Figure 2.1 under the action of the pair of tracking controllers presented in the previous sections. From the three architectures of PLLOs discussed in Chapter 2, we take into account the minimally actuated PLLO at the hips. This architecture allows the users of [9] attaining dynamically stable level-ground gait cycles that look more natural when compared to the ones achieved with PLLOs equipped with more actuators. Nevertheless, it demands the application of greater loads with the arms to perform STS movements (as can be concluded from the comparison of Figures 2.6, 2.7, and 2.8), and makes it more challenging to design controllers that guarantee a safe transition to the standing position in the presence of parameter uncertainties, mainly due to weight fluctuations of the users and manufacturing variability of the links of the PLLO.

The gain matrices of the synthetic input in (3.2) are obtained from the LQR optimal gain for the error dynamics (3.3) using the weight matrices $Q := I_6$, and $R := \frac{1}{100} I_3$. When solving the control allocation problem in (3.4) to obtain the feedback linearizing input, we want to reflect that the contributions from the torque at the hips $\tau_h(t)$, the torque at the shoulders $\tau_s(t)$, and the vertical force $F_y(t)$ outweigh the horizontal force $F_x(t)$; we do this by considering the matrix $W_u = \text{diag}([1, 1, 10, 1])$ and, because the user always pushes the crutches down to propel upwards, we specify the constraint $F_y(t) \geq 0$. All other inputs are unconstrained.

Applying the feedback linearizing input to the three-link robot model in (2.2) with the generalized force matrix in (2.3) for tracking the movements STS 1 & 2 defined in Section 2.5, we obtain the simulations in Figures 3.1 to 3.3. The dashed white lines represent the evolution of the variables when the parameters of the system equal their nominal values $p = \hat{p}$; thus overlapping with the reference trajectories for STS 1 & 2. The collection of continuous lines represent the evolution of the variables when the values for p are randomly chosen, within the interval $\left[\underline{p}, \overline{p}\right]$ in Table 3.1, by Latin hypercube sampling [35] of 200 experiments.

Table 3.1: Nominal values of the parameters of the three-link robot and bounds for their uncertainties in an initial robustness assessment of the controllers

Link	m_i [kg]	I_i $\left[\text{kg}\cdot\text{m}^2\right]$	l_i [m]	l_{ci} [m]
1	9.68 ± 0.1	1.16 ± 0.1	0.53 ± 0.01	$\frac{l_1}{2} \pm 0.01$
2	12.59 ± 0.1	0.52 ± 0.1	0.41 ± 0.01	$\frac{l_2}{2} \pm 0.01$
3	44.57 ± 0.1	2.56 ± 0.1	0.52 ± 0.01	$\frac{l_3}{2} \pm 0.01$

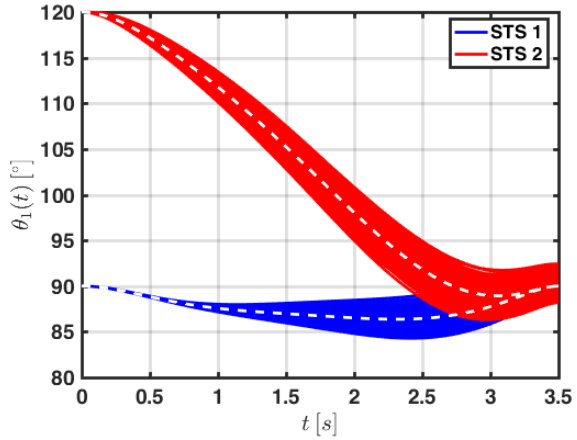

(a) Angular position of link 1 relative to the horizontal.

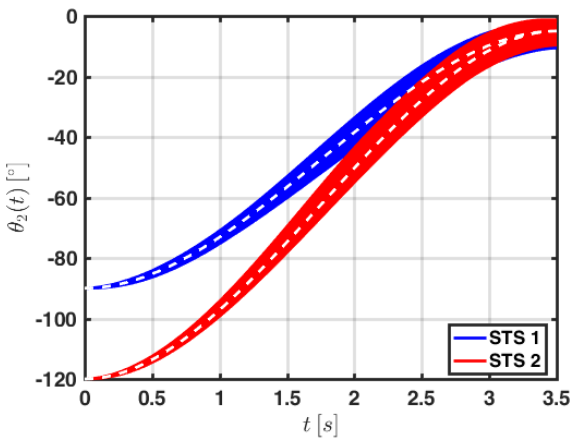

(b) Angular position of link 2 relative to link 1.

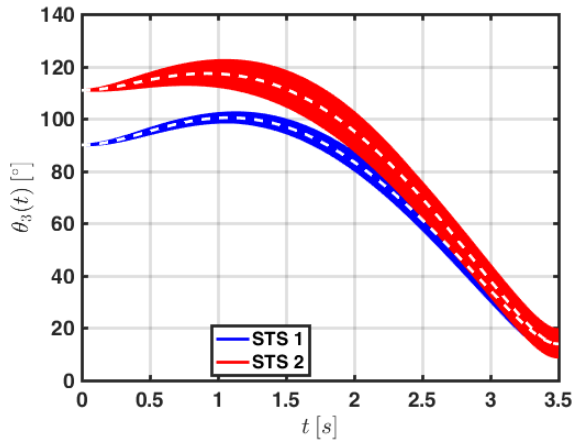

(c) Angular position of link 3 relative to link 2.

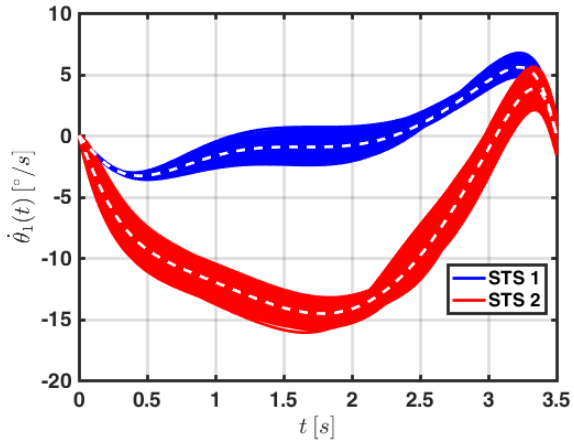

(d) Angular velocity of link 1.

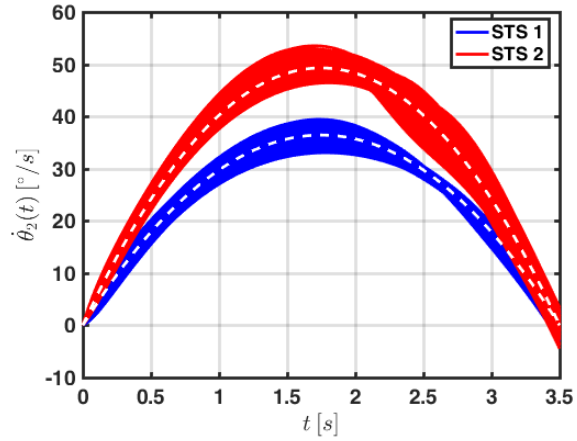

(e) Angular velocity of link 2.

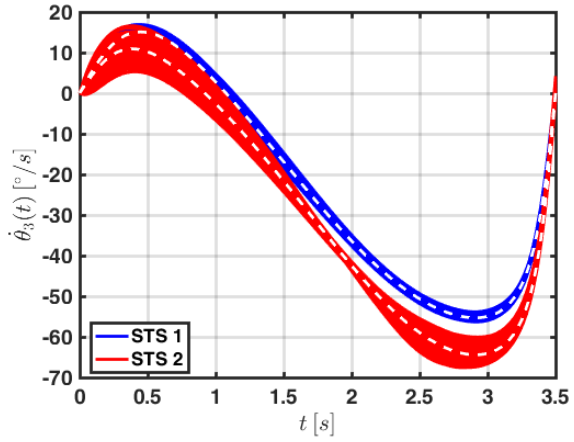

(f) Angular velocity of link 3.

Figure 3.1: Angular positions and velocities of the links of the robot under feedback linearization and control allocation for two relevant STS movements.

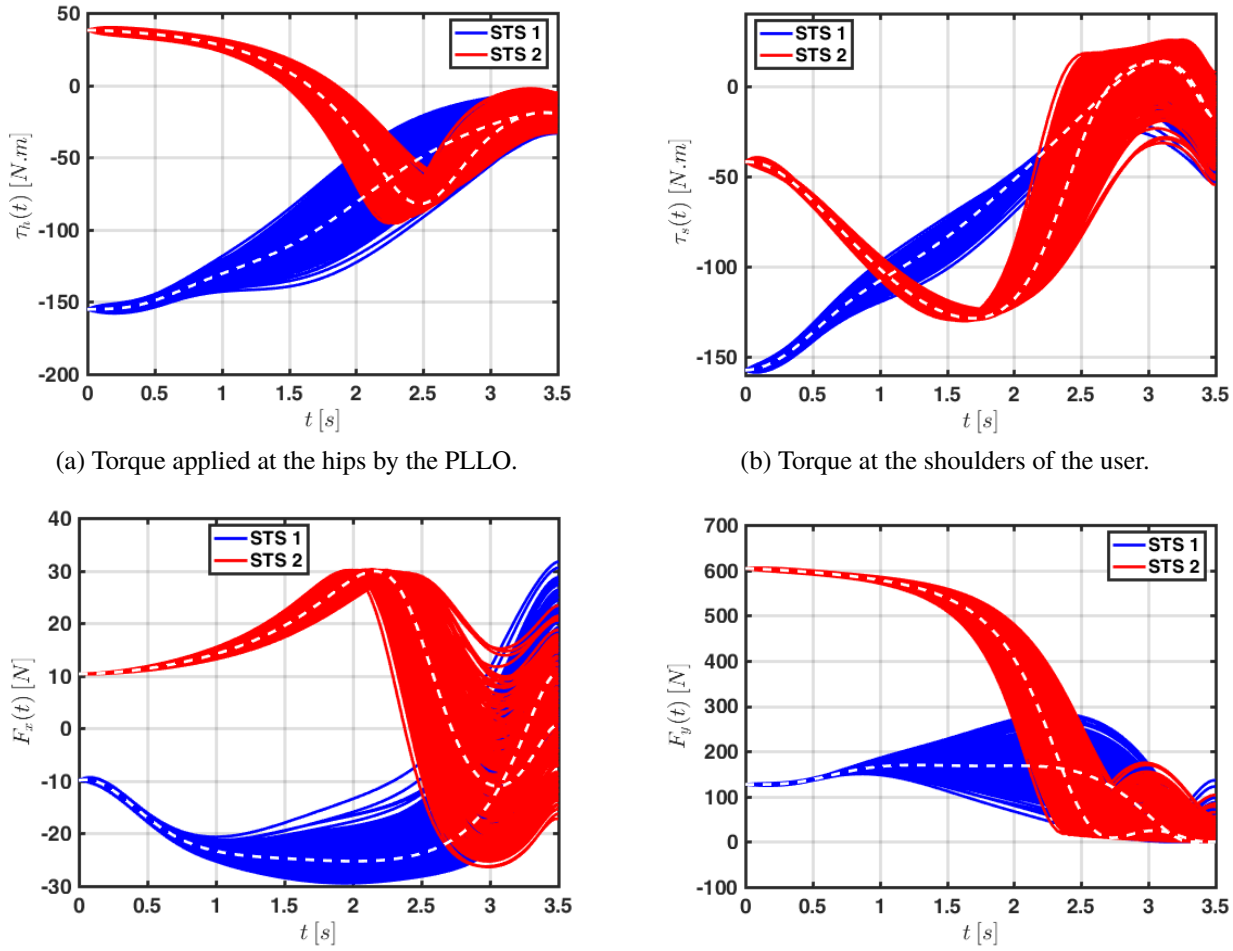

(a) Torque applied at the hips by the PLLO.

(b) Torque at the shoulders of the user.

(c) Horizontal force at the shoulders of the user.

(d) Vertical force at the shoulders of the user.

Figure 3.2: Feedback linearizing input for two relevant STS movements.

Since the feedback linearizing input is calculated with $\hat{p}$, the deviation of the solid curves from the reference trajectories is expected with $p \neq \hat{p}$; nevertheless, it is a positive feature of the controller to find that the observed offsets do not lead to sit-back or step failures [15] nor to a condition of hyperextension of the knees, since all trajectories end in a small neighborhood of the final desired state and keep $\theta_2(t) \leq 0$. Based solely on the observed variance from the reference trajectories, STS 2 appears to be more sensitive to parameter uncertainty than STS 1, this is more noticeable in Figure 3.3b.

From the plots in Figure 3.2, we can tell that STS 1 significantly reduces $F_y(t)$ when compared to STS 2, which in turn requires a greater magnitude of $\tau_h(t)$. The values of $F_x(t)$ differ by one order of magnitude from $F_y(t)$ and remain within approximately the same range in both movements, what is also observed for $\tau_s(t)$. It is interesting that for every STS 2 trajectory $F_y(t)$ decreases from a maximum value observed at seat-off, while STS 1 trajectories peak over $t \in [0.75, 2.25]$ [s].

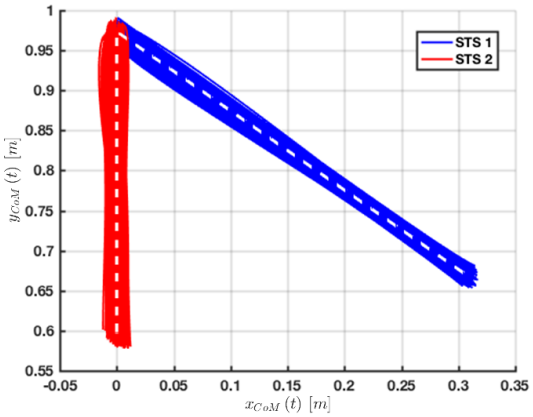

(a) Position trajectories of the three-link robot CoM.

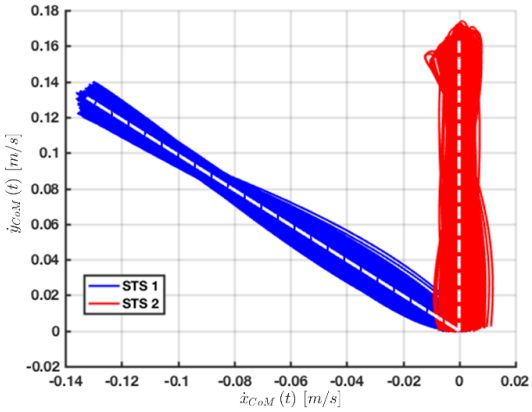

(b) Velocity trajectories of the three-link robot CoM.

Figure 3.3: Center of Mass trajectories achieved with feedback linearization and control allocation for two relevant STS movements.

Although the simulations with feedback linearization exhibit acceptable tracking errors for the angular positions and velocities of the links in the presence of parameter uncertainties, we observe a high sensitivity in the variability of the required control input. Since the upper body loads at the joint of the shoulders $\tau_s(t)$, $F_x(t)$, and $F_y(t)$ are expected to be executed by the user for successfully completing the movements and there is no feedback control/computer authority over them, a key concern that arises is to find a controller that reduces their deviation from reference trajectories without compromising the desired kinematics for the CoM, especially in the final standing position, in order to decrease the likelihood of observing sit-back or step failures [15]. To address this issue we resort to induced gains for LTV systems from [36] to evaluate the behavior of the three-link robot under different finite time horizon LQR controllers. The use of induced gains for robustness analysis of nonlinear systems was first explored in [37].

The linearization of the three-link robot dynamics under finite time horizon LQR control in (3.10) about $\hat{x}(t)$, $\hat{p}$, and $\hat{u}(t)$ is

$$\dot{\delta}_x(t) = \left(A(t) - B_2(t) K_{\text{LQR}}(t)\right) \delta_x(t) + B_1(t) \delta_p. \tag{3.11}$$

In order to define a metric that captures the effect of constant, uncertain parameters on the performance of this linear system, and to minimize the deviation of the variables of interest in the space of z from their reference trajectories $\delta_z := \left[z(t) - \hat{z}(t); \dot{z}(t) - \dot{\hat{z}}(t)\right]$, we construct the extended LTV system in Figure 3.4. The input signal $d : [0,t] \to \mathbb{R}^{12}$ is assigned to be drawn from $\mathcal{L}_2[0,t]$ with a given norm $\|d\|_{2,[0,t]} \leq \overline{d}$ for a fixed horizon at $t \in \left[0, t_f\right]$. The output $e \in \mathbb{R}^6$ is the linear approximation of δ_z weighted by $W_e \in \mathbb{R}^{6\times 6}$.

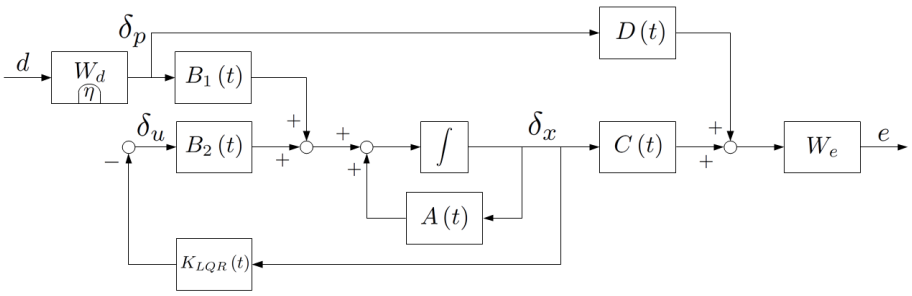

Figure 3.4: Extended LTV system for robust performance analysis against parameter uncertainty.

In terms of x and p, the variables of interest in the space of z are computed from (2.5) to (2.8) as

$$\begin{bmatrix} z \\ \dot{z} \end{bmatrix} = \begin{bmatrix} \theta_2 \\ x_{\text{CoM}} \\ y_{\text{CoM}} \\ \dot{\theta}_2 \\ \dot{x}_{\text{CoM}} \\ \dot{y}_{\text{CoM}} \end{bmatrix} = \begin{bmatrix} \theta_2 \\ k_0(k_1c_1 + k_2c_{12} + k_3c_{123}) \\ k_0(k_1s_1 + k_2s_{12} + k_3s_{123}) \\ \dot{\theta}_2 \\ -\dot{\theta}_1 y_{\text{CoM}} - \dot{\theta}_2 k_0(k_2s_{12} + k_3s_{123}) - \dot{\theta}_3 k_0 k_3 s_{123} \\ \dot{\theta}_1 x_{\text{CoM}} + \dot{\theta}_2 k_0(k_2c_{12} + k_3c_{123}) + \dot{\theta}_3 k_0 k_3 c_{123} \end{bmatrix} =: \varkappa(x,p).$$

The deviation from their desired trajectories

$$\delta_z(t) = \varkappa(x(t),p) - \varkappa(\hat{x}(t),\hat{p})$$

is approximated by a first order Taylor series expansion of $\varkappa(x,p)$ about $\hat{x}(t)$ and $\hat{p}$:

$$\delta_z(t) \approx C(t)\delta_x(t) + D(t)\delta_p, \tag{3.12}$$

with

$$C(t) := \left.\frac{\partial \varkappa(x,p)}{\partial x}\right|_{\substack{x=\hat{x}(t) \\ p=\hat{p}}}, \qquad D(t) := \left.\frac{\partial \varkappa(x,p)}{\partial p}\right|_{\substack{x=\hat{x}(t) \\ p=\hat{p}}}.$$

Although $\delta_p := p - \hat{p}$ is an unknown constant, for the purpose of this analysis it is treated as a time-varying perturbation signal, modeled by the output of the strictly proper system W_d:

$$\begin{aligned} \dot{\eta}(t) &= A_d\eta(t) + B_d d(t) \\ \delta_p(t) &= C_d\eta(t), \end{aligned} \tag{3.13}$$

where $\eta \in \mathbb{R}^{12}$, $A_d := -aI_{12}$, $B_d := I_{12}$, and $C_d := \frac{a}{2}\,\text{diag}\left(\overline{p} - \underline{p}\right)$. For a bandwidth of 50[Hz] we set $a := 100\pi$, and penalize the deviations of the variables of interest with $W_e := \text{diag}([1,1,1,10,10,10])$.

Defining

$$\tilde{A}(t) := \begin{bmatrix} A(t) - B_2(t)K_{\text{LQR}}(t) & B_1(t)C_d \\ 0 & A_d \end{bmatrix}, \qquad \tilde{B}(t) := \begin{bmatrix} 0 \\ B_d \end{bmatrix},$$
$$\tilde{C}(t) := \begin{bmatrix} W_e C(t) & W_e D(t) C_d \end{bmatrix},$$

the state space realization of the extended LTV system in Figure 3.4 is

$$\begin{aligned} \begin{bmatrix} \dot{\delta}_x(t) \\ \dot{\eta}(t) \end{bmatrix} &= \tilde{A}(t) \begin{bmatrix} \delta_x(t) \\ \eta(t) \end{bmatrix} + \tilde{B}(t)\, d(t) \\ e(t) &= \tilde{C}(t) \begin{bmatrix} \delta_x(t) \\ \eta(t) \end{bmatrix}, \end{aligned} \tag{3.14}$$

and its *finite-horizon $\mathcal{L}_2$-to-Euclidean gain* [36] is

$$\gamma_{[0,t]} := \sup \left\{ \frac{\|e(t)\|_2}{\|d\|_{2,[0,t]}} \middle| \begin{bmatrix} \delta_x(0) \\ \eta(0) \end{bmatrix} = 0, 0 \neq d \in \mathcal{L}_2[0,t] \right\}.$$

If $\gamma_{[0,t]}$ is bounded by $\overline{\gamma}$, then $\|e(t)\|_2 \leq \overline{\gamma}\, \|d\|_{2,[0,t]}$ and hence $e(t)$ is contained in a sphere of radius $\overline{\gamma}\, \overline{d}$ at the fixed time $t \in [0, t_f]$. The most important feature of the LQR controller is to guarantee a safe transition to the standing position in the presence of parameter uncertainty by the end of the ascension phase, without loosing track of the reference trajectories. For this purpose, we choose the performance metric:

$$J_{\text{G}} := (1-\alpha)\, \gamma_{[0,t_m]} + \alpha \gamma_{[0,t_f]}, \tag{3.15}$$

where $\alpha \in [0,1]$ weights the induced gains at an intermediate time t_m and the final time t_f.

Since J_{G} depends on the choice of Q, R, S in the design of the LQR controller (3.8)-(3.9), we choose finite sets of candidates $\mathcal{Q} \subset \mathbb{R}^{6\times 6}$, $\mathcal{R} \subset \mathbb{R}^{4\times 4}$ and $\mathcal{S} \subset \mathbb{R}^{6\times 6}$, draw an element from each of them, obtain their corresponding finite horizon LQR gain, and compute J_{G} with $\alpha := 0.7$ and $t_m := 2\,[s]$. Taking a brute force approach, the weight matrices

$$Q^*, R^*, S^* = \underset{Q\in\mathcal{Q},\, R\in\mathcal{R},\, S\in\mathcal{S}}{\arg\min} \; J_{\text{G}}(Q,R,S) \tag{3.16}$$

characterize the best LQR gain from the pool of candidates $K^*_{\text{LQR}}(t)$, relative to (3.15).

The finite time horizon LQR controllers tested for tracking STS 1 & 2 with the input configuration of a minimally actuated PLLO at the hips, are obtained from a pool of weight matrices limited to be diagonal, positive definite, with their entries sampled from a Latin hypercube of 16 variables and 1350 experiments. The entries of $\mathcal{Q}$ and $\mathcal{S}$ are in $(0, 10^4)$, while the entries of $\mathcal{R}$ belong to $(0,1)$. After numerically computing the linearizations in (3.6) and (3.12) about the reference trajectories, we use the tools documented in [37] to obtain the finite time horizon LQR optimal gain in (3.8), and the induced gains in (3.15). The arg min triplets in (3.16) for the STS movements are:

$$\begin{aligned} Q_1^* &= \text{diag}([3237,\ 5534,\ 6546,\ 7918,\ 4003,\ 8516]), \\ R_1^* &= \text{diag}([0.366,\ 0.016,\ 0.143,\ 0.155]), \\ S_1^* &= \text{diag}([1068,\ 5396,\ 1324,\ 9467,\ 3975,\ 5819]), \end{aligned} \tag{3.17}$$

$$
\begin{aligned}
Q_2^* &= \text{diag}([3766,\ 9550,\ 2932,\ 8378,\ 9552,\ 9242]),\\
R_2^* &= \text{diag}([0.112,\ 0.025,\ 0.360,\ 0.305]),\\
S_2^* &= \text{diag}([9565,\ 820,\ 5316,\ 5779,\ 6083,\ 8877]).
\end{aligned}
\tag{3.18}
$$

Their corresponding performance metrics are $J_{\text{G1}} = 0.1571$, and $J_{\text{G2}} = 0.1553$.

The simulations of the nonlinear system (3.10) in state feedback with $K^*_{\text{LQR1}}(t) \in \mathbb{R}^{4\times 6}$ for STS 1, and $K^*_{\text{LQR2}}(t) \in \mathbb{R}^{4\times 6}$ for STS 2 are in Figures 3.5 to 3.7. The dashed white lines represent the evolution of the variables when $p = \hat{p}$. The collection of continuous lines represents the evolution of the variables for the same 200 sets of $p \in \left[\underline{p}, \overline{p}\right]$ used for assessing the performance of the minimally actuated PLLO under feedback linearization. Comparing these results with the ones in Figures 3.1 to 3.3, it is clear that the LQR optimal gains dramatically improve tracking, with most of the trajectories essentially overlapping with the references of both STS movements, regardless of the parameter uncertainty.

Note that the variation of the lengths and masses of the links from their nominal values causes the initial conditions for x_{CoM} and y_{CoM} in Figure 3.7a not being the same across simulations, despite each STS movement having a single initial condition for x. In the same figure, it is interesting to observe how the selected LQR controller for STS 2, whose performance metric is slightly smaller than the one for the controller of STS 1, effectively decreases the Euclidean norm of the position of the CoM at the end of the finite horizon, in accordance to the induced gain at t_f in (3.15). Given that all the final positions of the CoM are approximately aligned with the ankle (with an error less than or equal to 5[mm] in x_{CoM}) and the magnitude of its final velocity in Figure 3.7b is less than or equal to 1[cm/s], there is no risk of sit-back or step failures during the STS movements with the proposed LQR optimal gains.

Even though it might seem unrealistic that users would be able to exactly mimic the inputs from the LQR controllers in Figures 3.6b to 3.6d, we believe that it should be easier for them, through training, to achieve a good coordination with the PLLO and consistently execute safe STS movements if the required loads at their shoulders do not vary much with parameter changes, e.g., due to daily weight fluctuation, mechanical wear of the braces or links. This idea will be further developed in Chapter 5 using an ILC algorithm as a proxy for human user.

The parameter uncertainties considered for the initial robustness assessment of the tracking controllers in Table 3.1 are small. In the next chapter we increase the parameter uncertainties and evaluate finite horizon LQR gains with a robust performance metric that takes into account the nonlinearities in both the dynamics of the system (3.10), and the mappings to compute the position and velocity of the CoM of the three-link robot in (2.5) to (2.8).

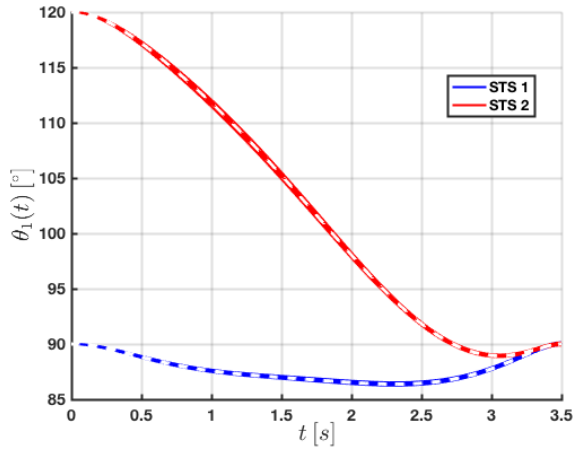

(a) Angular position of link 1 relative to the horizontal.

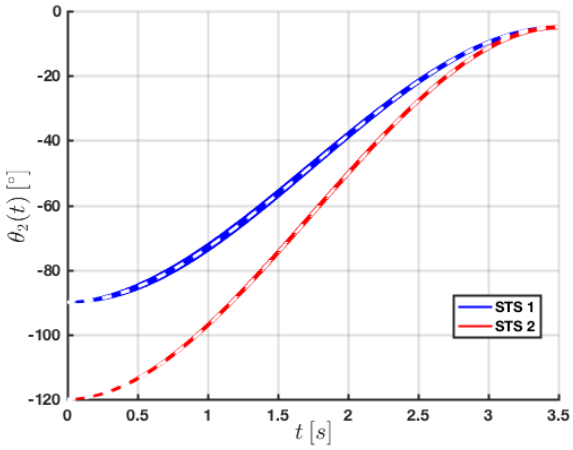

(b) Angular position of link 2 relative to link 1.

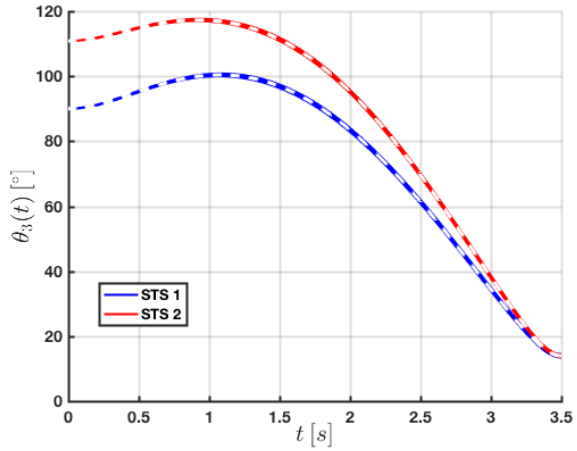

(c) Angular position of link 3 relative to link 2.

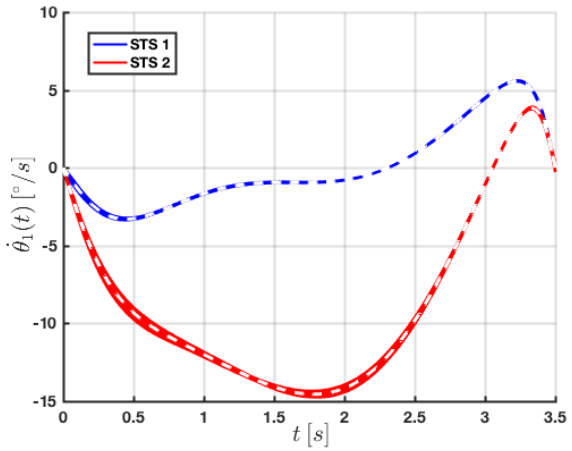

(d) Angular velocity of link 1.

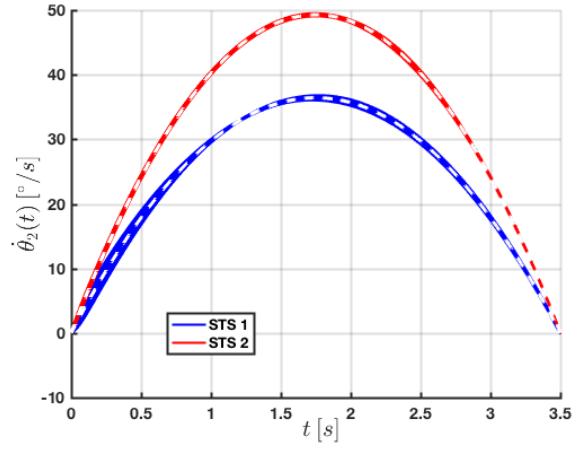

(e) Angular velocity of link 2.

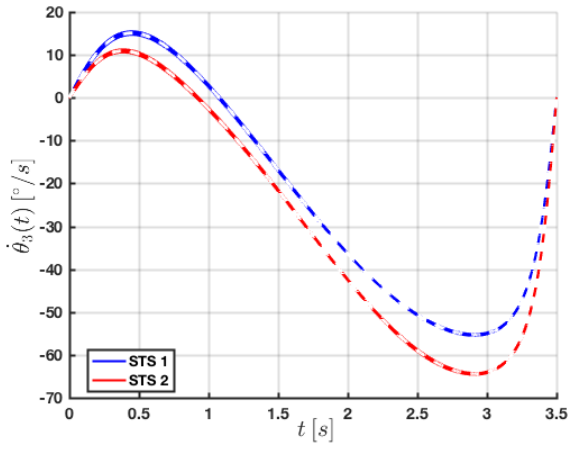

(f) Angular velocity of link 3.

Figure 3.5: Angular positions and velocities of the links of the robot in state feedback with $K^*_{\text{LQR1}}(t)$ and $K^*_{\text{LQR2}}(t)$ for tracking two relevant STS movements.

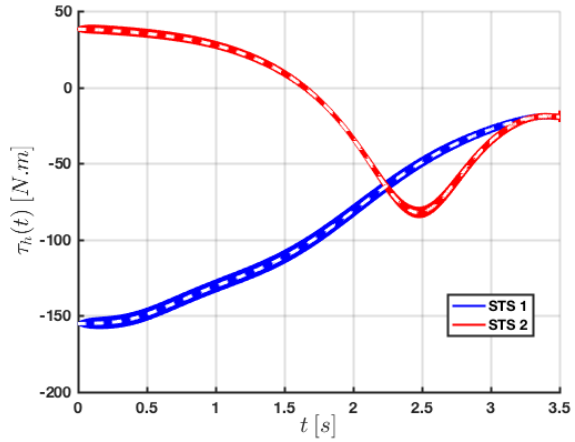

(a) Torque applied at the hips by the PLLO.

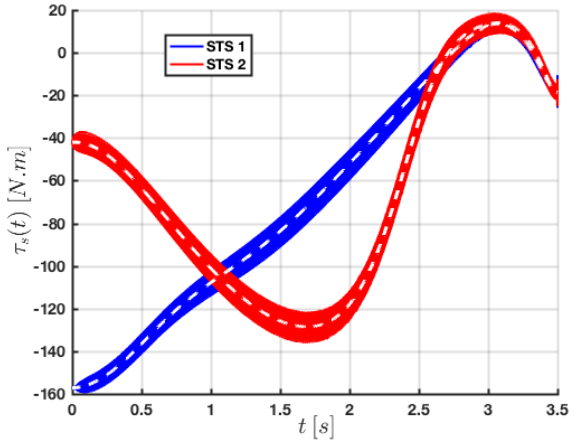

(b) Torque at the shoulders of the user.

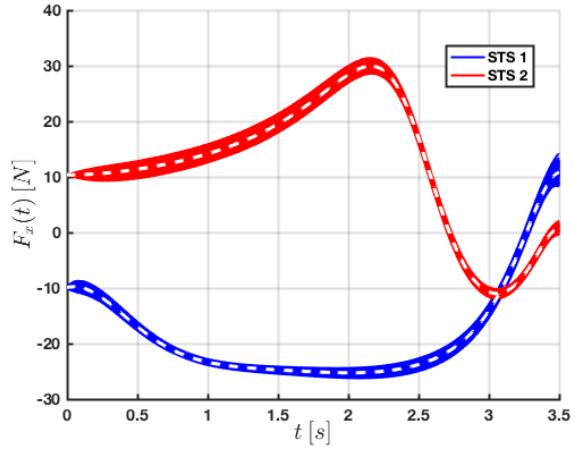

(c) Horizontal force at the shoulders of the user.

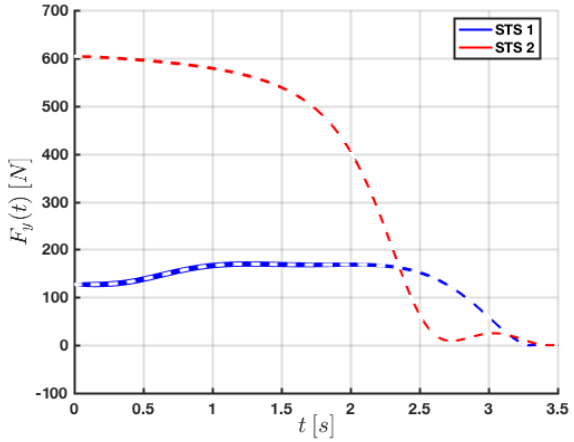

(d) Vertical force at the shoulders of the user.

Figure 3.6: Inputs from the finite time horizon LQR controllers chosen using the performance metric J_G for tracking two relevant STS movements.

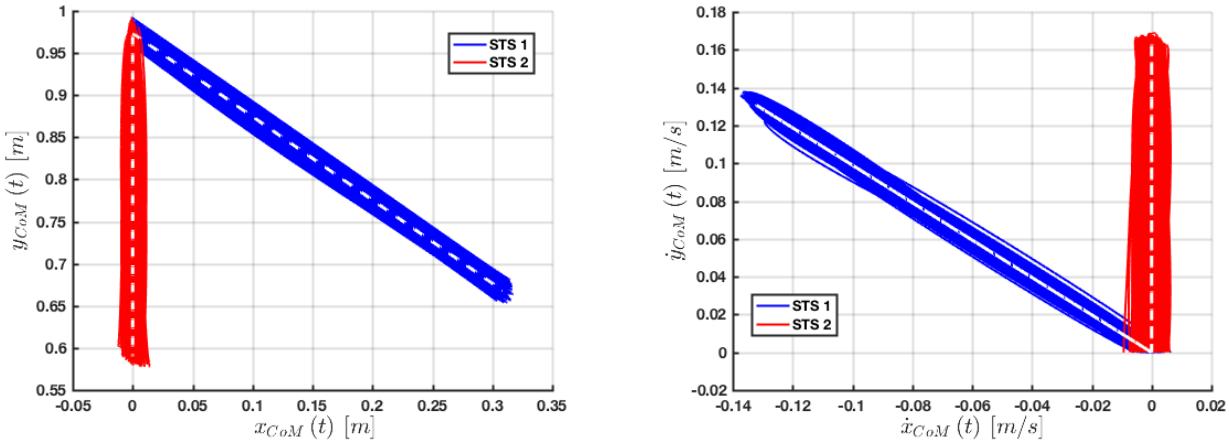

(a) Position trajectories of the three-link robot CoM.

(b) Velocity trajectories of the three-link robot CoM.

Figure 3.7: Center of Mass trajectories achieved with the finite time horizon LQR controllers chosen using the performance metric J_{G} for tracking two relevant STS movements.

The technique presented in this chapter to evaluate the performance of a nonlinear system in closed-loop with a finite horizon LQR gain can be directly applied without modification to other systems that undergo finite-time trajectories, e.g., robotic manipulators, and space launch vehicles [38]. We summarize the main tasks as follows:

- Calculate reference trajectories for the state, input, and other variables of interests of the system from its nonlinear equations, with the nominal values of its parameters.
- Obtain linear expressions for the deviations of states and other variables of interests, about the reference trajectories and nominal parameters.
- Considering a finite horizon LQR controller for the Jacobian linearization of the dynamics, construct a LTV system with a perturbation signal to model the parameter variation as its input, and the deviation from the variables of interest as output.
- Define a performance metric to assess the robustness of the LTV system over a finite time horizon involving the induced gains in [37].
- Choose finite sets of weight matrices candidates and search for those that lead to the LQR gain that optimizes the robust performance metric.
- Use the best time-varying LQR gain for tracking the reference trajectories under the nonlinear dynamics of the system subject to parameter uncertainty.
- If the simulations are not satisfactory, choose different sets of weight matrices candidates to improve the robust performance metric.

Chapter 4

Robust Performance Under Parameter Uncertainty

This chapter provides a performance metric to quantify the robustness against parameter uncertainty of a controller for the ascension phase of PLLOs. The robustness is evaluated through the use of reachability analysis, which deals with the problem of bounding the trajectories of a system, given a set of initial states, and a set of admissible parameters.

Since a reachable set can rarely be computed exactly except in simple cases [39], we instead rely on the computation of over-approximations, for which various methods and representations exist, such as ellipsoids [40], polytopes [41] or level-sets [42]. The considered approach is based on the results presented in [43], where the computation of interval over-approximations for an uncertain system relies on its sensitivity matrices, i.e., the partial derivatives of its trajectories with respect to the uncertain parameters.

A proper evaluation of the robustness of a controller for the STS movement of a PLLO should not be limited to quantify the deviation from reference trajectories of the angular positions and velocities of the links, but also include the deviations of the position and velocity of the CoM, and the control input. Therefore, we extend the method in [43] to be able to apply the reachability analysis to auxiliary static systems, such as those defined by an output function or a feedback controller. The over-approximations for the reachable sets of the variables of interest become the basis of our proposed robust performance metric.

The reachability analysis of the dynamics of the three-link robot under state feedback with the LQR gain obtained from (3.16) for tracking STS 1, shows that the parameter uncertainties due to fluctuations of ±5% of the nominal weight of the user lead to undesired variations of the required loads at the shoulders. Based on our robust performance metric to evaluate a pool of controller candidates, we choose a finite horizon LQR gain that effectively addresses this shortcoming.

4.1 Sensitivity-based Reachability Analysis Under Parameter Uncertainty

Consider a continuous-time, time-varying system

$$\dot{\eta} = g(t, \eta, \rho) \tag{4.1}$$

with state $\eta \in \mathbb{R}^{n_\eta}$, constant but uncertain parameter $\rho \in \left[\underline{\rho}, \overline{\rho}\right] \subseteq \mathbb{R}^{n_\rho}$, and continuously differentiable vector field $g : \mathbb{R} \times \mathbb{R}^{n_\eta} \times \mathbb{R}^{n_\rho} \to \mathbb{R}^{n_\eta}$. The state reached by this system at time $t \geq t_0$ from fixed initial state η_0 is

$$\Phi(t; t_0, \eta_0, \rho) := \eta_0 + \int_{t_0}^{t} g\left(s, \eta\left(s, \rho\right), \rho\right) ds.$$

We denote the reachable set under parameter uncertainty as

$$\text{Reach}\left(t, \left[\underline{\rho}, \overline{\rho}\right]\right) := \left\{\Phi(t; t_0, \eta_0, \rho) \mid \rho \in \left[\underline{\rho}, \overline{\rho}\right]\right\} \subseteq \mathbb{R}^{n_\eta},$$

and the sensitivity function of the state trajectories with respect to the parameter as

$$S(t; t_0, \eta_0, \rho) := \frac{\partial \Phi(t; t_0, \eta_0, \rho)}{\partial \rho} \in \mathbb{R}^{n_\eta \times n_\rho}. \tag{4.2}$$

We take the following lemma from [43].

Lemma 1 *Assume that there exist* $\underline{\mathcal{S}}, \overline{\mathcal{S}} : [t_0, +\infty) \to \mathbb{R}^{n_\eta \times n_\rho}$ *such that* $S(t; t_0, \eta_0, \rho) \in \left[\underline{\mathcal{S}}(t), \overline{\mathcal{S}}(t)\right]$ *for all* $t \geq t_0$, *and* $\rho \in \left[\underline{\rho}, \overline{\rho}\right]$. *Let the functions* $\underline{r}, \overline{r} : [t_0, +\infty) \to \mathbb{R}^{n_\eta}$ *be defined as*

$$\begin{aligned} \underline{r}_i(t) &:= \Phi_i(t; t_0, \eta_0, \underline{\pi}^i(t)) - d^i(t)(\underline{\pi}^i(t) - \overline{\pi}^i(t)), \\ \overline{r}_i(t) &:= \Phi_i(t; t_0, \eta_0, \overline{\pi}^i(t)) + d^i(t)(\underline{\pi}^i(t) - \overline{\pi}^i(t)), \end{aligned} \tag{4.3}$$

where the j^{th} *elements of the parameter values* $\underline{\pi}^i(t), \overline{\pi}^i(t) \in \left[\underline{\rho}, \overline{\rho}\right]$ *and row vector* $d^i(t) \in \mathbb{R}^{n_\rho}$ *are determined according to the sign of the entries of the center of the interval matrix* $\left[\underline{\mathcal{S}}(t), \overline{\mathcal{S}}(t)\right]$ *as*

$$\left.\begin{aligned} &\underline{\pi}^i_j(t) := \underline{\rho}_j,\ \overline{\pi}^i_j(t) := \overline{\rho}_j, \\ &d^i_j(t) := \min\left(0, \underline{\mathcal{S}}_{ij}(t)\right) \end{aligned}\right\} \text{ if } \hat{\mathcal{S}}_{ij}(t) \geq 0;$$

$$\left.\begin{aligned} &\underline{\pi}^i_j(t) := \overline{\rho}_j,\ \overline{\pi}^i_j(t) := \underline{\rho}_j, \\ &d^i_j(t) := \max\left(0, \overline{\mathcal{S}}_{ij}(t)\right) \end{aligned}\right\} \text{ if } \hat{\mathcal{S}}_{ij}(t) < 0. \tag{4.4}$$

Then $\left[\underline{r}(t), \overline{r}(t)\right]$ *is an interval over-approximation of the reachable set of states at time* $t \geq t_0$*, so that*

$$\text{Reach}\left(t, \left[\underline{\rho}, \overline{\rho}\right]\right) \subseteq \left[\underline{r}(t), \overline{r}(t)\right].$$

If in addition $d^i_j(t) = 0 \; \forall (i,j) \in \{1,\ldots,n_\eta\} \times \{1,\ldots,n_\rho\}$*, then* $\left[\underline{r}(t), \overline{r}(t)\right]$ *is the smallest interval containing* $\text{Reach}\left(t, \left[\underline{\rho}, \overline{\rho}\right]\right)$.

We aim to compute over-approximations of reachable sets not only for the state η of the system dynamics in (4.1), but also of other variables of interests that are described by static mappings of η and the parameter ρ. To clearly distinguish such over-approximations, and the functions required in Lemma 1, we write the variables of interest as superscripts, e.g., Φ^η, S^η, $\underline{r}^\eta$, and $\overline{r}^\eta$ for conducting the over-approximation of $\text{Reach}^\eta\left(t, \left[\underline{\rho}, \overline{\rho}\right]\right)$.

In order to apply the reachability analysis in the space of η, we need to find bounds for the sensitivity matrix of (4.1) at each time $t \in \left[t_0, t_f\right]$ where $\underline{r}^\eta(t)$ and $\overline{r}^\eta(t)$ are to be computed. The sensitivity function $S^\eta(t; t_0, \eta_0, \rho)$ along the state trajectory $\Phi^\eta(t; t_0, \eta_0, \rho)$ satisfies

$$\dot{S}^\eta(t; t_0, \eta_0, \rho) = \left.\frac{\partial g(t,\eta,\rho)}{\partial \eta}\right|_{\eta=\Phi^\eta(t;t_0,\eta_0,\rho)} S^\eta(t; t_0, \eta_0, \rho) \quad + \left.\frac{\partial g(t,\eta,\rho)}{\partial \rho}\right|_{\eta=\Phi^\eta(t;t_0,\eta_0,\rho)}, \tag{4.5}$$

with zero initial condition $S^\eta(t; t_0, \eta_0, \rho) = 0_{n_\eta \times n_\rho}$ [44]. The sensitivity bounds $\left[\underline{S}^\eta(t), \overline{S}^\eta(t)\right]$ can be estimated through a sampling approach consisting in first numerically solving the matrix differential equation (4.5) for a finite set of randomly chosen parameters $\mathcal{P} \subset [\underline{\rho}, \overline{\rho}]$. Then, an approximation $\left[\underline{S}^\eta(t), \overline{S}^\eta(t)\right]$ of the sensitivity bounds $\left[\underline{S}^\eta(t), \overline{S}^\eta(t)\right]$ is obtained by minimizing/maximizing the ij entries of the solutions for $S^\eta(t; t_0, \eta_0, \rho)$ over all $\rho \in \mathcal{P}$, at time t:

$$\begin{aligned} \overline{S}^\eta_{ij}(t) &= \max_{\rho \in \mathcal{P}} S^\eta_{ij}(t; t_0, \eta_0, \rho), \\ \underline{S}^\eta_{ij}(t) &= \min_{\rho \in \mathcal{P}} S^\eta_{ij}(t; t_0, \eta_0, \rho). \end{aligned} \tag{4.6}$$

The boundedness assumption on (4.2) required in Lemma 1, i.e., $\left[\underline{S}^\eta(t), \overline{S}^\eta(t)\right] \subseteq \left[\underline{S}^\eta(t), \overline{S}^\eta(t)\right]$, is not guaranteed to hold. However, a more reliable approximation may be found by iteratively enlarging the bounds through a falsification approach. An iteration of the falsification at time t looks for $\rho \in \left[\underline{\rho}, \overline{\rho}\right]$ whose sensitivity does not lie within the bounds determined from sampling, which is achieved by solving the optimization problem

$$J_{\text{F}}(t) := \min_{\rho \in \left[\underline{\rho}, \overline{\rho}\right]} \left(\min_{i,j} \left(\tfrac{1}{2}\left(\overline{S}^\eta_{ij}(t) - \underline{S}^\eta_{ij}(t)\right) - \left| S^\eta_{ij}(t; t_0, \eta_0, \rho) - \tfrac{1}{2}\left(\underline{S}^\eta_{ij}(t) + \overline{S}^\eta_{ij}(t)\right)\right| \right) \right). \tag{4.7}$$

The cost function used in this minimization problem is defined for each pair $(i,j) \in \{1,\ldots,n_\eta\} \times \{1,\ldots,n_\rho\}$ by an inverted and translated absolute value function, such that it returns a negative value

if and only if $S^\eta(t;t_0,\eta_0,\rho) \notin \left[\underline{S}^\eta(t), \overline{S}^\eta(t)\right]$. As a result, finding $J_\mathrm{F}(t) < 0$ means that there exists a pair (i,j) for which the bounds from sampling $\left[\underline{S}^\eta(t), \overline{S}^\eta(t)\right]$ have been falsified, and they need to be updated according to $S^\eta_{ij}(t;t_0,\eta_0,\rho^*)$, where $\rho^* \in \left[\underline{\rho}, \overline{\rho}\right]$ is the optimizer associated with a local minimum found for (4.7). This falsification procedure is then repeated until we obtain $J_\mathrm{F}(t) \geq 0$.

Although falsification can help to improve the approximation of the sensitivity bounds, it cannot provide formal guarantees that $\left[\underline{S}^\eta(t), \overline{S}^\eta(t)\right] \subseteq \left[\underline{\mathcal{S}}^\eta(t), \overline{\mathcal{S}}^\eta(t)\right]$ is satisfied, because the optimization problem can only find local minima. There exists an alternative approach based on interval analysis presented in [43] for which such guarantees are provided, but it has been shown to be of limited practical use, due to the overly conservative nature of the obtained sensitivity bounds.

Applying Lemma 1 with the updated sensitivity bounds $\underline{S}^\eta, \overline{S}^\eta : [t_0, +\infty) \to \mathbb{R}^{n_\eta \times n_\rho}$ thus results in two functions $\underline{r}^\eta, \overline{r}^\eta : [t_0, +\infty) \to \mathbb{R}^{n_\eta}$ over-approximating the reachable set of (4.1) at each time $t \geq t_0$:

$$\mathrm{Reach}^\eta\left(t, \left[\underline{\rho}, \overline{\rho}\right]\right) := \left\{\Phi^\eta(t;t_0,\eta_0,\rho) \mid \rho \in \left[\underline{\rho}, \overline{\rho}\right]\right\} \subseteq \left[\underline{r}^\eta(t), \overline{r}^\eta(t)\right]. \tag{4.8}$$

Consider now a map $\zeta : \mathbb{R}^{n_\eta} \times \left[\underline{\rho}, \overline{\rho}\right] \to \mathbb{R}^{n_y}$ defining the output $y = \zeta(\eta, \rho)$ of (4.1) according to its state η and parameter ρ. A reachability analysis on the output $y \in \mathbb{R}^{n_y}$ is done by applying Lemma 1 to the static system describing the evolution of y in terms of the trajectories of η:

$$\Phi^y(t;t_0,\eta_0,\rho) := \zeta(\Phi^\eta(t;t_0,\eta_0,\rho),\rho). \tag{4.9}$$

Following the definition in (4.2), the sensitivity of output y with respect to parameter ρ is determined by using the chain rule on ζ:

$$\begin{aligned} S^y(t;t_0,\eta_0,\rho) :=& \frac{\partial \Phi^y(t;t_0,\eta_0,\rho)}{\partial \rho} \\ =& \frac{\partial \zeta(\Phi^\eta(t;t_0,\eta_0,\rho),\rho)}{\partial \rho} \\ =& \left.\frac{\partial \zeta(\eta,\rho)}{\partial \eta}\right|_{\eta=\Phi^\eta(t;t_0,\eta_0,\rho)} \frac{\partial \Phi^\eta(t;t_0,\eta_0,\rho)}{\partial \rho} + \left.\frac{\partial \zeta(\eta,\rho)}{\partial \rho}\right|_{\eta=\Phi^\eta(t;t_0,\eta_0,\rho)} \\ =& \left.\frac{\partial \zeta(\eta,\rho)}{\partial \eta}\right|_{\eta=\Phi^\eta(t;t_0,\eta_0,\rho)} S^\eta(t;t_0,\eta_0,\rho) + \left.\frac{\partial \zeta(\eta,\rho)}{\partial \rho}\right|_{\eta=\Phi^\eta(t;t_0,\eta_0,\rho)}. \end{aligned} \tag{4.10}$$

With knowledge of $S^\eta(t;t_0,\eta_0,\rho)$ from the solution to (4.5), and the mapping $\zeta : \mathbb{R}^{n_\eta} \times [\underline{\rho}, \overline{\rho}] \to \mathbb{R}^{n_y}$, the sensitivity bounds $\underline{S}^y, \overline{S}^y : [t_0, +\infty) \to \mathbb{R}^{n_y \times n_\rho}$ can be computed. Thus we use $\underline{S}^y, \overline{S}^y$ in (4.4) to apply Lemma 1 on the static system (4.9) and obtain over-approximation functions $\underline{r}^y, \overline{r}^y : [t_0, +\infty) \to \mathbb{R}^{n_y}$, such that for each time $t \geq t_0$

$$\mathrm{Reach}^y\left(t, \left[\underline{\rho}, \overline{\rho}\right]\right) := \left\{\Phi^y(t;t_0,\eta_0,\rho) \mid \rho \in \left[\underline{\rho}, \overline{\rho}\right]\right\} \subseteq \left[\underline{r}^y(t), \overline{r}^y(t)\right]. \tag{4.11}$$

Assuming that (4.1) is actually a closed-loop system obtained from the use of a feedback controller $u = \mathcal{K}(t, \eta, \rho)$ with $\mathcal{K} : [t_0, +\infty) \times \mathbb{R}^{n_\eta} \times \mathbb{R}^{n_\rho} \to \mathbb{R}^{n_u}$, we can apply the same approach as for the output y, by defining the static system

$$\Phi^u(t; t_0, \eta_0, \rho) := \mathcal{K}(t, \Phi^\eta(t; t_0, \eta_0, \rho), \rho). \tag{4.12}$$

The sensitivity of input u with respect to parameter ρ is obtained similarly to S^y in (4.10):

$$\begin{aligned} S^u(t; t_0, \eta_0, \rho) :=& \frac{\partial \Phi^u(t; t_0, \eta_0, \rho)}{\partial \rho} \\ =& \frac{\partial \mathcal{K}(t, \Phi^\eta(t; t_0, \eta_0, \rho), \rho)}{\partial \rho} \\ =& \left.\frac{\partial \mathcal{K}(t, \eta, \rho)}{\partial \eta}\right|_{\eta = \Phi^\eta(t; t_0, \eta_0, \rho)} S^\eta(t; t_0, \eta_0, \rho) + \left.\frac{\partial \mathcal{K}(t, \eta, \rho)}{\partial \rho}\right|_{\eta = \Phi^\eta(t; t_0, \eta_0, \rho)}, \end{aligned} \tag{4.13}$$

which then leads to sensitivity bounds $\underline{S}^u, \overline{S}^u : [t_0, +\infty) \to \mathbb{R}^{n_u \times n_\rho}$ for the static system (4.12) that are used in Lemma 1 to obtain over-approximation functions $\underline{r}^u, \overline{r}^u : [t_0, +\infty) \to \mathbb{R}^{n_u}$, such that for each time $t \geq t_0$ we have

$$\text{Reach}^u\left(t, \left[\underline{\rho}, \overline{\rho}\right]\right) := \left\{\Phi^u(t; t_0, \eta_0, \rho) \mid \rho \in \left[\underline{p}, \overline{p}\right]\right\} \subseteq \left[\underline{r}^u(t), \overline{r}^u(t)\right]. \tag{4.14}$$

4.2 Numerical Application of the Reachability Analysis

Given fixed $x_0 := x(t_0)$ for the nonlinear dynamics of the three-link robot under finite time horizon LQR control in (3.10), the sensitivity function $S^x(t; t_0, x_0, p)$ of the state trajectory $\Phi^x(t; t_0, x_0, p)$ over the horizon $\left[t_0, t_f\right]$ for a STS movement, satisfies the differential equation

$$\dot{S}^x(t; t_0, x_0, p) = \left.\frac{\partial \varphi(t, x, p)}{\partial x}\right|_{x = \Phi^x(t; t_0, x_0, p)} S^x(t; t_0, x_0, p) \quad + \left.\frac{\partial \varphi(t, x, p)}{\partial p}\right|_{x = \Phi^x(t; t_0, x_0, p)}, \tag{4.15}$$

with zero initial condition $S^x(t; t_0, x_0, p) = 0_{6 \times 12}$.

Define the output $y := [x_{\text{CoM}}; y_{\text{CoM}}; \dot{x}_{\text{CoM}}; \dot{y}_{\text{CoM}}]$, and consider the gain $K^*_{\text{LQR1}}(t) \in \mathbb{R}^{4 \times 6}$ obtained for tracking STS 1 in Section 3.3. The successors of the output, and input of the minimally actuated PLLO at the hips are

$$\Phi^y(t; t_0, x_0, p) = \zeta\left(\Phi^x(t; t_0, x_0, p), p\right), \tag{4.16}$$

$$\Phi^u(t; t_0, x_0, p) = \hat{u}(t) - K^*_{\text{LQR1}}(t)\left(\Phi^x(t; t_0, x_0, p) - \hat{x}(t)\right), \tag{4.17}$$

where the static mapping $\zeta : \mathbb{R}^6 \times \mathbb{R}^{12} \to \mathbb{R}^4$ is defined from the kinematic equations (2.5) to (2.8) as

$$\zeta(x, p) := \begin{bmatrix} k_0(k_1 c_1 + k_2 c_{12} + k_3 c_{123}) \\ k_0(k_1 s_1 + k_2 s_{12} + k_3 s_{123}) \\ -\dot{\theta}_1 y_{\text{CoM}} - \dot{\theta}_2 k_0(k_2 s_{12} + k_3 s_{123}) - \dot{\theta}_3 k_0 k_3 s_{123} \\ \dot{\theta}_1 x_{\text{CoM}} + \dot{\theta}_2 k_0(k_2 c_{12} + k_3 c_{123}) + \dot{\theta}_3 k_0 k_3 c_{123} \end{bmatrix}. \tag{4.18}$$

From (4.10) and (4.13), the sensitivity functions for the output y and input u are

$$S^y(t;t_0,x_0,p) := \left.\frac{\partial \zeta(x,p)}{\partial x}\right|_{x=\Phi^x(t;t_0,x_0,p)} S^x(t;t_0,x_0,p) + \left.\frac{\partial \zeta(x,p)}{\partial p}\right|_{x=\Phi^x(t;t_0,x_0,p)} \in \mathbb{R}^{4\times 12}, \tag{4.19}$$

$$S^u(t;t_0,x_0,p) := -K^*_{\mathrm{LQR1}}(t)\, S^x(t;0,x_0,p) \in \mathbb{R}^{4\times 12}. \tag{4.20}$$

The goal of this section is to apply Lemma 1 to compute over-approximation functions for the reachable sets of the state $\mathrm{Reach}^x\left(t, \left[\underline{p}, \overline{p}\right]\right) \subseteq \left[\underline{r}^x(t), \overline{r}^x(t)\right]$, output $\mathrm{Reach}^y\left(t, \left[\underline{p}, \overline{p}\right]\right) \subseteq \left[\underline{r}^y(t), \overline{r}^y(t)\right]$, and input $\mathrm{Reach}^u\left(t, \left[\underline{p}, \overline{p}\right]\right) \subseteq \left[\underline{r}^u(t), \overline{r}^u(t)\right]$, at each time t in $T_s := \{0 : 0.01 : 3.5\}$ [s]. The parameter uncertainties lie within the interval $\left[\underline{p}, \overline{p}\right] \subseteq \mathbb{R}^{12}$ in Table 4.1, whose bounds were calculated with anthropometric data from [45] for a user with a nominal weight and height of 50[kg] and 1.75[m].

Table 4.1: Bounds for the parameter uncertainty of the three-link robot for a fluctuation of ±5% in the nominal weight of the user, and a variation of ±1[cm] in the nominal lengths of the links

Link	m_i [kg]	I_i [kg · m^2]	l_i [m]	l_{ci} [m]
1	[9.2, 10.2]	[1.10, 1.21]	[0.52, 0.54]	[0.23, 0.30]
2	[11.9, 13.2]	[0.49, 0.54]	[0.40, 0.42]	[0.18, 0.23]
3	[42.3, 46.8]	[2.39, 2.65]	[0.51, 0.53]	[0.24, 0.28]

Randomly drawing a set $\mathcal{P}_b \subset \left[\underline{p}, \overline{p}\right]$ of 500 parameter values from a Latin hypercube, the first step in the analysis is to numerically solve the sensitivity equation (4.15) over the time horizon $[0, 3.5]$ for all $p \in \mathcal{P}_b$. The sensitivity bounds $\underline{S}^x, \overline{S}^x : [0, 3.5] \to \mathbb{R}^{6\times 12}$ are estimated by minimizing/maximizing the entries of the solutions for $S^x(t;0,x_0,p)$ at each $t \in T_s$ as in (4.6), and then we attempt to refine them through the falsification approach. The time spent in a single falsification iteration over the bounds estimated by sampling $\left[\underline{S}^x(t), \overline{S}^x(t)\right]$ for the first 17 elements in T_s are shown in Figure 4.1, together with the calculated cost $J_{\mathrm{F}}(t)$. It can be seen that the falsification is done quickly for the first few time steps, but going further into T_s, it grows to the point where it becomes unpractical to continue executing it. In addition, the positive values of $J_{\mathrm{F}}(t)$ mean that no enlargement of the sensitivity bounds is achieved over the first iteration. On the basis of these observations, and that falsification does not provide formal guarantees of satisfying $\left[\underline{S}^x(t), \overline{S}^x\right] \subseteq \left[\underline{\mathcal{S}}^x(t), \overline{\mathcal{S}}^x(t)\right]$, the results that follow only rely on the sampling approach with the assumption that $\left[\underline{S}^x(t), \overline{S}^x(t)\right]$ are close enough to an over-approximation of $\left[\underline{\mathcal{S}}^x(t), \overline{\mathcal{S}}^x(t)\right]$. A consequence of this assumption is that even though the reachability analysis result in Lemma 1 might not always be a true over-approximation of the reachable set, it still provides an accurate measure of the worst-case performances for the closed-loop system (3.10).

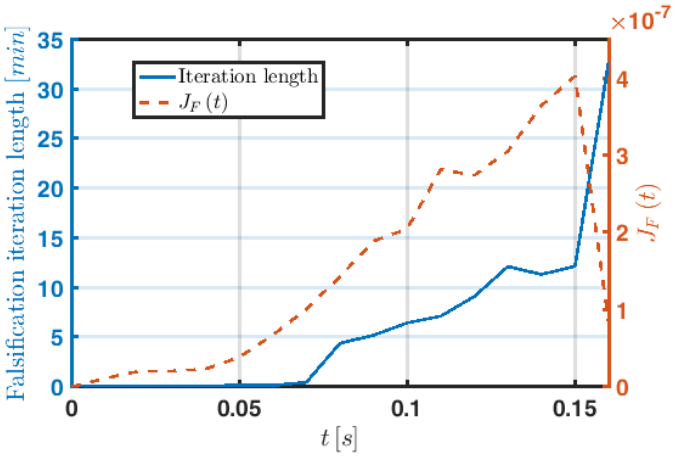

Figure 4.1: Length of a falsification iteration for the state sensitivity bounds at time $t \in [0, 0.16]$, and cost $J_{\mathrm{F}}(t)$.

Once $[\underline{S}^x(t), \overline{S}^x(t)]$ are known, Lemma 1 is applied to obtain the over-approximation functions $\underline{r}^x(t)$, $\overline{r}^x(t)$ for every $t \in T_s$, which are displayed in green in Figure 4.2. To visualize their tightness, the plots also provide, in blue, the trajectories of the closed-loop system (3.10) for a set $\mathcal{P}_s \subseteq [\underline{p}, \overline{p}]$ of 500 values of p from a Latin hypercube sampling (note that this set is different from $\mathcal{P}_b$). The reference trajectory $\Phi^x(t; 0, x_0, \hat{p})$ for STS 1, with the nominal parameter $\hat{p}$ in (2.23), is in red. The over-approximations for $\theta_1(t)$ in Figure 4.2a show that the terminal position of the shank segment under the parameter uncertainties will only be slightly off the vertical ($\pm 0.5°$), easing the stabilization phase for completing standing. The ones for $\theta_2(t)$ in Figure 4.2b do not become positive, meaning that the controller will not cause the PLLO to hyperextend the knees of the user. Also, since $\theta_3(t)$ in Figure 4.2c never goes negative, and only approaches zero at the end of the horizon, the torso will have natural configurations while ascending.

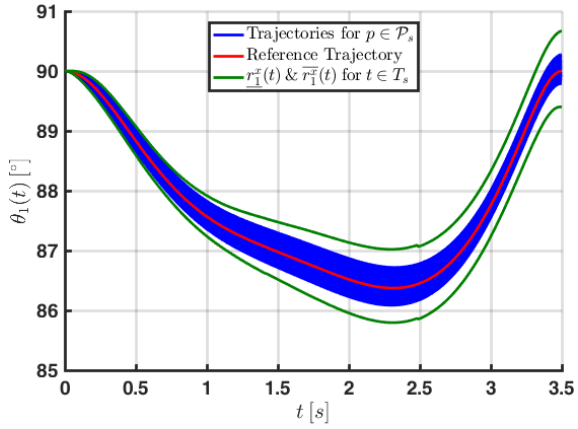

(a) Angular position of link 1 relative to the horizontal.

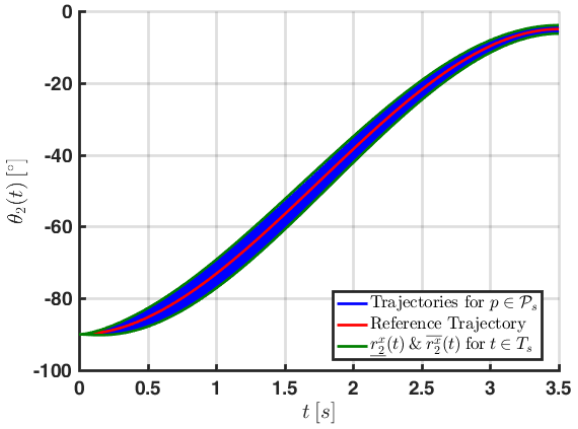

(b) Angular position of link 2 relative to link 1.

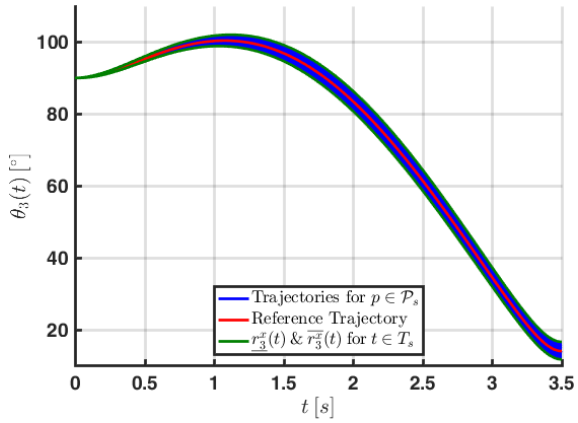

(c) Angular position of link 3 relative to link 2.

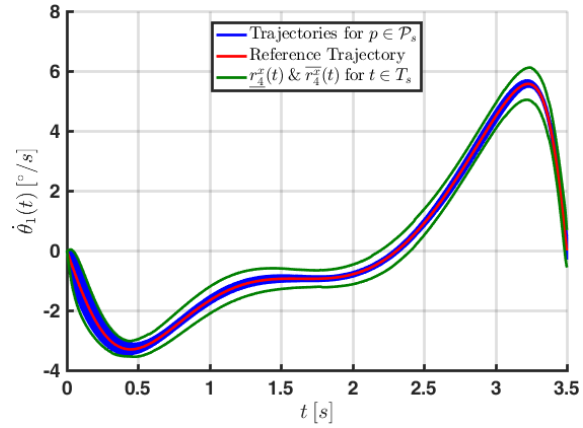

(d) Angular velocity of link 1.

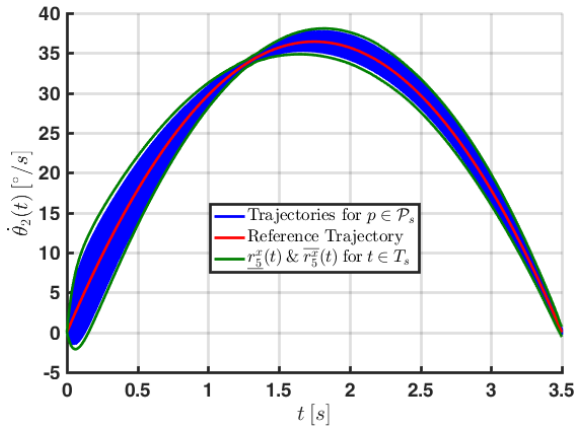

(e) Angular velocity of link 2.

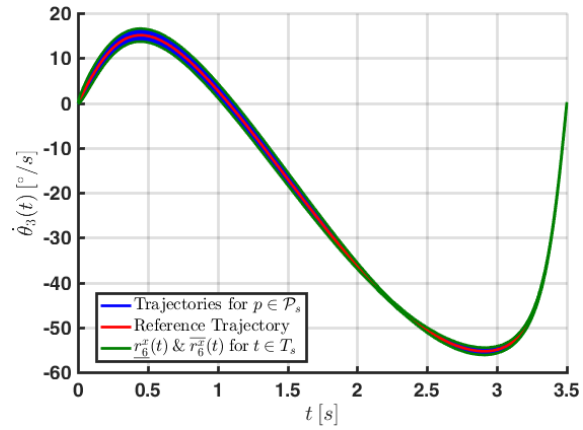

(f) Angular velocity of link 3.

Figure 4.2: Over-approximation functions of the successors $\Phi^x(t;0,x_0,p)$ at every $t \in T_s$ for a PLLO actuated at the hips in state feedback with $K^*_{\text{LQR1}}(t)$.

Define

$$
\begin{aligned}
k_4(\theta,p) &:= k_0(p)\left(k_2(p)s_{12}+k_3(p)s_{123}\right),\\
k_5(\theta,p) &:= k_0(p)k_3(p)s_{123},\\
k_6(\theta,p) &:= k_0(p)\left(k_2(p)c_{12}+k_3(p)c_{123}\right),\\
k_7(\theta,p) &:= k_0(p)k_3(p)c_{123},\\
k_8\left(\theta,\dot{\theta},p\right) &:= k_0(p)\left(\left(k_2(p)s_{12}+k_3(p)s_{123}\right)\dot{\theta}_2+l_{c3}m_3s_{123}\dot{\theta}_3\right),\\
k_9\left(\theta,\dot{\theta},p\right) &:= k_0(p)\left(\left(k_2(p)c_{12}+k_3(p)c_{123}\right)\dot{\theta}_2+l_{c3}m_3c_{123}\dot{\theta}_3\right),
\end{aligned}
$$

whose explicit dependence with respect to θ, $\dot{\theta}$, and p is omitted onwards for compactness. The partial derivative of (4.18) with respect to x is written as

$$
\frac{\partial\zeta(x,p)}{\partial x}=\begin{bmatrix}\zeta_{11}^{x} & 0\\ \zeta_{21}^{x} & \zeta_{11}^{x}\end{bmatrix}\in\mathbb{R}^{4\times6}, \tag{4.21}
$$

with entries $\zeta_{ij}^{x}\in\mathbb{R}^{2\times3}$ given by

$$
\begin{aligned}
\zeta_{11}^{x} &= \begin{bmatrix}-y_{\text{CoM}} & -k_4 & -k_5\\ x_{\text{CoM}} & k_6 & k_7\end{bmatrix},\\
\zeta_{21}^{x} &= -\begin{bmatrix}x_{\text{CoM}}\dot{\theta}_1+k_6\dot{\theta}_2+k_7\dot{\theta}_3 & k_7\dot{\theta}_3-k_6\left(\dot{\theta}_1+\dot{\theta}_2\right) & -k_7\left(\dot{\theta}_1+\dot{\theta}_2+\dot{\theta}_3\right)\\ y_{\text{CoM}}\dot{\theta}_1+k_4\dot{\theta}_2+k_5\dot{\theta}_3 & k_5\dot{\theta}_3-k_4\left(\dot{\theta}_1+\dot{\theta}_2\right) & -k_5(\theta,p)\left(\dot{\theta}_1+\dot{\theta}_2+\dot{\theta}_3\right)\end{bmatrix}.
\end{aligned}
$$

The partial derivative of (4.18) with respect to p is

$$
\frac{\partial\zeta(x,p)}{\partial p}=\begin{bmatrix}\zeta_{11}^{p} & 0 & \zeta_{13}^{p} & \zeta_{14}^{p}\\ \zeta_{21}^{p} & 0 & \zeta_{23}^{p} & \zeta_{24}^{p}\end{bmatrix}\in\mathbb{R}^{4\times12}, \tag{4.22}
$$

where the entries $\zeta_{ij}^{p}\in\mathbb{R}^{2\times3}$ are

$$
\begin{aligned}
\zeta_{11}^{p} &= k_0\begin{bmatrix}l_{c1}c_1-x_{\text{CoM}} & l_1c_1+l_{c2}c_{12}-x_{\text{CoM}} & l_1c_1+l_2c_{12}+l_{c3}c_{123}-x_{\text{CoM}}\\ l_{c1}s_1-y_{\text{CoM}} & l_1s_1+l_{c2}s_{12}-y_{\text{CoM}} & l_1s_1+l_2s_{12}+l_{c3}s_{123}-y_{\text{CoM}}\end{bmatrix},\\
\zeta_{13}^{p} &= k_0\begin{bmatrix}(m_2+m_3)c_1 & m_3c_{12} & 0\\ (m_2+m_3)s_1 & m_3s_{12} & 0\end{bmatrix},\\
\zeta_{14}^{p} &= k_0\begin{bmatrix}m_1c_1 & m_2c_{12} & m_3c_{123}\\ m_1s_1 & m_2s_{12} & m_3s_{123}\end{bmatrix},\\
\zeta_{21}^{p} &= k_0\dot{\theta}_1\begin{bmatrix}y_{\text{CoM}}-l_{c1}s_1 & y_{\text{CoM}}-(l_1s_1+l_{c2}s_{12}) & y_{\text{CoM}}-(l_1s_1+l_2s_{12}+l_{c3}s_{123})\\ l_{c1}c_1-x_{\text{CoM}} & l_1c_1+l_{c2}c_{12}-x_{\text{CoM}} & l_1c_1+l_2c_{12}+l_{c3}c_{123}-x_{\text{CoM}}\end{bmatrix}\\
&\quad+k_0\dot{\theta}_2\begin{bmatrix}0 & -l_{c2}s_{12} & -(l_2s_{12}+l_{c3}s_{123})\\ 0 & l_{c2}c_{12} & l_2c_{12}+l_{c3}c_{123}\end{bmatrix}+k_0\begin{bmatrix}k_8 & k_8 & k_8-l_{c3}s_{123}\dot{\theta}_3\\ -k_9 & -k_9 & l_{c3}c_{123}\dot{\theta}_3-k_9\end{bmatrix},\\
\zeta_{23}^{p} &= k_0\begin{bmatrix}-(m_2+m_3)s_1\dot{\theta}_1 & -m_3s_{12}\left(\dot{\theta}_1+\dot{\theta}_2\right) & 0\\ (m_2+m_3)c_1\dot{\theta}_1 & m_3c_{12}\left(\dot{\theta}_1+\dot{\theta}_2\right) & 0\end{bmatrix},\\
\zeta_{24}^{p} &= k_0\begin{bmatrix}-m_1s_1\dot{\theta}_1 & -m_2s_{12}\left(\dot{\theta}_1+\dot{\theta}_2\right) & -m_3s_{123}\left(\dot{\theta}_1+\dot{\theta}_2+\dot{\theta}_3\right)\\ m_1c_1\dot{\theta}_1 & m_2c_{12}\left(\dot{\theta}_1+\dot{\theta}_2\right) & m_3c_{123}\left(\dot{\theta}_1+\dot{\theta}_2+\dot{\theta}_3\right)\end{bmatrix}.
\end{aligned}
$$

To determine $\underline{S}^y, \overline{S}^y : [0, 3.5] \to \mathbb{R}^{4\times 12}$ we plug (4.21), (4.22), and the solutions to (4.15) for all $p \in \mathcal{P}_b$ into (4.19), and then compute the extremal values of the entries of the sensitivity matrices at each $t \in T_s$. With the estimates for $\left[\underline{\mathcal{S}}^y(t), \overline{\mathcal{S}}^y(t)\right]$ we use Lemma 1 on (4.16) to calculate the over-approximation functions $\underline{r^y}(t)$, $\overline{r^y}(t)$ shown in Figure 4.3 in green. The reference trajectory $\Phi^y(t; 0, x_0, \hat{p})$ is in red, and the trajectories $\Phi^y(t; 0, x_0, p)$ for all $p \in \mathcal{P}_s$ are in blue. It is clear that the good trajectory tracking in the space of x observed in Figure 4.2, does not translate well under parameter uncertainty into the space of y. The bounds for $y_{\text{CoM}}(t)$ in Figure 4.3b are up to ±5[cm] from its reference trajectory, while $\dot{y}_{\text{CoM}}(t)$ in Figure 4.3d can exhibit deviations of ±2[cm/s].

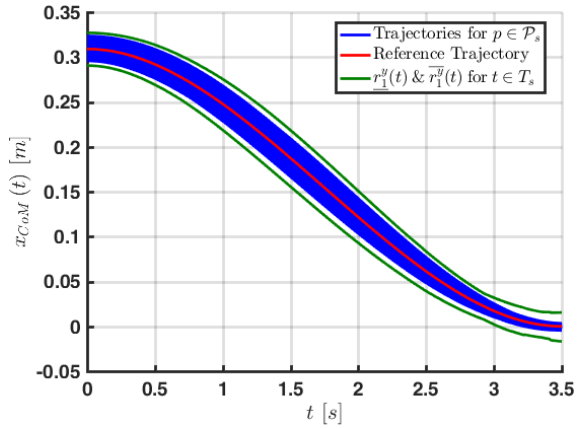

(a) x_{CoM} coordinate of the position of the three-link robot CoM.

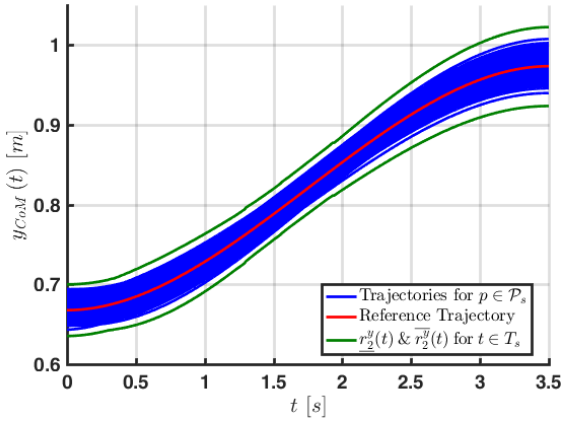

(b) y_{CoM} coordinate of the position of the three-link robot CoM.

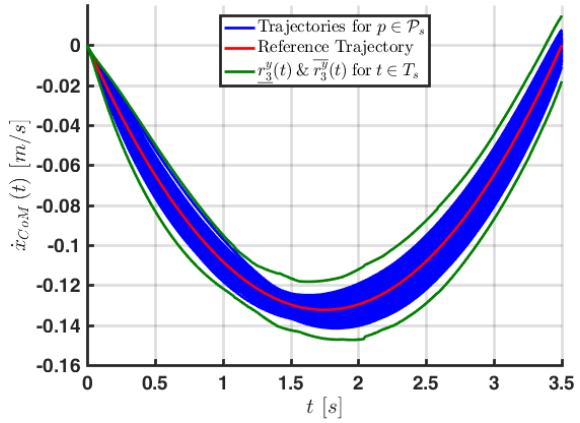

(c) $\dot{x}_{\text{CoM}}$ coordinate of the velocity of the three-link robot CoM.

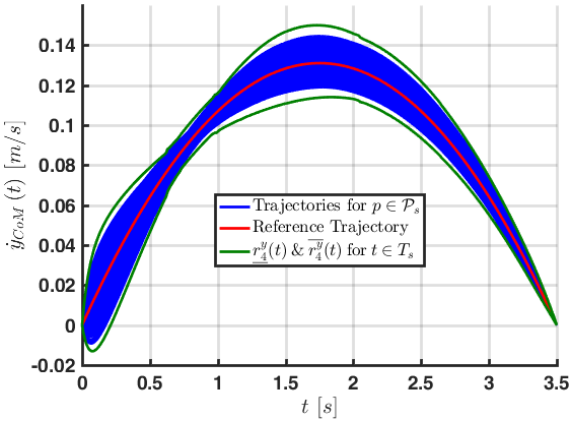

(d) $\dot{y}_{\text{CoM}}$ coordinate of the velocity of the three-link robot CoM.

Figure 4.3: Over-approximation functions of the successors $\Phi^y(t; t_0, x_0, p)$ at every $t \in T_s$ for a PLLO actuated at the hips in state feedback with $K^*_{\text{LQR1}}(t)$.

Figure 4.4a shows the bounds of the over-approximation interval $\left[\underline{r}^y(t), \overline{r}^y(t)\right]$ for the position of the CoM $[x_{\text{CoM}}; y_{\text{CoM}}]$ at $t_0 = 0$[s] (cyan), $t = 1.75$[s] (magenta), and $t_f = 3.5$[s] (green). The clouds of successors $\Phi^y(t; 0, x_0, p)$ for $p \in \mathcal{P}_s$ are in blue for each of these three time instants. The nominal trajectory for STS 1 is in red. Note that despite having a single initial state x_0 for the closed-loop system (3.10), the over-approximation $\left[\underline{r}^y(0), \overline{r}^y(0)\right]$ at $t_0 = 0$ is not reduced to a single point, due to the effect of the parameter uncertainty $p \in \left[\underline{p}, \overline{p}\right]$ on the initial position of the CoM through the mapping $y(0) = \zeta(x_0, p)$. The size of the box enclosing the final position of the CoM allows to assess that there is no risk of sit-back or step failures.

Figure 4.4b depicts the bounds of the over-approximation interval $\left[\underline{r}^y(t), \overline{r}^y(t)\right]$ for the velocity of the CoM $[\dot{x}_{\text{CoM}}; \dot{y}_{\text{CoM}}]$. The reference trajectory in red goes from $[0; 0]$ at $t_0 = 0$[s], to $[-0.13; 0.13]$ at $t = 1.75$[s], and back to $[0; 0]$ at $t_f = 3.5$[s]. In this plane, the projection of $\left[\underline{r}^y(0), \overline{r}^y(0)\right]$ is reduced to the single state $\{[0; 0]\}$ due to the starting conditions at rest $\dot{\theta}_1(0) = \dot{\theta}_2(0) = \dot{\theta}_3(0) = 0$. Notice that the projection of $\left[\underline{r}^y(3.5), \overline{r}^y(3.5)\right]$ at the final time is almost flat, since $\dot{y}_{\text{CoM}}(3.5)$ goes close to 0 for every $p \in [\underline{p}, \overline{p}]$, which is beneficial to avoid the feet to lose contact with the ground.

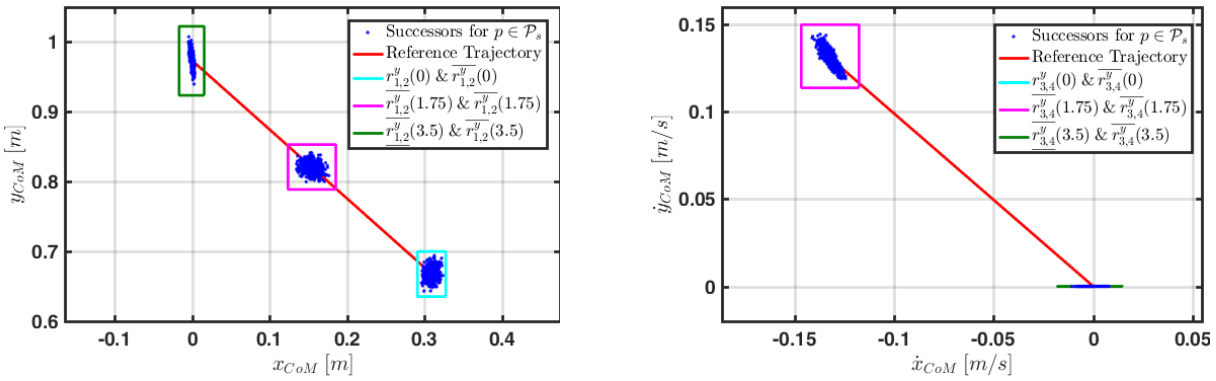

(a) Position trajectories of the three-link robot CoM.

(b) Velocity trajectories of the three-link robot CoM.

Figure 4.4: Over-approximations for the CoM trajectories achieved with $K^*_{\text{LQR1}}(t)$ at three time instants of STS 1.

The estimates for $\left[\underline{S}^u(t), \overline{S}^u(t)\right]$ are obtained by plugging the solutions of (4.15) into (4.20), and minimizing/maximizing the entries of the matrices over all $p \in \mathcal{P}_b$ at every $t \in T_s$. Applying Lemma 1 on (4.17) with $\underline{S}^u, \overline{S}^u : [0, 3.5] \to \mathbb{R}^{4\times 12}$, allows to compute the over-approximation functions $\underline{r}^u(t)$, $\overline{r}^u(t)$ shown in green in Figure 4.5, alongside the reference input $\hat{u}(t)$ in red, and the trajectories $\Phi^u(t; 0, x_0, p)$ for the 500 random $p \in \mathcal{P}_s$ in blue. Since the inputs related to the upper body loads at the joint of the shoulders are expected to be learnt by the user through training, it is not a good feature of this particular finite time horizon LQR controller that the over-approximations for $\tau_s(t)$, $F_x(t)$, and $F_y(t)$ exhibit deviations of up to ±40[N.m], ±10[N], and ±13[N], respectively. Although it could be feasible to apply such loads, the predicted variability under parameter uncertainty might make it difficult for a user to properly time the actions for a successful ascending phase.

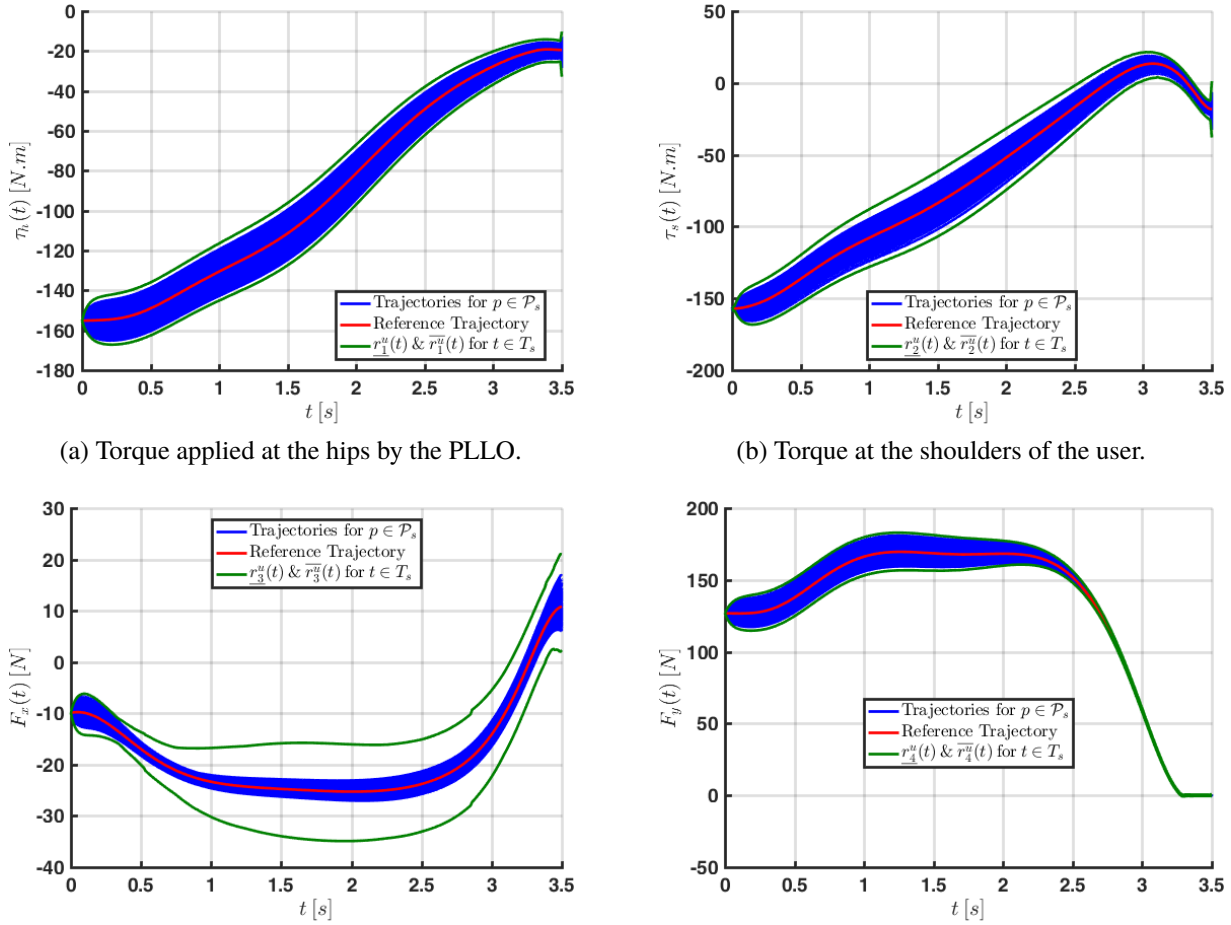

(a) Torque applied at the hips by the PLLO.

(b) Torque at the shoulders of the user.

(c) Horizontal force at the shoulders of the user.

(d) Vertical force at the shoulders of the user.

Figure 4.5: Over-approximation functions of the successors $\Phi^u(t; t_0, x_0, p)$ at every $t \in T_s$ for a PLLO actuated at the hips in state feedback with $K^*_{\text{LQR1}}(t)$.

Despite conducting the reachability analysis with sensitivity bounds estimated from the finite set $\mathcal{P}_b$, which are not guaranteed to contain all possible sensitivity values over the parameter interval $\left[\underline{p}, \overline{p}\right]$, Figures 4.2 to 4.5 show that all the trajectories simulated with random parameters in blue $\Phi^x(t; 0, x_0, p)$, $\Phi^y(t; 0, x_0, p)$, and $\Phi^u(t; 0, x_0, p)$ are indeed contained within their computed over-approximations $\forall t \in T_s$, and are overly conservative only for $F_x(t)$ in Figure 4.5c.

Figures 4.3c and 4.3d highlight that the over-approximations obtained with Lemma 1 may present non-smooth behaviors. This is due to the definition of the compensation term $d^i_j(t)$ in (4.4), which may have non-continuous jumps over time between a constant value at 0, and the sensitivity bound functions $\underline{S}_{ij}, \overline{S}_{ij} : [t_0, t_f] \to \mathbb{R}$. As an illustration, Figure 4.6 presents a zoom of Figure 4.3d, where two such non-smooth behaviors are visible on the bounds of the over-approximation (in green) corresponding to the jump from 0 to $\overline{S}^y_{48}$ at time $t = 0.62$[s] and the jump from $\overline{S}^y_{48}$ to $\underline{S}^y_{48}$ at time $t = 0.63$[s].

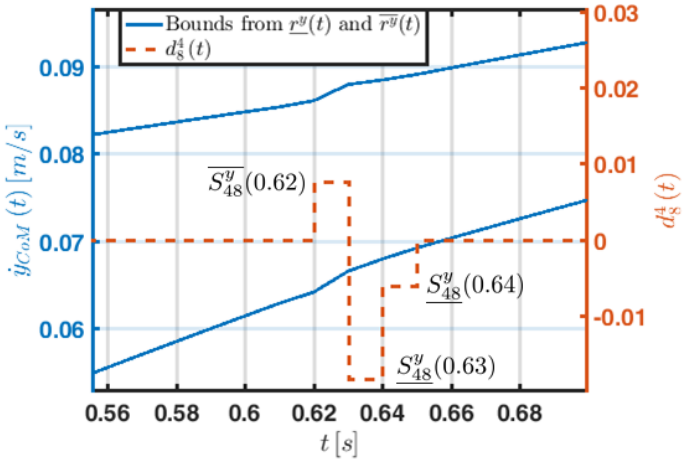

Figure 4.6: Effect of $d_j^i(t)$ on over-approximation bounds.

A workstation of 4 cores at 2.7[GHz] running Matlab Parallel Toolbox completes the sensitivity-based reachability analysis of this section in 5.9[h]. 1.05[h] are spent in solving the sensitivity equation (4.15) for $p \in \mathcal{P}_b$. Computing $\underline{S}^x, \overline{S}^x : [0, 3.5] \to \mathbb{R}^{6\times 12}$ and $\underline{r}^x, \overline{r}^x : [0, 3.5] \to \mathbb{R}^6$ take 1.92[h], $\underline{S}^y, \overline{S}^y : [0, 3.5] \to \mathbb{R}^{4\times 12}$ and $\underline{r}^y, \overline{r}^y : [0, 3.5] \to \mathbb{R}^4$ take 1.89[h], and $\underline{S}^u, \overline{S}^u : [0, 3.5] \to \mathbb{R}^{4\times 12}$ and $\underline{r}^u, \overline{r}^u : [0, 3.5] \to \mathbb{R}^4$ take 1.03[h].

4.3 Robust Performance Metric

To evaluate the robustness against parameter uncertainty of controllers for the STS movement of PLLOs, we propose a performance metric for assessing the worst-case deviations of the state $x(t)$, output $y(t) := [x_{\text{CoM}}(t); y_{\text{CoM}}(t); \dot{x}_{\text{CoM}}(t); \dot{y}_{\text{CoM}}(t)]$, and input $u(t)$ from their desired trajectories $\hat{x}(t)$, $\hat{y}(t) := \zeta(\hat{x}(t), \hat{p})$, and $\hat{u}(t)$, based on over-approximations of their reachable sets at particular instants of time within the horizon $[t_0, t_f]$.

For $[a, b] \subseteq \mathbb{R}^n$, and $c \in \mathbb{R}^n$, let $\nu([a, b], c) \in \mathbb{R}$ be

$$\nu([a, b], c) := \prod_{i=\{1,\ldots,n\}} \left| \frac{a_i + b_i}{2} - c_i \right|.$$

To evaluate the worst-case performance for tracking $\hat{x}(t)$, $\hat{u}(t)$, and $\hat{y}(t)$, we propose the metric:

$$J_{\text{P}} := \sum_{t\in T_{\text{P}}} w_{\text{v}}^\top \begin{bmatrix} \text{vol}\left([\underline{r}^x(t), \overline{r}^x(t)]\right) \\ \text{vol}\left([\underline{r}^y(t), \overline{r}^y(t)]\right) \\ \text{vol}\left([\underline{r}^u(t), \overline{r}^u(t)]\right) \end{bmatrix} + \sum_{t\in T_{\text{P}}} w_{\text{o}}^\top \begin{bmatrix} \nu\left([\underline{r}^x(t), \overline{r}^x(t)], \hat{x}(t)\right) \\ \nu\left([\underline{r}^y(t), \overline{r}^y(t)], \hat{y}(t)\right) \\ \nu\left([\underline{r}^u(t), \overline{r}^u(t)], \hat{u}(t)\right) \end{bmatrix}, \tag{4.23}$$

where $T_{\text{P}} \subseteq \left[t_0, t_f\right]$ is the set of time instants where the over-approximation functions are computed, $w_{\text{v}} \in \mathbb{R}^3$ weighs the volumes enclosed by the intervals defined by such functions, and $w_{\text{o}} \in \mathbb{R}^3$ weighs the volumes of the offsets between the center of the intervals and their reference trajectories.

To have a baseline value for J_{P}, we choose $T_{\text{P}} := \{0, 0.875, 1.75, 2.625, 3.5\}$[s], and compute

$$\begin{array}{ll} \sum_{t\in T_{\text{P}}} \text{vol}\left(\left[\underline{r}^x(t), \overline{r}^x(t)\right]\right), & \sum_{t\in T_{\text{P}}} \nu\left(\left[\underline{r}^x(t), \overline{r}^x(t)\right], \hat{x}(t)\right), \\ \sum_{t\in T_{\text{P}}} \text{vol}\left(\left[\underline{r}^y(t), \overline{r}^y(t)\right]\right), & \sum_{t\in T_{\text{P}}} \nu\left(\left[\underline{r}^y(t), \overline{r}^y(t)\right], \hat{y}(t)\right), \\ \sum_{t\in T_{\text{P}}} \text{vol}\left(\left[\underline{r}^u(t), \overline{r}^u(t)\right]\right), & \sum_{t\in T_{\text{P}}} \nu\left(\left[\underline{r}^u(t), \overline{r}^u(t)\right], \hat{u}(t)\right), \end{array}$$

for the system in (3.10) under state feedback with the finite horizon LQR gain $K^*_{\text{LQR1}}(t)$, whose reachability analysis was performed in the previous section. Using the reciprocals of these values, we set the weights in (4.23) to

$$\begin{aligned} w_{\text{v}} &:= [6.98\times 10^7;\ 9.67\times 10^{-7};\ 9.71\times 10^4], \\ w_{\text{o}} &:= [1.85\times 10^{18};\ 7.24;\ 1.07\times 10^{13}], \end{aligned} \tag{4.24}$$

so that the performance metric for this baseline controller is $J_{\text{P}} = 6$. The large difference in the order of magnitude of the weight entries is due to the units and dimensionality of the hypercubes from which they are calculated.

4.4 Optimal Finite Time Horizon LQR Relative to Robust Performance Metric

The analysis in Section 4.2 highlighted the weaknesses of the controller with the state feedback gain $K^*_{\text{LQR1}}(t)$ to track the reference trajectories for the kinematics of the CoM, and guarantee small variations of the inputs at the joint of the shoulders, in the presence of the parameter uncertainty from Table 4.1. This is noticed in the large projections of the over-approximation bounds in Figures 4.5b to 4.5d. Since in practice, the loads on shoulders are applied by the user with no intervention of the controller, it is desirable to observe small differences between the bounds set by the over-approximations while aiming to minimize the training time needed for the user to perform safe, and autonomous STS movements. We thus exploit the performance metric in (4.23) for choosing a more suitable finite time horizon LQR gain for implementation.

Computing the over-approximation functions in (4.23) is too expensive to implement a derivative free optimization method, such as the one used in Section 5.2 to tune the ILC gains. Hence here we opt for a brute force approach analogous to (3.16), where we construct sets of 300 diagonal, positive definite matrices of LQR weight candidates $\mathcal{Q} \subset \mathbb{R}^{6\times 6}$, $\mathcal{R} \subset \mathbb{R}^{4\times 4}$, and $\mathcal{S} \subset \mathbb{R}^{6\times 6}$. Their entries are randomly drawn from a Latin hypercube of 300 samples on 16 variables, with the values for $\mathcal{Q}$ and $\mathcal{S}$ in $(0, 100)$, and the ones for $\mathcal{R}$ in $(0, 0.01)$. Each of the sampled triplets of weights are plugged into (3.9), which is solved with the tools in [37] to obtain their corresponding time-varying matrix gain $K_{\text{LQR}}(t)$ from (3.8). Then the technique described in Section 4.2 is applied to find the over-approximation functions $\forall t \in T_{\text{P}}$, and calculate J_{P} for every controller. The triplet of weight

matrices

$$Q^\star, R^\star, S^\star = \underset{Q\in\mathcal{Q},R\in\mathcal{R},S\in\mathcal{S}}{\arg\min} \; J_{\mathrm{P}}(Q,R,S) \tag{4.25}$$

characterizes the best LQR gain for tracking STS 1 from the pool of candidates, with respect to the performance metric. The values found after 8.2 days of computation with a workstation of 4 cores at 2.7[GHz] running Matlab Parallel Toolbox, are

$$\begin{aligned} Q^\star &= \mathrm{diag}\left([80, 95, 95, 68, 90, 84]\right), \\ R^\star &= \mathrm{diag}\left(\left[1.0\times10^{-3}, 2.0\times10^{-4}, 6.0\times10^{-4}, 4.4\times10^{-3}\right]\right), \\ S^\star &= \mathrm{diag}\left([30, 37, 19, 29, 92, 82]\right). \end{aligned} \tag{4.26}$$

Their matrix gain $K^\star_{\mathrm{LQR}}(t)$ leads to $J^\star_{\mathrm{P}} = 1.31$. The improvement in tracking the reference trajectories using this controller over the baseline is illustrated in Figures 4.7 to 4.9 through simulations of STS 1 for the same set of 500 random $p \in \mathcal{P}_s$ used to verify the over-approximations for $\Phi^x(t;0,x_0,p)$, $\Phi^y(t;0,x_0,p)$, and $\Phi^u(t;0,x_0,p)$ in Section 4.2. The dashed red lines are the reference trajectories for the STS movement, the continuous lines in blue are obtained with the baseline controller $K^*_{\mathrm{LQR1}}(t)$ from Section 3.3, and the ones in green result from using $K^\star_{\mathrm{LQR}}(t)$. Although the deviations of the green trajectories from the references are expected to be smaller than the deviations of the blue trajectories at the time instants in T_{P}, the same behavior holds gracefully along the entire horizon. With the choice of weights in (4.24) for the performance metric in 4.23, the most significant improvement is observed at tracking $\hat{F}_y(t)$ in Figure 4.9d.

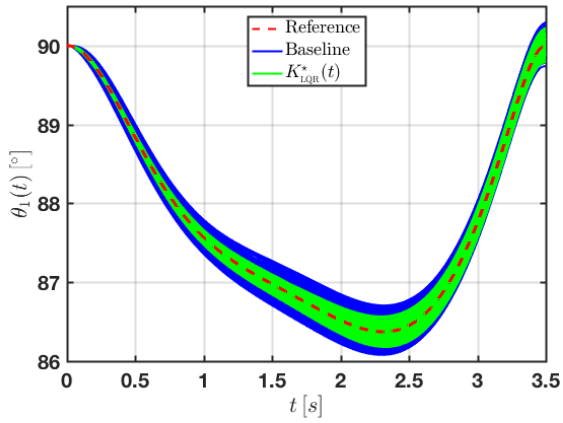

(a) Angular position of link 1 relative to the horizontal.

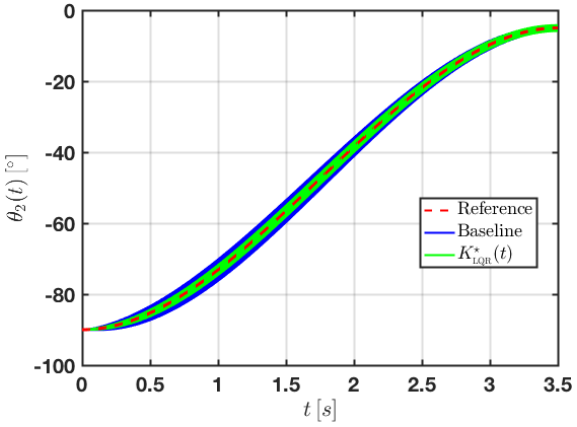

(b) Angular position of link 2 relative to link 1.

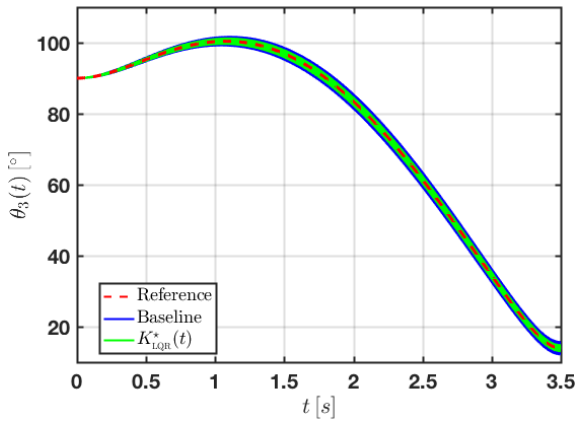

(c) Angular position of link 3 relative to link 2.

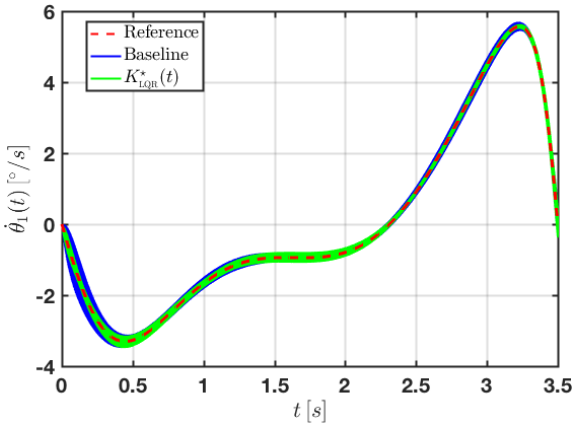

(d) Angular velocity of link 1.

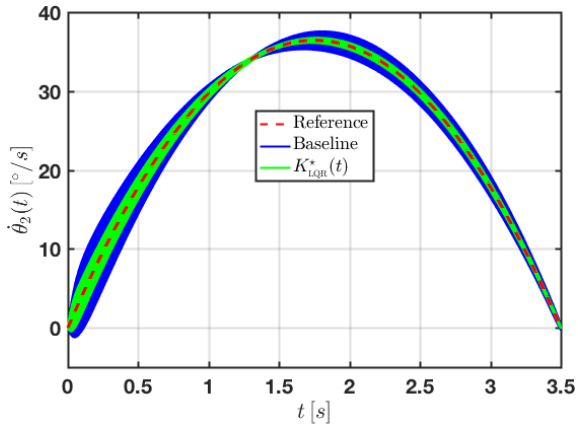

(e) Angular velocity of link 2.

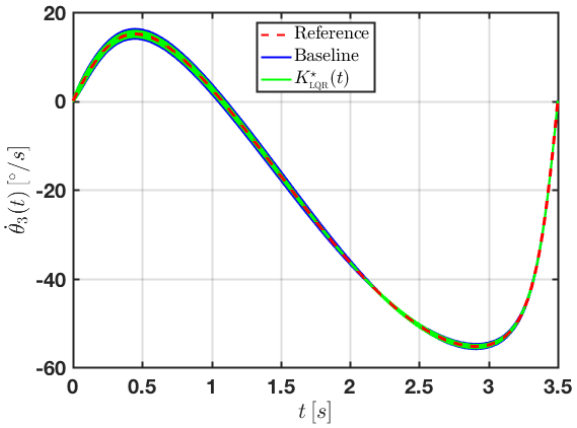

(f) Angular velocity of link 3.

Figure 4.7: State trajectories of the three-link robot when controlled with the baseline gain (blue), and the optimal gain relative to the performance metric J_{P} (green) for all $p \in \mathcal{P}_s$.

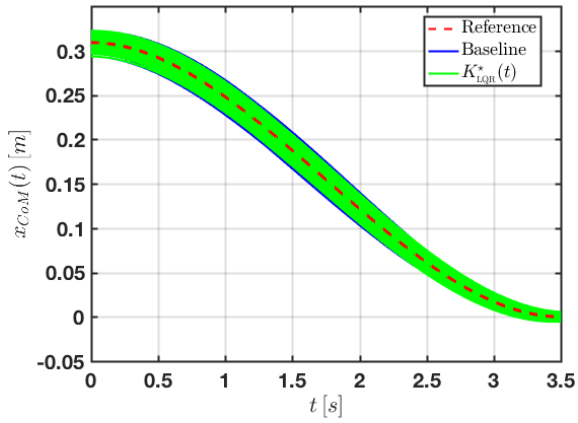

(a) x_{CoM} coordinate of the position of the three-link robot CoM.

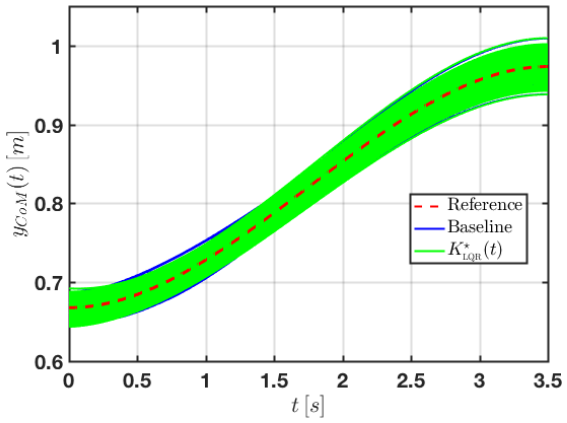

(b) y_{CoM} coordinate of the position of the three-link robot CoM.

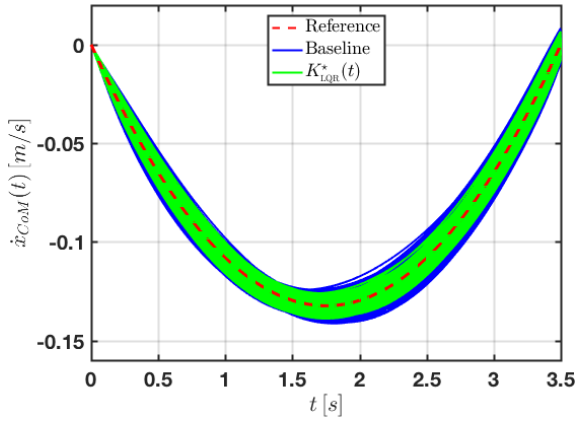

(c) $\dot{x}_{\text{CoM}}$ coordinate of the velocity of the three-link robot CoM.

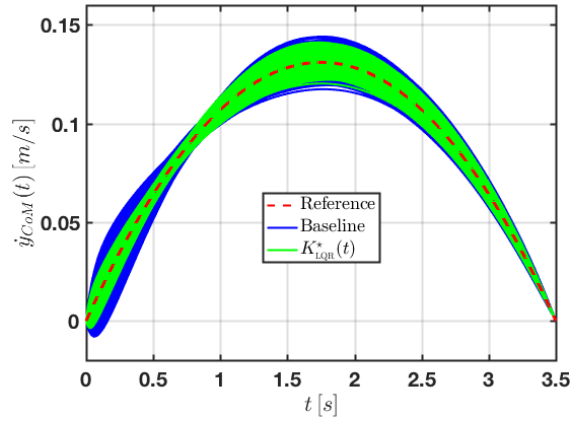

(d) $\dot{y}_{\text{CoM}}$ coordinate of the velocity of the three-link robot CoM.

Figure 4.8: Output trajectories of the three-link robot when controlled with the baseline gain (blue), and the optimal gain relative to the performance metric J_{P} (green) for all $p \in \mathcal{P}_s$.

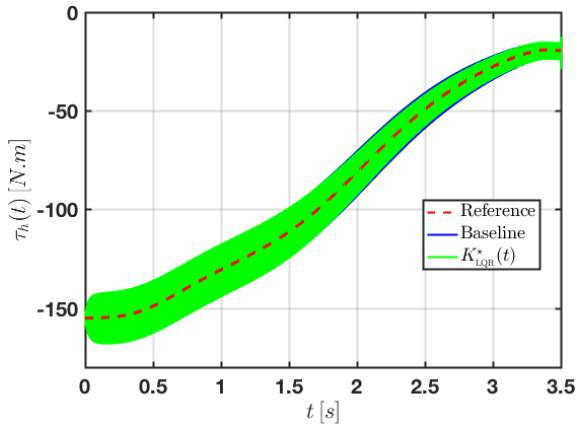

(a) Torque applied at the hips by the PLLO.

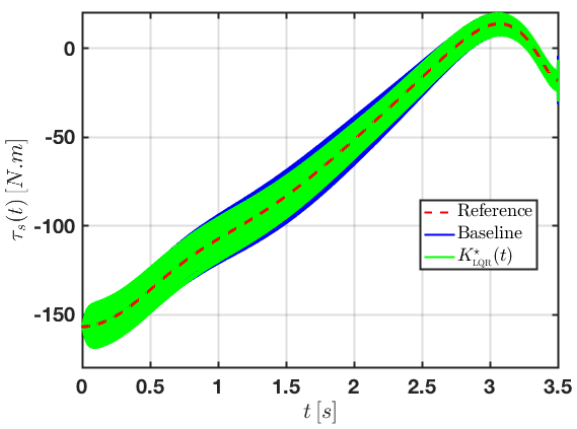

(b) Torque at the shoulders of the user.

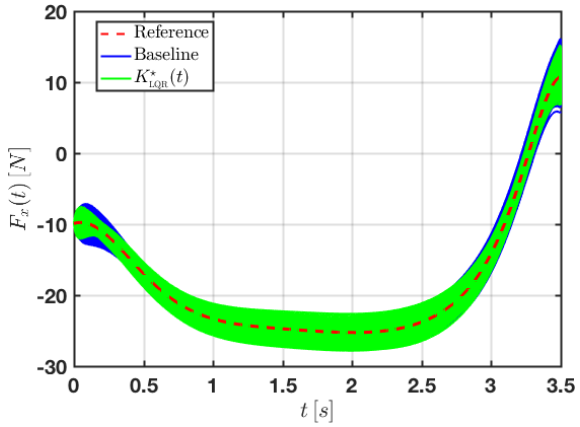

(c) Horizontal force at the shoulders of the user.

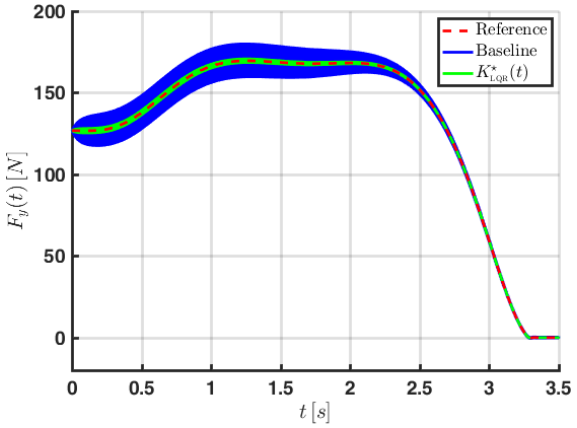

(d) Vertical force at the shoulders of the user.

Figure 4.9: Input trajectories of the three-link robot when controlled with the baseline gain (blue), and the optimal gain relative to the performance metric J_{P} (green) for all $p \in \mathcal{P}_s$.

In the next chapter we assess through numerical simulation if $K^{\star}_{\text{LQR}}(t)$ would be suitable for clinical implementation, using an Iterative Learning Control (ILC) algorithm as a proxy for the human loads at the shoulders τ_s, F_x, and F_y.

Chapter 5

Iterative Learning Control as a Proxy for User Action

Although the feedback controller

$$u(t) = \hat{u}(t) - K^{\star}_{\mathrm{LQR}}(t)(x(t) - \hat{x}(t)) \tag{5.1}$$

obtained in Section 4.4 is the optimal choice from a batch of candidates, actual execution of the STS movement relies on the interaction of two agents driving different control inputs of the system. More precisely, of the 4-dimensional control input $u = [\tau_h; \tau_s; F_x; F_y]$, only the torque at the hips τ_h is executed by the actuators of the PLLO under the authority of its onboard computer, while the three other controls (torque τ_s, horizontal F_x, and vertical F_y forces at the shoulders) are to be applied solely by the user interacting with the ground through crutches. Thus, unlike the accurate computer implementation at the hips, the human implementation at the shoulders will rely on a limited perception of the state of the system due to paraplegia, and no preconceived knowledge of reference trajectories. Therefore, a controller which is optimal in simulations for (3.10), when assuming perfect state feedback and actuation by the user, is not guaranteed to work experimentally.

The purpose of this chapter is thus to assess whether a proxy for the user actions can learn to cooperate with the LQR controller in (5.1) through repeated trials and achieve a safe STS movement. For this, we use an Iterative Learning Control (ILC) algorithm to represent the actions of the user while training with the PLLO to perform the STS movement during rehabilitation and physical therapy sessions. We believe that evaluating the performance of a controller for the hips combined with an ILC controller for the shoulders is a reasonable test prior to actual implementation of the PLLO.

5.1 Iterative Learning Control Algorithm

We start by rewriting the dynamics in (3.5) to better encompass the separate actions of the controller of the PLLO and the user. This is done by plugging the closed-loop expression for the input at the hips obtained from the finite horizon LQR controller in (5.1), and leaving the input of the user in open-loop. For a more realistic representation, this model also incorporates saturation of the inputs; so far, constraints on their values have only been taken into account while solving the control allocation in (2.22) for $\hat{u}(t)$. We assume the user has healthy enough vestibular and visual systems, and adequate proprioception of the upper body to know the angular position $\theta_3(t)$, velocity $\dot{\theta}_3(t)$, and acceleration $\ddot{\theta}_3(t)$ of the torso; and that the PLLO is instrumented to display in a monitor the real time trajectories of the position $[x_{\text{CoM}}(t); y_{\text{CoM}}(t)]$, velocity $[\dot{x}_{\text{CoM}}(t); \dot{y}_{\text{CoM}}(t)]$, and acceleration $[\ddot{x}_{\text{CoM}}(t); \ddot{y}_{\text{CoM}}(t)]$ of the CoM, together with their references. This is in similar fashion as for the Robot Suit HAL, where users can see plots of the desired center of pressure and its actual position during training of the STS movement, in order to achieve proper synchronization with the device [32].

The input applied at the hips with state feedback from the finite horizon LQR controller, and within the limits of operation of the PLLO actuators, is

$$\tau_{\text{h}}^{\star}(t,x) := [1\ 0\ 0\ 0]\,\text{sat}\left(\hat{u}(t) - K_{\text{LQR}}^{\star}(t)\,(x - \hat{x}(t)),\, \left[\underline{u},\, \overline{u}\right]\right). \tag{5.2}$$

Denote the loads at the shoulders as $\mu := [\tau_s; F_x; F_y] \in \mathbb{R}^3$, and the output measured by the user as $\Upsilon := \left[\theta_3;\ x_{\text{CoM}};\ y_{\text{CoM}};\ \dot{\theta}_3;\ \dot{x}_{\text{CoM}};\ \dot{y}_{\text{CoM}};\ \ddot{\theta}_3;\ \ddot{x}_{\text{CoM}};\ \ddot{y}_{\text{CoM}}\right] \in \mathbb{R}^9$. Taking $D_1 \in \mathbb{R}^{3\times 4}$ as $D_1 := [0_{3\times 1}\ I_3]$, we define $\hat{\mu}(t) := D_1\hat{u}(t)$, $\underline{\mu} := D_1\underline{u}$, and $\overline{\mu} := D_1\overline{u}$, from the input bounds

$$\begin{aligned} \underline{u} &:= [-200\ [\text{N}\cdot\text{m}];\ -175\ [\text{N}\cdot\text{m}];\ -40\ [\text{N}];\ 0\ [\text{N}]], \\ \overline{u} &:= [200\ [\text{N}\cdot\text{m}];\ 50\ [\text{N}\cdot\text{m}];\ 40\ [\text{N}];\ 650\ [\text{N}]]. \end{aligned} \tag{5.3}$$

Υ can be determined from the state x, angular acceleration of the links $\ddot{\theta}$, and parameter p with a mapping $\Psi : \mathbb{R}^6 \times \mathbb{R}^3 \times \mathbb{R}^{12} \to \mathbb{R}^9$ that clusters the kinematic equations of the CoM of the three-link robot in (2.5) to (2.10). Plugging $\tau_{\text{h}}^{\star}(t,x)$ into (3.5), the nonlinear dynamics of the system with user input μ and output Υ are

$$\begin{aligned} \dot{x}(t) &= f\left(x(t), p, \begin{bmatrix} \tau_h^{\star}(t,x) \\ \mu(t) \end{bmatrix}\right) =: \Xi(t, x(t), p, \mu(t)) \\ \Upsilon(t) &= \Psi\left(x(t), \ddot{\theta}(t), p\right). \end{aligned} \tag{5.4}$$

The algorithm to emulate the loads applied at the shoulders by a user, over N ascension attempts with the PLLO, is built upon the general current-iteration ILC referred to in [46]. Translating such control strategy to our problem, for successive iterations indexed by $j \in \{1, \ldots, N\}$, the user input $\mu^j(t)$ at $t \in [t_0, t_f]$ is given by

$$\mu^j(t) := \gamma_j \mu^{j-1}(t) + L\left(\hat{\Upsilon}(t) - \Upsilon^{j-1}(t)\right) + K\left(\hat{\Upsilon}(t) - \Upsilon^{j}(t)\right), \tag{5.5}$$

where $\gamma_j \in \mathbb{R}^{3\times3}$, $L, K \in \mathbb{R}^{3\times9}$, $\hat{\Upsilon}(t) := \Psi\left(\hat{x}(t), \ddot{\hat{\theta}}(t), \hat{p}\right)$ is the desired trajectory for $\Upsilon(t)$ during the ascension phase of the STS movement, and $\Upsilon^0(t) := \hat{\Upsilon}(t)$.

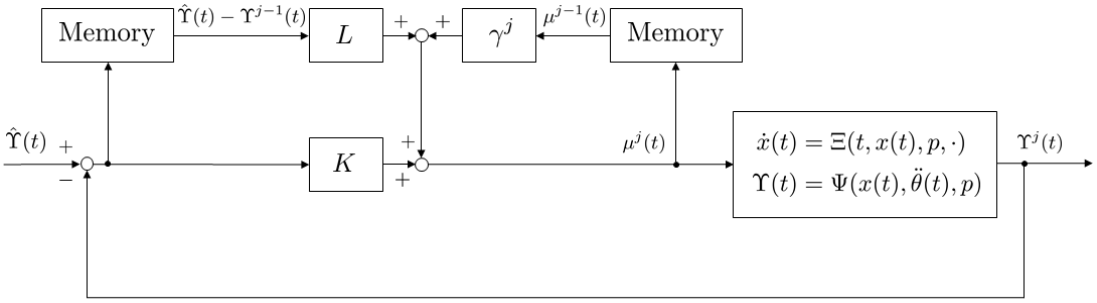

Figure 5.1: Basic ILC algorithm to emulate the loads applied at the shoulders by a user of a PLLO with feedback gain K, feedforward gain L, and recalling matrix γ^j.

The block diagram in Figure 5.1 shows that the feedforward component of this basic learning algorithm consists of two terms relying on the memory of the user about the past-iteration $j-1$. The feedforward gain L modifies the input $\mu^j(t)$ according to the error of the output $\hat{\Upsilon}(t) - \Upsilon^{j-1}(t)$, while the recalling matrix γ_j is inspired by [47] and is used to capture the ability of the user to remember and execute $\mu^{j-1}(t)$. If $\gamma_j = I_3$ then $\mu^{j-1}(t)$ is perfectly incorporated into $\mu^j(t)$, but if $\gamma_j \neq I_3$ we will interpret the mismatch between the values of $\gamma_j\mu^{j-1}(t)$ and $\mu^{j-1}(t)$ to be the consequence of either a memory flaw, an imperfect execution of the required loads at the shoulders, or a combination of both. The feedback component changes the input of the user by multiplying the error of the outputs at the current-iteration j by the feedback gain K. Although at the beginning of training there is no preconceived notion of the input that needs to be exerted to attempt a STS movement with the PLLO, we consider that the values $\hat{\mu}(t_0)$ and $\hat{\mu}(t_f)$ are known to the user, so that the ILC can be initialized with the linear interpolation

$$\mu^0(t) = \frac{\hat{\mu}(t_f) - \hat{\mu}(t_0)}{t_f - t_0}(t - t_0) + \hat{\mu}(t_0). \tag{5.6}$$

When the input $\mu^j(t)$ from the basic ILC algorithm in (5.5) acts on (5.4), the state trajectory $x(t)$ might lead to a configuration of the links of the PLLO which is harmful for the user, or even mechanically impossible to reach. To elaborate on this situation, we delimit the feasible ranges of motion for the user and the PLLO with the state bounds

$$\begin{aligned} \underline{x} &:= [80\,[^\circ];\ -120\,[^\circ];\ 0\,[^\circ];\ -20\,[^\circ/\mathrm{s}];\ -5\,[^\circ/\mathrm{s}];\ -70\,[^\circ/\mathrm{s}]], \\ \overline{x} &:= [120\,[^\circ];\ 0\,[^\circ];\ 130\,[^\circ];\ 10\,[^\circ/\mathrm{s}];\ 60\,[^\circ/\mathrm{s}];\ 20\,[^\circ/\mathrm{s}]], \end{aligned} \tag{5.7}$$

and let $t_s^j \in [t_0, t_f]$ be the maximum value such that the state at iteration j satisfies $x(t) \in \left[\underline{x}, \overline{x}\right]$ for all $t \in [t_0, t_s^j]$. To account for situations where the user would need to abort execution of the STS movement due to safety concerns, we stop the ongoing iteration when $x(t)$ goes out of bounds, reset the state of the system to the initial condition x_0, and proceed to the next one.

Suppose the human input caused the STS movement in the past-iteration $j-1$ to stop prematurely, so that $t_0 < t_s^{j-1} < t_f$. In this scenario, the error $\hat{\Upsilon}(t) - \Upsilon^{j-1}(t)$ and $\mu^{j-1}(t)$ in (5.5) only exist for $t \in \left[t_0, t_s^{j-1}\right]$. In order to compute $\mu^j(t)$ for $t > t_s^{j-1}$, define $\Gamma^j(t) \in \mathbb{R}^3$ for $j \in \{1, \ldots, N\}$ as

$$\Gamma^j(t) := \begin{cases} \gamma_j \mu^{j-1}(t) + L\left(\hat{\Upsilon}(t) - \Upsilon^{j-1}(t)\right) + K\left(\hat{\Upsilon}(t) - \Upsilon^{j}(t)\right), & t < t_s^{j-1} \\ \alpha^j t + \beta^j, & t \geq t_s^{j-1} \end{cases}, \tag{5.8}$$

where $\alpha^j := \frac{\hat{\mu}(t_f) - \mu^{j-1}(t_s^{j-1})}{t_f - t_s^{j-1}}$ and $\beta^j := \hat{\mu}(t_f) - \alpha^j t_f$ implement a linear extrapolation of time for the human input, between $\mu^{j-1}(t_s^{j-1})$ and $\hat{\mu}(t_f)$. This is to simulate the torque and forces that the user would begin to apply at t_s^{j-1} while attempting to counteract the negative effects of the past-iteration input on the ascension. For initialization purposes, $t_s^0 := t_f$.

Adding saturation to the extremal loads that the user is physically capable of exerting at the shoulders, we complete our ILC algorithm as:

$$\mu^j(t) := \text{sat}\left(\Gamma^j(t), \left[\underline{\mu}, \overline{\mu}\right]\right). \tag{5.9}$$

5.2 Tuning the ILC gains

We reason that if we can find ILC gains for simulating a realistic ascension phase, then a real user, who has a more complex learning process and has tuned the muscles for the precise movement of the upper limbs since birth, would be able to coordinate with the controller for the hips of the PLLO through training and complete a successful STS movement. Therefore, we resort to a reinforcement learning approach to numerically search for the values of the feedforward L and feedback K gains in (5.8).

Define the j^{th} iteration cost

$$J_{\text{L}}^j := \begin{cases} \infty, & t_s^j < t_f \\ \int_{t_0}^{t_f} \left(\left\| \hat{\Upsilon}(t) - \Upsilon^j(t) \right\|_2 + w_\mu \left\| \dot{\mu}^j(t) \right\|_2 \right) dt, & t_s^j = t_f \end{cases}, \tag{5.10}$$

where the weight $w_\mu := 10^{-4}$ is used to account for the different units of $\Upsilon^j(t)$ and $\dot{\mu}^j(t)$. If a particular choice of gains causes the final iteration N to stop the STS movement prematurely $\left(t_s^N < t_f\right)$, it must be discarded for modeling the behavior of the user. Otherwise $\left(\text{if } t_s^N = t_f\right)$, the quality of its corresponding ILC algorithm should be assessed, based on the deviation of the output in (5.4) from its desired trajectory $\hat{\Upsilon}(t)$, and the rate of change of the input $\dot{\mu}^N(t) \in \mathbb{R}^3$. With the nominal parameter $p = \hat{p}$ in (5.4), a time step of $4\,[\text{ms}]$ for computing a discrete version of the iteration cost J_{L}^j, $\gamma_j = I_3$ for all $j \in \{1, \ldots, N\}$, and $N := 30$ iterations, we select the gains in (5.8) as

$$K^\star, L^\star := \underset{K, L \in \mathbb{R}^{3\times 9}}{\arg\min} J_{\text{L}}^N(K, L). \tag{5.11}$$

There are two major difficulties for computing the solution to (5.11). The first is that the problem is in general non-convex and hence global minimization is intractable. The second is that computing derivatives with respect to K and L is cumbersome. The first issue is typically dealt with in practice via heuristic local search; we find this to be effective for our problem. To deal with the second issue, we apply a standard technique from the optimization literature for minimizing a function using only black-box function calls, which we describe briefly.

Suppose we want to minimize $g : \mathbb{R}^n \to \mathbb{R}$ over $\eta \in \mathbb{R}^n$. For $\sigma > 0$, we define a smoothed function $G_\sigma(\eta) := \mathbb{E}_\xi \{g(\eta + \sigma\xi)\}$, where $\xi \sim \mathcal{N}(0, I_n)$ is an isotropic Gaussian random vector, and $\mathbb{E}$ denotes the expectation. Under reasonable regularity conditions on g, a standard calculation shows that the gradient of G_σ is given by

$$\nabla G_\sigma(\eta) = \mathbb{E}_\xi \left\{ \frac{g(\eta + \sigma\xi) - g(\eta - \sigma\xi)}{2\sigma} \xi \right\}.$$

That is, we can differentiate $G_\sigma(\eta)$ by only using function calls of g. We can interpret this as a finite-difference method applied in a random direction. Furthermore, it is clear that as $\sigma \to 0$, $G_\sigma(\eta)$ approaches $g(\eta)$. Hence, optimizing G_σ is a reasonable proxy for optimizing g; this is made formal in [48]. The most basic way to apply derivative free optimization is to run stochastic gradient descent:

$$\eta_{k+1} = \eta_k - \rho_k \frac{g(\eta_k + \sigma\xi_k) - g(\eta_k - \sigma\xi_k)}{2\sigma} \xi_k, \tag{5.12}$$

where $\{\rho_k\}_{k\geq 0}$ is an appropriate sequence of step sizes and $\{\xi_k\}_{k\geq 0}$ is an independent and identically distributed sequence of $\mathcal{N}(0, I_n)$ random vectors. We apply a slightly modified version of (5.12) as described in [49]. First, at every iteration k we draw n_d random directions $\{\xi_k^i\}_{i=1}^{n_d}$. We then sort the indices $i = 1, ..., n_d$ in ascending order with the value assigned to each index given by $\min\left(g(\eta_k + \sigma\xi_k^i), g(\eta_k - \sigma\xi_k^i)\right)$, and compute the update direction as:

$$\eta_{k+1} = \eta_k - \frac{\rho_k}{n_t} \sum_{i=1}^{n_t} \frac{g\left(\eta_k + \sigma\xi_k^{(i)}\right) - g\left(\eta_k - \sigma\xi_k^{(i)}\right)}{2\sigma_{n_t}} \xi_k^{(i)}. \tag{5.13}$$

Here, $n_t \leq n_d$, $\xi_k^{(i)}$ denotes the sorted directions, and σ_{n_t} denotes the *empirical* standard deviation of the $2n_t$ costs used in the update.

We run this method for 10,000 iterations with $g = J_{\mathrm{L}}^N$, $n_d = 30$, $n_t = 10$, $\sigma = 0.01$, and $\rho_k \equiv 0.04$ on a machine with 72 physical cores running at 2.10 [GHz]. After approximately two days of computation, we obtain the gains

$$K^\star = \begin{bmatrix} -104.6 & -56.53 & 73.46 & -115.3 & -210 & 66.66 & 0.729 & -4.647 & 1.569 \\ 64.05 & -24.18 & -52.05 & -16.31 & 165.7 & -28.16 & 0.049 & 0.138 & -4.384 \\ 29.36 & 20.89 & 141.7 & 47.26 & -31.51 & 126.8 & 0.2208 & -5.419 & -3.226 \end{bmatrix},$$

$$L^\star = \begin{bmatrix} 0.523 & 7.495 & 47.08 & -1.319 & -5.141 & -29.98 & -1 & -1.616 & -2.123 \\ -4.673 & -26.10 & -26.80 & 1.215 & -2.939 & 26.57 & 0.1023 & 4.034 & 4.459 \\ -76.22 & -60.77 & 109.9 & 16.94 & 9.401 & 128.8 & -0.3326 & 8.539 & 3.776 \end{bmatrix}.$$

The values of (5.10) achieved over 30 iterations of the ILC algorithm are shown in Figure 5.2, where blue crosses identify the iterations that terminate prematurely and are assigned a cost of ∞. After 9 unsuccessful attempts to complete the movement STS 1 in Section 2.5, the cost per iteration decreases monotonically and reaches a final value of $J_{\text{L}}^\star := 8.29$ when $\mu^{30}(t)$ is applied. As a reference, plugging $\Upsilon^N(t) = \hat{\Upsilon}(t)$ and $\dot{\mu}^N(t) = \dot{\hat{\mu}}(t)$ into (5.10) gives $\hat{J}_{\text{L}} = 8.75$.

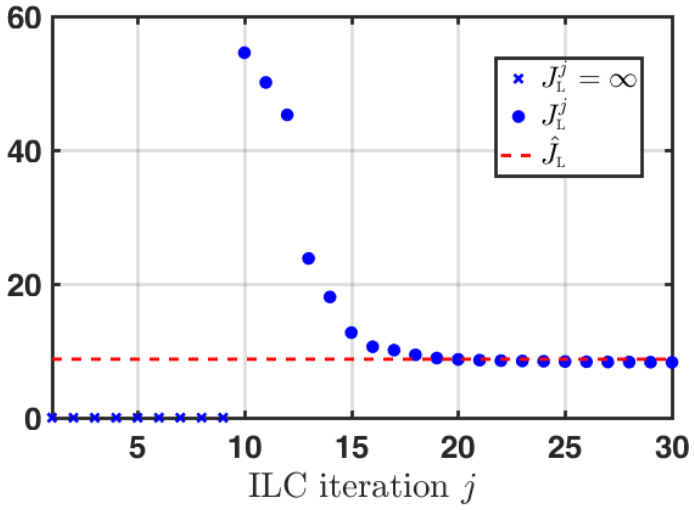

Figure 5.2: Cost J_{L}^j attained by plugging $K^\star$ and $L^\star$ into the ILC algorithm with $\gamma_j = I_3$, and $p = \hat{p}$.

Figures 5.3 to 5.5 show the trajectories of $x = \left[\theta_1; \theta_2; \theta_3; \dot{\theta}_1; \dot{\theta}_2; \dot{\theta}_3\right]$, $y = [x_{\text{CoM}}; y_{\text{CoM}}; \dot{x}_{\text{CoM}}; \dot{y}_{\text{CoM}}]$, and $u = \left[\tau_h; \tau_s; F_x; F_y\right]$ for the three-link robot model in (5.4) simulated under $\mu^{30}(t)$ in green. The dashed red lines are their respective reference trajectories $\hat{x}(t)$, $\hat{y}(t)$, and $\hat{u}(t)$.

The ILC algorithm with gains $K^\star$ and $L^\star$ achieves almost perfect tracking of $\hat{\theta}_3(t)$, $\dot{\hat{\theta}}_3(t)$, and $\hat{y}(t)$; as a consequence, the plots in Figures 5.3c, 5.3f, and 5.4, show the trajectories in green essentially overlapping with the red ones. Deviations from the reference in Figures 5.3a, 5.3b, 5.3d, and 5.3e are expected because θ_1, θ_2, $\dot{\theta}_1$, and $\dot{\theta}_2$ are not included in the output measured by the user Υ and hence their values are not penalized in (5.10). Nevertheless, θ_1 is off the vertical at the end of the ascension just by 0.5[°], with the absolute values of both angular velocities less than 1.2[°/s], which should not compromise the ability of a controller for the stabilization phase to reach the standing position with ease. As $\theta_2(t)$ remains less than zero for the entire time horizon, there is no hyperextension of the knees, and thus the input $\mu^{30}(t)$ should not pose a threat to the physical integrity of the user.

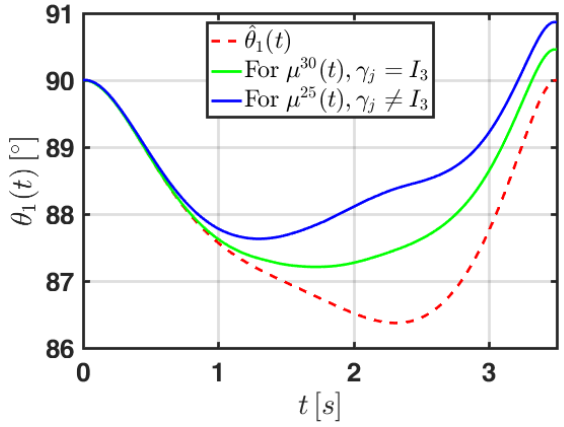

(a) Angular position of link 1 relative to the horizontal.

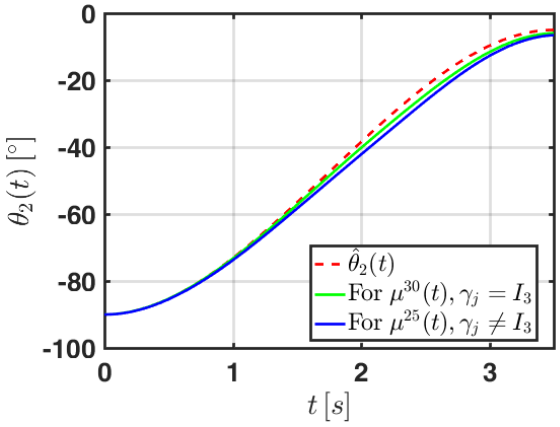

(b) Angular position of link 2 relative to link 1.

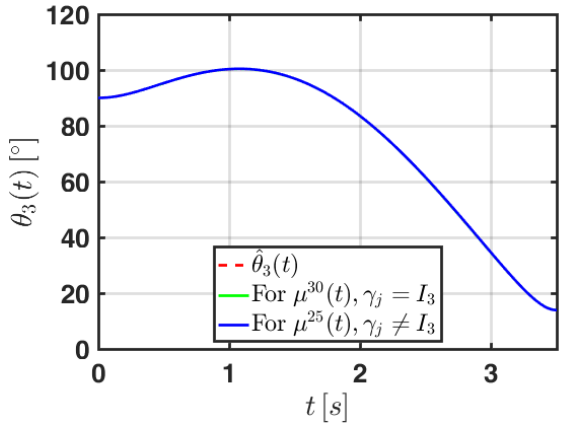

(c) Angular position of link 3 relative to link 2.

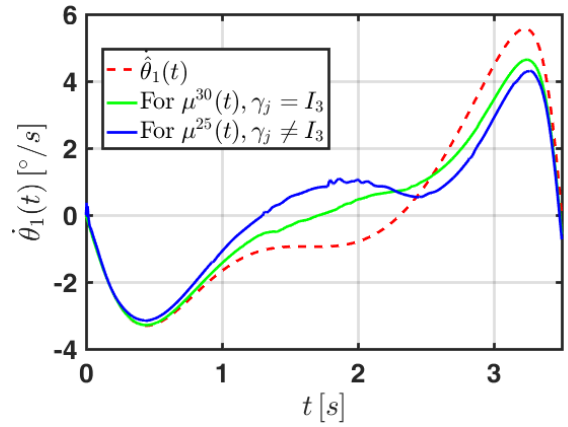

(d) Angular velocity of link 1.

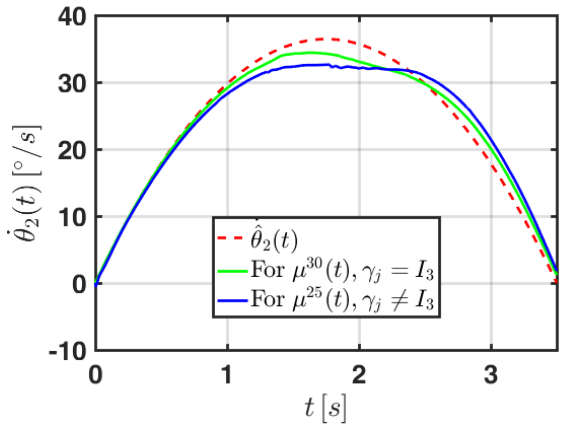

(e) Angular velocity of link 2.

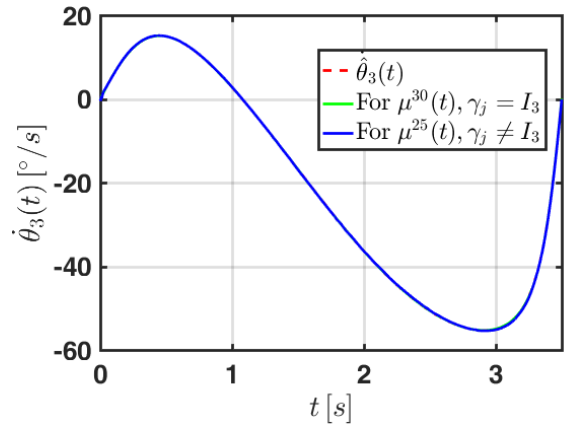

(f) Angular velocity of link 3.

Figure 5.3: State of the system for input trajectories $\mu^j(t)$ obtained from the ILC algorithm with gains $K^\star$ and $L^\star$, nominal parameter $\hat{p}$, and different values of γ_j.

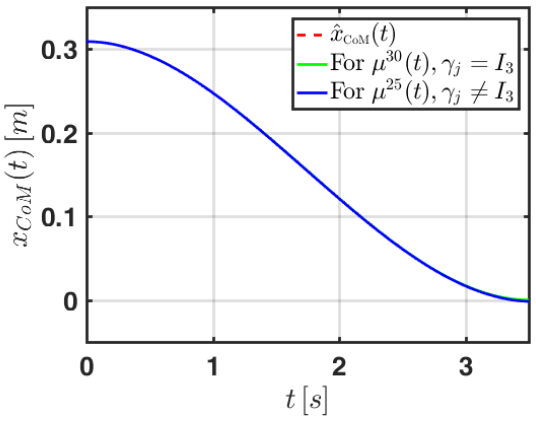

(a) x_{CoM} coordinate of the position of the CoM.

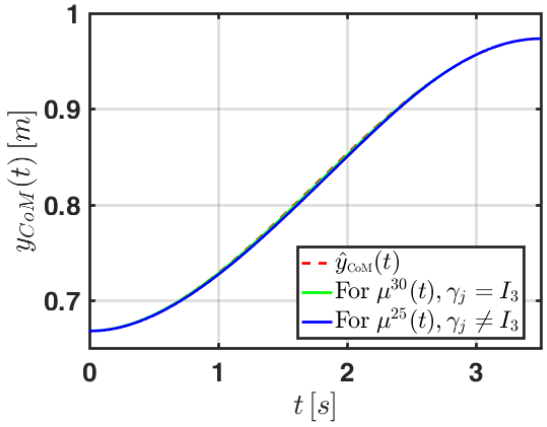

(b) y_{CoM} coordinate of the position of the CoM.

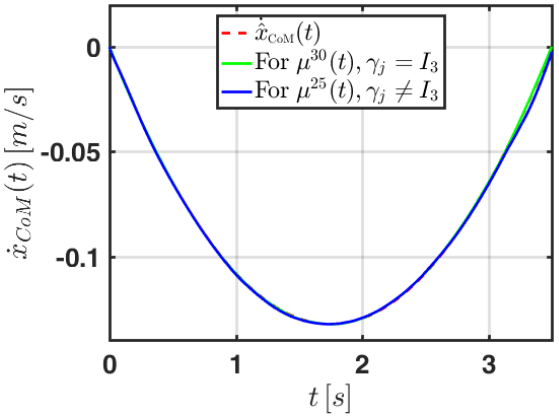

(c) $\dot{x}_{\text{CoM}}$ coordinate of the velocity of the CoM.

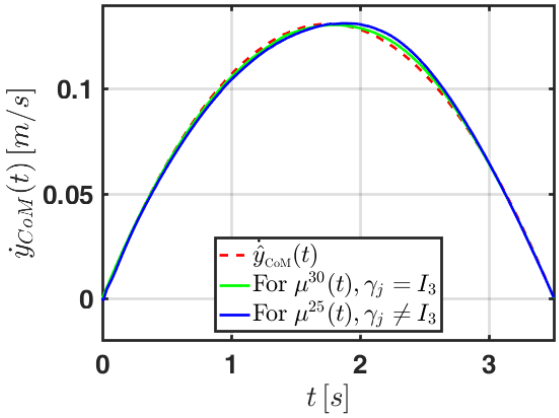

(d) $\dot{y}_{\text{CoM}}$ coordinate of the velocity of the CoM.

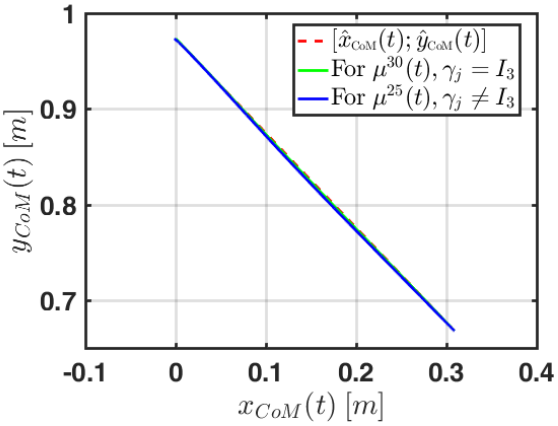

(e) Position trajectories of the three-link robot CoM.

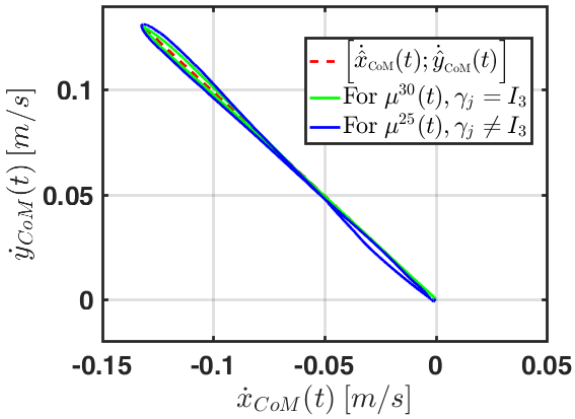

(f) Velocity trajectories of the three-link robot CoM.

Figure 5.4: Position and velocity of the three-link robot CoM for input trajectories $\mu^j(t)$ obtained from the ILC algorithm with gains $K^\star$ and $L^\star$, nominal parameter $\hat{p}$, and different values of γ_j.

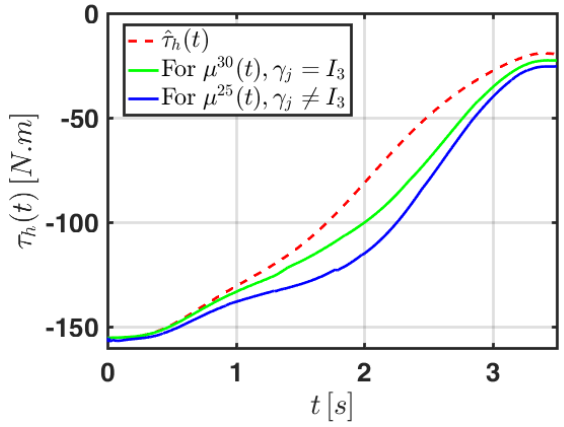

(a) Torque applied at the hips by the PLLO with state feedback from $K^{\star}_{\text{LQR}}(t)$.

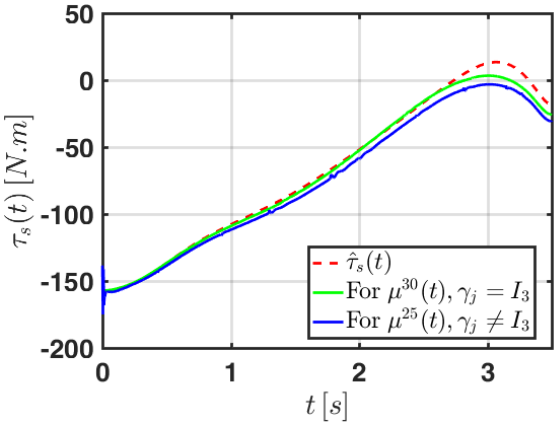

(b) Torque applied at the shoulders by the ILC algorithm.

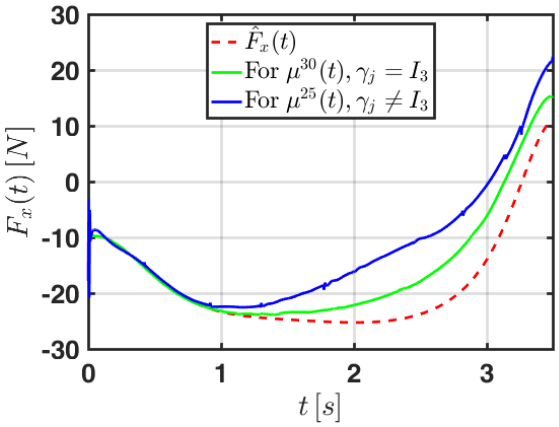

(c) Horizontal force applied at the shoulders by the ILC algorithm.

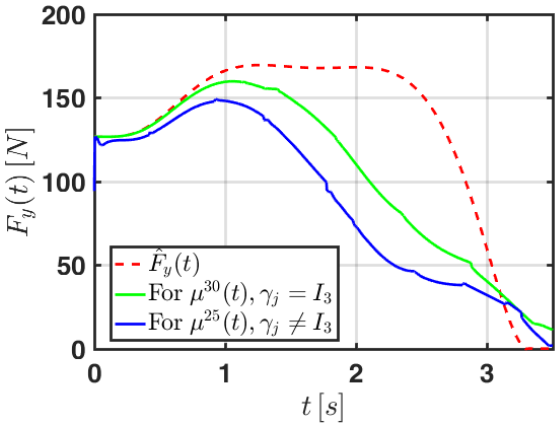

(d) Vertical force applied at the shoulders by the ILC algorithm.

Figure 5.5: Loads applied at the hips and shoulders for input trajectories $\mu^j(t)$ obtained from the ILC algorithm with gains $K^{\star}$ and $L^{\star}$, nominal parameter $\hat{p}$, and different values of γ_j.

Even though the tracking errors for the angular position and velocity of the links of the shanks and thighs do not directly affect the computation of $\mu^j(t)$ in (5.9), they do determine (together with the tracking errors of the angular position and velocity of the torso) the value of the torque at the hips through the state feedback of the finite horizon LQR, causing it to differ from $\hat{\tau}_h(t)$ in Figure 5.5a. It is especially interesting that although we did not consider $\hat{\mu}(t)$ in (5.10), both the torque and horizontal force at the shoulders in Figures 5.5b and 5.5c follow their reference trajectories reasonably well, within errors of 15[N$\cdot$m], and 10[N], respectively. The absolute value of the torque applied at the hips in Figure 5.5a is in general greater than $\hat{\tau}_h(t)$, which compensates for lower vertical forces attained in Figure 5.5d relative to $\hat{F}_y(t)$. Observing the rate of change of the vertical force $\dot{F}_y(t)$ from $\dot{\mu}^{30}(t)$ in Figure 5.5d, we can infer that $J^{\star}_L < \hat{J}_L$ is mostly due to the

difference of its values over time with respect to $\dot{\hat{F}}_y(t)$. Although $\hat{F}_y(t)$ remains constant for about 1[s], it decreases 165[N] in 1.4[s], while the trajectory in green decreases 150[N] over 2.5[s] for a lower average rate of change.

5.3 ILC Robustness Evaluations

The results discussed above indicate that the ILC in (5.9) is able to successfully coordinate with the LQR controller driving the actuators at the hips in (5.2) to complete the desired ascension phase with no risk of sit-back or step failures [15]. Moreover, it does so exhibiting input trajectories that could be realistically executed by both the PLLO and the user after 30 learning iterations. Since the gains $K^\star$ and $L^\star$ that make this behavior possible were found considering a constant recalling matrix $\gamma_j = I_3$ in (5.8) across every iteration, and the nominal value of the parameter $\hat{p}$ in (5.4), the purpose of this section is to evaluate the robustness of the ILC algorithm to perform the STS movement in two scenarios: imperfect recalling and execution of $\mu^{j-1}(t)$, and parameter uncertainty.

For the imperfect recalling and execution of $\mu^{j-1}(t)$ we plug the iteration-varying matrix $\gamma_j = I_3 + q^{j-1}\vartheta_j$ in (5.5), with $q := 0.6$, and randomly sample the entries of $\vartheta_j \in \mathbb{R}^{3\times 3}$ at every iteration $j \in 1, \ldots, N$ within the interval $[-0.05, 0.05]$. While the off-diagonal entries in ϑ_j couple the loads at the shoulders, the decay to zero of the power function q^{j-1} as the number of trials increases, captures the idea that a user would eventually recall and apply the appropriate values of $\mu^{j-1}(t)$. With the nominal parameter value $\hat{p}$, and starting the learning algorithm from the linear interpolation in (5.6), the values of (5.10) achieved over 30 iterations of the ILC algorithm are shown in Figure 5.6. Since the minimum value of J_{L}^j is observed at iteration 25, Figures 5.3 to 5.5 depict the behavior of the system under $\mu^{25}(t)$ in blue lines.

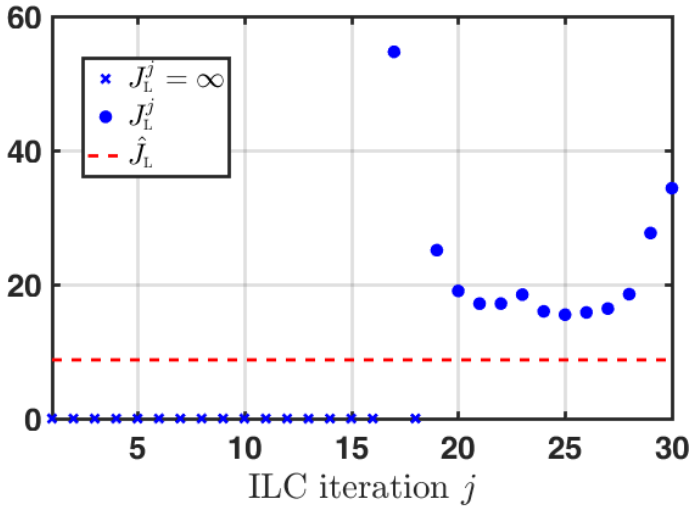

Figure 5.6: Cost J_{L}^j attained by plugging $K^\star$ and $L^\star$ into the ILC algorithm with $\gamma_j = I_3 + q^{j-1}\vartheta_j$, and $p = \hat{p}$.

Despite degraded tracking of $\hat{\theta}_1(t)$, $\hat{\theta}_2(t)$, $\dot{\hat{\theta}}_1(t)$, and $\dot{\hat{\theta}}_2(t)$ when compared to $\mu^{30}(t)$ in Figure 5.3, the system (5.4) under $\mu^{25}(t)$ still manages to complete the ascension phase of STS 1 with very good tracking of the position and velocity of the CoM in Figure 5.4. The control inputs of the PLLO and those from the ILC algorithm in Figure 5.5 remain between the bounds $\left[\underline{u}, \overline{u}\right]$, verifying that $K^\star$ and $L^\star$ still lead to realistic input trajectories with $\gamma_j \neq I_3$, although their oscillations and sudden changes do result in an increased value of the cost $J_{\text{L}}^{25} = 15.49$.

We now study the effect of parameter uncertainty after the ILC algorithm has completed 30 iterations under the nominal value of the parameter $\hat{p}$, and constant recalling matrix $\gamma_j = I_3$. For this purpose, we set the new $\mu^0(t)$ in (5.8) equal to the trajectories in green from Figures 5.5b to 5.5d, and simulate the system in (5.4) under the action of (5.9) for the set of 500 parameter values $\mathcal{P}_s \subset \mathbb{R}^{12}$ obtained from Latin hypercube sampling in Section 4.2, and the parameter bounds $\underline{p}, \overline{p} \in \mathbb{R}^{12}$ in Table 4.1. Keeping track of the cost J_{L}^j over $j = \{1, \ldots, 30\}$ for each sampled parameter, we identify the iterations where the ILC algorithm reaches the minimum values, and present their corresponding simulations in Figures 5.7 to 5.9. The trajectories for all $p \in \mathcal{P}_s$ are in blue, the results for the lower bound $\underline{p}$ after 14 iterations are in magenta, and the ones for the upper bound $\overline{p}$ after 16 are in green. The costs associated with the parameter bounds are $J_L^{14} := 59.59$, and $J_L^{16} := 28.31$. The evolution of the system with the original input obtained without parameter uncertainty is in dashed red lines.

It is clear that the mismatch of the parameter values with respect to $\hat{p}$ causes significant deviation from the reference trajectories $\hat{x}(t)$ in Figure 5.7, and $\hat{y}(t)$ in Figure 5.9. In particular, Figures 5.8e and 5.8f show that at the end of the ascension phase $\left[x_{\text{CoM}}(t_f); y_{\text{CoM}}(t_f)\right] \subseteq [[-0.1; 0.94], [0.1; 1]]$ [m], and $\left[\dot{x}_{\text{CoM}}(t_f); \dot{y}_{\text{CoM}}(t_f)\right] \subseteq [[-0.09; -0.02], [0.1; 0]]$ [m/s]. Given that there are final positions of the CoM that are not vertically aligned with the ankle joint, and the terminal velocities of the CoM are nonzero, we can predict that the stabilization phase for the STS 1 movement would be more challenging. Nevertheless, all trajectories for θ_2 in Figure 5.7b are less than zero, so that the integrity of the knee joints is preserved. Figures 5.9b to 5.9d exhibit that the inputs obtained with the ILC algorithm are very sensitive to parameter uncertainty. However, the LQR controller enhances the torque applied at the hips in Figure 5.9a helping to keep all the loads at the shoulders within admissible bounds.

According to the larger offsets from the desired position and velocity of the CoM that exhibit the trajectories for $\underline{p}$ with respect to $\overline{p}$ in Figures 5.8e and 5.8f, we can tell that the stabilization phase for a situation where the total mass of the user decreases by 5% of its nominal value, might be more challenging than the one where the total mass increases by the same amount. Figures 5.9c and 5.9d show that an increased mass of the user requires applying forces of larger magnitude at the shoulders. The oscillations and sudden changes of the loads in magenta and green of Figures 5.9b to 5.9d, together with the deviations of their corresponding trajectories from $\hat{y}(t)$ in Figure 5.8, contribute to the higher values of J_L^{14} and J_L^{16} relative to $J_L^\star$. It is interesting that the most abrupt changes of $\dot{\mu}^{14}(t)$ happen when the velocity of the CoM achieves its maximum (approximately at 1.77[s]), and in the last 0.1[s] of the ascension phase.

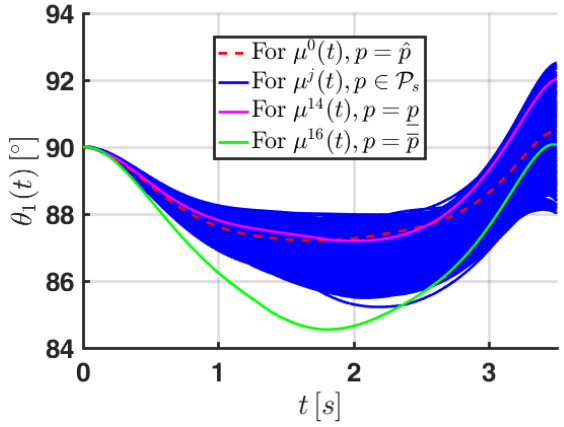

(a) Angular position of link 1 relative to the horizontal.

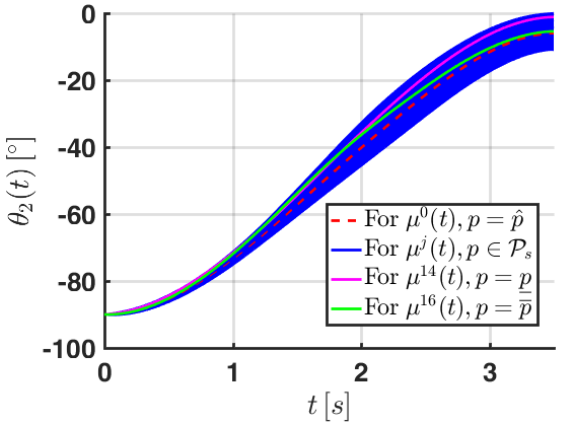

(b) Angular position of link 2 relative to link 1.

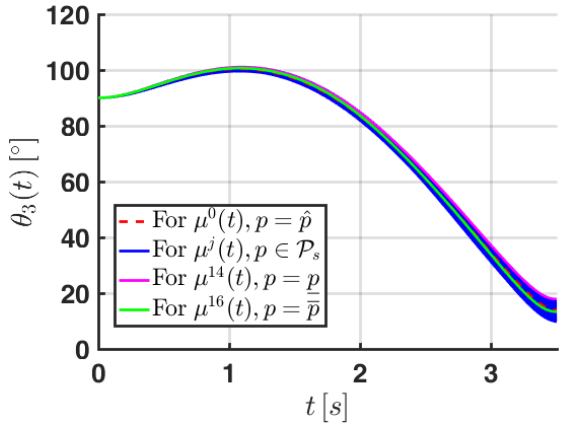

(c) Angular position of link 3 relative to link 2.

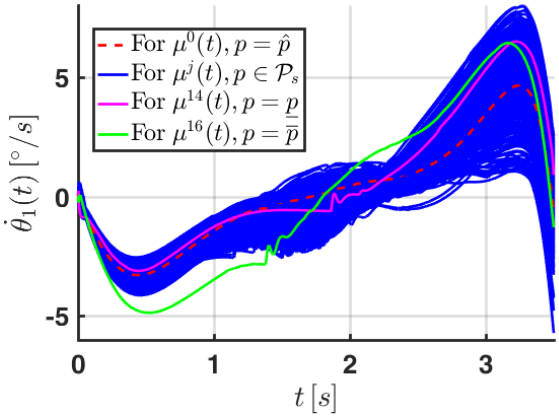

(d) Angular velocity of link 1.

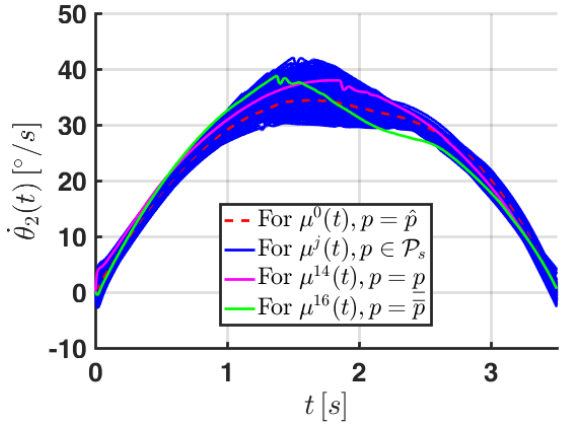

(e) Angular velocity of link 2.

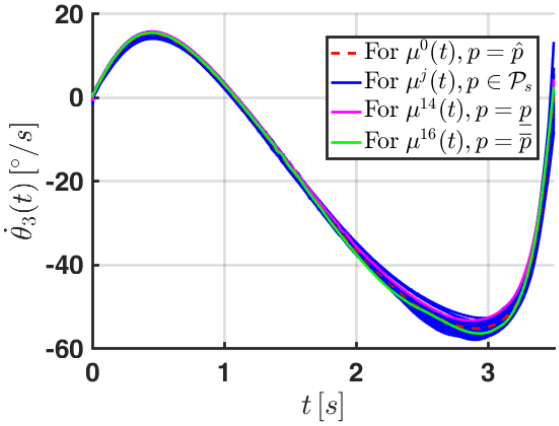

(f) Angular velocity of link 3.

Figure 5.7: State of the system for input trajectories $\mu^j(t)$ obtained from the ILC algorithm with gains $K^\star$ and $L^\star$, $\gamma_j = I_3$, and different values of the parameter p.

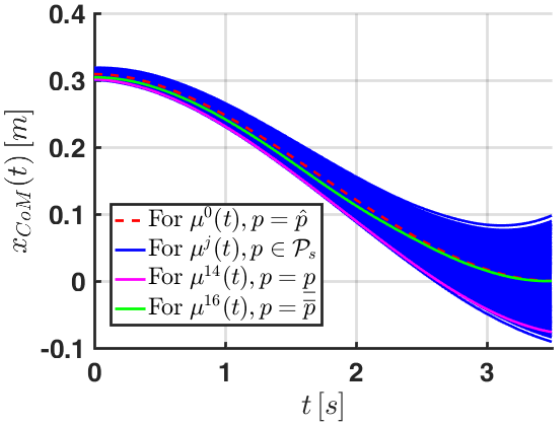

(a) x_{CoM} coordinate of the CoM.

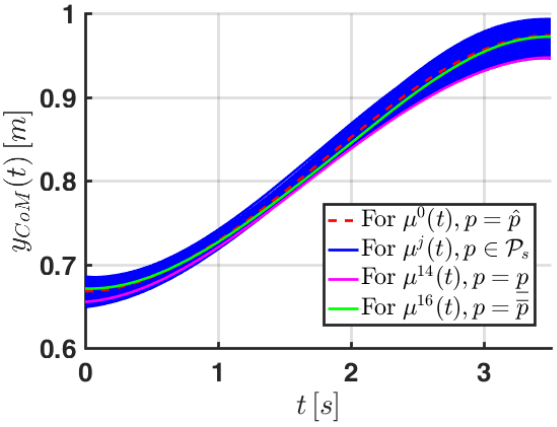

(b) y_{CoM} coordinate of the CoM.

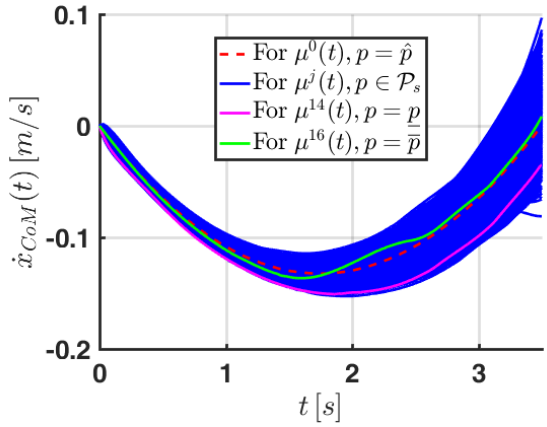

(c) $\dot{x}_{\text{CoM}}$ coordinate of the velocity of the CoM.

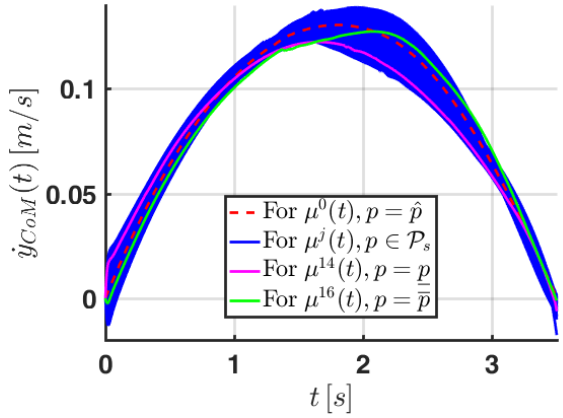

(d) $\dot{y}_{\text{CoM}}$ coordinate of the velocity of the CoM.

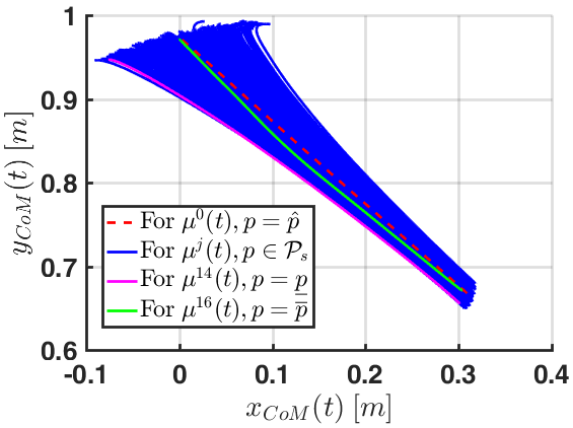

(e) Position trajectories of the three-link robot CoM.

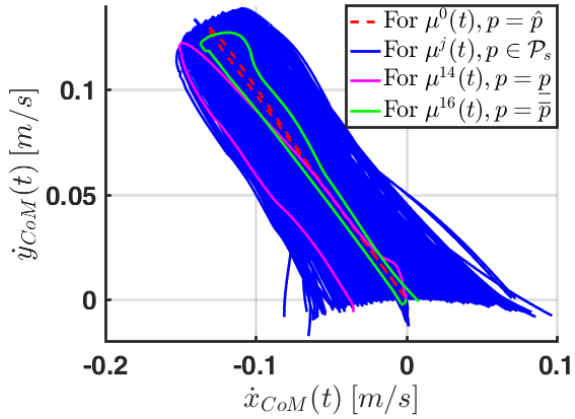

(f) Velocity trajectories of the three-link robot CoM.

Figure 5.8: Position and velocity of the three-link robot CoM for input trajectories $\mu^j(t)$ obtained from the ILC algorithm with gains $K^\star$ and $L^\star$, $\gamma_j = I_3$, and different values of the parameter p.

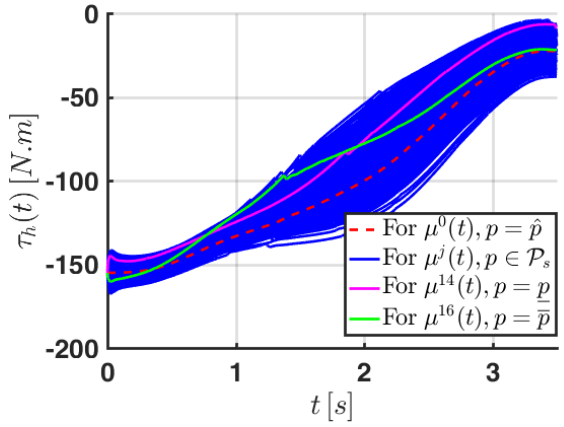

(a) Torque applied at the hips by the PLLO with state feedback from $K^{\star}_{\text{LQR}}(t)$.

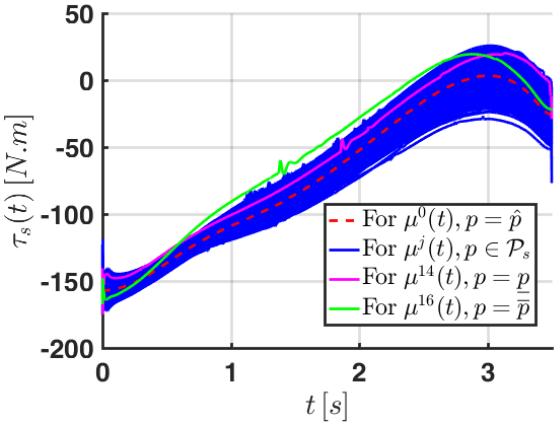

(b) Torque applied at the shoulders by the ILC algorithm.

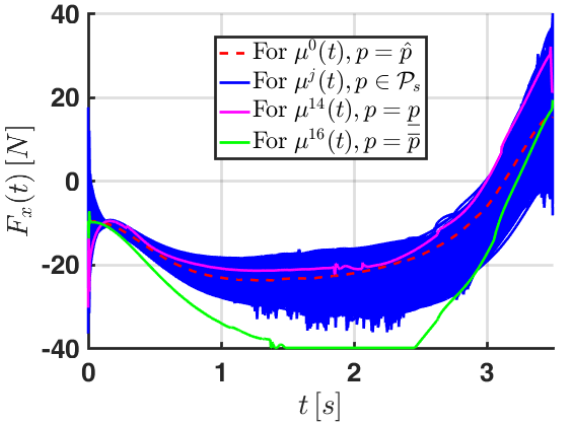

(c) Horizontal force applied at the shoulders by the ILC algorithm.

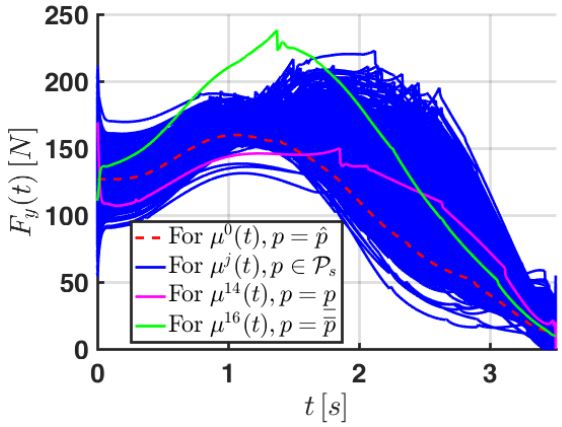

(d) Vertical force applied at the shoulders by the ILC algorithm.

Figure 5.9: Loads applied at the hips and shoulders for input trajectories $\mu^j(t)$ obtained from the ILC algorithm with gains $K^{\star}$ and $L^{\star}$, $\gamma_j = I_3$, and different values of the parameter p.

We conclude that the finite time horizon LQR controller found in Section 4.4 by using our robust performance metric works in harmony with the ILC algorithm substituting for the shoulder actions. It is remarkable that we incur only limited performance degradation for tracking the reference trajectories under scenarios of flawed memory and lack of coordination at the shoulders, and that even in the presence of extreme parameter uncertainties all simulations exhibit safe, realistic, and successful STS 1 movements.

5.4 ILC Algorithm with a Reduced Number of Variables in the Output Measured by the User

In this section we will explore the effects on the performance of the ILC algorithm described in Section 5.1 when the output measured by the user Υ does not include the angular acceleration of the torso $\ddot{\theta}_3(t)$, nor the acceleration of the CoM $[\ddot{x}_{\text{CoM}}(t); \ddot{y}_{\text{CoM}}(t)]$.

Redefining $\Upsilon := [\theta_3;\ x_{\text{CoM}};\ y_{\text{CoM}};\ \dot{\theta}_3;\ \dot{x}_{\text{CoM}};\ \dot{y}_{\text{CoM}}] \in \mathbb{R}^6$, its value can be determined from the state x, and parameter p with a mapping $\Psi : \mathbb{R}^6 \times \mathbb{R}^{12} \to \mathbb{R}^6$ that lumps the kinematic equations of the CoM of the three-link robot in (4.18). The nonlinear dynamics of the system with user input μ and the output with the reduced number of variables Υ are

$$\begin{aligned} \dot{x}(t) &= \Xi(t, x, p, \mu) \\ \Upsilon(t) &= \Psi(x(t), p). \end{aligned} \tag{5.14}$$

The desired trajectory for $\Upsilon(t)$ during the ascension phase of the STS movement is computed as $\hat{\Upsilon}(t) = \Psi(\hat{x}(t), \hat{p})$.

Setting $p = \hat{p}$ in (5.14), we use the ILC algorithm in (5.8) and (5.9) with $\gamma_j = I_3$ to emulate the loads applied at the shoulders by a user over $N = 30$ ascension attempts, and solve (5.11) to tune the gains $L, K \in \mathbb{R}^{3\times 6}$ for the updated output $\Upsilon \in \mathbb{R}^6$. Running the stochastic gradient descent method in (5.13) for 10,000 iterations with $g = J_{\text{L}}^N$, $B = 30$, $B_t = 10$, $\sigma = 0.01$, and $\rho_k \equiv 0.04$ on a machine with 72 physical cores running at 2.10 [GHz] we obtain the values

$$K^\star = \begin{bmatrix} -100.6 & -53.26 & 71.59 & -123.9 & -208.5 & 66.02 \\ 57.98 & -21.06 & -47.92 & -24.67 & 166.9 & -31.92 \\ 28.86 & 20.20 & 139.9 & 46.62 & -29.75 & 123.5 \end{bmatrix},$$

$$L^\star = \begin{bmatrix} -0.6381 & 2.376 & 46.31 & -2.514 & -5.255 & -28.89 \\ -2.948 & -29.34 & -25.24 & 2.851 & -3.559 & 24.48 \\ -73.09 & -58.25 & 114.1 & 19.82 & 13.09 & 126.9 \end{bmatrix},$$

with a cost of $J_L^\star = 8.66$ when $\mu^{30}(t)$ is applied, which is less than the reference $\hat{J}_L = 8.75$, but greater than the cost of 8.29 obtained with the original definition of $\Upsilon \in \mathbb{R}^9$ in Section 5.2.

Figures 5.10 and 5.11 show in black the phase planes for the state x, position and velocity of the CoM in the sagittal plane, and input trajectories $u(t)$ of the three-link robot model in (5.14) simulated under $\mu^{30}(t)$. The ILC algorithm with $K^\star, L^\star \in \mathbb{R}^{3\times 6}$ achieves almost perfect tracking of $\hat{\Upsilon}(t) \in \mathbb{R}^6$; as a consequence, Figures 5.10c, 5.10d, and 5.10e show the trajectories in black essentially overlapping with the red dashed lines. Deviations from the reference in the phase planes $\theta_1 - \dot{\theta}_1$ (Figure 5.10a) and $\theta_2 - \dot{\theta}_2$ (Figure 5.10b) are expected, since they are not penalized in (5.10). Nevertheless, θ_1 is off the vertical at the end of the ascension just by $0.5[^\circ]$, with the absolute values of both angular velocities less than $1.2[^\circ/s]$, which should not compromise the ability of a controller for the stabilization phase to reach the standing position with ease. As $\theta_2(t)$ remains less than zero for the entire trajectory, there is no hyperextension of the knees, and thus the input $\mu^{30}(t)$ should not

pose a threat to the physical integrity of the user. Even though the tracking errors for the angular position and velocity of the shanks and thighs links do not directly affect the computation of $\mu^j(t)$ in (5.9), they do determine (together with the tracking errors of the angular position and velocity of the torso) the value of the torque at the hips through the state feedback of the LQR, hence causing it to differ from $\hat{\tau}_h(t)$ in Figure 5.11a. It is especially interesting that although we did not consider $\hat{\mu}(t)$ in (5.10), both the torque and horizontal force at the shoulders in Figures 5.11b and 5.11c follow their reference trajectories reasonably well, within errors of 15[N.m], and 10[N], respectively. The absolute value of the torque applied at the hips in Figure 5.11a is in general greater than $\hat{\tau}_h(t)$, which compensates for lower vertical forces attained by $\mu_3^{30}(t)$ in Figure 5.11d relative to $\hat{F}_y(t)$. From the rate of change $\dot{\mu}_3^{30}(t)$ observed in Figure 5.11d, we can infer that $J_L^\star < \hat{J}_L$ is mostly due to the difference of its values over time with respect to $\dot{\hat{F}}_y(t)$. Although $\hat{F}_y(t)$ remains constant for about 1[s], it decreases 165[N] in 1.4[s], while $\mu_3^{30}(t)$ decreases 155[N] over 2.5[s] for a lower average rate of change.

Despite the reduced number of variables in the output measured by the user, the results discussed above indicate that the ILC input in (5.9) is still able to successfully coordinate with the LQR controller driving the actuators at the hips in (5.2) to complete STS 1, with no risk of sit-back or step failures [15] under nominal parameter conditions. Moreover, it does so exhibiting input trajectories that could be realistically executed by both the PLLO and the user after 30 learning iterations.

To test the ILC algorithm under imperfect recalling and execution of $\mu^{j-1}(t)$ we plug the iteration-varying matrix $\gamma_j = I_3 + q^{j-1}\vartheta_j$ in (5.8), with $q := 0.8$, and randomly sample the entries of $\vartheta_j \in \mathbb{R}^{3\times 3}$ at every iteration $j \in 1, \ldots, N$ within the interval $[-0.05, 0.05]$. With the nominal parameter value $\hat{p}$, starting the learning algorithm from the linear interpolation in (5.6), and applying 30 iterations, we obtained the behavior of the system (5.14) shown in blue in Figures 5.10 and 5.11. The degraded tracking of $\hat{\Upsilon}(t)$ and $\hat{x}(t)$ is evident in Figures 5.10a to 5.10e. However, the trajectory of the CoM position in Figure 5.10d shows that it is still possible to complete the ascension. Furthermore, Figure 5.10b affirms that the integrity of the knee joints will be preserved. Judging from the deviation from the reference in the phase plane for the angular position and velocity of the shanks in Figure 5.10a, and most importantly the non-zero final velocity of the CoM observed in Figure 5.10e, we predict that the stabilization phase of this STS movement would be more challenging than the one obtained for $\mu^{30}(t)$ when $\gamma_j = I_3$. The control inputs of the PLLO (Figure 5.11a) and those obtained in the ILC algorithm (Figures 5.11b to 5.11d) remain between the bounds in (5.3), verifying that $K^\star$, $L^\star \in \mathbb{R}^{3\times 6}$ still attain realistic trajectories after the same number of iterations with $\gamma_j \neq I_3$, although their oscillations and sudden changes do lead to an increased value for the cost in (5.10) of $J_L^{30} = 40$.

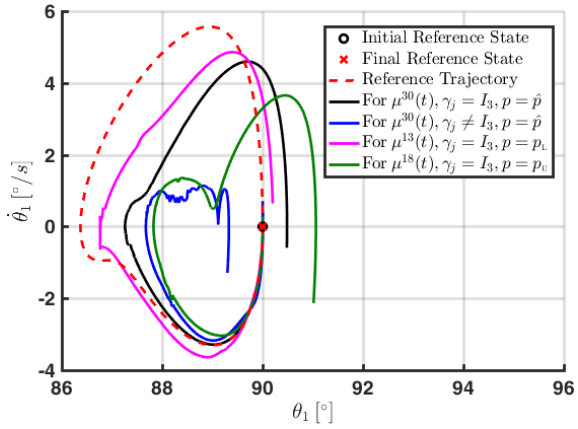

(a) Phase plane of trajectories $\theta_1(t)$ and $\dot{\theta}_1(t)$.

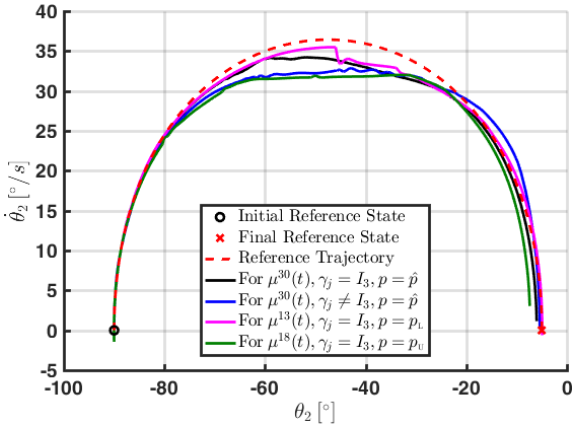

(b) Phase plane of trajectories $\theta_2(t)$ and $\dot{\theta}_2(t)$.

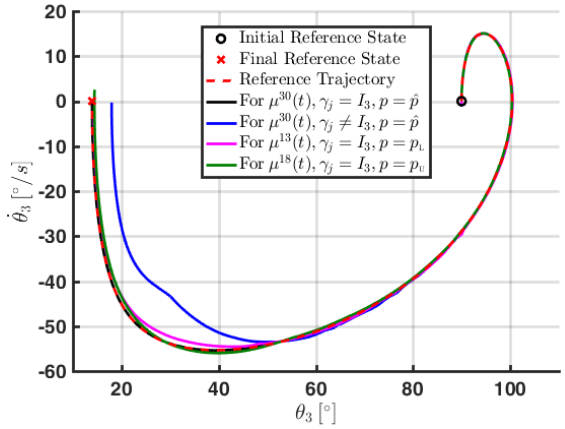

(c) Phase plane of trajectories $\theta_3(t)$ and $\dot{\theta}_3(t)$.

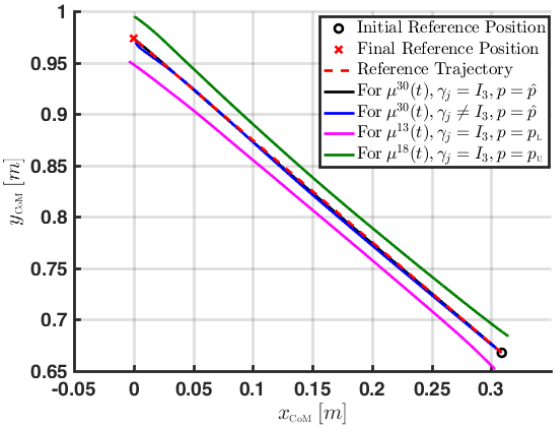

(d) Trajectories for the position of the CoM in the sagittal plane.

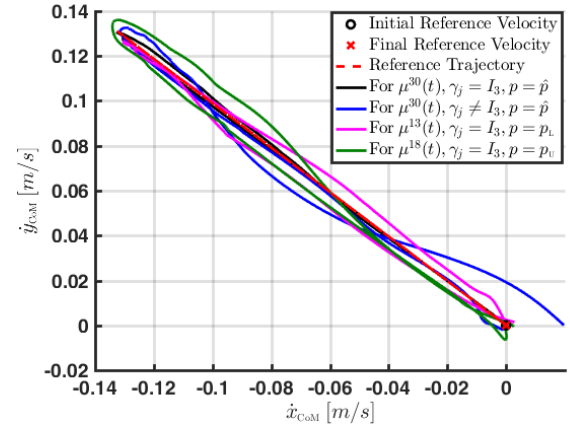

(e) Trajectories for the velocity of the CoM in the sagittal plane.

Figure 5.10: Phase planes for the state x, position, and velocity of the CoM obtained from the ILC algorithm with $\Upsilon := [\theta_3;\ x_{\text{CoM}};\ y_{\text{CoM}};\ \dot{\theta}_3;\ \dot{x}_{\text{CoM}};\ \dot{y}_{\text{CoM}}] \in \mathbb{R}^6$.

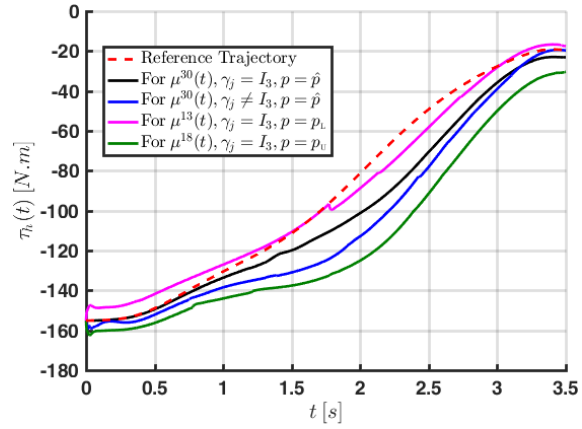

(a) Torque applied at the hips by the LQR controller.

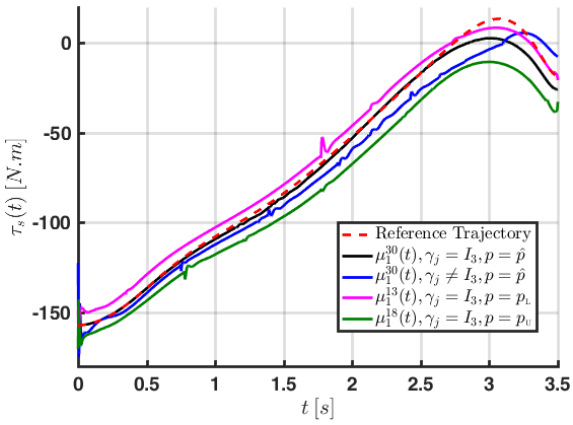

(b) Torque applied at the shoulders by the ILC algorithm.

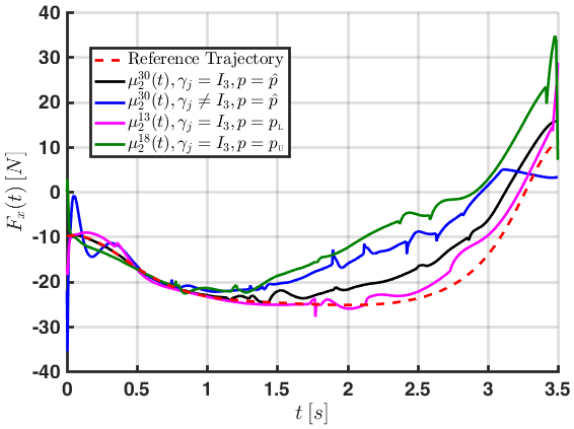

(c) Horizontal force applied at the shoulders by the ILC algorithm.

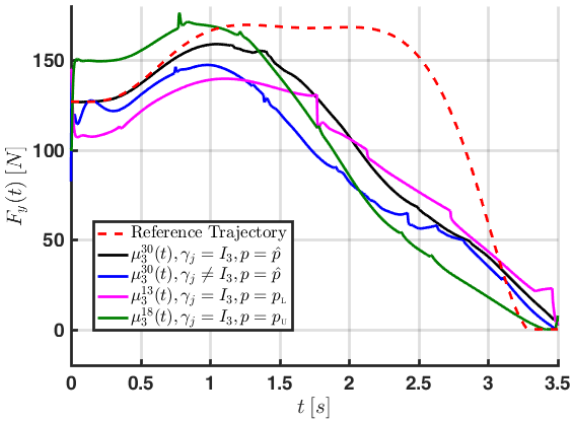

(d) Vertical force applied at the shoulders by the ILC algorithm.

Figure 5.11: Loads applied at the hips of the PLLO and shoulders of the user under the action of the ILC algorithm with $\Upsilon := [\theta_3;\ x_{\text{CoM}};\ y_{\text{CoM}};\ \dot{\theta}_3;\ \dot{x}_{\text{CoM}};\ \dot{y}_{\text{CoM}}]$.

We now study the effect of parameter uncertainty after the ILC algorithm has completed 30 iterations under the nominal value of the parameter $p = \hat{p}$, and constant recalling matrix $\gamma_j = I_3$. For this purpose, we set the new $\mu^0(t)$ in (5.8) equal to the trajectories in black from Figures 5.11b to 5.11d, and simulate the system in (5.14) under the action of (5.9) for two different parameter values:

$$p_{\text{L}} := [9.2\,[\text{kg}];\ 11.2\,[\text{kg}];\ 42.3\,[\text{kg}];1.10\,[\text{kg}\cdot\text{m}^2];\ 0.49\,[\text{kg}\cdot\text{m}^2];\ 2.40\,[\text{kg}\cdot\text{m}^2];\ldots$$
$$0.529\,[\text{m}];\ 0.409\,[\text{m}];\ 0.519\,[\text{m}];0.23\,[\text{m}];\ 0.17\,[\text{m}];\ 0.24\,[\text{m}]],$$

$$p_{\text{U}} := [10.2\,[\text{kg}];\ 13.2\,[\text{kg}];\ 46.8\,[\text{kg}];1.21\,[\text{kg}\cdot\text{m}^2];\ 0.54\,[\text{kg}\cdot\text{m}^2];\ 2.65\,[\text{kg}\cdot\text{m}^2];\ldots$$
$$0.531\,[\text{m}];\ 0.411\,[\text{m}];\ 0.521\,[\text{m}];0.30\,[\text{m}];\ 0.23\,[\text{m}];\ 0.28\,[\text{m}]].$$

All entries match the bounds in Table 4.1, except for the ones representing the lengths of the links, which come from subtracting (for p_{L}), and adding (for p_{U}) 1[mm] to the nominal lengths in $\hat{p}$. This choice puts more emphasis on studying changes in performance stemming from fluctuations of the total mass of the user, rather than from variations on the length of the links, since, in practice, the latter are only expected to occur due to wear of mechanical components after an extended period of use, while the former are bound to happen several times through the day. Keeping track of the cost J_{L}^{j} over $j = \{1, \ldots, 30\}$, we identify the iterations where the ILC algorithm attains the minimum values, and present their corresponding simulations in Figures 5.10 and 5.11. The results for p_{L} after 13 iterations are in magenta, while the ones for p_{U} after 18 are in green. The associated costs are $J_L^{13} := 27.9$ and $J_L^{18} := 29.1$.

Since $\hat{x}(t)$ and $\hat{\Upsilon}(t)$ are determined based on the nominal value $\hat{p}$, the reference for the position of the CoM in Figure 5.10d cannot be perfectly tracked with the mismatch in the parameter values. Their simulations run approximately parallel to the reference, with the lower bounds for l_{c_i} in p_{L} causing its trajectory to be below it, and the upper bounds for l_{c_i} in p_{U} putting its trajectory above. Although the velocities of the CoM for both parameter values in Figure 5.10e also deviate from the reference, zero velocity is achieved at the end of the movements, which together with the behavior observed in the phase plane in Figure 5.10b, proves that the proxy for the user action can safely complete the ascension phase. According to the larger offsets from the final desired state that exhibit the trajectories for p_{U} with respect to p_{L} in Figures 5.10a to 5.10c, we predict that the stabilization phase for a situation where the total mass of the user increases by 5% of its nominal value, might be more challenging than the one where the total mass decreases by the same amount. Figures 5.11a and 5.11b show that an increased mass of the wearer also requires larger contributions from the torque executed by the PLLO at the hips and the torque applied by the user at the shoulders. The oscillations and sudden changes of the force profiles (in magenta, and green) in Figures 5.11c and 5.11d, together with the deviations from $\hat{\Upsilon}(t)$ in Figures 5.10c to 5.10e, contribute to the larger values of J_L^{13} and J_L^{18} relative to $J_L^{\star}$. It is interesting that the most abrupt changes of $\dot{\mu}^{13}(t)$ happen when the velocity of the CoM achieves its maximum (approximately at 1.77[s]), and in the last 0.1[s] of the ascension; where $\dot{\mu}^{18}(t)$ also experiences its most significant changes. To further analyze the effect of parameter uncertainty on the performance of our proposed ILC algorithm in (5.9), we also considered 500 random parameter values $p \in [p_L, p_U]$ from a Latin Hypercube sampling to perform analogous evaluations to the ones in Figures 5.7 to 5.9. All simulations exhibited safe, realistic, and successful ascending STS movements.

Chapter 6

Output Feedback

Resume the assumption (used in Chapters 3 and 4) that the controller of a PLLO has authority not only over the torque of the actuators available in its architecture, but also over the torque and forces at the shoulders of the user, this chapter presents the design of an output feedback controller for the ascension phase of the STS movement. Since the controller relies on a Kalman-Bucy filter to estimate from a noisy output the deviation of the system from its reference trajectory, and then takes such estimate to implement the state feedback from the finite time horizon LQR in Section 3.2, this controller is referred as a finite time horizon LQG (linear-quadratic Gaussian). In order to make the estimation of the Kalman-Bucy filter robust against parameter uncertainty, we regard the deviation of the parameters of the three-link robot from its nominal values as process noise in the Jacobian linearization of the system.

Our main motivation for designing output feedback controllers for PLLOs is to evaluate if we can attain successful and safe STS movements with the finite time horizon LQR gain in (3.8) when readings of the full state of the system $x \in \mathbb{R}^6$ are not available due to hardware constraints. In particular when the installation of angular velocity sensors at the revolute joints is to be avoided, and the number of angular position sensors must be minimized in order to decrease the complexity of the mechatronics design. Hence, we use finite time horizon LQG controllers to track STS 1 with the minimally actuated PLLO at the hips for each one of the seven outputs that can be obtained when using rotary encoders at the joints of the PLLO to acquire measurements of the angular positions θ_1, θ_2, and θ_3 in Figure 2.1. By analyzing the performance of the nonlinear dynamics of the three-link robot through simulations with the controllers in the presence of parameter uncertainty, and measurement noise, we conclude on the most suitable configuration for the sensors to provide robust STS movements.

6.1 Finite Time Horizon LQG

Consider the Jacobian linearization of the system (3.5) about the reference state trajectory $\hat{x}(t)$, nominal parameter $\hat{p}$, and reference input trajectory $\hat{u}(t)$ presented in (3.6) using the deviation variables $\delta_x(t) := x(t) - \hat{x}(t)$, $\delta_p := p - \hat{p}$, and $\delta_u(t) := u(t) - \hat{u}(t)$. Even though δ_p is an unknown constant over the execution of a STS movement, in this section we assume it to be a stochastic process disturbance $\delta_p : \mathbb{R} \to \mathbb{R}^{12}$. Therefore, the linear dynamics of the state deviation $\delta_x \in \mathbb{R}^6$ with output $\delta_y \in \mathbb{R}^{n_o}$ subject to white measurement noise $v : \mathbb{R} \to \mathbb{R}^{n_o}$ are

$$\begin{aligned} \dot{\delta}_x(t) &= A(t)\,\delta_x(t) + B_1(t)\,\delta_p(t) + B_2(t)\,\delta_u(t) \\ \delta_y(t) &= C_1(t)\,\delta_x(t) + v(t), \end{aligned} \tag{6.1}$$

where $A(t) \in \mathbb{R}^{6\times 6}$, $B_1(t) \in \mathbb{R}^{6\times 12}$, $B_2(t) \in \mathbb{R}^{6\times m}$, and $C_1(t) \in \mathbb{R}^{n_o \times 6}$. The signals $\delta_p(t)$ and $v(t)$ are independent, Gaussian distributed, with zero mean, and known covariances, as reflected in the following statistical properties for all $t \in \left[t_0, t_f\right]$:

$$\mathbb{E}\left\{\delta_p(t)\right\} = 0, \quad \mathbb{E}\left\{\delta_p(t)\,\delta_p^\top(t)\right\} = Q_n \in \mathbb{R}^{12\times 12},$$

$$\mathbb{E}\left\{v(t)\right\} = 0, \quad \mathbb{E}\left\{v(t)\,v^\top(t)\right\} = R_n \in \mathbb{R}^{n_o \times n_o}.$$

Let $\tilde{\delta}_x(t) \in \mathbb{R}^6$ be the estimate of $\delta_x(t)$ in terms of the set of outputs gathered up to time t. Defining the set of stochastic outputs as $Y_t := \left\{\delta_y(\tau) : 0 \le \tau \le t\right\}$, we can write $\tilde{\delta}_x(t) := \mathbb{E}\left\{\delta_x(t) | Y_t\right\}$. From [50], the dynamics of the linear observer that minimizes the cost

$$J_{\text{KF}} = \mathbb{E}\left\{ \left\| \delta_x(\tau) - \tilde{\delta}_x(\tau) \right\|^2_{2,[0,t]} \middle| Y_t \right\},$$

are

$$\begin{aligned} \dot{\tilde{\delta}}_x(t) &= \left(A(t) - L_{\text{KF}}(t)\,C_1(t)\right)\tilde{\delta}_x(t) + B_2(t)\,\delta_u(t) + L_{\text{KF}}(t)\,\delta_y(t) \\ &= \left(A(t) - L_{\text{KF}}(t)\,C_1(t)\right)\tilde{\delta}_x(t) + B_2(t)\,\delta_u(t) + L_{\text{KF}}(t)\left(C_1(t)\,\delta_x(t) + v(t)\right) \end{aligned} \tag{6.2}$$

with zero initial condition $\tilde{\delta}_x(0) = 0$. The time-varying matrix gain $L_{\text{KF}}(t) \in \mathbb{R}^{6\times n_o}$ is known as the Kalman-Bucy filter gain, and is given by

$$L_{\text{KF}}(t) = P_n(t)\,C_1^\top(t)\,R_n^{-1}, \tag{6.3}$$

where $P_n(t) \in \mathbb{R}^{6\times 6}$ is the solution of the Riccati matrix differential equation

$$\dot{P}_n(t) = A(t)\,P_n(t) + P_n(t)\,A^\top(t) - P_n(t)\,C_1^\top(t)\,R_n^{-1}C_1(t)\,P_n(t) + B_1 Q_n B_1^\top, \tag{6.4}$$

with the boundary condition $P_n\left(t_f\right) = 0$.

Using the finite time horizon LQR gain $K_{\text{LQR}}(t) \in \mathbb{R}^{m\times 6}$ in (3.8), the nonlinear dynamics of the three-link robot under finite time horizon LQG control become

$$\dot{x}(t) = f\left(x(t), p, \hat{u}(t) - K_{\text{LQR}}(t)\,\tilde{\delta}_x\right). \tag{6.5}$$

6.2 Simulation of a PLLO Under Finite Time Horizon LQG with Different Configurations for the Rotary Encoders

The time-varying matrices $A(t) \in \mathbb{R}^{6\times 6}$, $B_1(t) \in \mathbb{R}^{6\times 12}$, and $B_2(t) \in \mathbb{R}^{6\times 4}$ in the Jacobian linearization for the minimally actuated PLLO at the hips in (6.1) are computed as in (3.6) for the STS 1 reference trajectories obtained in Section 2.5 for $t \in [0, 3.5]\,[s]$. The values of the output matrix $C_1(t) \in \mathbb{R}^{n_o\times 6}$ that characterize the seven different outputs $\delta_y \in \mathbb{R}^{n_o}$ that can be acquired from rotary encoders at the joints of the ankle, knee, and hip to measure the angular positions of the links are in Table 6.1.

Table 6.1: Configuration of rotary encoders and output matrices for designing the finite time horizon LQG controllers to track the reference trajectories of STS 1

LQG	n_o	Location of rotary encoders	$C_1(t) \in \mathbb{R}^{n_o\times 6}$
1	1	Ankle.	$\begin{bmatrix} 1 & 0 & 0 & 0 & 0 & 0 \end{bmatrix}$
2	1	Knee.	$\begin{bmatrix} 0 & 1 & 0 & 0 & 0 & 0 \end{bmatrix}$
3	1	Hip.	$\begin{bmatrix} 0 & 0 & 1 & 0 & 0 & 0 \end{bmatrix}$
4	2	Ankle, and knee.	$\begin{bmatrix} 1 & 0 & 0 & 0 & 0 & 0 \\ 0 & 1 & 0 & 0 & 0 & 0 \end{bmatrix}$
5	2	Knee, and hip.	$\begin{bmatrix} 0 & 1 & 0 & 0 & 0 & 0 \\ 0 & 0 & 1 & 0 & 0 & 0 \end{bmatrix}$
6	2	Ankle, and hip.	$\begin{bmatrix} 1 & 0 & 0 & 0 & 0 & 0 \\ 0 & 0 & 1 & 0 & 0 & 0 \end{bmatrix}$
7	3	Ankle, knee, and hip.	$\begin{bmatrix} 1 & 0 & 0 & 0 & 0 & 0 \\ 0 & 1 & 0 & 0 & 0 & 0 \\ 0 & 0 & 1 & 0 & 0 & 0 \end{bmatrix}$

With the bounds for the parameter uncertainty $p \in \left[\underline{p}, \overline{p}\right]$ in Table 4.1 we set

$$Q_n = \frac{1}{9}\left(\text{diag}\left(\max\left(\hat{p} - \underline{p}, \overline{p} - \hat{p}\right)\right)\right)^2, \tag{6.6}$$

where the max operator returns the element-wise maximum over its two vector arguments. For the covariance of $v(t)$ we consider rotary encoders common in robotics applications with an accuracy of $\pm 0.02[^\circ]$ such as [51], so that

$$R_n = \left(\frac{0.02\,[^\circ]}{3}\right)^2 I_{n_o} = \left(\frac{0.02\pi}{540}\right)^2 I_{n_o}. \tag{6.7}$$

To compute the Kalman-Bucy filter gains $L_{\text{KF}}(t) \in \mathbb{R}^{6\times n_o}$ for the finite time horizon LQG controllers, identified with the numbers 1-7, we solve the Riccati matrix differential equation in 6.4

with the numerical tools described in [37] for their corresponding values of $C_1(t)$, and substitute the solution for $P_n(t)$ in (6.3). All the controllers use the finite time horizon LQR gain $K^{\star}_{\text{LQR}}(t)$ from Section 4.4.

Setting $p = \hat{p}$ in (6.5), and sampling the noise measurement at every $t \in [0, 3.5][s]$ so that $v(t) \sim \mathcal{N}(0, R_n)$, we simulate the response of the three-link robot with the LQG controllers for the different configurations of the sensors by simultaneously solving the differential equations for the nonlinear dynamics in (6.5) starting from $x(0) = \hat{x}(0)$, and the linear observer in (6.2) with zero initial condition. The results are depicted in Figures 6.1 to 6.3 with the reference trajectories shown in red dashed lines.

Despite the presence of measurement noise, the trajectories in Figure 6.1 show that the LQG controllers with outputs comprising measurements from a single rotary encoder ($n_o = 1$) are the only ones that lead to noticeable deviations of the system in (6.5) from the state reference $\hat{x}(t)$. Among these controllers, the one using readings of θ_1 (LQG 1) causes the smallest deviations, and the one using readings of θ_3 (LQG 3) causes the largest deviations.

It is remarkable that regardless of their different levels of success at tracking $\hat{x}(t)$, every LQG controller manages to complete STS 1 in the absence of parameter uncertainty showing no signs of hyperextension of the knees in Figure 6.1b, and excellent tracking of the reference trajectory for the position of the CoM in Figures 6.2a, 6.2b, and 6.2e. However, the controllers with $n_o = 1$ do show deviations from the reference trajectory for the velocity of the CoM in Figures 6.2c, 6.2d, and 6.2f.

Given the errors for tracking $\hat{x}(t)$ registered with LQG 1, 2, and 3, deviations from the input reference trajectory $\hat{u}(t)$ with these controllers are expected. Although the deviations induced by LQG 1 can be neglected, LQG 2, and 3 behave very poorly, applying large spikes of loads in Figures 6.3a to 6.3c with significant oscillations. It can be seen in Figure 6.3c that the only controller with $n_o > 1$ making the horizontal force at the shoulder to jitter is LQG 5, which has no rotary sensor at the ankle joint.

To test the robustness against parameter uncertainty of the LQG controllers for the different configurations of the rotary encoders, we opted to perform simulations under multiple bounds for the values of p in (6.5). Starting from the bounds for a fluctuation of ±5% in the nominal weight of the user in Table 4.1, we use Latin hypercube sampling to pick 500 random values of $p \in \left[\underline{p}, \overline{p}\right]$, which we denote as the set $\mathcal{P}_g$. If the nonlinear system in (6.5) completes STS 1 with its input and state trajectories within the bounds in (5.3) and (5.7) for all $p \in \mathcal{P}_g$, we infer that the tested LQG controller is robust to the parameter uncertainty in the sampled bounds. If there are values of p whose trajectories do not complete the STS 1 movement, we shrink the interval $\left[\underline{p}, \overline{p}\right]$ decreasing the fluctuations assumed from the nominal weight of the user by one percent, recompute Q_n from (6.6) and the Kalman-Bucy filter gain in (6.3), update $\mathcal{P}_g$ by Latin hypercube sampling of 500 values of p within the new bounds, and simulate (6.5) for all $p \in \mathcal{P}_g$. If the three-link robot in output feedback with the LQG controller is still not robust to the parameter uncertainty, we repeat the procedure above, and stop when the bounds for p reflect no fluctuation from the nominal weight of the user. The LQR gain $K^{\star}_{\text{LQR}}(t)$, the value for R_n in (6.7), the measurement noise $v(t) \sim \mathcal{N}(0, R_n)$, and the uncertainty of ±1[cm] for the lengths of the links are fixed across every iteration.

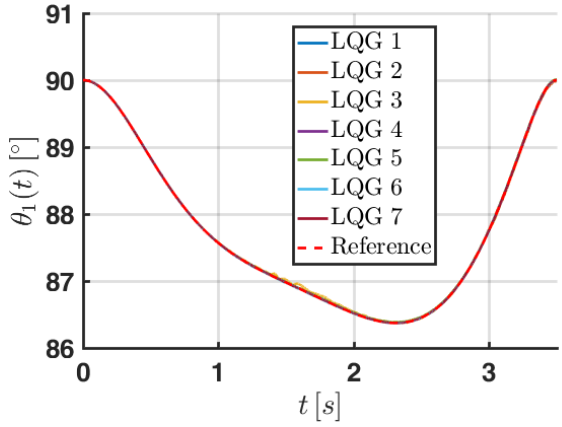

(a) Angular position of link 1 relative to the horizontal.

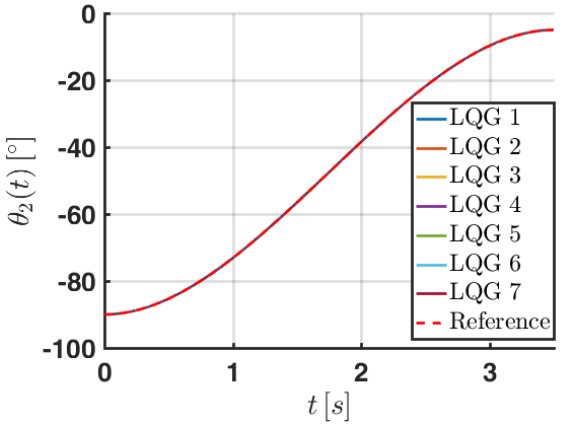

(b) Angular position of link 2 relative to link 1.

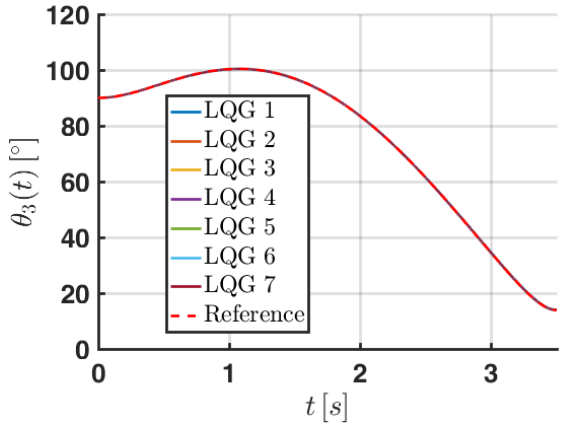

(c) Angular position of link 3 relative to link 2.

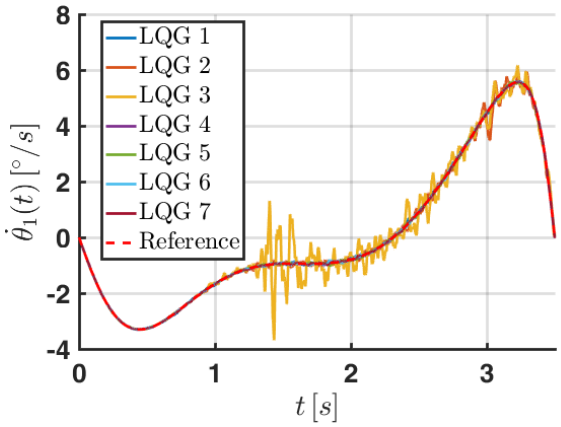

(d) Angular velocity of link 1.

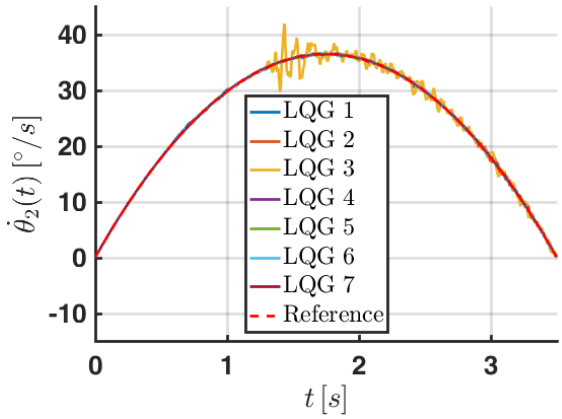

(e) Angular velocity of link 2.

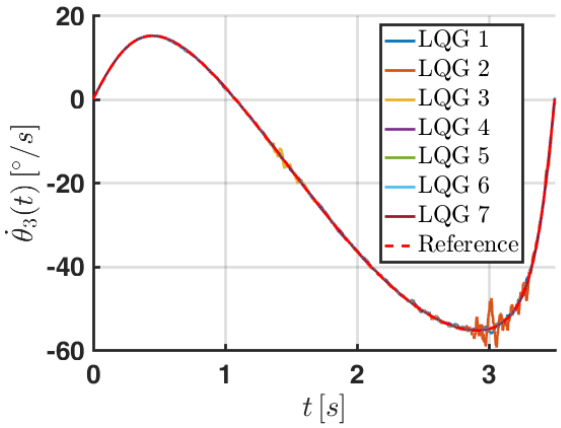

(f) Angular velocity of link 3.

Figure 6.1: State trajectories of the three-link robot using the LQG controllers for the seven output configurations in the presence of measurement noise, and no parameter uncertainty with $p = \hat{p}$.

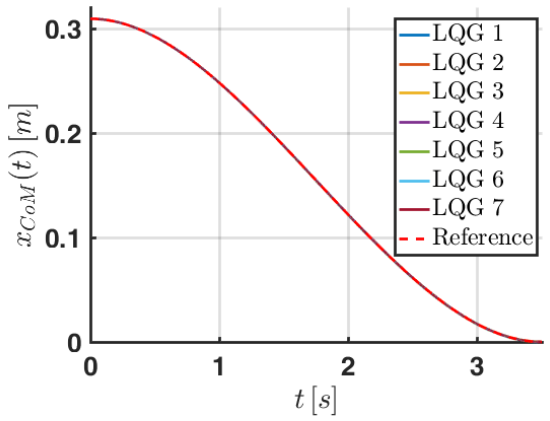

(a) x_{CoM} coordinate of the position of the three-link robot CoM.

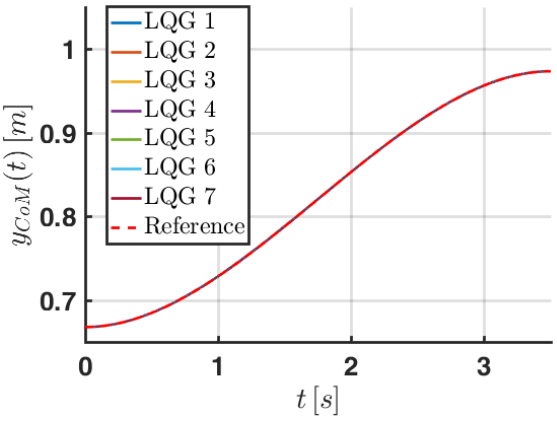

(b) y_{CoM} coordinate of the position of the three-link robot CoM.

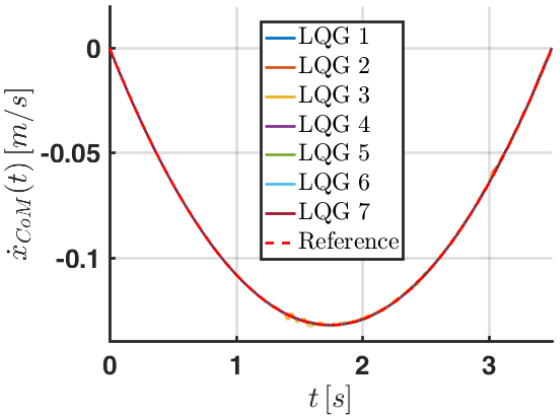

(c) $\dot{x}_{\text{CoM}}$ coordinate of the velocity of the three-link robot CoM.

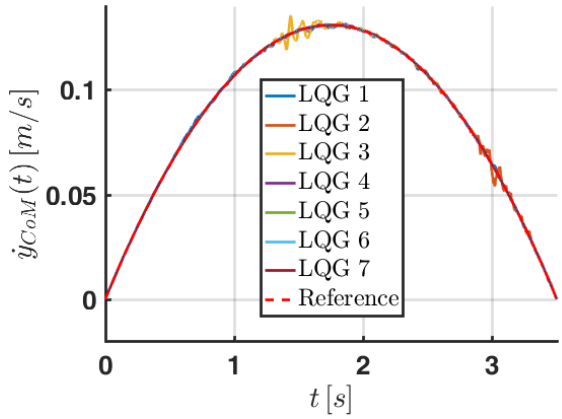

(d) $\dot{y}_{\text{CoM}}$ coordinate of the velocity of the three-link robot CoM.

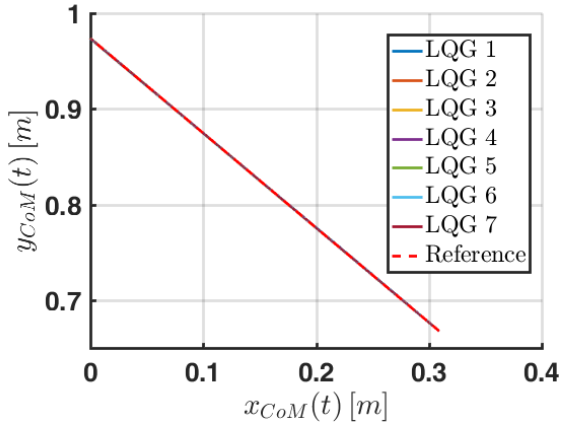

(e) $\dot{x}_{\text{CoM}}$ coordinate of the velocity of the three-link robot CoM.

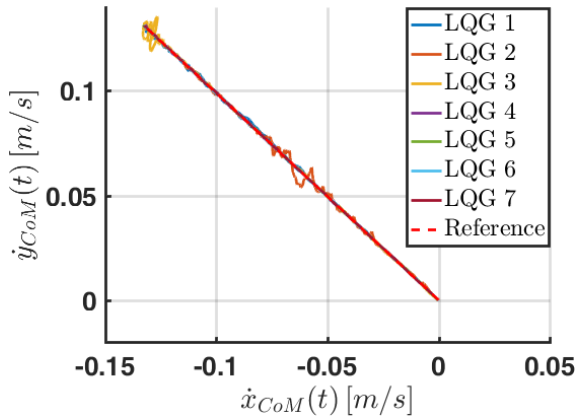

(f) $\dot{y}_{\text{CoM}}$ coordinate of the velocity of the three-link robot CoM.

Figure 6.2: Trajectories of the three-link robot CoM using the LQG controllers for the seven output configurations in the presence of measurement noise, and no parameter uncertainty with $p = \hat{p}$.

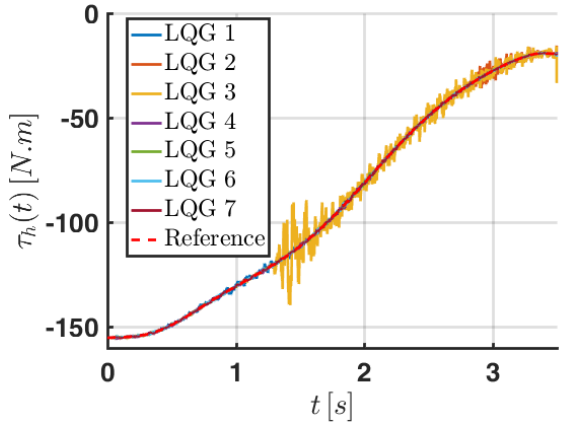

(a) Torque applied at the hips by the PLLO.

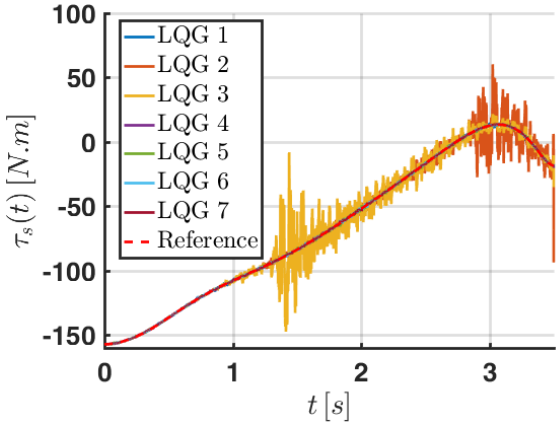

(b) Torque at the shoulders of the user.

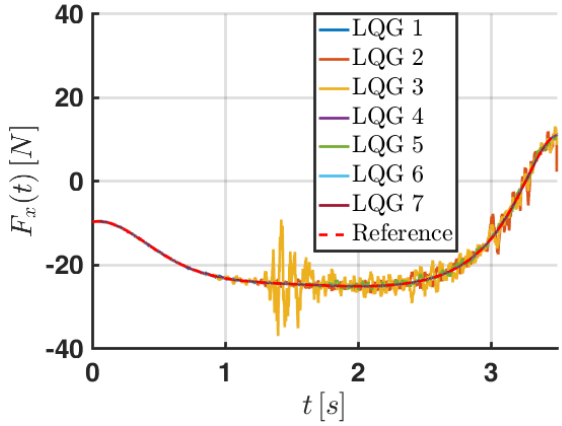

(c) Horizontal force at the shoulders of the user.

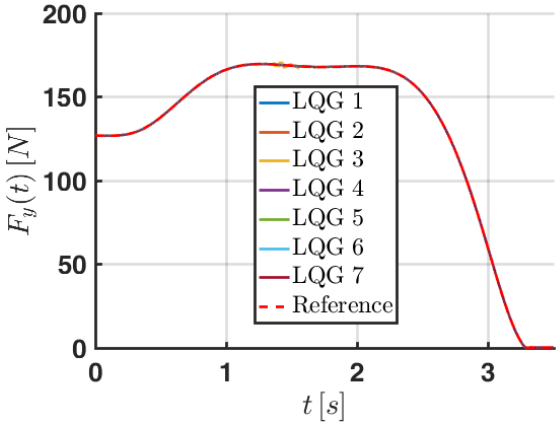

(d) Vertical force at the shoulders of the user.

Figure 6.3: Input trajectories of the three-link robot using the LQG controllers for the seven output configurations in the presence of measurement noise, and no parameter uncertainty with $p = \hat{p}$.

The tests against parameter uncertainty for the seven finite time horizon LQG designs take 8.34[h] using a node in the Savio cluster with 28 cores at 2.4[GHz] running Matlab Parallel Toolbox. LQG 4 is robust to fluctuations of ±1% from the nominal weight of the user, which are bounded by the parameter values in Table 6.2. LQG 7 is robust to fluctuations of ±5% from the nominal weight of the user in Table 4.1. The remaining LQG controllers reach the end of the test, failing to complete STS 1 for all sampled $p \in \mathcal{P}_g$.

To further analyze if LQG 1, 2, 3, and 5 could be robust against small variations from $\hat{p}$, we sampled a set $\mathcal{P}_g$ from an interval encompassing fluctuations of ±0.1% from the nominal weight of the user and ±1[mm] for the lengths of the links. Nevertheless, even in the face of this minuscule deviations with no practical meaning, the simulations of (6.5) cannot complete STS 1 for some values of $p \in \mathcal{P}_g$. Thus, we declare these controllers not robust to parameter uncertainty. Their corresponding configurations of rotary encoders at the joints of the PLLO also proved to be the

most sensitive to noise in Figure 6.3.

LQG 6 is found to be robust by shrinking the fluctuations from the nominal weight of the user to ±0.05%, and the variation in length of the links to ±1[cm]; which makes the configuration of rotary sensors at the ankle and knee used in LQG 4, the one that leads to the best performance among the controllers with $n_o = 2$. Figures 6.4 to 6.6 show in blue the trajectories for the state, CoM, and input of the three-link robot under the action of LQG 4 for the 500 $p \in \mathcal{P}_g$ bounded by the values in Table 6.2. The reference trajectories for STS 1 are in red. We can tell that the LTV observer in (6.2) is able to overcome the deviations δ_p, and measurement noise $v(t)$ with the choice of weights in (6.6) and (6.7) for computing the Kalman-Bucy filter gain in (6.3), so that it can estimate δ_x within an error suitable for completing STS 1 movements without compromising the knee of the users by keeping $\theta_2(t) < 0$ in Figure 6.4b. The trajectories of $\theta(t)$ in Figures 6.4a to 6.4c are smooth, and the ones for $\dot{\theta}(t)$ in Figures 6.4d to 6.4f only experience small oscillations that do not induce sudden changes in the loads of Figures 6.6a to 6.6c. However, since the fluctuation for the mass of the user in this scenario is very limited, the only reason to rely in two rotary sensors for controlling the PLLO is if the requirement to reduce the number of components in the mechatronics design surpasses the requirement to guarantee the robustness of the STS movement for a wider parameter uncertainty.

Table 6.2: Bounds for the parameter uncertainty of the three-link robot for a fluctuation of ±1% in the nominal weight of the user, and a variation of ±1[cm] in the nominal lengths of the links

Link	m_i [kg]	I_i $\left[\text{kg}\cdot\text{m}^2\right]$	l_i [m]	l_{ci} [m]
1	[9.58, 9.78]	[1.14, 1.16]	[0.52, 0.54]	[0.23, 0.30]
2	[12.5, 12.7]	[0.51, 0.52]	[0.39, 0.42]	[0.18, 0.23]
3	[44.1, 45.0]	[2.49, 2.55]	[0.51, 0.53]	[0.24, 0.28]

Figures 6.7 to 6.9 include the results from the simulation of LQG 7 for the 500 $p \in \mathcal{P}_g$ bounded by the values in Table 4.1 in blue, and the reference trajectories for STS 1 in red. Although the volumes of the tunnels enclosing the simulations for the state, position and velocity of the CoM, and the inputs of the system with this controller are larger when compared to the volumes of the corresponding tunnels for the trajectories of the system under state feedback with $K^{\star}_{\text{LQR}}(t)$ shown in green in Figures 4.7 to 4.9, the degradation in tracking performance does not cause hyperextension of the knees in Figure 6.7b, nor saturation of the inputs in Figure 6.9. Furthermore, Figures 6.8c and 6.8d show that at the end of the STS movements $\dot{y}_{\text{CoM}}(3.5) \approx 0$[cm/s], and $|\dot{x}_{\text{CoM}}(3.5)| \leq 2.4$[cm/s] for all $p \in \mathcal{P}_g$, what contributes to ease the stabilization phase.

We can conclude that a minimally actuated PLLO at the hips using the finite time horizon LQG controller in Section 6.1 requires three rotary encoders providing readings of θ_1, θ_2, and θ_3 in Figure 2.1 to execute the STS 1 movement under the parameter uncertainty in Table 4.1, for which the finite time horizon LQR gain $K^{\star}_{\text{LQR}}(t)$ was optimized in Section 4.4. We identify the corresponding Kalman-Bucy filter gain as $L^{\star}_{\text{KF}}(t) \in \mathbb{R}^{6\times 3}$.

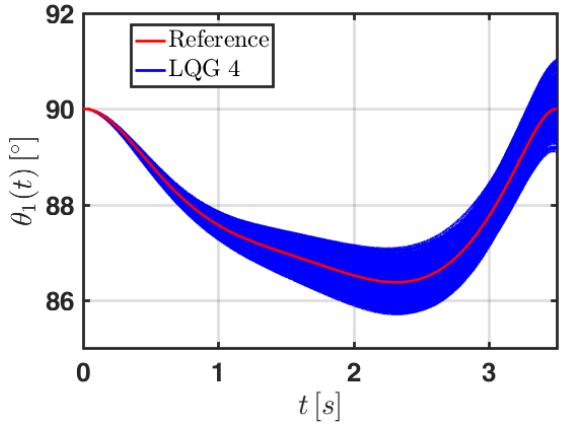

(a) Angular position of link 1 relative to the horizontal.

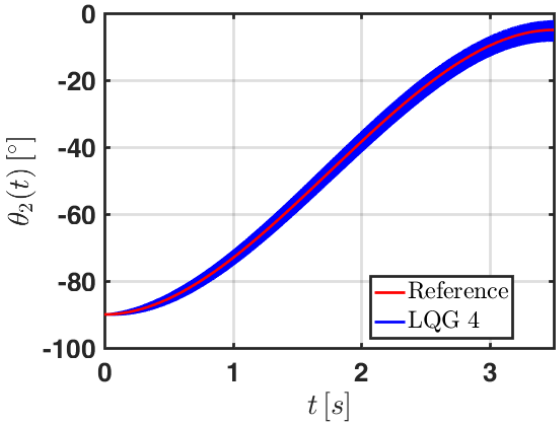

(b) Angular position of link 2 relative to link 1.

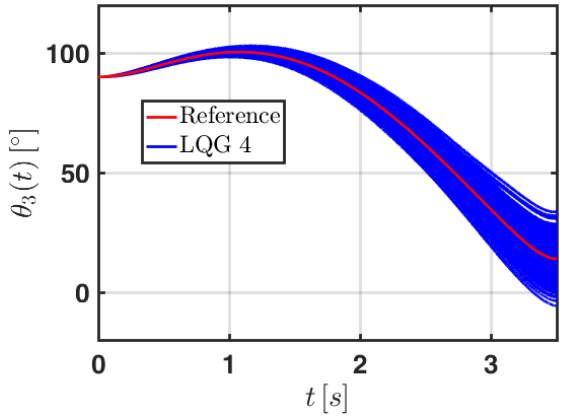

(c) Angular position of link 3 relative to link 2.

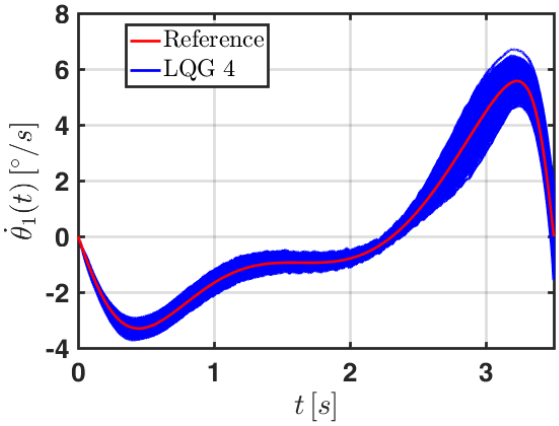

(d) Angular velocity of link 1.

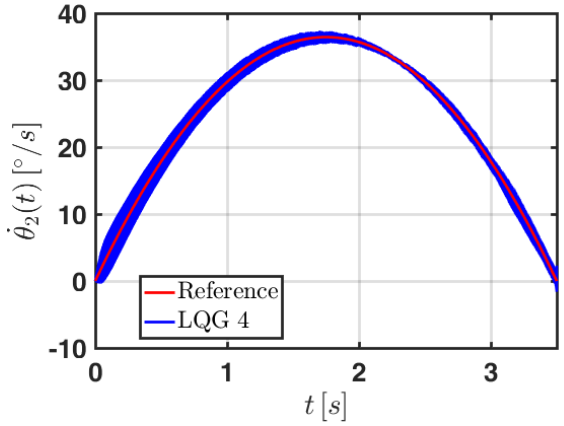

(e) Angular velocity of link 2.

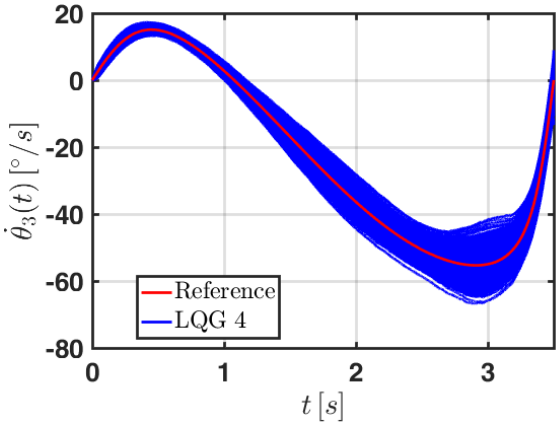

(f) Angular velocity of link 3.

Figure 6.4: State trajectories of the three-link robot using the LQG 4 controller with noisy measurement of θ_1, and θ_2 for all $p \in \mathcal{P}_s$ sampled within the bounds in Table 6.2.

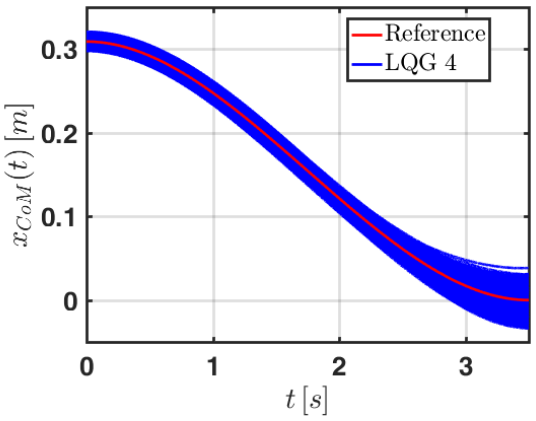

(a) x_{CoM} coordinate of the position of the three-link robot CoM.

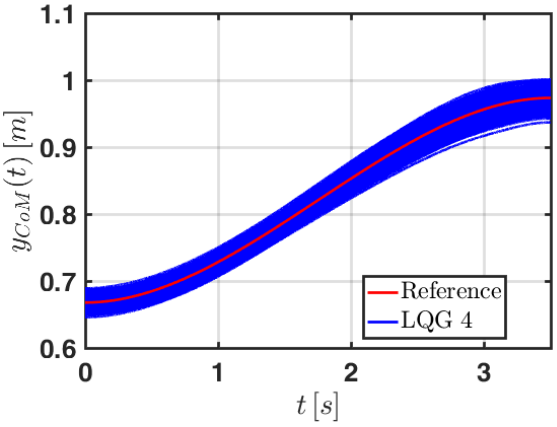

(b) y_{CoM} coordinate of the position of the three-link robot CoM.

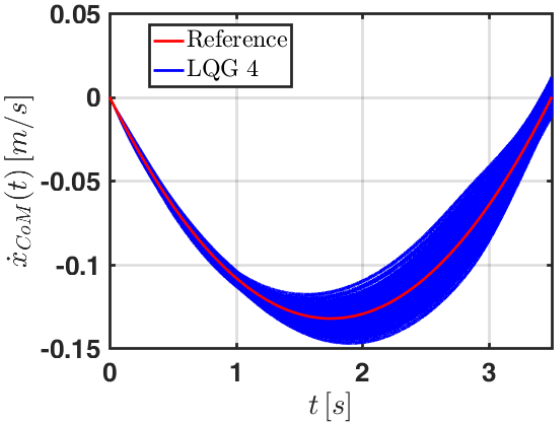

(c) $\dot{x}_{\text{CoM}}$ coordinate of the velocity of the three-link robot CoM.

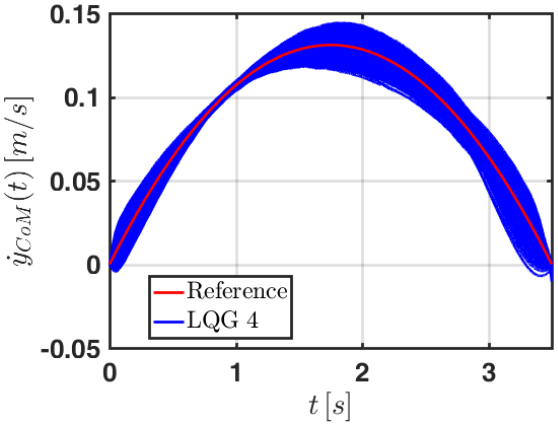

(d) $\dot{y}_{\text{CoM}}$ coordinate of the velocity of the three-link robot CoM.

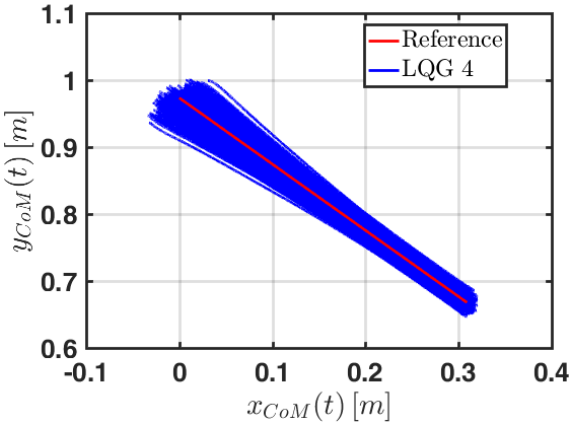

(e) $\dot{x}_{\text{CoM}}$ coordinate of the velocity of the three-link robot CoM.

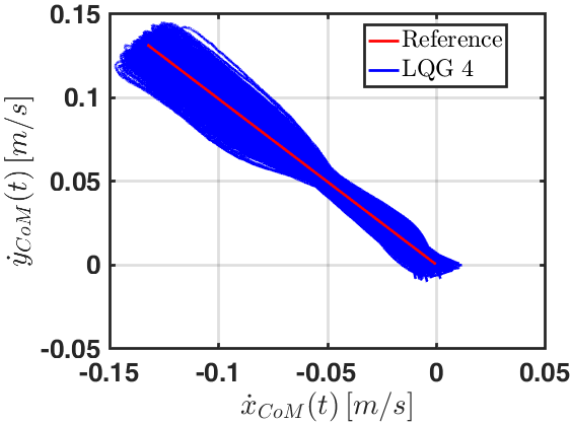

(f) $\dot{y}_{\text{CoM}}$ coordinate of the velocity of the three-link robot CoM.

Figure 6.5: Trajectories of the three-link robot CoM using the LQG 4 controller with noisy measurement of θ_1, and θ_2 for all $p \in \mathcal{P}_s$ sampled within the bounds in Table 6.2.

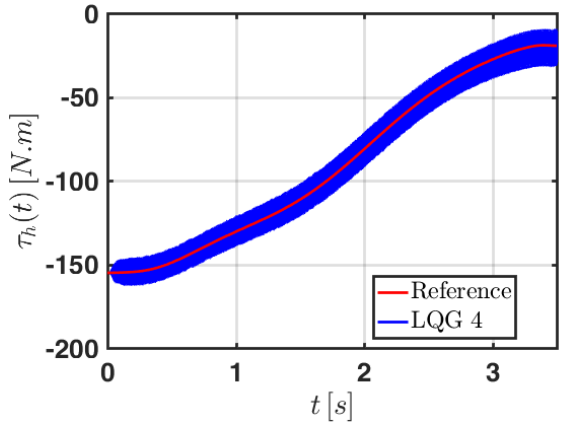

(a) Torque applied at the hips by the PLLO.

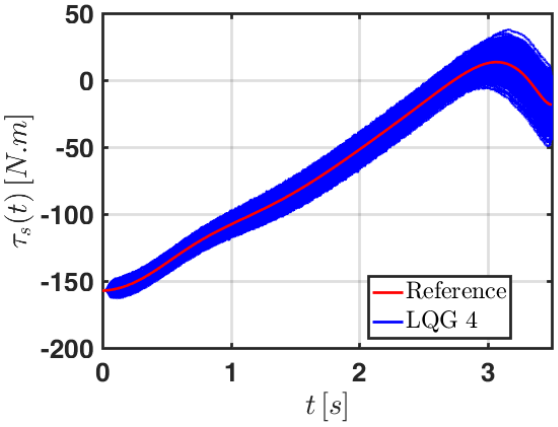

(b) Torque at the shoulders of the user.

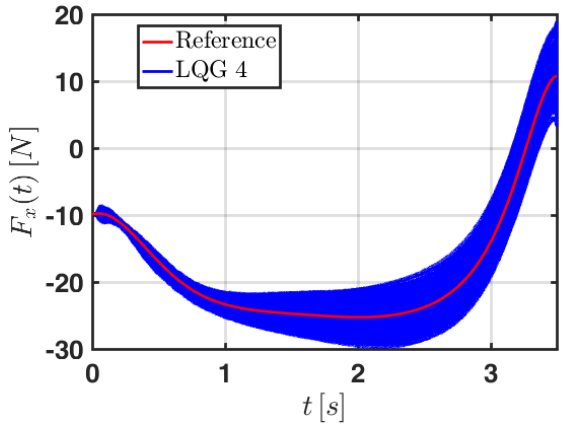

(c) Horizontal force at the shoulders of the user.

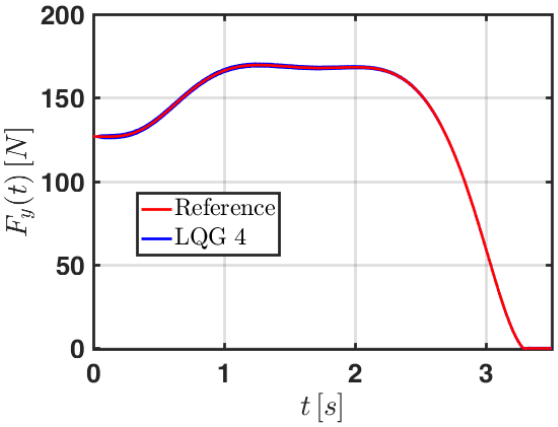

(d) Vertical force at the shoulders of the user.

Figure 6.6: Input trajectories of the three-link robot using the LQG 4 controller with noisy measurement of θ_1, and θ_2 for all $p \in \mathcal{P}_s$ sampled within the bounds in Table 6.2.

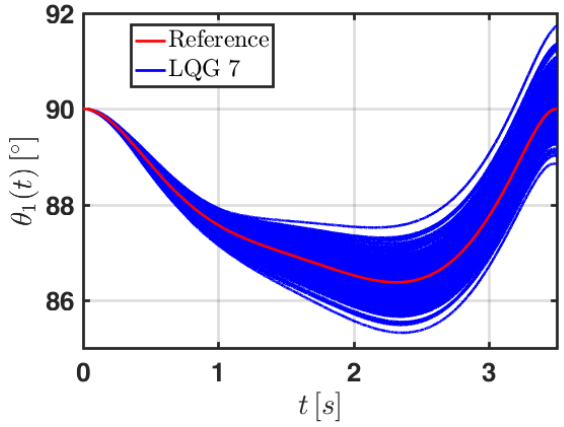

(a) Angular position of link 1 relative to the horizontal.

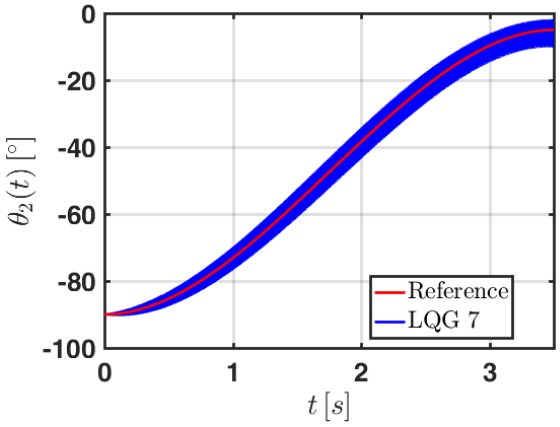

(b) Angular position of link 2 relative to link 1.

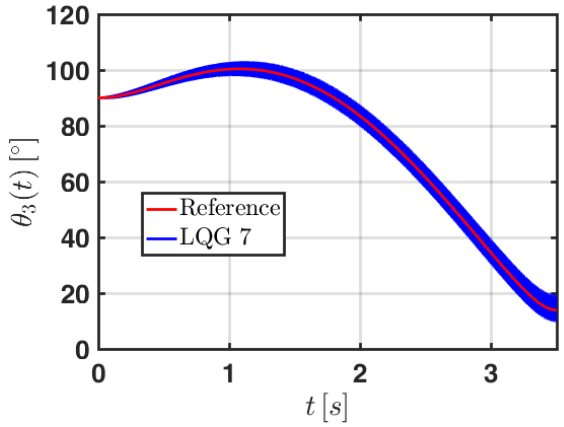

(c) Angular position of link 3 relative to link 2.

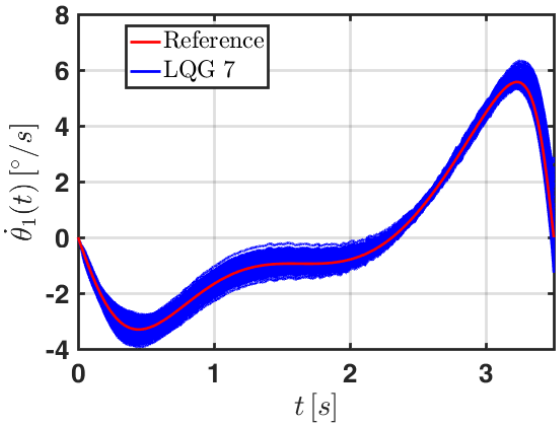

(d) Angular velocity of link 1.

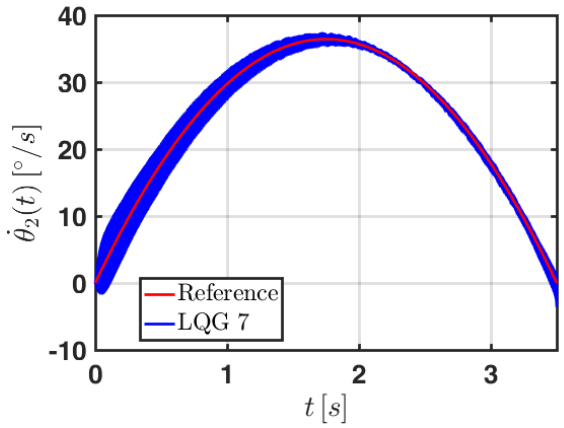

(e) Angular velocity of link 2.

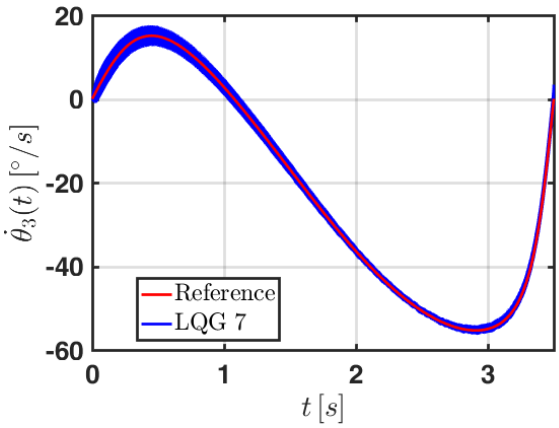

(f) Angular velocity of link 3.

Figure 6.7: State trajectories of the three-link robot using LQG 7 with noisy measurement of θ_1, θ_2, and θ_3 for all $p \in \mathcal{P}_s$ sampled within the bounds in Table 4.1.

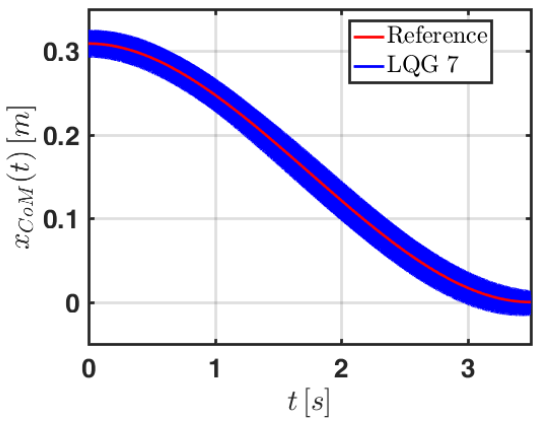

(a) x_{CoM} coordinate of the position of the three-link robot CoM.

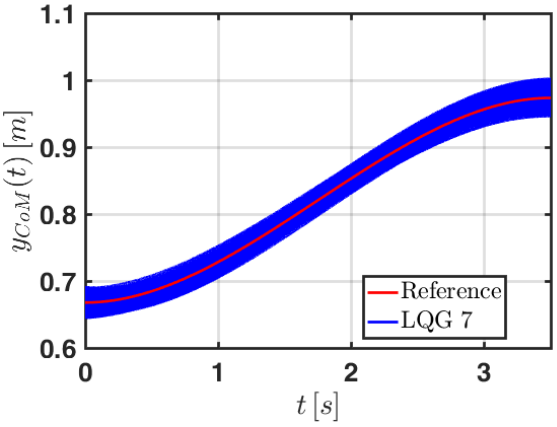

(b) y_{CoM} coordinate of the position of the three-link robot CoM.

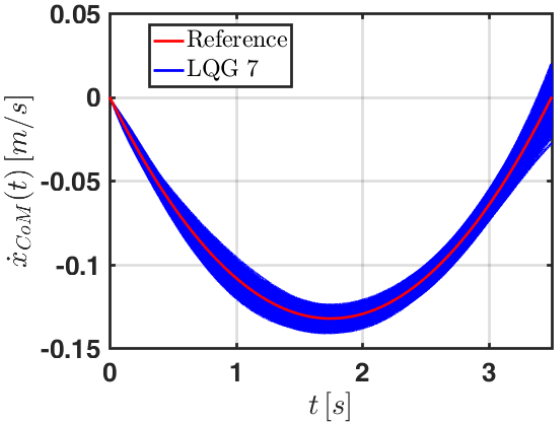

(c) $\dot{x}_{\text{CoM}}$ coordinate of the velocity of the three-link robot CoM.

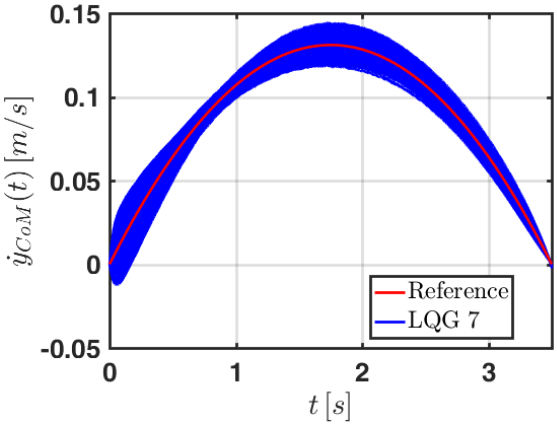

(d) $\dot{y}_{\text{CoM}}$ coordinate of the velocity of the three-link robot CoM.

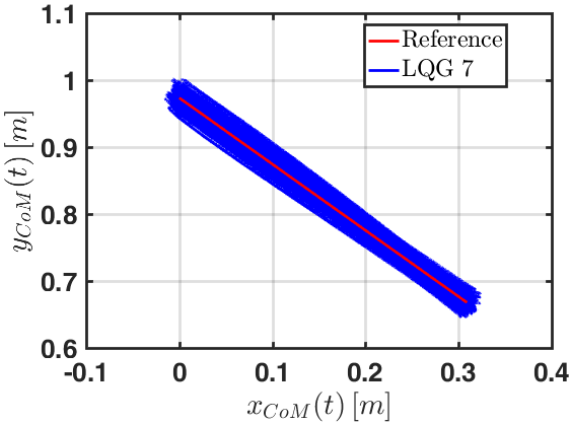

(e) $\dot{x}_{\text{CoM}}$ coordinate of the velocity of the three-link robot CoM.

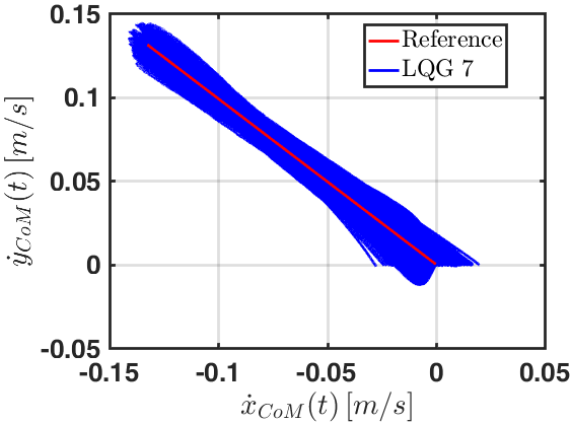

(f) $\dot{y}_{\text{CoM}}$ coordinate of the velocity of the three-link robot CoM.

Figure 6.8: Trajectories of the three-link robot CoM using LQG 7 with noisy measurement of θ_1, θ_2, and θ_3 for all $p \in \mathcal{P}_s$ sampled within the bounds in Table 4.1.

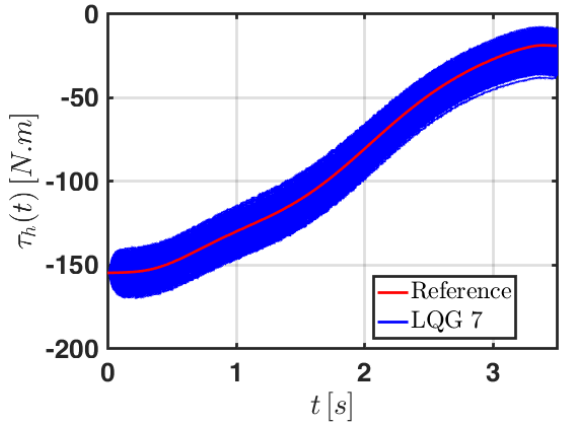

(a) Torque applied at the hips by the PLLO.

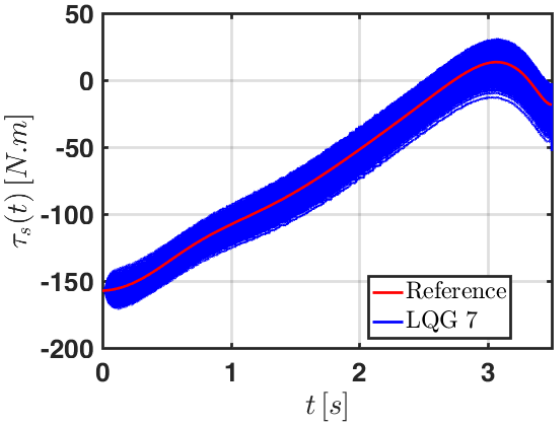

(b) Torque at the shoulders of the user.

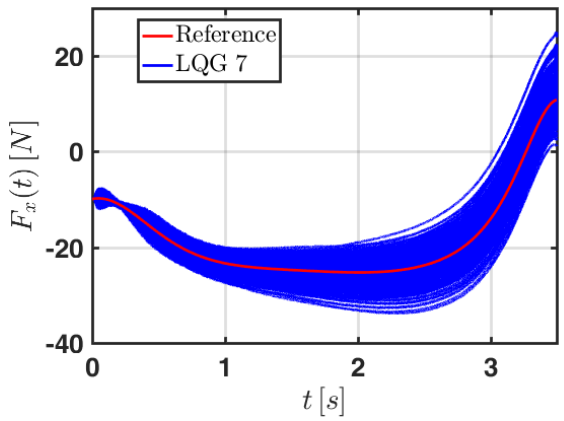

(c) Horizontal force at the shoulders of the user.

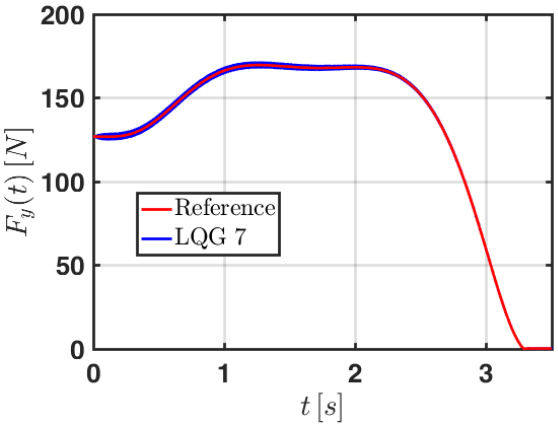

(d) Vertical force at the shoulders of the user.

Figure 6.9: Input trajectories of the three-link robot using LQG 7 with noisy measurement of θ_1, θ_2, and θ_3 for all $p \in \mathcal{P}_s$ sampled within the bounds in Table 4.1.

Chapter 7

Robustness Against Model Uncertainty

The design of the finite time horizon LQR gain $K^{\star}_{\text{LQR}}(t)$ in Section 4.4 is based on the dynamics of the three-link planar robot introduced in Section 2.1. One of the assumptions taken into account for the use of this simplified model is that the position of the neck, and head relative to the torso remain fixed during the STS movement. However, in practice, achieving this behavior requires the active intervention of the neck muscles.

To capture the relative movement of the neck and head with respect to the torso, we add a link to our model with a revolute joint coaxial to the location of an intervertebral joint in the thoracic spine of the user, so that the STS movement of the system is now represented with a four-link planar robot. After making the proper adjustments to the values of the parameters of the four-link robot to make it match the behavior of the three-link robot when the links of the torso, and the neck and head are aligned, we design a finite time horizon LQR controller for a minimally actuated PLLO at the hips to track the STS 1 movement defined in Section 2.5.

The state feedback controller has command over the torque at the hips of the PLLO, the torque at the shoulders of the user, the horizontal and vertical forces at the shoulder, and the torque at the neck. The LQR gain is obtained by using the values of the weights for computing $K^{\star}_{\text{LQR}}(t)$, and its robustness in the presence of parameter uncertainty is assessed through simulation of the four-link robot model in closed-loop with the controller for the same variation of weight and length of the links considered in Section 4.2. Since the good performance observed for tracking STS 1 in Section 4.4 holds despite the dynamics of the fourth link, we claim that the controller chosen with the reachability-based performance metric in (4.23) is robust against model uncertainty.

7.1 Four-link Robot Model

The four-link planar robot with revolute joints coaxial to the ankles, knees, hips, and an intervertebral thoracic joint of the user of a PLLO is shown in Figure 7.1. The feet are assumed to be fixed to the ground and the movement of the limbs is considered to have sagittal symmetry. θ_1 is the angular position of link 1 (shanks) measured from the horizontal, θ_2 is the angular position of link 2 (thighs) relative to link 1, θ_3 is the angular position of link 3 (torso) relative to link 2, and θ_4 is the angular position of link 4 (neck and head) relative to link 3. The system parameters are the masses of the links m_1, m_2, m'_3, and m_4; the moments of inertia about their respective CoMs I_1, I_2, I'_3, and I_4; their lengths l_1, l_2, l_n, and l_4; the distances of their CoMs from the joints l_{c_1}, l_{c_2}, l'_{c_3}, and l_{c_4}; and the distance between the joints of the hips and shoulders l_3. According to the architecture of a minimally actuated PLLO at the hips, the actuators of the orthosis exert the torque τ_h. The torque τ_s, horizontal force F_x, and vertical force F_y aim to capture the inertial and gravitational forces of the arms, as well as the loads applied on the shoulders by the user. The torque applied by the user to move the neck and head is labeled τ_n.

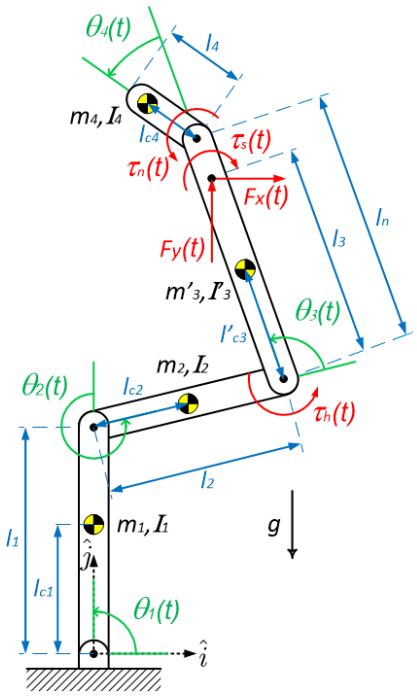

Figure 7.1: Four-link planar robot for modeling PLLOs during a STS movement.

Lumping the parameters of the system in

$$\tilde{p} := \left[m_1;\ m_2;\ m'_3;\ m_4;\ I_1;\ I_2;\ I'_3;\ I_4;\ l_1;\ l_2;\ l_3;\ l_n;\ l_4;\ l_{c_1};\ l_{c_2};\ l'_{c_3};\ l_{c_4}\right] \in \mathbb{R}^{17}, \tag{7.1}$$

we define the coefficients

$$k_{10}(\tilde{p}) := \left(m_1 + m_2 + m_3' + m_4\right)^{-1}, \qquad k_{11}(\tilde{p}) := l_{c_1} m_1 + l_1\left(m_2 + m_3' + m_4\right),$$
$$k_{12}(\tilde{p}) := l_{c_2} m_2 + l_2\left(m_3' + m_4\right), \qquad k_{13}(\tilde{p}) := l_{c_3}' m_3' + l_n m_4, \qquad k_{14}(\tilde{p}) := l_{c_4} m_4,$$

whose explicit dependence with respect to $\tilde{p}$ is omitted onwards for compactness.

The Euler-Lagrange equations of the four-link planar robot in Figure 7.1 were obtained by using the symbolic multibody dynamics package PyDy [28]. In terms of the joint angles $\tilde{\theta} := [\theta_1;\ \theta_2;\ \theta_3;\ \theta_4] \in \mathbb{R}^4$, input $u = \left[\tau_h;\ \tau_s;\ F_x;\ F_y;\ \tau_n\right] \in \mathbb{R}^5$, and $\tilde{p}$ the Euler-Lagrange equations of the four-link planar robot modeling the PLLO are

$$\tilde{M}\left(\tilde{\theta}, \tilde{p}\right) \ddot{\tilde{\theta}} + \tilde{F}\left(\tilde{\theta}, \dot{\tilde{\theta}}, \tilde{p}\right) = \tilde{A}_\tau\left(\tilde{\theta}, \tilde{p}\right) u, \tag{7.2}$$

where $\tilde{M}\left(\tilde{\theta}, \tilde{p}\right) \in \mathbb{R}^{4\times4}$, $\tilde{M}\left(\tilde{\theta}, \tilde{p}\right) \succ 0$ is the symmetric mass matrix of the system, $\tilde{F}\left(\tilde{\theta}, \dot{\tilde{\theta}}, \tilde{p}\right) \in \mathbb{R}^4$ is the vector of energy contributions due to the acceleration of gravity and Coriolis forces, and $\tilde{A}_\tau(\theta, \tilde{p}) \in \mathbb{R}^{4\times5}$ is the generalized force matrix.

The entries of the symmetric mass matrix $\tilde{M}\left(\tilde{\theta}, \tilde{p}\right) \in \mathbb{R}^{4\times4}$ in (7.2) are

$$\begin{aligned}
\tilde{M}_{11} =& I_1 + I_2 + I_3' + I_4 + l_{c_1}^2 m_1 + m_2\left(l_1^2 + 2l_1 l_{c_2} c_2 + l_{c_2}^2\right) \\
&+ m_3'\left(l_1^2 + 2l_1 l_2 c_2 + 2l_1 l_{c_3}' c_{23} + l_2^2 + 2l_2 l_{c_3}' c_3 + \left(l_{c_3}'\right)^2\right) \\
&+ m_4\left(l_1^2 + 2l_1 l_2 c_2 + 2l_1 l_{c_4} c_{234} + 2l_1 l_n c_{23} + l_2^2 + 2l_2 l_{c_4} c_{34} + 2l_2 l_n c_3 + l_{c_4}^2 + 2l_{c_4} l_n c_4 + l_n^2\right) \\
\tilde{M}_{12} =& I_2 + I_3' + I_4 + l_{c_2} m_2\left(l_1 c_2 + l_{c_2}\right) + m_3'\left(l_1 l_2 c_2 + l_1 l_{c_3}' c_{23} + l_2^2 + 2l_2 l_{c_3}' c_3 + \left(l_{c_3}'\right)^2\right) \\
&+ m_4\left(l_1 l_2 c_2 + l_1 l_{c_4} c_{234} + l_1 l_n c_{23} + l_2^2 + 2l_2 l_{c_4} c_{34} + 2l_2 l_n c_3 + l_{c_4}^2 + 2l_{c_4} l_n c_4 + l_n^2\right) \\
\tilde{M}_{13} =& I_3' + I_4 + l_{c_3}' m_3'\left(l_1 c_{23} + l_2 c_3 + l_{c_3}'\right) \\
&+ m_4\left(l_1 l_{c_4} c_{234} + l_1 l_n c_{23} + l_2 l_{c_4} c_{34} + l_2 l_n c_3 + l_{c_4}^2 + 2l_{c_4} l_n c_4 + l_n^2\right) \\
\tilde{M}_{14} =& I_4 + l_{c_4} m_4\left(l_1 c_{234} + l_2 c_{34} + l_{c_4} + l_n c_4\right) \\
\tilde{M}_{22} =& I_2 + I_3' + I_4 + l_{c_2}^2 m_2 + m_3'\left(l_2^2 + 2l_2 l_{c_3}' c_3 + \left(l_{c_3}'\right)^2\right) \\
&+ m_4\left(l_2^2 + 2l_2 l_{c_4} c_{34} + 2l_2 l_n c_3 + l_{c_4}^2 + 2l_{c_4} l_n c_4 + l_n^2\right) \\
\tilde{M}_{23} =& I_3' + I_4 + l_{c_3}' m_3'\left(l_2 c_3 + l_{c_3}'\right) + m_4\left(l_2 l_{c_4} c_{34} + l_2 l_n c_3 + l_{c_4}^2 + 2l_{c_4} l_n c_4 + l_n^2\right) \\
\tilde{M}_{24} =& I_4 + l_{c_4} m_4\left(l_2 c_{34} + l_{c_4} + l_n c_4\right)
\end{aligned}$$

$$
\begin{aligned}
\tilde{M}_{33} =& I_3' + I_4 + \left(l_{c_3}'\right)^2 m_3' + m_4\left(l_{c_4}^2 + 2 l_{c_4} l_n c_4 + l_n^2\right) \\
\tilde{M}_{34} =& I_4 + l_{c_4} m_4 \left(l_{c_4} + l_n c_4\right) \\
\tilde{M}_{44} =& I_4 + l_{c_4}^2 m_4 .
\end{aligned}
$$

The vector of energy contributions due to the acceleration of gravity $g := 9.81\,[m/s^2]$ and Coriolis forces $\tilde{F}\left(\tilde{\theta}, \dot{\tilde{\theta}}, \tilde{p}\right) \in \mathbb{R}^4$ is

$$
\tilde{F}\left(\tilde{\theta}, \dot{\tilde{\theta}}, \tilde{p}\right) = \tilde{\Omega}\left(\tilde{\theta}, \tilde{p}\right) \begin{bmatrix} \dot{\theta}_1^2 \\ \left(\dot{\theta}_1 + \dot{\theta}_2\right)^2 \\ \left(\dot{\theta}_1 + \dot{\theta}_2 + \dot{\theta}_3\right)^2 \\ \left(\dot{\theta}_1 + \dot{\theta}_2 + \dot{\theta}_3 + \dot{\theta}_4\right)^2 \end{bmatrix} + g \begin{bmatrix} k_{11} c_1 + k_{12} c_{12} + k_{13} c_{123} + k_{14} c_{1234} \\ k_{12} c_{12} + k_{13} c_{123} + k_{14} c_{1234} \\ k_{13} c_{123} + k_{14} c_{1234} \\ k_{14} c_{1234} \end{bmatrix},
$$

with $\tilde{\Omega}\left(\tilde{\theta}, \tilde{p}\right) \in \mathbb{R}^{4\times 4}$ defined as

$$
\begin{aligned}
\tilde{\Omega}\left(\tilde{\theta}, \tilde{p}\right) := \begin{bmatrix} l_1\left(k_{12} s_2 + k_{13} s_{23} + k_{14} s_{234}\right) & -k_{12} l_1 s_2 + l_2\left(k_{13} s_3 + k_{14} s_{34}\right) \\ l_1\left(k_{12} s_2 + k_{13} s_{23} + k_{14} s_{234}\right) & l_2\left(k_{13} s_3 + k_{14} s_{34}\right) \\ l_1\left(k_{13} s_{23} + k_{14} s_{234}\right) & l_2\left(k_{13} s_3 + k_{14} s_{34}\right) \\ k_{14} l_1 s_{234} & k_{14} l_2 s_{34} \end{bmatrix} \quad \cdots \\
\begin{bmatrix} -k_{13}\left(l_1 s_{23} + l_2 s_3\right) + k_{14} l_n s_4 & -k_{14}\left(l_1 s_{234} + l_2 s_{34} + l_n s_4\right) \\ -k_{13} l_2 s_3 + k_{14} l_n s_4 & -k_{14}\left(l_2 s_{34} + l_n s_4\right) \\ k_{14} l_n s_4 & -k_{14} l_n s_4 \\ k_{14} l_n s_4 & 0 \end{bmatrix}.
\end{aligned}
$$

The generalized force matrix $\tilde{A}_\tau\left(\tilde{\theta}, \tilde{p}\right) \in \mathbb{R}^{4\times 5}$ is

$$
\tilde{A}_\tau\left(\tilde{\theta}, \tilde{p}\right) = \begin{bmatrix} 0 & -1 & -l_1 s_1 - l_2 s_{12} - l_3 s_{123} & l_1 c_1 + l_2 c_{12} + l_3 c_{123} & 0 \\ 0 & -1 & -l_2 s_{12} - l_3 s_{123} & l_2 c_{12} + l_3 c_{123} & 0 \\ 1 & -1 & -l_3 s_{123} & l_3 c_{123} & 0 \\ 0 & 0 & 0 & 0 & 1 \end{bmatrix}. \tag{7.3}
$$

In order to draw valid comparisons in our study, $\tilde{p}$ must be chosen so that the dynamics of the four-link robot in (7.2) match the dynamics of the three-link robot in (2.2) when the links 3 and 4 in Figure 7.1 are aligned with each other, i.e., when $\theta_4 = 0[^\circ]$, $\dot{\theta}_4 = 0[^\circ/s]$, and $\ddot{\theta}_4 = 0[^\circ/s^2]$. To achieve this behavior we plug the values of the parameters for the three-link robot m_1, m_2, I_1, I_2, l_1, l_2, l_3, l_{c_1}, and l_{c_2} used for (2.1) into (7.1), and then compute m_3', I_3', and l_{c_3}' based on the choice of m_4, I_4, l_{c_4}, l_n, and the values of m_3, I_3, and l_{c_3} used for the three-link robot in Figure 2.1.

From the conservation of mass of the torso, neck, and head, it is clear that m'_3 must satisfy

$$m'_3 = m_3 - m_4. \tag{7.4}$$

To compute l'_{c_3} we rely on the position $[\tilde{x}_{\text{CoM}}; \tilde{y}_{\text{CoM}}] \in \mathbb{R}^2$, and velocity $\left[\dot{\tilde{x}}_{\text{CoM}}; \dot{\tilde{y}}_{\text{CoM}}\right] \in \mathbb{R}^2$ coordinates of the CoM of the four-link robot, relative to the inertial frame $\hat{i}\hat{j}$ in Figure 7.1:

$$\begin{aligned}
\tilde{x}_{\text{CoM}} =& k_{10}\left(k_{11}c_1 + k_{12}c_{12} + k_{13}c_{123} + k_{14}c_{1234}\right), && (7.5)\\
\tilde{y}_{\text{CoM}} =& k_{10}\left(k_{11}s_1 + k_{12}s_{12} + k_{13}s_{123} + k_{14}s_{1234}\right), && (7.6)
\end{aligned}$$

$$\begin{aligned}
\dot{\tilde{x}}_{\text{CoM}} =& -\dot{\theta}_1\tilde{y}_{\text{CoM}} - \dot{\theta}_2 k_{10}\left(k_{12}s_{12} + k_{13}s_{123} + k_{14}s_{1234}\right)\\
&- \dot{\theta}_3 k_{10}\left(k_{13}s_{123} + k_{14}s_{1234}\right) - \dot{\theta}_4 k_{10}k_{14}s_{1234}, && (7.7)\\
\dot{\tilde{y}}_{\text{CoM}} =& \dot{\theta}_1\tilde{x}_{\text{CoM}} + \dot{\theta}_2 k_{10}\left(k_{12}c_{12} + k_{13}c_{123} + k_{14}c_{1234}\right)\\
&+ \dot{\theta}_3 k_{10}\left(k_{13}c_{123} + k_{14}c_{1234}\right) + \dot{\theta}_4 k_{10}k_{14}c_{1234}, && (7.8)
\end{aligned}$$

When $\theta_4 = 0[^\circ]$ the horizontal position of the CoM in (7.5) becomes

$$\begin{aligned}
\tilde{x}_{\text{CoM}} &= \frac{\left(l_{c_1}m_1 + l_1\left(m_2 + m'_3 + m_4\right)\right)c_1 + \left(l_{c_2}m_2 + l_2\left(m'_3 + m_4\right)\right)c_{12} + \left(l'_{c_3}m'_3 + l_n m_4\right)c_{123} + l_{c_4}m_4 c_{1234}}{m_1 + m_2 + m'_3 + m_4}\\
&= \frac{\left(l_{c_1}m_1 + l_1\left(m_2 + m_3\right)\right)c_1 + \left(l_{c_2}m_2 + l_2 m_3\right)c_{12} + \left(l'_{c_3}m'_3 + l_n m_4 + l_{c_4}m_4\right)c_{123}}{m_1 + m_2 + m_3}\\
&= k_0\left(k_1 c_1 + k_2 c_{12} + \left(l'_{c_3}m'_3 + \left(l_n + l_{c_4}\right)m_4\right)c_{123}\right), && (7.9)
\end{aligned}$$

and to make it equal to the expression for the horizontal position of the CoM of the three-link robot in (2.5), the distance from the joint of the hips to the CoM of the link 3 in Figure 7.1 has to be

$$l'_{c_3} = \frac{m_3 l_{c_3} - \left(l_n + l_{c_4}\right)m_4}{m'_3}, \tag{7.10}$$

which also guarantees that $\tilde{y}_{\text{CoM}} = y_{\text{CoM}}$, $\dot{\tilde{x}}_{\text{CoM}} = \dot{x}_{\text{CoM}}$, and $\dot{\tilde{y}}_{\text{CoM}} = \dot{y}_{\text{CoM}}$ when $\theta_4 = 0[^\circ]$, and $\dot{\theta}_4 = 0[^\circ/s]$.

Once that we know the value for l'_{c_3}, the remaining moment of inertia in $\tilde{p}$ is computed from the parallel-axis theorem as

$$I'_3 = I_3 - I_4 - m_4\left(l_n + l_{c_4} - l'_{c_3}\right)^2. \tag{7.11}$$

It can be verified that plugging (7.4), (7.10), (7.11), and setting $\theta_4 = 0[^\circ]$, $\dot{\theta}_4 = 0[^\circ/s]$, and $\ddot{\theta}_4 = 0\left[^\circ/s^2\right]$ into (7.2) make the first three equations in (7.2) match the dynamics of the three-link robot in (2.2).

7.2 Reference Trajectories for the STS Movement of the Four-link Robot

Let $\hat{\theta}_4(t) := 0[°]$, $\dot{\hat{\theta}}_4(t) := 0[°/s]$, and $\ddot{\hat{\theta}}_4(t) := 0\left[°/s^2\right]$ for all $t \in \left[t_0, t_f\right]$. Using the reference trajectories for STS movements $\hat{\theta}(t)$, $\dot{\hat{\theta}}(t)$, and $\ddot{\hat{\theta}}(t)$ obtained in Section 2.4, the reference trajectories in the joint space of the four-link robot in Figure 7.1 are

$$\hat{\bar{\theta}}(t) := \left[\hat{\theta}(t); \hat{\theta}_4(t)\right] \in \mathbb{R}^4, \quad \dot{\hat{\bar{\theta}}}(t) := \left[\dot{\hat{\theta}}(t); \dot{\hat{\theta}}_4(t)\right] \in \mathbb{R}^4, \quad \ddot{\hat{\bar{\theta}}}(t) := \left[\ddot{\hat{\theta}}(t); \ddot{\hat{\theta}}_4(t)\right] \in \mathbb{R}^4. \tag{7.12}$$

Since we assume that the torque applied by the user of the PLLO at the thoracic intervertebral joint aims to keep the neck, and head aligned with the torso during the STS movement, to compute the reference trajectory $\hat{\tau}_n(t) \in \mathbb{R}$ we treat the links 3, and 4 as a single rigid body, and draw the free-body diagram for writing the Newton-Euler equations of motion that allow to find the internal forces F_{n_x}, F_{n_y}, and torque τ_n across the intervertebral joint, as it is shown in Figure 7.2.

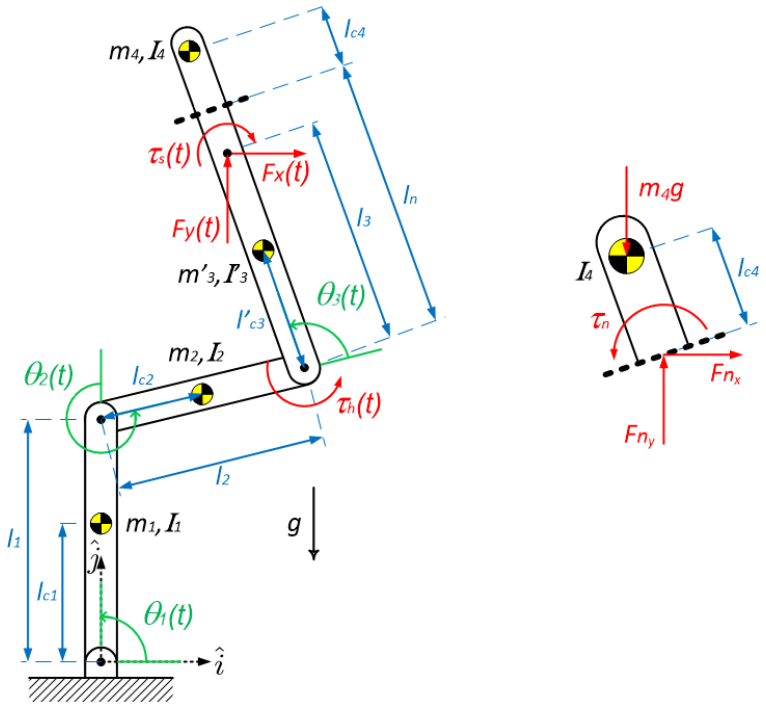

Figure 7.2: Robot model with the torso, neck, and head as a single rigid link and a cut across the thoracic intervertebral joint at a distance l_n from the hips (left). Free-body diagram to calculate the internal loads F_{n_x}, F_{n_y}, and τ_n , at the location of the intervertebral joint (right).

The force equation for the free-body diagram in Figure 7.2 is

$$\begin{bmatrix} F_{n_x} \\ F_{n_y} \end{bmatrix} = \begin{bmatrix} 0 \\ m_4 g \end{bmatrix} + m_4 a_{c_4},$$

where the acceleration of the CoM of the fourth link in the inertial frame $\hat{i}\hat{j}$ is

$$a_{c_4} = l_1 \begin{bmatrix} -\dot{\theta}_1^2 & -\ddot{\theta}_1 \\ \ddot{\theta}_1 & -\dot{\theta}_1^2 \end{bmatrix} \begin{bmatrix} c_1 \\ s_1 \end{bmatrix} + l_2 \begin{bmatrix} -\left(\dot{\theta}_1+\dot{\theta}_2\right)^2 & -\left(\ddot{\theta}_1+\ddot{\theta}_2\right) \\ \ddot{\theta}_1+\ddot{\theta}_2 & -\left(\dot{\theta}_1+\dot{\theta}_2\right)^2 \end{bmatrix} \begin{bmatrix} c_{12} \\ s_{12} \end{bmatrix}$$
$$+ \left(l_n + l_{c_4}\right) \begin{bmatrix} -\left(\dot{\theta}_1+\dot{\theta}_2+\dot{\theta}_3\right)^2 & -\left(\ddot{\theta}_1+\ddot{\theta}_2+\ddot{\theta}_3\right) \\ \ddot{\theta}_1+\ddot{\theta}_2+\ddot{\theta}_3 & -\left(\dot{\theta}_1+\dot{\theta}_2+\dot{\theta}_3\right)^2 \end{bmatrix} \begin{bmatrix} c_{123} \\ s_{123} \end{bmatrix}.$$

Hence, the internal forces across the thoracic intervertebral joint are

$$F_{n_x} = -m_4 \left(\begin{bmatrix} l_1 c_1 \\ l_2 c_{12} \\ \left(l_n + l_{c_4}\right) c_{123} \end{bmatrix}^\top \begin{bmatrix} \dot{\theta}_1^2 \\ \left(\dot{\theta}_1+\dot{\theta}_2\right)^2 \\ \left(\dot{\theta}_1+\dot{\theta}_2+\dot{\theta}_3\right)^2 \end{bmatrix} + \begin{bmatrix} l_1 s_1 \\ l_2 s_{12} \\ \left(l_n + l_{c_4}\right) s_{123} \end{bmatrix}^\top \begin{bmatrix} \ddot{\theta}_1 \\ \ddot{\theta}_1+\ddot{\theta}_2 \\ \ddot{\theta}_1+\ddot{\theta}_2+\ddot{\theta}_3 \end{bmatrix} \right) \tag{7.13}$$

$$F_{n_y} = m_4 \left(\mathrm{g} - \begin{bmatrix} l_1 s_1 \\ l_2 s_{12} \\ \left(l_n + l_{c_4}\right) s_{123} \end{bmatrix}^\top \begin{bmatrix} \dot{\theta}_1^2 \\ \left(\dot{\theta}_1+\dot{\theta}_2\right)^2 \\ \left(\dot{\theta}_1+\dot{\theta}_2+\dot{\theta}_3\right)^2 \end{bmatrix} + \begin{bmatrix} l_1 c_1 \\ l_2 c_{12} \\ \left(l_n + l_{c_4}\right) c_{123} \end{bmatrix}^\top \begin{bmatrix} \ddot{\theta}_1 \\ \ddot{\theta}_1+\ddot{\theta}_2 \\ \ddot{\theta}_1+\ddot{\theta}_2+\ddot{\theta}_3 \end{bmatrix} \right). \tag{7.14}$$

From the moment equation for the free-body diagram in Figure 7.2 we have

$$\tau_n = I_4 \left(\ddot{\theta}_1+\ddot{\theta}_2+\ddot{\theta}_3\right) - \begin{bmatrix} -l_{c_4} c_{123} \\ -l_{c_4} s_{123} \end{bmatrix} \times \begin{bmatrix} F_{n_x} \\ F_{n_y} \end{bmatrix} = I_4 \left(\ddot{\theta}_1+\ddot{\theta}_2+\ddot{\theta}_3\right) + l_{c_4} c_{123} F_{n_y} - l_{c_4} s_{123} F_{n_x}. \tag{7.15}$$

Plugging (7.13), and (7.14) into (7.15) we obtain

$$\begin{aligned} \tau_n &= I_4 \left(\ddot{\theta}_1+\ddot{\theta}_2+\ddot{\theta}_3\right) + l_{c_4} m_4 \mathrm{g} c_{123} \\ &\quad + l_{c_4} m_4 c_{123} \left(\begin{bmatrix} l_1 c_1 \\ l_2 c_{12} \\ \left(l_n + l_{c_4}\right) c_{123} \end{bmatrix}^\top \begin{bmatrix} \ddot{\theta}_1 \\ \ddot{\theta}_1+\ddot{\theta}_2 \\ \ddot{\theta}_1+\ddot{\theta}_2+\ddot{\theta}_3 \end{bmatrix} - \begin{bmatrix} l_1 s_1 \\ l_2 s_{12} \\ \left(l_n + l_{c_4}\right) s_{123} \end{bmatrix}^\top \begin{bmatrix} \dot{\theta}_1^2 \\ \left(\dot{\theta}_1+\dot{\theta}_2\right)^2 \\ \left(\dot{\theta}_1+\dot{\theta}_2+\dot{\theta}_3\right)^2 \end{bmatrix} \right) \\ &\quad + l_{c_4} m_4 s_{123} \left(\begin{bmatrix} l_1 s_1 \\ l_2 s_{12} \\ \left(l_n + l_{c_4}\right) s_{123} \end{bmatrix}^\top \begin{bmatrix} \ddot{\theta}_1 \\ \ddot{\theta}_1+\ddot{\theta}_2 \\ \ddot{\theta}_1+\ddot{\theta}_2+\ddot{\theta}_3 \end{bmatrix} + \begin{bmatrix} l_1 c_1 \\ l_2 c_{12} \\ \left(l_n + l_{c_4}\right) c_{123} \end{bmatrix}^\top \begin{bmatrix} \dot{\theta}_1^2 \\ \left(\dot{\theta}_1+\dot{\theta}_2\right)^2 \\ \left(\dot{\theta}_1+\dot{\theta}_2+\dot{\theta}_3\right)^2 \end{bmatrix} \right) \\ &=: \varrho\left(\theta, \dot{\theta}, \ddot{\theta}, \tilde{p}\right). \end{aligned}$$

Therefore, the reference trajectory for the torque applied to the neck by the user during a STS movement is computed as

$$\hat{\tau}_n(t) = \varrho\left(\hat{\theta}(t), \dot{\hat{\theta}}(t), \ddot{\hat{\theta}}(t), \hat{\tilde{p}}\right) \tag{7.16}$$

for all $t \in \left[t_0, t_f\right]$.

Using the input trajectories from Section 2.4, the input reference trajectory for the four-link robot is

$$\hat{\tilde{u}}(t) := \left[\hat{\tau}_h(t); \hat{\tau}_s(t); \hat{F}_x(t); \hat{F}_y(t); \hat{\tau}_n(t)\right] \in \mathbb{R}^5. \tag{7.17}$$

7.3 Simulation of the Four-link Robot with Finite Time Horizon LQR Control Under Parameter Uncertainty

Defining $\tilde{x} := \left[\tilde{\theta}; \dot{\tilde{\theta}}\right] \in \mathbb{R}^8$, the first order dynamics of the four-link planar robot in Figure 7.1 are

$$\begin{aligned}\dot{\tilde{x}}(t) &= \begin{bmatrix} \dot{\tilde{\theta}}(t) \\ \tilde{M}^{-1}\left(\tilde{\theta}(t), \tilde{p}\right)\left(\tilde{A}_\tau\left(\tilde{\theta}(t), \tilde{p}\right) u(t) - \tilde{F}\left(\tilde{\theta}(t), \dot{\tilde{\theta}}(t), \tilde{p}\right)\right) \end{bmatrix} \\ &=: \tilde{f}\left(\tilde{x}(t), \tilde{p}, u(t)\right). \end{aligned} \tag{7.18}$$

Next we linearize (7.18) to design a finite time horizon LQR controller for tracking the reference state trajectory $\hat{\tilde{x}}(t) := \left[\hat{\tilde{\theta}}(t), \dot{\hat{\tilde{\theta}}}(t)\right]$. The state deviation variable $\tilde{\delta}_x(t) := \tilde{x}(t) - \hat{\tilde{x}}(t)$ satisfies

$$\dot{\tilde{\delta}}_x(t) = \tilde{f}\left(\tilde{x}(t), \tilde{p}, u(t)\right) - \tilde{f}\left(\hat{\tilde{x}}(t), \hat{\tilde{p}}, \hat{\tilde{u}}(t)\right),$$

which can be approximated with a first order Taylor series expansion of $\tilde{f}\left(\tilde{x}(t), \tilde{p}, u(t)\right)$ about $\hat{\tilde{x}}(t)$, nominal parameter $\hat{\tilde{p}}$, and reference input trajectory $\hat{\tilde{u}}(t)$:

$$\begin{aligned}\dot{\tilde{\delta}}_x(t) \approx{}& \left.\frac{\partial \tilde{f}(\tilde{x}, \tilde{p}, u)}{\partial \tilde{x}}\right|_{\substack{\tilde{x}=\hat{\tilde{x}}(t) \\ \tilde{p}=\hat{\tilde{p}} \\ u=\hat{\tilde{u}}(t)}} \left(\tilde{x}(t) - \hat{\tilde{x}}(t)\right) + \left.\frac{\partial \tilde{f}(\tilde{x}, \tilde{p}, u)}{\partial \tilde{p}}\right|_{\substack{\tilde{x}=\hat{\tilde{x}}(t) \\ \tilde{p}=\hat{\tilde{p}} \\ u=\hat{\tilde{u}}(t)}} \left(\tilde{p} - \hat{\tilde{p}}\right) \\ &+ \left.\frac{\partial \tilde{f}(\tilde{x}, \tilde{p}, u)}{\partial u}\right|_{\substack{\tilde{x}=\hat{\tilde{x}}(t) \\ \tilde{p}=\hat{\tilde{p}} \\ u=\hat{\tilde{u}}(t)}} \left(u(t) - \hat{\tilde{u}}(t)\right) \\ =:{}& \tilde{A}(t)\tilde{\delta}_x(t) + \tilde{B}_1(t)\tilde{\delta}_p + \tilde{B}_2(t)\tilde{\delta}_u(t). \end{aligned} \tag{7.19}$$

From [34], for unconstrained $\tilde{\delta}_u(t)$, symmetric matrices $\tilde{Q}, \tilde{S} \succeq 0$, and $\tilde{R} \succ 0$, the optimal control of the stabilizable linear time-varying system in (7.19) with quadratic cost

$$\tilde{J}_{\text{LQR}} = \frac{1}{2}\tilde{\delta}_x^\top\left(t_f\right)\tilde{S}\tilde{\delta}_x\left(t_f\right) + \frac{1}{2}\int_{t_0}^{t_f}\left(\tilde{\delta}_x^\top(t)\tilde{Q}\tilde{\delta}_x(t) + \tilde{\delta}_u^\top(t)\tilde{R}\tilde{\delta}_u(t)\right)dt \tag{7.20}$$

exists, and is unique, given by the time-varying formula

$$\begin{aligned}\tilde{\delta}_u(t) &= -\tilde{R}^{-1}\tilde{B}_2^\top(t)\tilde{P}(t)\tilde{\delta}_x(t) \\ &=: -\tilde{K}_{\text{LQR}}(t)\tilde{\delta}_x(t), \end{aligned} \tag{7.21}$$

where $\tilde{P}(t) \in \mathbb{R}^{8\times 8}$ is the solution of the Riccati matrix differential equation

$$\dot{\tilde{P}}(t) = -\tilde{P}(t)\tilde{A}(t) - \tilde{A}^\top(t)\tilde{P}(t) + \tilde{P}(t)\tilde{B}_2(t)\tilde{R}^{-1}\tilde{B}_2^\top(t)\tilde{P}(t) - \tilde{Q}, \tag{7.22}$$

with the boundary condition $\tilde{P}\left(t_f\right) = \tilde{S}$.

The nonlinear dynamics of the four-link robot under state feedback control with the time-varying matrix gain $\tilde{K}_{\text{LQR}}(t) \in \mathbb{R}^{5\times 8}$, become

$$\dot{\tilde{x}}(t) = \tilde{f}\left(\tilde{x}(t), \tilde{p}, \hat{\tilde{u}}(t) - \tilde{K}_{\text{LQR}}(t)\left(\tilde{x}(t) - \hat{\tilde{x}}(t)\right)\right). \tag{7.23}$$

Using the nominal parameter values of the three-link planar robot in (2.23), anthropometric data from [45] for a subject with total body mass of 50 [kg] and 1.75 [m] height, and the expressions in (7.4), (7.10), and (7.11), the nominal values for the parameters of the four-link robot are

$$\begin{aligned}\hat{\tilde{p}} := [&9.68\,[\text{kg}];\ 12.59\,[\text{kg}];\ 40.52\,[\text{kg}];\ 4.05\,[\text{kg}];\ldots\\ &1.16\left[\text{kg}\cdot\text{m}^2\right];\ 0.52\left[\text{kg}\cdot\text{m}^2\right];\ 1.86\left[\text{kg}\cdot\text{m}^2\right];\ 0.03\left[\text{kg}\cdot\text{m}^2\right];\ldots\\ &0.53\,[\text{m}];\ 0.41\,[\text{m}];\ 0.52\,[\text{m}];0.58\,[\text{m}];0.22\,[\text{m}];0.27\,[\text{m}];\ 0.20\,[\text{m}];\ 0.22\,[\text{m}];\ 0.05\,[\text{m}]].\end{aligned}$$

The trajectories $\hat{\tilde{x}}(t)$, and $\hat{\tilde{u}}(t)$ for computing the LTV system in (7.19) are obtained by plugging the references for STS 1 presented in Section 2.5 into (7.12), (7.16), and (7.17).

As we look to retain the robust behavior of the PLLO to track the STS 1 movement in the presence of parameter uncertainty achieved with the optimal weights in (4.26), we fix the corresponding entries of $\tilde{Q}, \tilde{S} \in \mathbb{R}^{8\times 8}$, and $\tilde{R} \in \mathbb{R}^{5\times 5}$ in (7.20) to the same values, so that

$$\begin{aligned}\tilde{Q} &= \text{diag}([80,\ 95,\ 95,\ \tilde{q}_1,\ 68,\ 90,\ 83,\ \tilde{q}_2]),\\ \tilde{R} &= \text{diag}\left(\left[1\times 10^{-3},\ 2\times 10^{-4},\ 6\times 10^{-4},\ 4.4\times 10^{-3},\ \tilde{r}\right]\right),\\ \tilde{S} &= \text{diag}([30,\ 37,\ 19,\ \tilde{s}_1,\ 29,\ 92,\ 82,\ \tilde{s}_2]).\end{aligned}$$

For tuning the weights $\tilde{q}_1, \tilde{q}_2, \tilde{r}, \tilde{s}_1, \tilde{s}_2 \in \mathbb{R}$ we use a Latin Hypercube of a 1000 experiments in 5 variables to randomly sample their values within the intervals $\tilde{q}_1, \tilde{q}_2, \tilde{s}_1, \tilde{s}_2 \in [0, 100]$, and $\tilde{r} \in \left[1\times 10^{-4}, 1\times 10^{-2}\right]$. With the tools in [37] we solve the Riccati matrix differential equation in (7.22) for each one of the thousand triplets of $\tilde{Q}$, $\tilde{R}$, $\tilde{S}$, compute their corresponding LQR gains in (7.21), and simulate the system in (7.23) setting $\tilde{p} = \hat{\tilde{p}}$. Using a node in the Savio cluster with 28 cores at 2.4[GHz] running Matlab Parallel Toolbox, the simulations are completed in 4[h]. The triplet of matrix weights that minimize $|\tau_n(t)|$ over $t \in [0, 3.5]$ [s] among all simulations are

$$\begin{aligned}\tilde{Q}^* &= \text{diag}([80,\ 95,\ 95,\ 66.28,\ 68,\ 90,\ 83,\ 23.83]),\\ \tilde{R}^* &= \text{diag}\left(\left[1\times 10^{-3},\ 2\times 10^{-4},\ 6\times 10^{-4},\ 4.4\times 10^{-3},\ 4.4\times 10^{-3}\right]\right),\\ \tilde{S}^* &= \text{diag}\left(\left[30,\ 37,\ 19,\ 83,\ 29,\ 92,\ 82,\ 7.2\times 10^{-2}\right]\right).\end{aligned} \tag{7.24}$$

We denote the LQR gain associated with these weights as $\tilde{K}^*_{\text{LQR}}(t)$.

To evaluate the robustness of the finite time horizon LQR controller for tracking STS 1 in the presence of parameter uncertainty we take 500 values of $\hat{\tilde{p}}$ within the bounds $\left[\underline{\hat{\tilde{p}}}, \overline{\hat{\tilde{p}}}\right] \subseteq \mathbb{R}^{17}$ in Table 7.1 by Latin hypercube sampling, and simulate the closed-loop system in (7.23) setting

$\tilde{K}_{\text{LQR}}(t) = \tilde{K}^{*}_{\text{LQR}}(t)$ for each of the sampled values of $\tilde{p}$ starting from rest, with the initial condition $\tilde{\theta}(0) = [90[^\circ]; -90[^\circ]; 90[^\circ]; 0[^\circ]]$. Using a node in the Savio cluster with 28 cores at 2.4[GHz] running Matlab Parallel Toolbox the simulations are completed in 1[h]. The trajectories obtained for the different values of $\tilde{p}$ are shown in blue in Figures 7.3 to 7.6, while the reference trajectories for the STS 1 movement are in red.

Table 7.1: Bounds for the parameter uncertainty of the four-link robot for a fluctuation of ±5% in the nominal weight of the user, and a variation of ±1[cm] in the nominal lengths of the links

Link	m_i [kg]	I_i $\left[\text{kg}\cdot\text{m}^2\right]$	l_i [m]	l_{ci} [m]	l_n [m]
1	[9.2, 10.2]	[1.10, 1.21]	[0.52, 0.54]	[0.23, 0.30]	-
2	[11.9, 13.2]	[0.49, 0.54]	[0.40, 0.42]	[0.18, 0.23]	-
3	[38.5, 42.5]	[1.73, 1.92]	[0.51, 0.53]	[0.21, 0.24]	[0.57, 0.59]
4	[3.85, 4.25]	[0.02, 0.03]	[0.21, 0.23]	[0.04, 0.05]	-

Despite the mismatch of $\tilde{p}$ from its nominal value $\hat{\tilde{p}}$, we can tell from Figures 7.3d and 7.4d that the movement of link 4 relative to link 3 is negligible with the feedback action of $\tilde{K}^{*}_{\text{LQR}}(t)$, this is achieved keeping the absolute value of the torque applied at the neck in Figure 7.6e well below the maximum of 836 [N.m] reported among the human subjects in [52], which leads to believe that the user will indeed be able to generate a set of muscle actions to provide the torque commanded by the LQR controller at the neck. Furthermore, since the excellent properties observed for tracking the STS 1 reference trajectories in Section 4.4 also hold for the state, position and velocity of the CoM, and input of the four-link robot model in Figure 7.1, we can conclude that, to the extend of this study, the optimal controller $K^{\star}_{\text{LQR}}(t)$ is robust to the model uncertainty derived from neglecting the movement of the neck and head relative to the torso during its design stage.

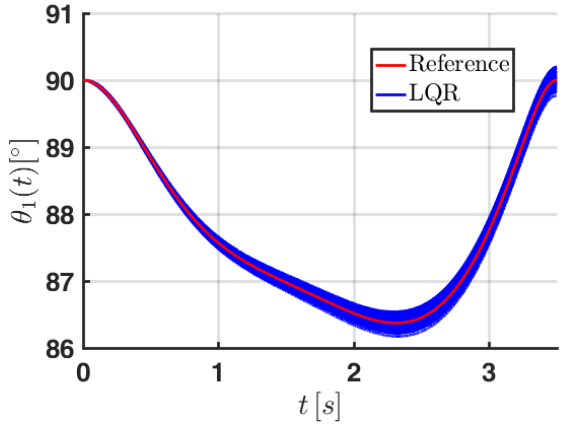

(a) Angular position of link 1 relative to the horizontal.

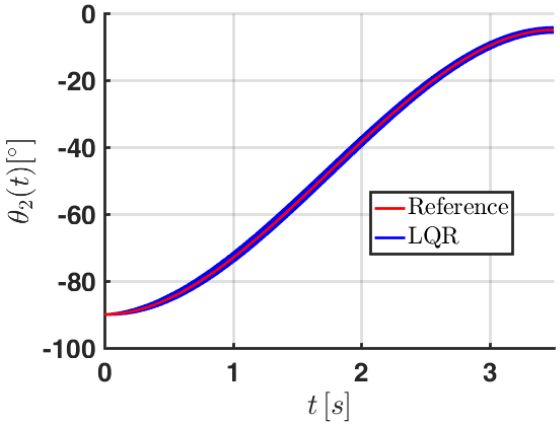

(b) Angular position of link 2 relative to link 1.

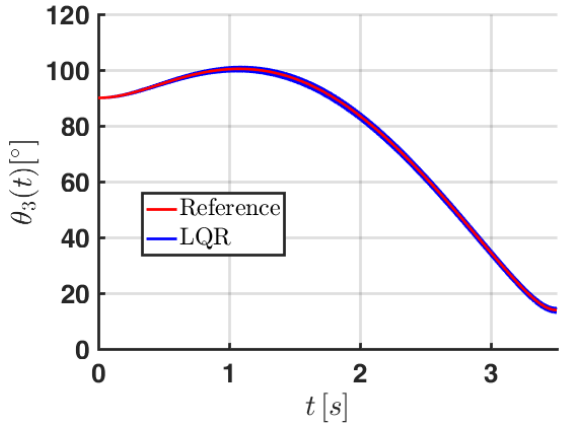

(c) Angular position of link 3 relative to link 2.

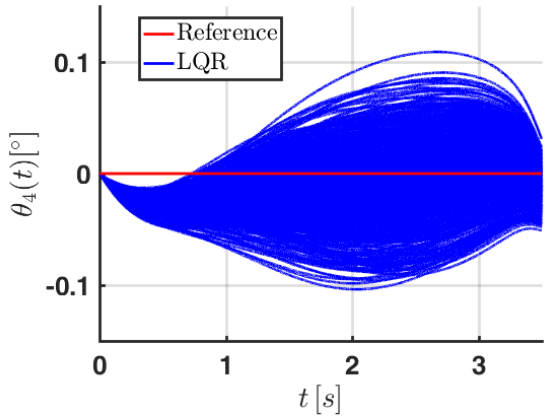

(d) Angular position of link 4 relative to link 3.

Figure 7.3: Angular positions of the links of the four-link robot under finite time horizon LQR control, performing STS 1 in the presence of parameter uncertainty.

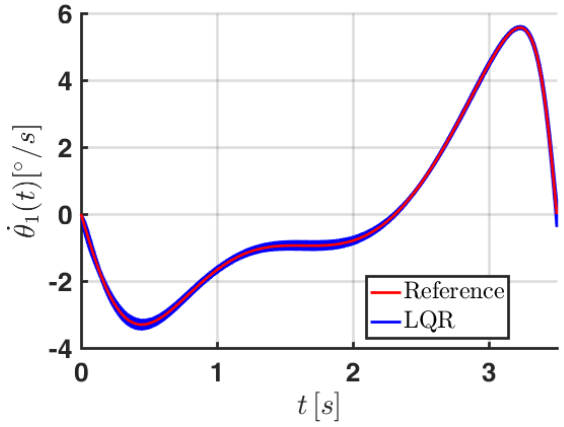

(a) Angular velocity of link 1.

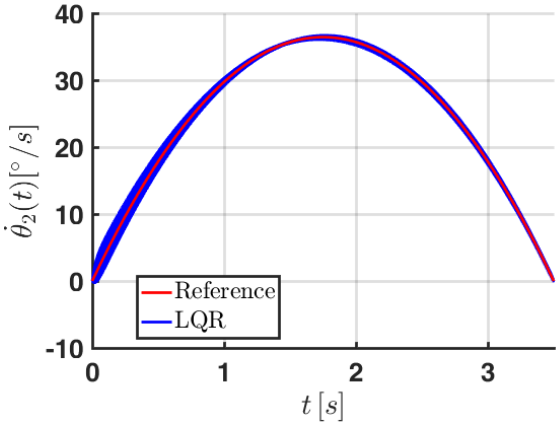

(b) Angular velocity of link 2.

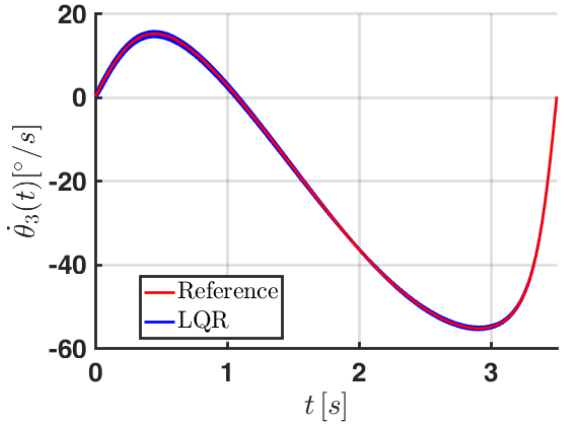

(c) Angular velocity of link 3.

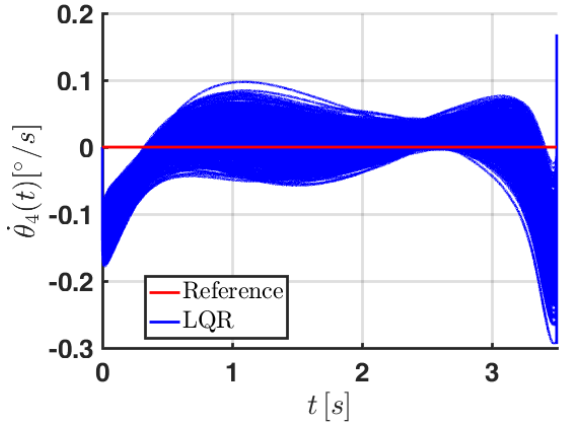

(d) Angular velocity of link 4.

Figure 7.4: Angular velocities of the links of the four-link robot under finite time horizon LQR control performing STS 1 in the presence of parameter uncertainty.

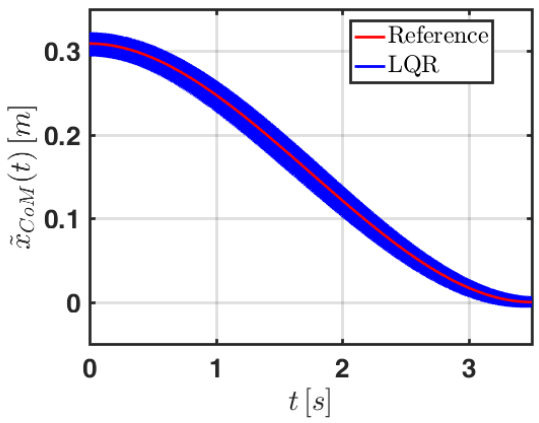

(a) Horizontal position of the four-link robot CoM.

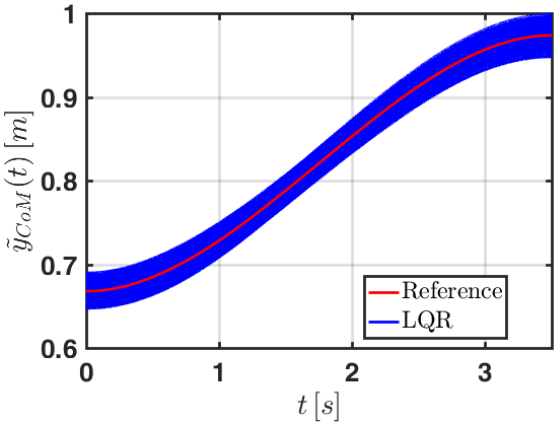

(b) Vertical position of the four-link robot CoM.

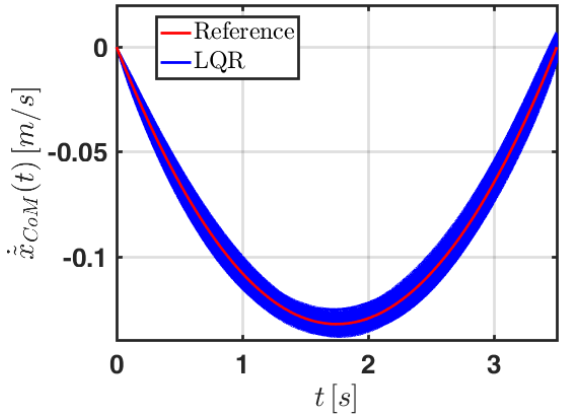

(c) Horizontal velocity of the four-link robot CoM.

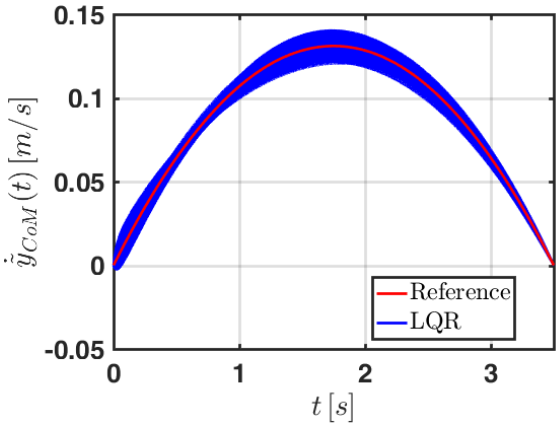

(d) Vertical velocity of the four-link robot CoM.

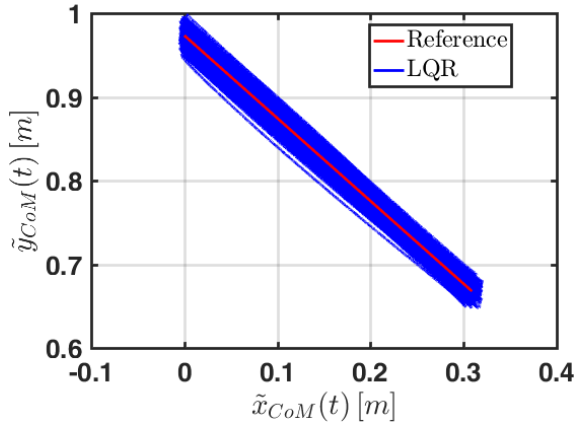

(e) Position of the CoM of the four-link robot.

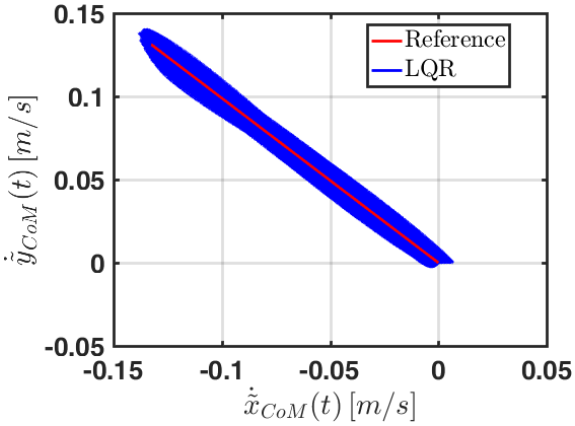

(f) Velocity of the CoM of the four-link robot.

Figure 7.5: Trajectories of the CoM of the four-link robot under finite time horizon LQR control performing STS 1 in the presence of parameter uncertainty.

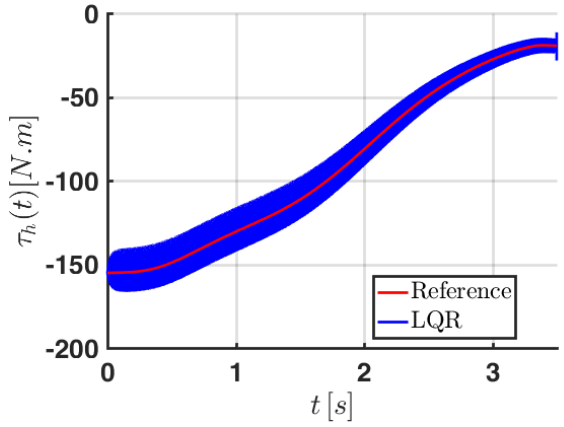

(a) Torque at the hips.

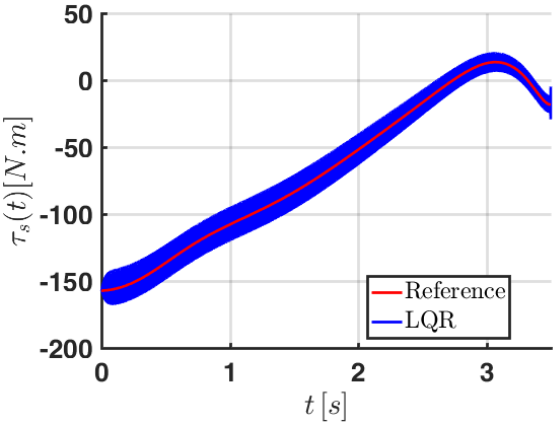

(b) Torque at the shoulders.

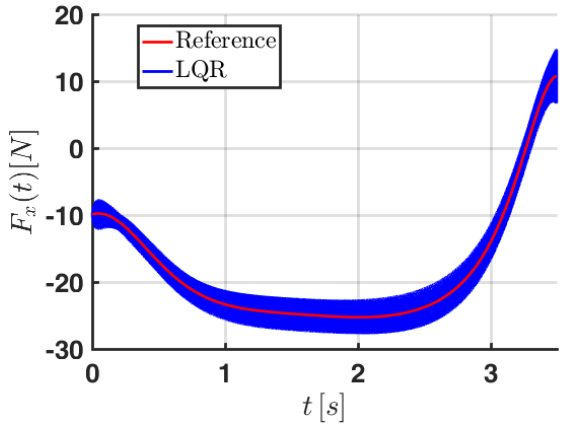

(c) Horizontal force at the shoulders.

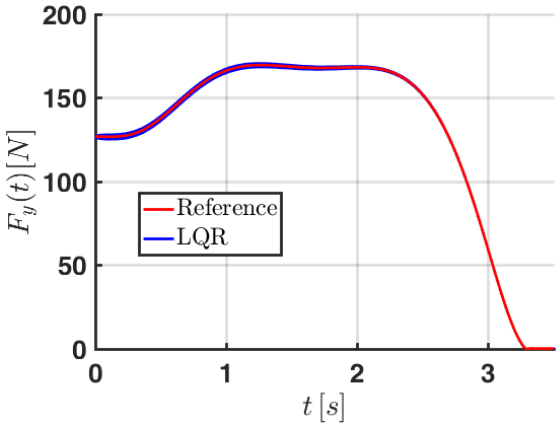

(d) Vertical force at the shoulders.

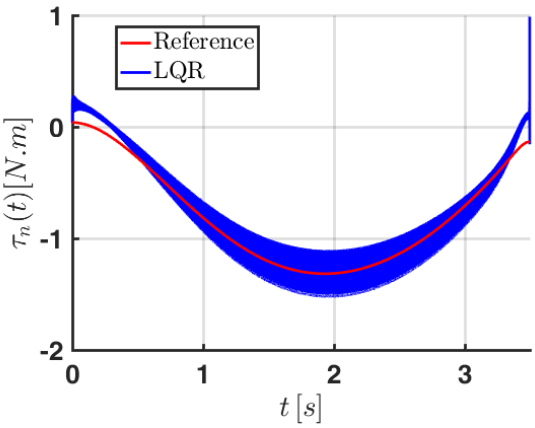

(e) Torque applied at the neck.

Figure 7.6: Input trajectories of the four-link robot under finite time horizon LQR control performing STS 1 in the presence of parameter uncertainty.

Chapter 8

Conclusions

Our motion planning strategy shows that it is possible to obtain biomechanically sound STS movements based on desired trajectories for the CoM of a three-link planar robot modeling the PLLO and the user. This task reduces to only choosing initial and final points with zero slope boundary conditions for the polynomials in time used to interpolate the trajectories. The advantage of the strategy is that no motion capture from healthy subjects is necessary for defining the movement of the device, and that it can be customized relative to the values of the parameters describing the system. The computed torque with control allocation approach can be used to obtain reference input trajectories for any possible architecture of PLLO once that the reference trajectories in the space of the angular joints are calculated.

The main assumption for designing the tracking controllers is that the computer has authority over both the actuators of the PLLO, and the loads applied by the user at the shoulders. Choosing a pool of candidates consisting of finite time horizon LQR controllers, we rely on our performance metric based on reachability analysis to assess the robustness against parameter uncertainty of the STS movement attained by each of the candidates. We denote the gain that optimizes the performance metric as $K^{\star}_{\mathrm{LQR}}(t)$. For minimizing the number of sensors in the PLLO, we find a Kalman-Bucy filter gain $L^{\star}_{\mathrm{KF}}(t)$ that coupled with $K^{\star}_{\mathrm{LQR}}(t)$ in an LQG scheme, implements an output feedback controller for the nonlinear dynamics of the three-link planar robot that leads to successful simulations of the STS movement in the presence of parameter uncertainty, and noise measurement. Once that these couple of time-varying gains are computed, one can proceed to implement the controller in the PLLO.

Since in reality the loads at the shoulders are applied solely by the user, in order to evaluate through simulation if a user would be able to coordinate with the control input commanded to the actuators of the PLLO by $K^{\star}_{\mathrm{LQR}}(t)$ through training, we resorted to an ILC algorithm to abstract the way in which a user shapes the loads applied at the shoulders over 30 consecutive trials to perform the STS movement during rehabilitation and physical therapy sessions. The learning and feedback gains of the ILC algorithm are tuned with 10,000 iterations of a gradient free optimization method under the basis that a human would have tuned the gains for the precise movement of the upper limbs in an optimal way, since birth. Because the simple ILC algorithm manages to synchronize with the controller of the PLLO in our tests, despite the factors that are deliberately introduced to

hinder learning, we conclude that taking further steps towards human testing with $K^{\star}_{\text{LQR}}(t)$ as the controller of the PLLO makes sense, as the learning process of an actual human is more complex. Notice that this analysis does not result in changes on the implementation of the actual controller in the PLLO.

Similarly to the test with the ILC as a proxy for human action at the shoulders, the tests against model uncertainty only encourage moving forward with the implementation of the LQG scheme with $K^{\star}_{\text{LQR}}(t)$ and $L^{\star}_{\text{KF}}(t)$ in the actual PLLO, but do not introduce additional changes to the controller.

We believe that the techniques in this work can set a good framework to systematically choose actuators of PLLOs to fit a larger variety of users, estimate if a prospective user has enough upper body strength to safely perform the STS movement, quantitatively study sit-back or step failures, and develop a protocol for better assessing the robustness of the STS movement in clinical trials. This would then help to close the gap between PLLOs and standing wheelchairs, which still remain the most reliable mobility solution for patients with complete paraplegia.

The feedback approach explored in this work has an explicit time dependance on the reference trajectories; however, in practice, the user of a PLLO might pause or act at a different time scale, which motivates exploring path dependant controllers in the future, such as the one proposed in [53].

Given the complexity of the closed-loop dynamics of the system, estimating the sensitivity bounds for computing the over-approximation functions in the performance metric required a time consuming sampling of the parameter interval. Improving this procedure is another appealing research direction.

Additionally, the control problem could be formulated with a Linear Fractional Transformation (LFT) framework, in order to apply a μ synthesis method [54] for obtaining a finite time horizon controller that is inherently robust to both parameter, and model uncertainties.

Appendix A

Motion Planning in the Space of θ

This appendix illustrates that using cubic expressions with zero slope boundary conditions to design the reference trajectory $\hat{\theta}(t) := \left[\hat{\theta}_1(t); \hat{\theta}_2(t); \hat{\theta}_3(t)\right]$ for connecting the starting $\hat{\theta}(t_0)$ and final $\hat{\theta}\left(t_f\right)$ angular positions of a STS movement leads to unrealistic configurations for the links of the robot in Figure 2.1, which represent the segments of the shanks, thighs, and torso of a PLLO and its user. For this purpose, we compute a reference trajectory in the space of θ over the time horizon $t \in \left[t_0, t_f\right]$ as

$$\hat{\theta}(t) = \hat{\theta}(t_0) + \left(\hat{\theta}\left(t_f\right) - \hat{\theta}(t_0)\right)\Theta\left(t, t_f\right), \tag{A.1}$$

where $\Theta\left(t, t_f\right) := -2\frac{t^3}{t_f^3} + 3\frac{t^2}{t_f^2}$ is the only cubic polynomial satisfying $\dot{\Theta}\left(t_0, t_f\right) = \dot{\Theta}\left(t_f, t_f\right) = 0$, $\Theta\left(t_0, t_f\right) = 0$, and $\Theta\left(t_f, t_f\right) = 1$.

We obtain the reference trajectories for the STS movements in the space of θ by plugging the initial and final angular positions for STS 1 and STS 2 defined in Section 2.5 into (A.1). To solve (2.22) for $\hat{u}(t)$ we take into account the architecture of a minimally actuated PLLO at the hips, $W_u = \mathrm{diag}([1, 1, 10, 1])$, and the nominal parameter value $\hat{p}$ in (2.23). The corresponding trajectories for the CoM $\hat{y}(t)$ are computed using $x = \left[\hat{\theta}(t); \dot{\hat{\theta}}(t)\right]$, and $p = \hat{p}$ in (4.18). These reference trajectories are shown in dashed white lines in Figures A.1 to A.3, where the collection of continuous blue and red lines represent the behavior of the system (2.2) under the action of the feedback linearizing input (3.4), and when the values for p are randomly chosen, within the interval $\left[\underline{p}, \overline{p}\right]$ in Table 3.1, by Latin hypercube sampling of 200 experiments.

Figures A.1a to A.1c show that the reference trajectory for STS 1 has no movement of the shanks about the joint of the ankles, involves no flexion of the hips, and it can be inferred from the almost mirrored evolution of $\theta_2(t)$ and $\theta_3(t)$ that the inclination of the torso with respect to the vertical remains small. Although the corresponding torques and forces in Figure A.2 remain within the admissible bounds in (5.3), and the trajectories of the CoM in Figures A.3 do not raise concerns about sit-back or step failures [15] with the offsets caused by the parameter uncertainty, the motion of the joints does look very stiff and unnatural for a human.

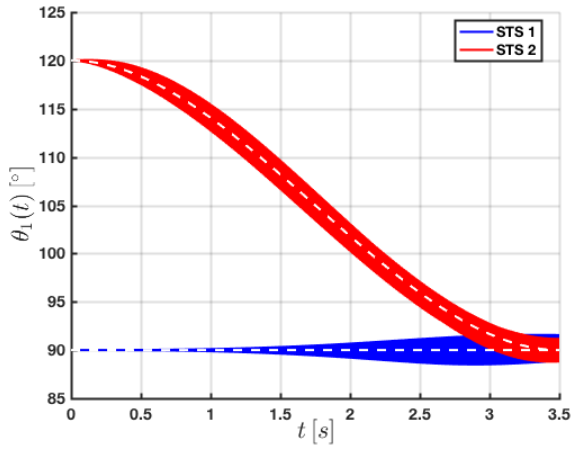

(a) Angular position of link 1 relative to the horizontal.

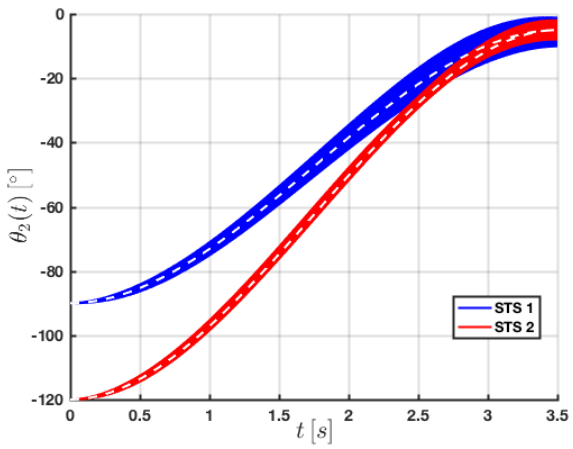

(b) Angular position of link 2 relative to link 1.

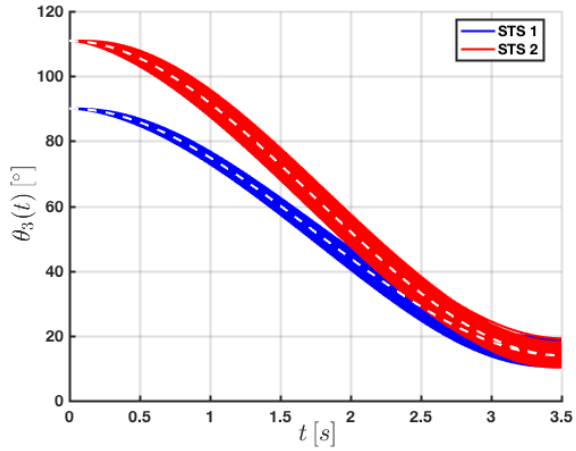

(c) Angular position of link 3 relative to link 2.

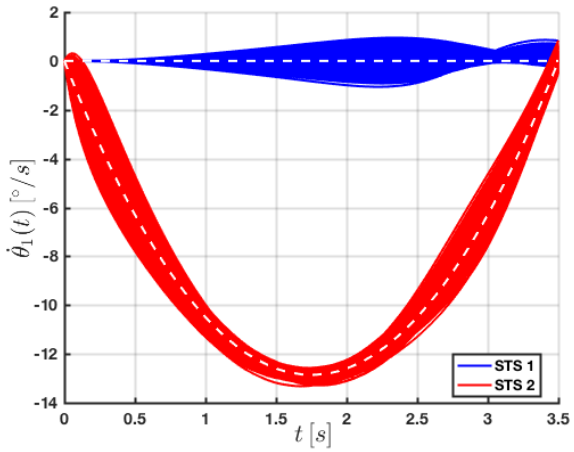

(d) Angular velocity of link 1.

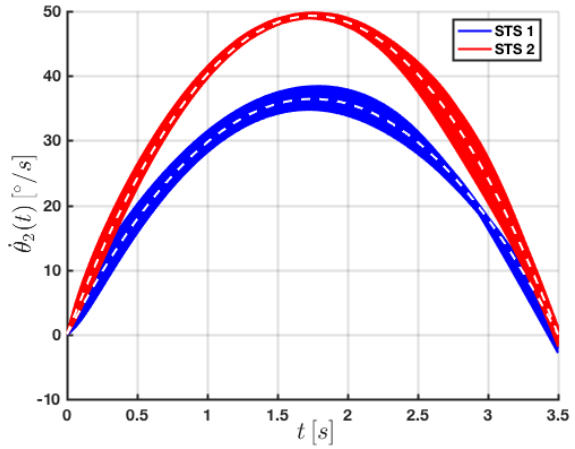

(e) Angular velocity of link 2.

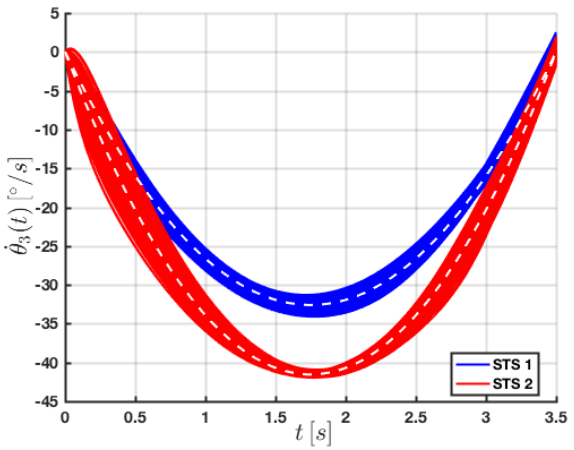

(f) Angular velocity of link 3.

Figure A.1: Angular positions and velocities of the links of the robot under feedback linearization and control allocation for two relevant STS movements planned in the space of θ.

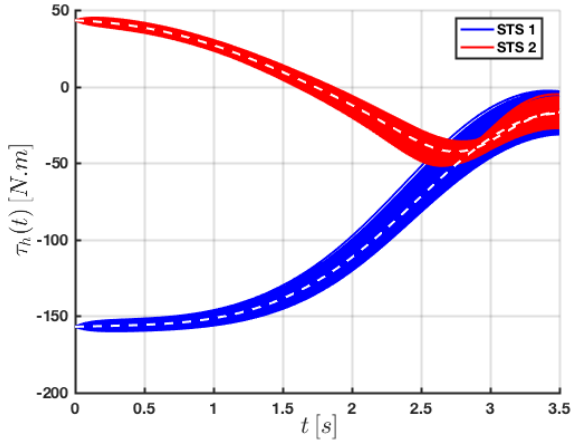

(a) Torque applied at the hips by the powered lower limb orthosis.

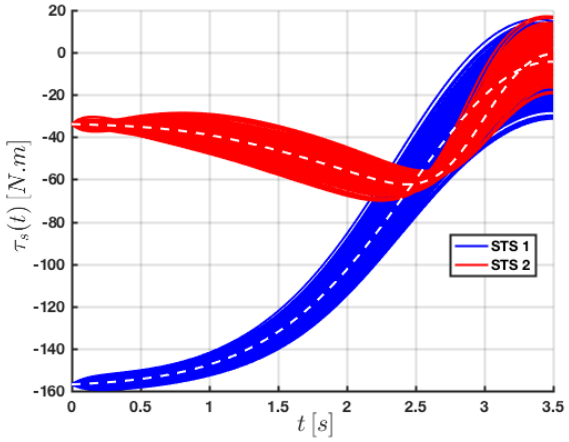

(b) Torque at the shoulders of the user.

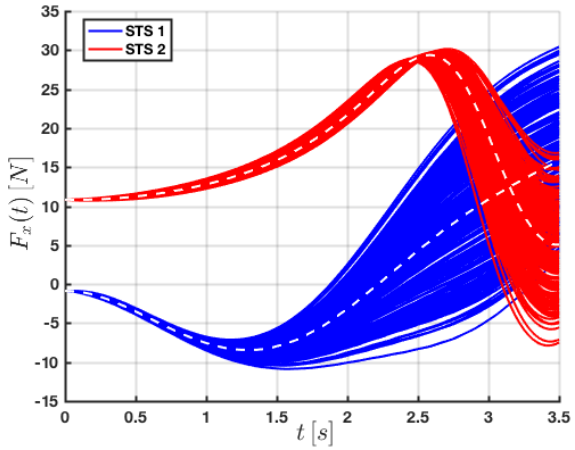

(c) Horizontal force at the shoulders of the user.

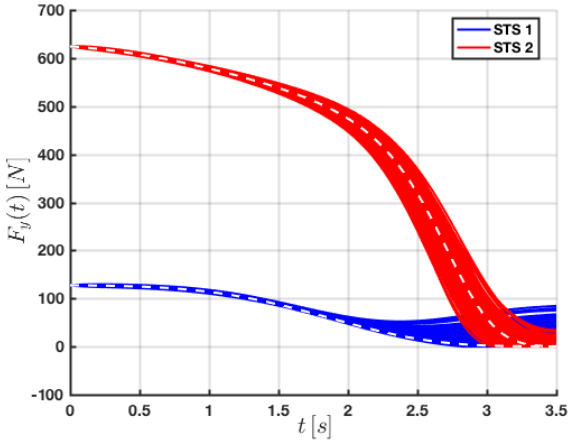

(d) Vertical force at the shoulders of the user.

Figure A.2: Feedback linearizing input for two relevant STS movements planned in the space of θ.

The extension of the ankles, knees, and hips observed in Figures A.1a to A.1c for STS 2 seems plausible for a quasi-static strategy [13], and the corresponding loads in Figure A.2 remain within the bounds in (5.3). Nevertheless, the backward displacement and velocity that exhibits the CoM in Figures A.3e and A.3f make a back-sit failure bound to happen in the presence of greater parameter uncertainties, deeming the reference trajectory in the space of θ unsuitable.

By giving direct consideration of proper extension of the knees and natural looking trajectories of the CoM, our motion planning strategy in the space of z proves to be more suitable to set safe and biomechanically sound reference trajectories for these STS movements, as exposed in Section 2.5.

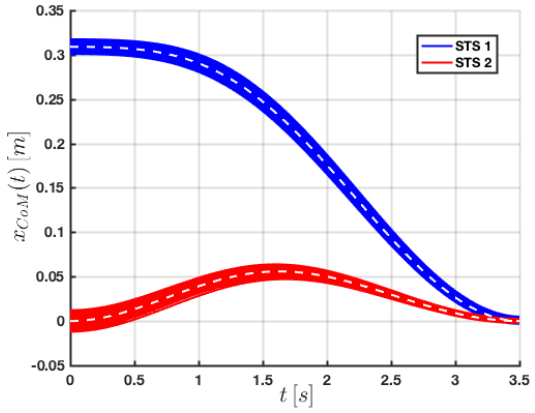

(a) Position trajectories of the three-link robot CoM.

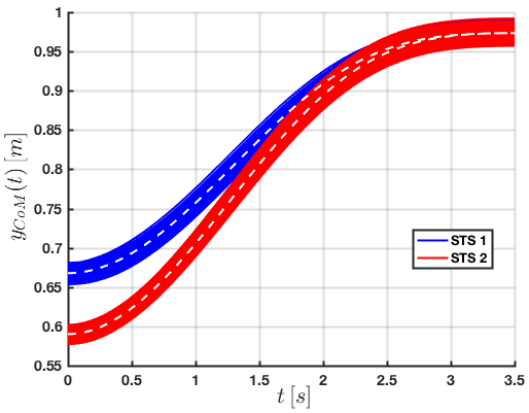

(b) Velocity trajectories of the three-link robot CoM.

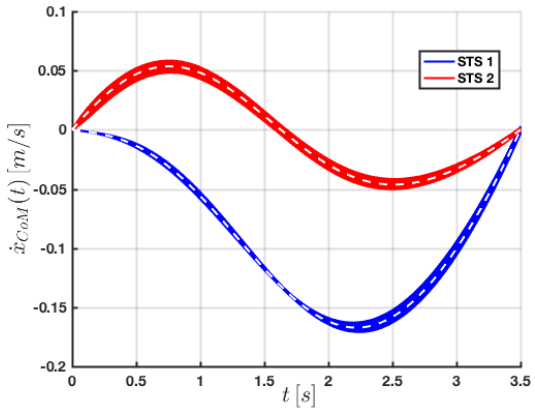

(c) Position trajectories of the three-link robot CoM.

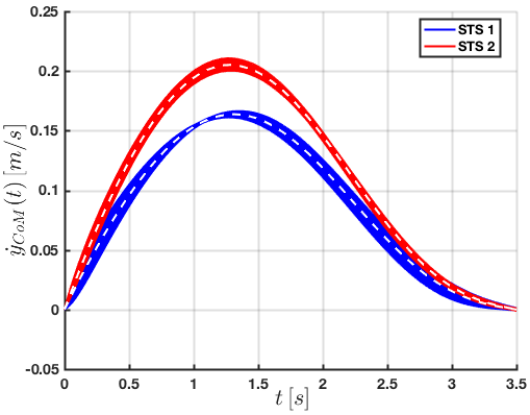

(d) Velocity trajectories of the three-link robot CoM.

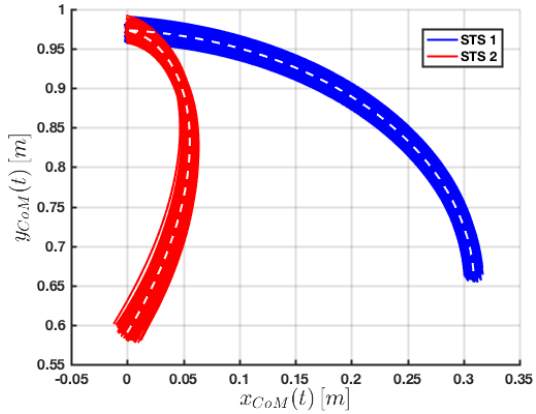

(e) Position trajectories of the three-link robot CoM.

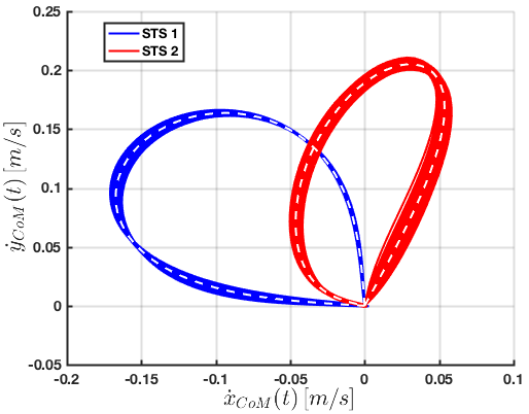

(f) Velocity trajectories of the three-link robot CoM.

Figure A.3: Center of mass trajectories achieved with feedback linearization and control allocation for two relevant STS movements planned in the space of θ.

Bibliography

[1] R. Vertechy, D. Accoto, and M. Fontana, "Wearable robotics [from the guest editors]," *IEEE Robotics Automation Magazine*, vol. 21, pp. 19–110, Dec 2014.

[2] National Spinal Cord Injury Statistical Center, "Spinal cord injury facts and figures at a glance," March 2018. URL https://www.nscisc.uab.edu.

[3] Ekso Bionics, "Ekso GT," May 2019. URL https://eksobionics.com/eksohealth/eksogt/patients/.

[4] Cyberdyne, "HAL for medical use," May 2019. URL https://www.cyberdyne.jp/english/products/LowerLimb_medical.html.

[5] Parker Hannifin Corp, "Indego personal features," May 2019. URL http://www.indego.com/indego/en/Indego-Personal.

[6] ReWalk Robotics, "ReWalk personal 6.0," May 2019. URL https://rewalk.com/rewalk-personal-3/.

[7] Roki Robotics, "An Exo created for you," May 2019. URL http://pro031jet.wixsite.com/roki.

[8] M. G. McKinley, *Design of Lightweight Assistive Exoskeletons for Individuals with Mobility Disorders*. PhD thesis, University of California, Berkeley, CA, 2014. pp. 46-48.

[9] SuitX, "PhoeniX Medical Exoskeleton," May 2019. URL https://www.suitx.com/phoenix-medical-exoskeleton.

[10] E. Strickland, "To build the best robotic exoskeleton, make it on the cheap," April 2016. URL https://tinyurl.com/y4pvzxlu.

[11] Wandercraft, "Exoskeleton companion of the mobility impaired," May 2019. URL http://wandercraft.eu/en/exoskeleton/.

[12] Rex Bionics, "Rex technology," May 2019. URL https://www.rexbionics.com/us/product-information/.

[13] M. Galli, V. Cimolin, M. Crivellini, and I. Campanini, "Quantitative analysis of sit to stand movement: Experimental set-up definition and application to healthy and hemiplegic adults," *Gait and Posture*, vol. 28, no. 1, pp. 80–85, 2008.

[14] M. A. Hughes and M. L. Schenkman, "Chair rise strategy in the functionally impaired elderly," *Journal of Rehabilitation Research and Development*, vol. 33, no. 4, pp. 409–412, 1996.

[15] W. R. Eby and E. Kubica, "Modeling and control considerations for powered lower-limb orthoses: A design study for assisted STS," *ASME Journal of Medical Devices*, vol. 1, no. 2, pp. 126–139, 2006.

[16] J. I. Reid, *Control Strategies for a Minimally Actuated Medical Exoskeleton for Individuals with Paralysis*. PhD thesis, University of California, Berkeley, CA, 2012.

[17] N. A. Alibeji, V. Molazadeh, F. Moore-Clingenpeel, and N. Sharma, "A muscle synergy-inspired control design to coordinate functional electrical stimulation and a powered exoskeleton: Artificial generation of synergies to reduce input dimensionality," *IEEE Control Systems Magazine*, vol. 38, pp. 35–60, Dec 2018.

[18] O. Harib, A. Hereid, A. Agrawal, T. Gurriet, S. Finet, G. Boeris, A. Duburcq, M. E. Mungai, M. Masselin, A. D. Ames, K. Sreenath, and J. W. Grizzle, "Feedback control of an exoskeleton for paraplegics: Toward robustly stable, hands-free dynamic walking," *IEEE Control Systems Magazine*, vol. 38, pp. 61–87, Dec 2018.

[19] G. Lv, H. Zhu, and R. D. Gregg, "On the design and control of highly backdrivable lower-limb exoskeletons: A discussion of past and ongoing work," *IEEE Control Systems Magazine*, vol. 38, pp. 88–113, Dec 2018.

[20] W. Dixon, "Control systems for assistive and rehabilitation robotics: A introduction to the special issue," *IEEE Control Systems Magazine*, vol. 38, pp. 32–34, Dec 2018.

[21] O. Narvaez-Aroche, A. Packard, and M. Arcak, "Motion planning of the sit-to-stand movement for powered lower limb orthoses," *ASME 2017 Dynamic Systems & Control Conference*, October 2017. Tysons, VA, USA.

[22] O. Narvaez-Aroche, A. Packard, and M. Arcak, "Finite time robust control of the sit-to-stand movement for powered lower limb orthoses," *2018 American Control Conference*, June 2018. Milwaukee, WI, USA.

[23] O. Narvaez-Aroche, P.-J. Meyer, M. Arcak, and A. Packard, "Reachability analysis for robustness evaluation of the Sit-to-Stand movement for powered lower limb orthoses," *ASME 2018 Dynamic Systems & Control Conference*, October 2018. Atlanta, GA, USA.

[24] O. Narvaez-Aroche, P.-J. Meyer, S. Tu, A. Packard, and M. Arcak, "Robust control of the sit-to-stand movement for a powered lower limb orthosis," *CoRR*, vol. abs/1811.07011, 2018.

[25] B. Baunsgaard *et al.*, "Gait training after spinal cord injury: safety, feasibility and gait function following 8 weeks of training with the exoskeletons from Ekso Bionics," *Spinal Cord*, vol. 56, no. 2, pp. 106–116, 2018.

[26] G. Zeilig, H. Weingarden, M. Zwecker, I. Dudkiewicz, A. Bloch, and A. Esquenazi, "Safety and tolerance of the Rewalk™ exoskeleton suit for ambulation by people with complete spinal cord injury: A pilot study," *The Journal of Spinal Cord Medicine*, vol. 35, no. 2, pp. 96–101, 2012.

[27] M. Fujimoto and L. Chou, "Dynamic balance control during Sit-to-Stand movement: An examination with the center of mass acceleration," *Journal of Biomechanics*, vol. 45, pp. 543–548, 2012.

[28] G. Gede, D. L. Peterson, A. S. Nanjangud, J. K. Moore, and M. Hubbard, "Constrained multibody dynamics with Python: From symbolic equation generation to publication," *ASME 9th International Conference on Multibody Systems, Nonlinear Dynamics, and Control*, August 2013.

[29] J. E. Slotine and W. Li, *Applied Nonlinear Control*. Upper Saddle River, New Jersey: Prentice Hall, 1991.

[30] T. A. Johansen and T. I. Fossen, "Control allocation - a survey," *Automatica*, vol. 49, no. 5, pp. 1087–1103, 2013.

[31] W. G. Janssen, J. B. Bussmann, H. L. Horemans, and H. J. Stam, "Validity of accelerometry in assessing the duration of the sit-to-stand movement," *Journal of the International Federation for Medical and Biological Engineering & Computing*, vol. 46, no. 9, pp. 879–887, 2008.

[32] A. Tsukahara, R. Kawanishi, Y. Hasegawa, and Y. Sankai, "Sit-to-stand and stand-to-sit transfer support for complete paraplegic patients with robot suit HAL," *Advanced Robotics*, vol. 24, no. 11, pp. 1615–1638, 2010.

[33] A. Isidori, *Nonlinear Control Systems*. Communications and Control Engineering, London: Springer-Verlag, third ed., 1995.

[34] M. Athans and P. L. Falb, *Optimal Control: An Introduction to the Theory and its Applications*. Lincoln Laboratory Publications, New York: McGraw-Hill Inc, 1966.

[35] M. D. McKay, R. J. Beckman, and W. J. Conover, "Comparison of three methods for selecting values of input variables in the analysis of output from a computer code," *Technometrics*, vol. 21, no. 2, pp. 239–245, 1979.

[36] P. Seiler, R. M. Moore, C. Meissen, M. Arcak, and A. Packard, "Finite horizon robustness analysis of LTV systems using integral quadratic constraints," *Automatica*, vol. 100, pp. 135 – 143, 2019.

[37] R. M. Moore, "Finite horizon robustness analysis using integral quadratic constraints," Master's thesis, University of California, Berkeley, CA, 2015.

[38] A. Marcos and S. Bennani, "LPV modeling, analysis and design in space systems: Rationale, objectives and limitations," *AIAA Guidance, Navigation, and Control Conference*, p. 5633, 2009.

[39] E. Asarin, O. Maler, and A. Pnueli, "Reachability analysis of dynamical systems having piecewise-constant derivatives," *Theoretical Computer Science*, vol. 138, no. 1, pp. 35–65, 1995.

[40] A. A. Kurzhanskiy and P. Varaiya, "Ellipsoidal techniques for reachability analysis of discrete-time linear systems," *IEEE TAC*, vol. 52, no. 1, pp. 26–38, 2007.

[41] A. Chutinan and B. H. Krogh, "Computational techniques for hybrid system verification," *IEEE Transactions on Automatic Control*, vol. 48, no. 1, pp. 64–75, 2003.

[42] I. Mitchell and C. J. Tomlin, "Level set methods for computation in hybrid systems," in *Hybrid Systems: Computation and Control*, pp. 310–323, Springer, 2000.

[43] P.-J. Meyer, S. Coogan, and M. Arcak, "Sampled-data reachability analysis using sensitivity and mixed-monotonicity," *IEEE Control Systems Letters*, vol. 2, no. 4, pp. 761–766, 2018.

[44] H. K. Khalil, *Nonlinear Systems*. Pearson, third ed., 2001.

[45] D. L. Bartel, D. T. Davy, and T. M. Keaveny, *Orthopaedic biomechanics: mechanics and design in musculoskeletal systems*. Upper Saddle River, NJ: Pearson, 2006.

[46] D. A. Bristow, M. Tharayil, and A. G. Alleyne, "A survey of iterative learning control," *IEEE Control Systems*, vol. 26, pp. 96–114, June 2006.

[47] M. Arif and H. Inooka, "Iterative manual control model of human operator," *Biological Cybernetics*, vol. 81, pp. 445–455, Nov 1999.

[48] Y. Nesterov and V. Spokoiny, "Random gradient-free minimization of convex functions," *Foundations of Computational Mathematics*, vol. 17, no. 2, p. 527–566, 2017.

[49] H. Mania, A. Guy, and B. Recht, "Simple random search provides a competitive approach to reinforcement learning," in *Neural Information Processing Systems*, 2018.

[50] I. B. Rhodes, "A tutorial introduction to estimation and filtering," *IEEE Transactions on Automatic Control*, vol. 16, pp. 688–706, December 1971.

[51] ams AG, "As5048b high resolution position sensor," April 2019. URL `https://ams.com/as0548b`.

[52] M. D. Kauther, M. Piotrowski, B. Hussmann, S. Lendemans, and C. Wedemeyer, "Cervical range of motion and strength in 4,293 young male adults with chronic neck pain," *European Spine Journal*, vol. 21, no. 8, pp. 1522–1527, 2012.

[53] J. Hauser and R. Hindman, "Maneuver regulation from trajectory tracking: Feedback linearizable systems," in *Proceedings of IFAC Symposium on Nonlinear Control Systems Design*, pp. 595–600, 1995.

[54] J. Doyle, A. Packard, and K. Zhou, "Review of LFTs, LMIs, and μ," in *Proceedings of the 30th IEEE Conference on Decision and Control*, pp. 1227–1232 vol.2, Dec 1991.